Universidade do Minho

Escola de Engenharia

Bahman Ghiassi

Durability analysis of bond between composite materials and masonry substrates

Tese de Doutoramento em Engenharia Civil

Trabalho efectuado sob a orientaçao do
Professor Doutor Paulo B. Lourenço
Co-orientador
Professor Doutor Giancarlo Marcari

October 2013

Acknowledgements

The research reported in this thesis has been carried out at the Civil Engineering Department of University of Minho, Portugal, under the supervision of Prof. Paulo Lourenço and co-supervision of Dr. Giancarlo Marcari. This work was partly funded by project FP7-ENV-2009-1-244123-NIKER of the 7th Framework Programme of the European Commission, and partly by the Portuguese Foundation for Science and Technology (FCT) under the grant SFRH/BD/80697/2011, both gratefully acknowledged.

I would like to express my deepest gratitude to my supervisor Prof. Paulo Lourenço for his guidance and patience along these years. He provided me continuous support for following my ideas and development of the work presented here. Also, I would like to thank to Dr. Giancarlo Marcari for his care and guidance throughout this work. I would like to thank Dr. Daniel Oliveira for all his great support, presence, inspirations and scientific discussions during all these years. Above the scientific cooperation, a strong friendship was established between all of us during this work which I really appreciate it.

I would like to thank Dr. Jose Xavier from University of Trás-os-Montes e Alto Douro, Portugal, for collaboration in performing tests with Digital Image Correlation technique and also the friendship established between us. I would also like to thank Sandra Silva for collaboration in performing Infrared Thermography tests. Her patience, presence and professionalism are greatly acknowledged. I would also like to thank Els Verstrynge from Department of Civil Engineering of University of KU Leuven, Belgium, for collaboration in performing Acoustic Emission tests, scientific discussions and also her friendship.

I would also like to thank the technicians of the laboratory of the Civil Engineering Department of University of Minho (LEST), engineers Marco, Mateus, Carlos, Fernando Pokee and Carlos Palha for the extreme efforts and assistance during my experimental tests. I am also grateful to all my friends that supported and encouraged me and stayed near me in the tough times during the execution of this work.

Finally, I would like to dedicate this work to my family who supported me all the way until here.

Abstract

In recent years, composites materials have been increasingly accepted as effective strengthening technique for civil engineering structures, particularly in the case of reinforced concrete. The reliability of this technique, when externally applied, depends on the long-term bond behavior between these materials and the masonry substrate, but research in this area is still very limited.

The main purpose of this thesis is to create a basis for a general approach to durability of masonry components strengthened with composite materials. As far as the research method is concerned, a combined experimental and numerical approach has been chosen. Through systematic testing, fundamental knowledge is developed concerning the physical and mechanical properties of the basic materials and the strengthened components under environmental degradation. The strengthened specimens are subjected to different hygrothermal conditions including water immersion and cycles of temperature with constant relative humidity. Non-destructive investigation tests are made for both un-exposed and exposed specimens. Analysis of the interface behavior for different exposure conditions are carried out and the results are discussed. Predictive models are also used for simulating the observed degradation and the reliability of each model is investigated in comparison to experimental results.

The numerical studies are conducted at two levels. Firstly, the bond behavior is modeled following detailed and simplified approaches. In the detailed approach, all material constituents with suitable constitutive laws are modeled. The model provides valuable information regarding less known aspects of bond behavior such as effect of mortar joints. In the simplified approach, the bond behavior is modeled using interface elements. A tri-linear bond-slip law is proposed based on the available experimental data and is used as the constitutive law for the interface elements. Both models are validated with experimental data. Secondly, the effect of local bond degradation on the global response of FRP-strengthened masonry panels is investigated. For the bond between FRP and masonry, the interface elements are used adopting the proposed bond-slip law. Based on the experimental results produced in this study, a degradation model is proposed and used for the interface behavior. The nonlinear performance of the strengthened panels after ageing in different environmental conditions is investigated and discussed.

Keywords: Durability, masonry, composite materials, bond, accelerated ageing, numerical analysis, degradation modeling.

Resumo

Nos últimos anos, os materiais compósitos têm sido cada vez mais aceites como uma técnica de reforço eficaz para estruturas de engenharia civil, particularmente em betão armado. A fiabilidade desta técnica, quando aplicada por colagem externa, depende do comportamento da aderência, a longo prazo entre esses materiais e o substrato de alvenaria, mas a investigação nesta área é ainda muito limitada.

O principal objetivo deste trabalho é criar uma base para uma abordagem geral sobre a durabilidade dos componentes de alvenaria reforçados com materiais compósitos, recorrendo a uma abordagem experimental e numérica. Através de ensaios desenvolve-se conhecimento fundamental sobre as propriedades físicas e mecânicas dos materiais, e sobre os componentes reforçados submetidos a degradação ambiental. Os provetes reforçados são submetidos a diferentes condições higrotérmicas, incluindo imersão em água e ciclos de temperatura com humidade relativa constante. Ensaios não destrutivos são realizados sobre provetes não-expostos e expostos. O comportamento de interface para diferentes condições de exposição é discutido. Modelos de previsão são também utilizadas para simular a degradação observada e a fiabilidade de cada modelo é investigada em comparação com os resultados experimentais.

Os estudos numéricos são conduzidos a dois níveis. Primeiro, o comportamento da aderência é modelado seguindo abordagens detalhadas e simplificadas. Na abordagem detalhada todos os componentes materiais com leis constitutivas adequadas são modelados. O modelo fornece informações sobre aspetos menos conhecidos da aderência, como o comportamento das juntas de argamassa. Na abordagem simplificada, o comportamento da aderência é modelado usando elementos da interface. Uma lei trilinear de comportamento do tipo *bond-slip* é proposta com base nos dados experimentais para elementos de interface. Ambos os modelos são validados com dados experimentais. Em segundo lugar, os efeitos locais de degradação da aderência sobre a resposta global dos painéis reforçados de alvenaria são investigados. Para a aderência entre FRP e alvenaria utilizam-se elementos da interface, adotando-se a lei de comportamento proposta. Com base nos resultados experimentais produzidos neste estudo, propõe-se um modelo de degradação que se utiliza o comportamento da interface. O desempenho não linear de painéis reforçados, após envelhecimento em diferentes condições ambientais, é investigado e discutido.

Palavras-chave: Durabilidade, alvenaria, materiais compósitos, aderência, envelhecimento acelerado, análise numérica, modelação da degradação.

Contents

Chapter 1

Introduction

Seismic assessment and strengthening of historical masonry structures has always been a challenge for engineers due to their unknown and complex behavior. The variations of masonry structures and materials have made this challenge more complicated. Although several techniques have been proposed and used for strengthening of these structures, the choice of a suitable material and strengthening technique is still a critical issue.

Modern composite materials such as fiber reinforced polymers (FRPs) have been accepted as effective strengthening materials for civil engineering structures, particularly in reinforced concrete. FRPs provide several advantages such as high mechanical properties, light weight and ease of application which have made them interesting for strengthening purposes. FRPs have also received an extensive attention in the last decades for externally strengthening of masonry structures.

In external strengthening techniques, the efficacy and reliability of the strengthening strongly depend on the short- and long-term behavior of bond between the composite material and the substrate. Investigation into the long-term bond behavior under service conditions is a key issue since service failures due to inaccurate assessment of bond response may result in costly repair or premature component' replacement. In this regard, it is worth noting that modern guidelines (CNR-DT 200/2004 [1] or ACI 440.7R-10 [2]) prescribe that FRP-based strengthening should meet requirements concerning the ultimate limit state (ULS), and additionally the service limit state (SLS). Hence, some reduction factors, which are not verified with experimental results, are proposed to account for the durability.

The durability of FRP composites or masonry itself due to environmental effects has been the subject of much interest for the last 30 years. Relevant degradation agents that can affect the durability or long-term in service behavior of FRP or masonry include cycles of temperature and/or moisture, UV radiation, carbon dioxide or alkaline environment. The behavior of the FRP matrices

alone is complex and their interaction with a variety of fiber types and configurations can increase this complexity. The interactions are time-dependent over years, and so FRP composites, masonry and FRP-strengthened masonry components often have properties that vary during their lifespan. In particular, the mechanical properties of FRP and masonry may decline considerably with time. The mechanisms responsible in FRP occur at the micro-structural level, normally at the fiber-matrix interface and inside the matrix. Moreover, service behavior of wet lay-up applications is frequently different for each fiber-matrix combination, especially as novel matrices are combined with a range of fibers such as biocomposites of flax and hemp, glass, basalt or steel fibers. Some fiber-matrix combinations are particularly prone to certain degradation mechanisms, while the dominant degradation mechanisms in other fibers are still the subject of research and debate.

FRP durability studies have been generally performed for high specific value applications (e.g. aerospace or military), and thus based on a short-life, strict quality control and monitoring and effective maintenance paradigm. This is in stark contrast to composite materials normally used in low specific value applications in civil engineering, where this philosophy does not apply.

Analysis of in service long-term behavior of FRP-masonry components involves laboratory and field testing, accelerated ageing and advanced computational modeling, but research in this area is still very scarce ([3]). Only limited studies have been conducted on durability of FRP externally applied to masonry ([4-6]). Available laboratory-based results on FRP composites need therefore to be supported by materials characterization and experimental activity on FRP-masonry components (Karbhari et al. [7], ASTM E632 [8]) in view of: (i) understanding the effects of critical degradation agents on the bond in regard to the serviceability state; (ii) assessing the bond behavior with the aim of accelerated ageing tests and (iii) developing feasible computational models capable to simulate degradation mechanisms and damage from accelerated ageing.

It is observed that standardized durability test procedures based on accelerated ageing methods are available in literature for masonry or FRP alone ([9-12]). As recognized in several research works, however, the real environmental conditions cannot be accurately simulated or reproduced by laboratory-based accelerated tests. Moreover, these environmental conditions may affect the mechanical, physical, or chemical properties of some materials while they might not change the properties of other ones. However, accelerated ageing tests represent the most common method to enhance durability of building materials. As for masonry systems, the test methods consist of applying repeated wet-dry cycles, thermal cycles and salt crystallization, while for FRP the methods deal with wet-dry cycle exposure, thermal cycles, UV or alkali exposure.

On the contrary, experimental methods to assess the long-term durability behavior of masonry reinforced with composite materials still lack standardization. Among the critical aspects

in this field that need to be elucidated are: (i) the degradation mechanisms of bond in FRP-masonry systems; (ii) the effect of the synergistic action of two or more degradation agents; (iii) the correlation between accelerated ageing and in-service environmental conditions; (iv) bond quality assessment techniques for structural health monitoring purposes and (iii) predictive models for simulation of long-term behavior.

Reliable numerical models and computational strategies able to capture the degradation mechanisms of bond due to environmental conditions are deemed. In this regard it is worth noting that predictive models for performance assessment of strengthened components in service conditions are still not well recognized. Moreover, few studies are available for the prediction of long-term durability of composites based on the coupled effects of different degradation mechanisms, see e.g. Martin et al. [13] and CIB W080 [14].

The main objective of this thesis is to investigate the degradation of bond in FRP-strengthened masonry systems under hygrothermal conditions. Application of advance nondestructive techniques for bond quality assessment and development of refined numerical models for engineering purposes are also among the main goals. It is expected that the overall research work carried out in this study provide a comprehensive understanding of the effect of the cyclic ageing on debonding mechanisms, with first contribution on future professional guidelines for design and maintenance purposes. The detailed objectives of the work are as follows:

- Build systematic knowledge for long-term behavior of bond between masonry and composite materials through an integrated experimental activity. Water immersion and three different accelerated hygrothermal exposure tests, representing dry, wet and cold regions will be performed. The tests will provide a baseline for further durability studies on FRP-strengthened masonry and give insight to the main degradation mechanisms and agents.
- Develop a large ageing database of properties of masonry constituents and composite materials as well as of the bond behavior. Fundamental ageing characterization of basic materials, namely brick, epoxy resins and FRP coupons will be achieved. As for the composite materials, glass fibers will be used due to their lower cost and better stiffness compatibility with masonry.
- Propose predictive models based on the obtained experimental results for modeling the long-term behavior of materials and bond in the considered exposure conditions. The models can be used as input for numerical or analytical modeling approaches.
- Application of advanced full-field measurement and nondestructive testing methods for bond characterization and quality assessment.

- Develop a fracture-based interface model for the strengthened specimens in which the mechanism of stress transfer across the bond-line is predicted from the experimental bond–slip relationships. The practice oriented model will include bond degradation mechanisms for different cyclic ageing, being its reliability and accuracy assessed by comparing with test data.
- Engineering application of the proposed interface model will be performed. In particular, the effects of local materials and bond degradation on the global performance of masonry components strengthened with composite materials will be investigated.

Based on the above mentioned objectives, the thesis outline is defined as shown in Figure 1-1. The thesis is presented in nine chapters including this introduction.

Chapter 2 provides a review of the available literature and current understandings about the subjects covered in this thesis. The bond mechanisms, available bond design models and numerical and experimental approaches adopted by different authors are primarily presented and discussed. This is followed by a discussion on environmental durability of bond and degradation mechanisms affecting its performance. After that, a review of available experimental and numerical studies on durability of bond and degradation predictive models is presented.

Chapter 3 presents the outline of the experimental program and detailed explanation of the test methods. The chapter includes characterization of the mechanical properties of the materials, specimens preparation techniques, environmental exposures and post-ageing test methods.

Chapter 4 and 5 present the results obtained from water immersion and hygrothermal exposure tests, respectively. The results include degradation data of mechanical properties of the materials and bond behavior. Durability predictive models are finally used for simulating the experimental degradation, which can be used as input for analytical and numerical modeling approaches.

Chapter 6 presents the application of advanced full-field measurement and nondestructive testing techniques, adopted here, for debonding characterization and bond quality assessment. The techniques include Digital Image Correlation (DIC), Infrared Thermography (IR) and Acoustic Emission (AE). The principles of each technique as well as the test method and the obtained results are presented and discussed.

Chapter 7 discusses numerical modeling of the bond behavior at detailed and simplified levels. The models are experimentally verified and advantages and disadvantages of each approach are analyzed. Based on the available experimental data, a simple bond-slip model is finally proposed and used for simplified numerical modeling approach.

Chapter 8 presents the effect of local bond degradation on the global performance of FRP-strengthened masonry components. The materials and bond degradation data are obtained from the

accelerated ageing tests and are used as the input for the numerical model. The performance of the strengthened components at the aged conditions are investigated and discussed.

Finally chapter 9 concludes the achievements and research findings and presents the research needs for the future work to be followed.

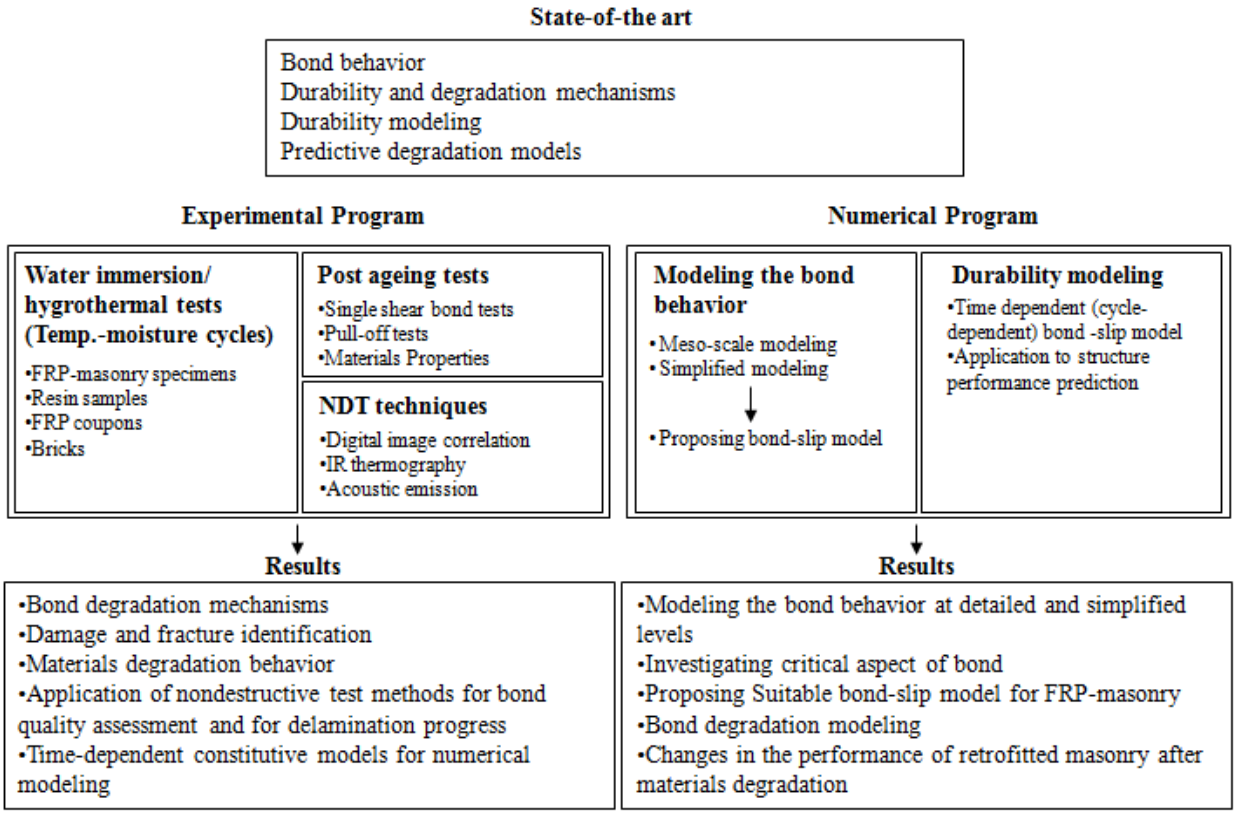

Figure 1-1: Thesis outline.

Chapter 2

Literature review on FRP-substrate bond

As the bond behavior is a key mechanism in the effectiveness of Fiber Reinforced Polymer (FRP) strengthened systems, a clear understanding of aspects such as durability and long-term performance is critical for structural design and service life prediction. It is well known that the bond behavior, and corresponding durability, is affected by different factors including the environmental condition, the composite material, the substrate, the interfacial adhesion and the surface preparation. Although durability of FRP composites and structural adhesives has been the subject of considerable research in the past years, the long-term durability of strengthened elements still requires attention, especially when innovative fiber-matrix combinations are used. Moreover, the available data on FRP composites and adhesives are scarce and sometimes not conclusive due to the variability of the used materials and adopted test methods. The lack of standard procedures for performing accelerated ageing tests has resulted in a large variety of test procedures adopted by different researchers. On the other hand, well established and reliable predictive models able to correlate accelerated ageing and in-service weathering are still missing.

This chapter presents a critical review on different aspects related to the durability of bond, addressing the following aspects: (i) the mechanisms involved in bond behavior; (ii) experimental and numerical studies related to the bond behavior in FRP-strengthened masonry elements; (iii) durability of bond and environmental degradation mechanisms; (iv) experimental and numerical studies on accelerated hygrothermal testing of FRP-strengthened elements; (v) durability prediction models;.(vi) nondestructive methods for bond durability assessment.

2.1 Bond behavior

The effectiveness of composite materials as an external strengthening technique is intrinsically dependent on the bond performance between the FRP and the masonry substrate. Any failure in the bond interface can lead to deterioration of composite action and result in a premature debonding

failure. The response of FRP-strengthened components has been extensively studied both analytically and experimentally with an emphasis on overall strengthening, ductility, and failure. However, detailed understanding of aspects such as failure initiation, interface bond mechanisms, and constituent property effects on local phenomena, still needs to be achieved.

2.1.1 Bond mechanics

The bond behavior between FRP composites and masonry and/or concrete substrates depends on many factors including the substrate strength, surface preparation, FRP mechanical properties (mainly stiffness), the FRP bonded length and FRP width. The bond between two materials can be due to any of the following six adhesion mechanisms [15-17]: adsorption, mechanical interlocking, diffusion, electrostatic, weak boundary layer theory and chemical bonding theory. The adsorption and mechanical interlocking theories are the main adhesion mechanisms in bonded systems (e.g. bonded joints or FRP-bonded concrete and masonry) [18], and will be explained briefly hereafter.

The adsorption theory, also known as the thermodynamic theory, applies to the adhesion resulted from the intermolecular forces between two materials which involves the surface energies developed between the atoms of the two surfaces. These forces between adhesive and substrate include: (a) Secondary bonds; (b) Van der Waals forces; (c) Hydrogen bonds; (d) Primary bonds; (e) Covalent; (f) Ionic; (g) Metallic and (h) Donor acceptor interactions which are intermediate between secondary and primary bonds. It has been experimentally observed that the secondary bonds are the main adhesion mechanisms in many adhesive joints [18]. The mechanical interlocking considers the adhesion as the result of mechanical interlocking between the adhesive penetrated into the pores of the substrate and the substrate's superficial surface. Therefore, it is related to the roughness of the substrate surface and the friction between the adhesive and the substrate.

When FRP passes across a crack on the substrate, the tensile stresses resulting from shear cracking must be transferred to the substrate. Before cracking the substrate, perfect bond between FRP and substrate is typically assumed [19]. When the substrate cracks and the load increases, there is a load level at which the shear stress at the crack tip reaches a peak and begins to decrease afterwards. This is followed by increment of the shear stress at the region adjacent of the crack tip. The decrease of the shear stress is the sign of crack progress in that region, while the increment of shear stress at the adjacent region shows that the stresses are being transferred there [20, 21]. This phenomenon, called delamination, progresses until the complete FRP debonding.

The bond behavior is usually evaluated based on the bond strength, strain profiles along the bonded length, local bond-slip laws and effective bond transfer length. Since the tensile strength of FRPs is relatively large, the bond strength is usually limited by the substrate shear strength or the

adhesion strength between the FRP and the substrate. It has been observed that the bond strength increases with increasing the bonded length. However, there is a length limit, called effective bond length, after which the bond strength does not increase. The specimens with long bonded lengths (longer than the effective bond length) show progressive delamination. During this progressive debonding, the shear stresses are shifted away across the bonded regions. The effective bonded length is related to the specimen's geometry, FRP width and FRP stiffness [20, 21].

The bond strength increases with increasing substrate strength. If the failure occurs in the substrate, the bond strength is proportional to the square root of the substrate compressive strength [22]. Some researchers even proposed that, in case of concrete structures, since the bond failure occurs inside the concrete, the bond strength is independent from the type of FRP and proportional to the 2/3 power of the substrate compressive strength [23].

The substrate surface properties also affect the bond strength. It has been reported that sandblasting, grinding and mechanical abrasion improve the bond strength until a limited level [22, 24]. This increase is due to the improvement of the mechanical interlocking between the composite material and substrate. Mechanical anchorage has also been approved to be an effective solution in improving the bond strength [25].

2.1.2 Experimental characterization

While considerable experimental and numerical researches have been performed for investigating the bond between FRP reinforcement and concrete elements, see e.g. [21, 22, 26-33], only few works can be found devoted to investigating the bond between FRP and masonry supports, see e.g. [34, 35].

Diverse test set-ups, with different advantages and disadvantages, have been developed and used for characterizing the bond behavior in FRP-concrete systems [36-38], see Figure 2-1. In case of FRP-masonry systems, due to the lack of a standard test method, the same test setups have been usually used. Nevertheless, some efforts have also been made for development of new test setups specifically for FRP-masonry systems to fulfill the required needs in testing this material, see e.g. [39]. Fedele and Milani [39] proposed new test setups in a recent study for investigating the bond in FRP-masonry elements, see Figure 2-2.

Momayez et al. [40] and Aiello and Leone [41] showed that the results obtained from different test set-ups may exhibit significant variation. Therefore, the selection of a suitable test set-up is of paramount importance to capture the critical aspects related to interfacial mechanics, as well as failure initiation and propagation. A comparison between the results obtained from different set-ups shows that the double-lap shear test, Figure 2-1(a, b), provides lower debonding values with

respect to single-lap shear tests, Figure 2-1(c, d) [42]. This can be explained by the unavoidable asymmetry of the specimen due to both load eccentricity and surface imperfections before bonding, with failure initiating on one side of the specimen. On the contrary, beam tests initially proposed for FRP sheets bonded to concrete [43], usually give higher values of bonding strength. In this case in fact, due to deflection of the concrete support (beam) during the load application, the FRP bonded length is subjected to a compression stress state orthogonal to the interface plane, which may increase the bond strength significantly. For these reasons, single-lap shear set-ups are considered the most reliable configurations for FRP–concrete debonding investigations [30, 41]. A well-recognized drawback of classical single-shear tests is that, due to the asymmetrical configuration, a significant amount of strain energy is stored in the specimen during loading. Hence, when debonding initiates, a remarkable energy release occurs. Debonding progress is then very brittle and cannot be experimentally followed even by conducting the test under displacement control [30].

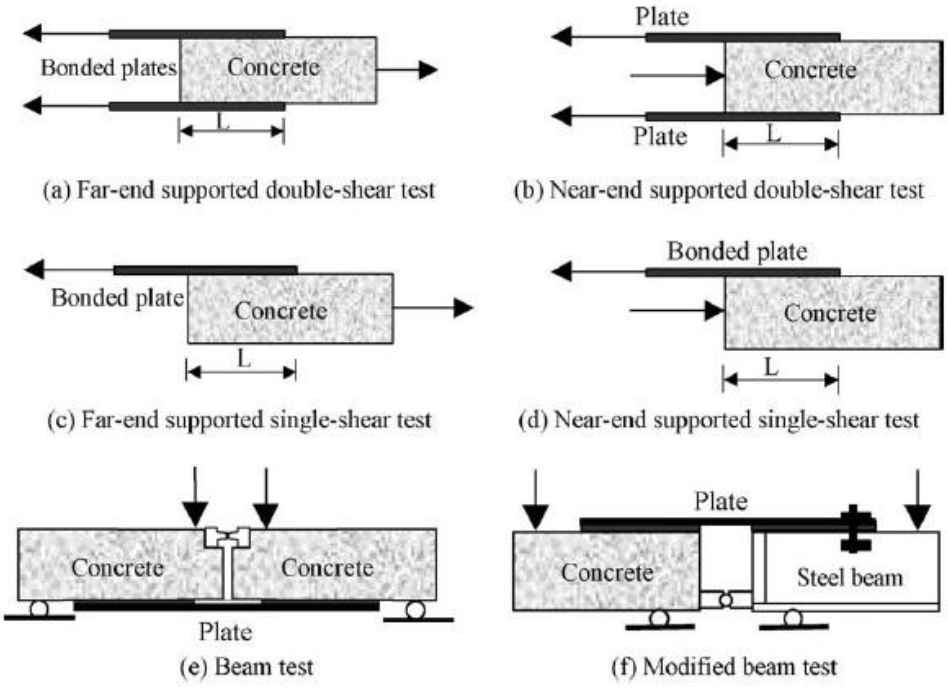

Figure 2-1: Test set-up for FRP-concrete bond characterization [37].

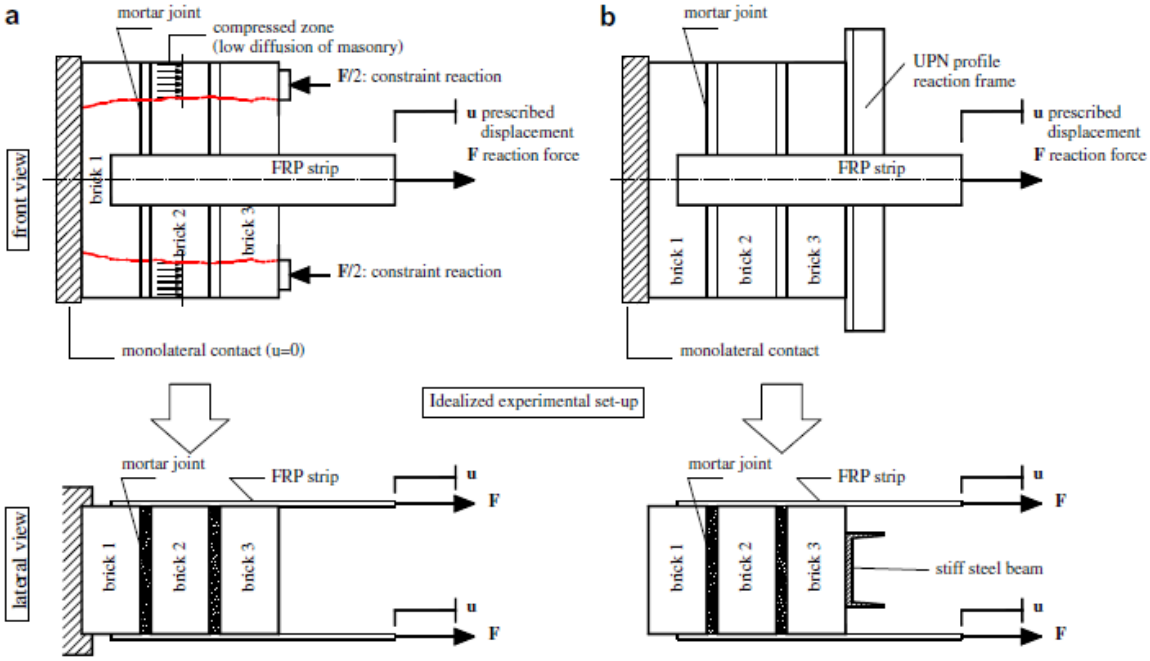

Figure 2-2: Shear bond tests used by Fedele and Milani [39].

An important issue in the experimental characterization of the bond behavior is the accurate measurement of the strains (or shear stresses) developed in the FRP and the slip of the FRP from the substrate. The strain development during the debonding tests is commonly monitored with strain gauges, while LVDTs are used for measuring the FRP slip. It is important however to ensure that the readings do not contain contributions from other sources such as support movements or deformations of the specimen [44]. Moreover, the measurements obtained with these techniques are discrete and limited to the location of the instrument. Therefore, the use of a full-field measurement technique, such as Digital Image Correlation (DIC), seems to be valuable in overcoming the mentioned problems and also in better understanding the unknown aspects of the bond behavior. These methods have been widely used for measurement of displacements or strains in different fields of solid mechanics [45-47]. However, only a few studies can be found using these techniques for investigating the interfacial bond behavior, see e.g. [48, 49].

The investigations performed on the bond behavior in FRP-masonry systems include experimental tests on different FRP composites bonded to new and old clay bricks [34, 50-54], stones mainly Naples tuff and Leccese limestone [54-57] and masonry prisms [35, 48, 58-60]. Depending on the substrate material, different failure modes have been observed and reported.

For clay brick masonry, some studies focused on the bond behavior between composite materials and new clay bricks [34, 50, 54, 57, 61]. Meanwhile, other researchers focused on this problem when old bricks are used [54, 57]. Briccoli Bati et al. [61] performed bond tests on 222

CFRP strengthened-brick specimens made of new clay bricks. Different bond lengths and FRP widths were considered in the specimens' configurations. The results had a clear dependence on the bond length and FRP width and also the test configuration, as also reported in [62, 63]. Valluzzi et al. [64] presented the results of 280 tests on new clay bricks strengthened with different composite materials. The tests included single-lap and double-lap shear tests performed in different laboratories. Valuable information in the failure modes and debonding forces was obtained and reported. A comparison between the bond behavior in old and new clay bricks was made by Grande et al. [65]. They observed that the bond behavior between Steel Reinforced Polymers (SRPs) and old clay bricks is not satisfactory in cases in which the bricks have macro-irregularities. On the contrary, the bricks with weak surfaces but high porosity can guarantee a good adhesion, even if they have a low bond strength.

In case of stone substrates, detachment of the FRP sheet with a thin layer of stone from the Leccese stone substrate was reported. In contrary, the failure in Naples tuff specimens was crushing a think stone layer [56]. As a consequence of the mechanical properties of the substrate, higher debonding loads were observed in the Leccese stone specimens. A summary of some available data on the bond strength of FRP-strengthened masonry is presented in Figure 2-3.

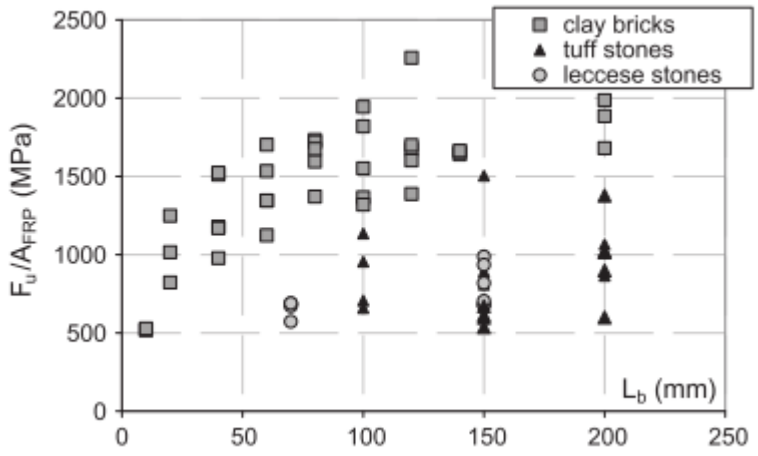

Figure 2-3: Some available data in literature on bond in FRP-masonry, taken from [53].

2.1.3 Numerical modeling

Numerical approaches for simulating the bond behavior usually follow one of the two main procedures namely detailed (meso-scale) modeling and simplified modeling [27]. A brief explanation of each approach together with relevant available literature are presented and discussed in this section.

In the detailed modeling approaches [66-68], the debonding phenomenon is directly simulated by modeling the cracking and failure of all the material constituents at a meso-scale level. All the materials (FRP, adhesive and substrate) are modeled in this approach usually with the assumption of perfect bond at the FRP/adhesive and adhesive/substrate interface. The advantage of this approach is that appropriate material constitutive laws are to be used. Moreover it provides a framework for investigating the local stresses and failure mechanisms which usually encompass the debonding phenomenon [39]. However, the role of the interfaces whose properties may be susceptible to environmental conditions (such as temperature and humidity changes) is not considered. Physical and mechanical characterization of the concrete or masonry layer near the epoxy resin layer is also important for a proper modeling. An advantage of this approach is that the complex stress conditions and interaction of cracks observed in real structural systems can be simulated. But as a disadvantage, this approach requires many parameters related to the constituent properties (pertaining to substrate, adhesive, and FRP), which affects its application in engineering usage and poses questions about the availability and selection of relevant data. Most of the available information in modeling the bond behavior following this approach is for FRP-concrete elements and only few investigations can be found for FRP-masonry. Usually, a two-dimensional modeling approach is used, e.g. [27, 39, 69], and only a few three-dimensional models can be found [70, 71]. Probably the only three-dimensional nonlinear modeling approach used for externally bonded FRP-strengthened masonry is presented by Fedele and Milani [9-10]. In this case, a damage model was used for representing the failure and damage propagation in masonry prisms.

In the simplified approach, the bond behavior is modeled by using a zero thickness interface element between FRP and substrate [66, 72, 73]. Within this approach the nonlinearities are usually concentrated at the FRP–substrate interface, while FRP and substrate are characterized by an elastic behavior. This approach is attractive, in principle, since it can potentially capture the critical aspects related to interfacial mechanics and bond failure initiation and propagation by using suitable interface (bond-slip) laws. Bond-slip laws are generally provided by relevant standards (e.g. CNR DT 200 [1]) or can be experimentally obtained on the basis of simple shear bond tests, see e.g. [53]. These models are not truly predictive, although they may be used to assess the experimental interfacial behavior [27, 39]. Moreover, they are unable to provide information on three-dimensional aspects of the debonding mechanism. The critical aspects that still need to be elucidated include the accurate prediction of strain distribution (local level) and force-slip evolution (global level), especially when the structural response becomes nonlinear. Again, little information in the literature can be found on the use of this approach for FRP-masonry systems. Panizza et al. [63], after calibrating the interface fracture with experimental results, proposed a simple bond-slip

law for modeling purposes. Grande et al. [53] used a three-dimensional finite element model with interface elements representing the bond behavior for simulating the single-lap shear bond tests. Based on the experimental results obtained, they adopted the bond-slip model proposed by Nakaba et al. [26] and Monti et al. [74] for the numerical simulation. In another study Grande et al. [75] proposed a bilinear interface model for simulating the bond behavior in FRP-masonry elements.

2.1.4 Prediction models for bond behavior

Development of analytical and predictive models for estimating the bond strength and related aspects of the bond behavior has been the subject of many research studies (again mostly on FRP-concrete elements). The models can be generally categorized into: (a) strength based models; (b) models based on linear elastic fracture mechanics (LEFM); (c) models based on nonlinear fracture mechanics (NLFM). Strength based models, although having the stress singularity problems, were used preliminary for developing simple theoretical models, see e.g. [76]. The, LEFM methods were therefore developed to overcome the singularity problem with the main aim of obtaining the debonding energy release rate. These models, mainly used for analysis of FRP-concrete elements, include a wide range of studies based on high order beam theories [77], cracking in the interfacial region of brittle substrates [78], semi-infinite interface crack between two elastic layers [79], tri-layer fracture models [80] and others. Using NLFM with the aim of nonlinear stress deformation laws has become more popular in the recent years and several publications can be found devoted to this area [73, 81]. The cohesive zone model (CZM) has also been used for analysis of crack propagation and has been found useful for large-scale fracture processing zones [82, 83].

The proposed models for bond strength prediction are generally similar with small differences in relations. Holzenkämpfer [84] proposed the following known model for estimating the maximum bond capacity:

$$P = b_{FRP}\sqrt{2G_c E_{FRP} t_{FRP}} \tag{2.1}$$

where b_{FRP} is the FRP width, G_{c} is the interface fracture energy and $E_{\mathrm{FRP}}t_{\mathrm{FRP}}$ is the FRP stiffness. The interface fracture energy has been estimated as [85]:

$$G_c = c_f f_t \tag{2.2}$$

where f_{t} is the concrete tensile strength and c_{f} is experimentally obtained equal to 0.204. Monti et al. [74] obtained Eq. (2.3) for the ultimate bond load based on a FEA parametric study and experimental results, (similar to Eq. 2.1).

$$P = b_{FRP}\beta\sqrt{\tau_{\max} E_{FRP} t_{FRP}/3} \tag{2.3}$$

where $\beta=1$ for $L \geq L_{\mathrm{e}}$ and $\beta=\sin(\pi L/2\, L_{\mathrm{e}})$ for $L < L_{\mathrm{e}}$. The effective bond length, L_{e}, is defined as:

$$L_e = \sqrt{\frac{E_{FRP} t_{FRP}}{\sqrt{4\tau_{\max}}}} \tag{2.4}$$

$$\tau_{\max} = 1.8 k_b f_t \tag{2.5}$$

$$k_b = \sqrt{1.5 \frac{2 - b_{FRP}/b_c}{1 + b_{FRP}/100}} \tag{2.6}$$

where b_c is the concrete width. Here k_b accounts for the effect of FRP width to concrete ratio. Taljsten [86], considering a three-layer model with a crack in the adhesive layer, proposed the following relation based on the work done for crack propagation:

$$P = b_{FRP} \sqrt{\frac{2 G_c E_{FRP} t_{FRP}}{1 + \alpha}} \tag{2.7}$$

$$\alpha = \frac{E_{FRP} t_{FRP}}{E_c t_c} \tag{2.8}$$

where $E_c t_c$ is the concrete prism stiffness and G_c is the adhesive fracture energy. In another study, based on nonlinear interfacial laws, Wu et al. [73] proposed the same relation as Eq. (2.7). However, the parameter α in this model is as follows:

$$\alpha = \frac{b_{FRP} E_{FRP} t_{FRP}}{b_c E_c t_c} \tag{2.9}$$

Chen and Teng [36] proposed a simple relation for calculating the ultimate bond capacity:

$$P = 0.427 \beta_w \beta_l L_e b_{FRP} \sqrt{f_c} \tag{2.10}$$

where f_c is the cylinder compressive strength of concrete (in MPa), and the other parameters are obtained as follows:

$$L_e = \sqrt{\frac{E_{FRP} t_{FRP}}{\sqrt{f_c}}} \tag{2.11}$$

$$\beta_w = \sqrt{\frac{2 - b_{FRP}/b_c}{1 + b_{FRP}/b_c}} \tag{2.12}$$

$$\beta_l = \begin{cases} 1.0 & (L_{FRP} \geq L_e) \\ \sin\left(\frac{\pi}{2} \frac{L_{FRP}}{L_e}\right) & (L_{FRP} < L_e) \end{cases} \tag{2.13}$$

Grande et al. [75] proposed the bond strength in FRP-masonry elements based on the Rankine-von Mises yield criterion as:

$$\tau_{\max} = \min(\sqrt{2/3} f_c, \sqrt{2} f_t) \tag{2.14}$$

CNR DT200 [1] proposes that the interfacial fracture energy of the FRP-masonry elements can be obtained as:

$$G_f = c_1\sqrt{f_{Mk} f_{Mtm}} \tag{2.15}$$

where c_1 is an empirical coefficient which should be obtained experimentally or can be assumed to be equal to 0.015. f_{Mk} is the characteristic compressive strength of masonry, and f_{Mtm} is the average masonry tensile strength. The characteristic compressive strength can be evaluated according to the Eurocode 6 [29], Eq. (2.2), and the masonry average tensile strength can be assumed to be equal to 10% of the characteristic compressive strength according to CNR DT200 [26]. Another approach for obtaining the characteristic values is multiplying the mean values by 1/0.7, which is followed in this study for obtaining the characteristic compressive strength of masonry bricks.

$$f_{Mk} = K f_{cb}^{0.7} f_{cm}^{0.3} \tag{2.16}$$

where K is assumed to be equal to 0.55, and f_{cb} and f_{cm} are the compressive strengths of brick and mortar, respectively.

Indicating that the fracture energy obtained by the CNR DT200 equation, Eq.(2.15), underestimates the fracture energy of FRP-masonry elements, Faella et al. [54] proposed the following relation based on regression analysis of some experimental data:

$$G_c = \alpha \frac{f_{cb}}{f_{cb} + b} \tag{2.17}$$

where f_{cb} is the masonry compressive strength and α and b are experimentally fitted parameters obtained equal to 1.874 and 21.134, respectively, for the database they used.

2.2 Durability and degradation mechanisms

Durability is defined as “the ability of the materials or structures to resist cracking, oxidation, chemical degradation, wear, and/or the effects or foreign object damage for a specified period of time, under the appropriate load conditions, under specified environmental conditions” [7]. The performance of the structure through its service life is therefore highly dependent on durability of its components and materials against the existing degradation agents. The parameters that affect the durability of structural components include (but not limited to) the choice of constituent materials, the design method, curing and installation quality, maintenance quality and environmental exposure conditions [87].

It is well known that the environmental conditions can affect the material properties. However, the type and rate of degradation varies with material, environmental condition and

exposure period [88]. The process of change in properties over time is called ageing or degradation. Ageing may be categorized by three primary mechanisms: chemical, physical and mechanical. Depending on the material characteristics and ageing environment, these mechanisms may have interaction with each other or may have additive or subtractive effect on the material performance [89]. Physical ageing (such as swelling due to moisture absorption) is usually associated to reversible changes of the material properties, while chemical ageing mainly involves irreversible changes which usually occur after long exposure periods. Mechanical ageing concerns the degradation of materials under mechanical stresses such as creep. Ageing has an important influence on the durability and serviceability of the materials and therefore understanding the active ageing mechanisms is of critical importance for long-term performance assessment.

The environmental degradation agents that likely affect the structural materials or components consist of temperature fluctuations (including temperature and freeze-thaw cycles), moisture, UV, alkaline or carbon dioxide exposure [3]. Each of these degradation agents may be of interest for a certain material, while might not produce any degradation in other ones. A survey in the literature shows that the long-term behavior of bond in FRP-strengthened elements change with exposure to moisture, temperature, chemical reactions, erosion, fatigue, etc. [3]. The coupled effect of temperature and moisture exposure, called hygrothermal exposure, appears to be of relevant interest for FRP-masonry strengthened components and is the main interest of this thesis.

Several studies focused on the effects of temperature and humidity variations on the bond behavior in FRP-strengthened concrete elements, but the available information on FRP-masonry elements is rare. However, even in case of FRP-strengthened concrete elements, the available data are sparse and the degradation mechanisms are not well identified. Moreover, the changes and degradation mechanisms in the bond behavior due to exposure to hygrothermal conditions are almost unknown. It is known that the temperature and moisture exposures may affect the properties of epoxy resins, FRPs, and the FRP/substrate interface but these effects are not well recognized and classified yet.

This section aims at providing a summary of the active degrading mechanisms involved in deterioration of bond under moisture and temperature conditions.

2.2.1 Moisture effects

Although many studies can be found on the effects of moisture on epoxy resins and FRP composites, the main degradation mechanisms including reversible and irreversible changes are still not well understood [88].

It is known that epoxy resins and FRP composites absorb water with exposure to humid conditions [88]. The water absorption is increased by formation of cracks and openings in the matrix, and can make changes in the polymer structure such as hydrolysis, plasticization, saponification, swelling, decrement of free surface energy and increment of free volume [88, 90, 91]. The main effect of the plasticization is decreasing the glass transition temperature, T_g, [90, 92, 93], and mechanical properties of the epoxy resin [94]. This is due to the interruption of Van der Waals bonds between the polymer chains which also leads to increase in the effective free volumes in the resin system [95]. The decrease of T_g as a consequence of immersion in water is a physical change that can be partially reversed upon drying, but it depends highly on the exposure time and also the moisture concentration level [88, 96]. This effect is of particular concern for cold-curing epoxy resins, whose glass transition temperatures are typically not much higher than the service temperature. Long-term exposure to moisture can cause irreversible changes in the polymer structure such as hydrolysis and micro-cracking. As stated before, micro-cracking contributes in further water absorption and mechanical degradation beyond the equilibrium state in the un-cracked polymer.

The chemical composition appears to influence both the solubility of water in the resin as well as its susceptibility towards hydrolysis. Therefore, a wide range of water diffusion and equilibrium contents has been reported in the literature. While the latter explains the rate of water diffusion in the polymer structure, the former indicates the extent of swelling stress. With increase in the equilibrium moisture content, the swelling stress increases resulting in higher hydrolysis and in the possibility of micro-cracking [97].

Moisture exposure may cause degradation in glass and aramid fibers [97]. The chemical reactions between water and glass fiber lead to degradation and formation of flaws at the glass fiber surface and consequently significant reduction of mechanical strength. Significant leaching and pitting may also occur in glass fibers when it is in direct contact with basic solutions. Moreover, moisture attack can accelerate the rate of crack growth in glass fibers [97] On the contrary, carbon fibers are generally resistant to moisture attack [88].

The mechanical properties of FRP composites are generally less sensitive to hygrothermal ageing when compared with those of resins because of the presence and influence of fibers [88]. Since the fibers are protected with epoxy resin, no degradation is expected due to the water attack. However, the presence of voids and non-uniformities in the specimens prepared following the wet lay-up procedure increases the vulnerability of the composite materials to moisture uptake [98]. On the other hand, plasticization of the matrix due to water uptake may result in mechanical degradation of the composite material. As a consequence of fibers, matrix, and interface

degradation due to moisture exposure, substantial reductions have been reported in longitudinal ([99]) and transverse tensile strength ([100]), compressive strength ([101]) and flexural strength ([102]) of FRP composites. The moisture can also penetrate along the fiber-matrix interface causing damages in the fiber-matrix bond [91, 103]. However, the degradation in the FRP composites depends on the size of molecules of the degrading agent and its chemical interactions with the matrix. On the other hand, polymerization and curing of epoxy resins take place over an extended period of time and can be accelerated due to moisture uptake resulting in an initial increase in the performance of the composite material [104]. This post-curing behavior can offset the degrading effect of water attack.

Water can also react with brick components (dissolving effect of water) resulting in reduction of mechanical properties of clay bricks. Excess lime gets hydrated and swells, which may affect the mechanical strength of the bricks [105]. Insufficient firing temperature in clay bricks can lead to a low degree of vitrification and a high moisture expansion coefficient [106]. The degree of vitrification is defined as the amount of glass formed in the brick during firing. The water can react with the remaining clay inside the brick resulting in micro-cracking, expansion and, consequently, strength degradation.

At the FRP-substrate interface, the decrease in T_g of the adhesive results in deterioration of the bond independently of the substrate [107, 108]. Degradation of bond up to 40-50 % has been reported under wet environment usually attributed to the high degree of plasticization of the resin and additional breakage of interfacial bonds [90, 109-114].

Gledhill et al. [115] distinguished three stages in degradation of adhesive joints (steel joints with epoxy resin adhesive) attacked by water, as follows:

1. Accumulation of a critical concentration of water in the interfacial region. The critical water concentration level depends on the epoxy adhesive type. The rate of attaining this critical water concentration is governed by the water diffusion rate through the adhesive to the interfacial regions. However, in some cases the rate of environmental attack may be governed by water diffusion rate through the substrate (in case of porous substrates such as brick) or other active mechanisms.
2. Loss of integrity in the interfacial regions. Generally, the general mechanisms involved in this phenomenon can be [116]: the rupture of interfacial secondary bonds; the rupture of interfacial primary bonds; the hydration and weakening of the oxide layer on metallic substrates; the hydrolytic attack on a boundary layer of adhesive adjacent to the interface. This boundary layer may have a different chemical/physical structure to that of the bulk adhesive due to the presence of the adjacent substrate surface; the hydrolysis of the primary

bonds of the primer leading to a cohesive failure though the primer layer. These mechanisms are often followed by adhesive plasticization (and maybe substrate), but this do not always lead to joint degradation and in some cases has a reverse effect.

3. Ultimate failure of the joint. However, fully weakening of the interfacial region is not usually necessary for severe degradation of the joint strength. From basic fracture mechanics consideration, only a relatively small environmental crack may lead to a large decrement of time to failure depending on the loading conditions and specimens' geometry.

The measurement of the critical water content is a complicated task which requires performing comprehensive experimental tests. It has been found that the presence of this critical level can be due to the following facts [116]: (a) the hydration of salts in the adhesive and at the interface limits the available water molecules for attacking the interfacial regions unless the water concentration is more than the critical level; (b) water molecules are trapped or clustered until the critical water concentration level is reached. After that level, the water molecules condense on –OH groups of the polymer resulting in breaking the inter-chain hydrogen bonds and displacing adsorbed –OH groups from the surface of the substrate.

It should be noted that Gledhill et al. [115] considered the simplest and most easily modeled mechanism of environmental attack (rupture of interfacial secondary bonds). Other attack mechanisms are not well investigated. The few available information on those mechanisms is just for simple adhesive systems and the available empirical modeling approaches have a limited range of applicability.

Degradation of the bond due to presence of moisture can also be explained by principles of adhesion thermodynamics. Mechanical interlocking and adsorption theories are the major governing mechanisms in the bond between composite materials and substrates, as stated before. Mechanical interlocking is the interlocking of the penetrated epoxy resin into the substrate pores and irregularities. Adsorption describes the intermolecular forces at the interface. Intermolecular forces consist of primary (ionic and covalent) and secondary (van der Waals) forces, with the latter being the most important mechanism in adhesion. The work of adhesion of secondary forces is usually a positive value in the dry state showing the stable thermodynamic state of the interface. However, in the presence of water molecules at the interface, this value becomes negative resulting in driving forces at the interfacial region [117, 118]. The decrease of the free surface energy of the interface (and consequently the work of adhesion), decreases the bond fracture energy and may result in the change of failure mode into an interfacial debonding. Accumulation of water molecules at the interface can also cause osmotic pressure which may lead to local debonding. Ouyang and Wan [118] investigated the relation between this reduction of adsorption strength and interfacial relative

humidity and proposed a constitutive law for modeling the interfacial degradation based on the equilibrium relative humidity at the interface. Similar to the concept of the critical water level, they have reported that the degradation rate increases when the interfacial relative humidity is more than about 65%.

Bowditch [119] categorized the moisture induced degradation mechanisms of bonded systems into three groups as presented in Figure 2-4. The lower curve represents the conditions in which there is only interfacial degradation in the system. In this case, the strength decreases until a residual value which occurs at the water solubility limit in the adhesive system. This residual value is explained by the fact that the quantity of water gaining access to the interface is less than the required water for complete adhesion loss. Ouyang and Wan [118] explained this residual strength in shear debonding case (mode II fracture) with the remaining interlocking actions between epoxy resin and substrate.

The upper curve represents the case in which only plasticization of the adhesive occurs which is expected wherever the work of adhesion in the presence of water is positive. This condition can be found where the substrate has a low free surface energy such as FRPs. The initial increase in the joint strength is due to the relief of internal stresses. Again, the curve reaches a residual joint strength at the water solubility limit.

The middle curve represents the cases in which both plasticization and interfacial attack occurs (this condition occurs in most of the real situations). Here, the weakening effect due to the interfacial attack is balanced with the plasticization effect.

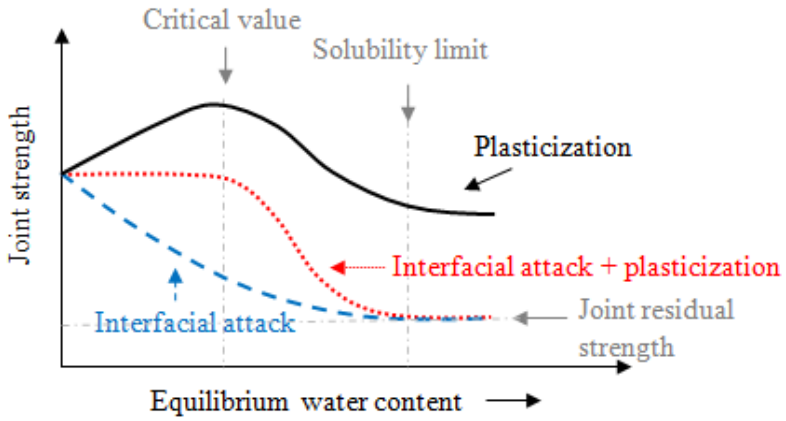

Figure 2-4: Typical degradation curves of joints due to moisture attack [119].

2.2.2 Temperature effects

Thermal effects include the changes in the properties of the matrix due to temperatures above the curing temperature, freezing, and freeze-thaw conditions. It is well known that epoxy resins soften

over the glass transition temperature (T_g), leading to an increment of the viscoelastic response, reduction of the elastic mechanical characteristics, and de-ageing of the epoxy resin. Exposing the epoxy resins below their T_g, may result in an increase in susceptibility to moisture absorption and mechanical degradation and also post-curing phenomenon (if exposed temperature is above the curing temperature) [7, 88, 120, 121]. Freeze exposure on the other hand results in embrittlement of the resin while it increases the effective stiffness, matrix hardening, matrix micro-cracking, and fiber-matrix bond deterioration [88, 122, 123].

The fibers are usually resistant to temperature (e.g. carbon fibers are resistant to temperature up to 600°C). Therefore, any degradation in composite materials due to exposure to temperature conditions is due to the degradation in the matrix or fiber/matrix interface. Thermal incompatibility problem in FRP composites and FRP-strengthened elements is an important issue to be considered when temperature cycles are investigated [88, 122, 123]. The thermal incompatibility is due to the considerable difference in thermal expansion between the fibers and polymer matrix, and/or between FRP and substrate. The majority of the epoxy resins used as matrices in FRPs have coefficients of thermal expansion in the range of 45 to 65 × 10^{-6} °C. Meanwhile, glass fibers used in most FRP systems have a coefficient of 5 × 10^{-6}/°C and carbon fibers generally have a coefficient in the range of - 0.2 to 0.6 × 10^{-6} °C [124]. The thermal expansion coefficient of clay bricks is in order of 5×10^{-6}/°C [125]. This large difference in expansion coefficients produces thermal stresses at the fiber/matrix and matrix/brick interfaces. The case is worse in carbon fibers since the fiber is anisotropic having a positive coefficient of thermal expansion in the transverse direction and a negative coefficient in the longitudinal direction, which usually results in debonding of the fibers from the surrounding matrix [98, 126, 127]. This is most often seen after thermal cycling, such as through repeated freeze-thaw exposures. As a results of thermal incompatibility, FRP debonding or severe degradation of the bond may be observed in FRP-strengthened elements [128].

On the other hand, exposure to high temperatures (still below the epoxy T_g) results in an increment of moisture diffusion coefficient and epoxy post-curing [129]. While the former lead to higher moisture uptake and consequently higher mechanical degradation, the latter can cause an improvement in the mechanical properties.

2.3 Durability studies

Several experimental and numerical modeling approaches have been adopted by researchers for investigating the durability of FRP-strengthened components. In case of experimental modeling, real exposure or accelerated ageing tests can be utilized. The real exposure tests take long time to be

completed, equal to expected service life of the material, but they can provide understanding of the real degradation phenomena. Accelerated tests are performed over a shorter time span, but the resulting degradation mechanisms should be then related to real exposure conditions. As already recognized in [3, 14, 88, 128, 130, 131], a substantial body of 'real time' weathering data is still lacking.

Accelerated ageing tests have been widely used in material characterization in different fields of science such as civil engineering, aeronautic studies, and medical sciences. The concept of accelerated ageing tests is applied to avoid long-lasting experiments. The duration of the experiments reduces significantly if the tests are performed at increased stresses [132, 133]. Most of the durability tests involve accelerated ageing by using large stresses to accelerate the degradation process or in some cases by reduction of the element size and thickness [134, 135]. Accelerated testing programs, if properly designed and performed, can provide a sound basis for predicting the performance and for assisting in service life prediction. [136-143].

This section provides a review of available durability studies on concrete and masonry components strengthened with composite materials, with emphasis on thermal and moisture exposure conditions. Focus is on experimental and numerical works performed on FRP-concrete and FRP-masonry systems.

2.3.1 Experimental tests

The effect of environmental exposures on the bond behavior in FRP-concrete systems has been studied extensively in the last decades, while this subject for FRP-masonry systems has become into consideration only in the last few years. No agreement exist in the methodology for selecting the parameters of accelerated ageing tests such as number of cycles, the rate of cycles, and the temperature/humidity ranges. Also, the presence of arbitrary artificial weathering tests unrelated to the field conditions makes it impossible to correlate the durability of the materials indicated by accelerated tests and their performance in service.

The number of cycles experienced by the materials is considerably influenced by geographic location. Some authors have tried to simulate the real condition of freeze-thaw cycles in different regions. Barnes [144] estimated that 2000 cycles was a conservative estimate for all temperature cycles in a worst-case scenario for 50-year building life for cycling from cold to warm using a rather large temperature range of 160°C. Lesko [145] reported that in average there is 30 freeze-thaw cycles yearly in Virginia. Soudki and Green [146] used a total of 50 freeze-thaw cycles to simulate conditions in Canada, while Gomez and Castro [147] used 300 cycles to simulate the structure's life. Karbhari et al. [148] used 201 cycles, each of 24 h to simulate 4-6 years of outdoor

exposure. In another study, Belarbi and Bae [149] used a combination of different thermal cycles to simulate the life time behavior of concrete columns. They assumed that 10 times repeating the full cycle results in prediction of 10 to 15 years life of the element. Myers et al. [150] also used a combined exposure test for studying the bond behavior in FRP-concrete systems.

As the main interest of this research program is investigating the bond degradation due to thermal cycles coupled with humid environment, a brief review of these tests performed on FRP-concrete and FRP-masonry systems is presented next.

2.3.1.1 Moisture exposure

Moisture condition is usually simulated by immersing the specimens in water or exposing them to wet-dry cycles. In some cases salt solutions are used instead of pure water to simulate the sea water conditions. The results show that moisture exposure may result in significant degradation of strength in FRP-strengthened concrete elements.

Chajes et al. [151] showed a 36% and 19% decrease in ultimate strength for GFRP and CFRP bonded concrete specimens respectively that were subjected to 100 wet-dry cycles. Toutanji and Gomez [109] found a strength reduction up to 33% on specimens made of various epoxy and FRP systems after exposure to 300 wet-dry cycles, which is similar to the results obtained by Toutanji and Ortiz [152]. In a recent study, Huitao et al. [153] concluded that the flexural strength and stiffness of CFRP bonded concrete beams do not change significantly after exposure to 180 wet-dry cycles (salt solution) but the failure mode may change. Karbhari and Zhao [154] observed 40% reduction in bending capacity of the GFRP- and CFRP-strengthened beams after 120 days of exposure. Silva and Biscaia [112] observed increase in the flexural strength and bond fracture energy of GFRP-strengthened RC beams after immersion in water or exposure to salt fog cycles. The observed strength increment was attributed to the concrete post-curing during the tests. Leung et al. [155] considered four exposure conditions and showed that the moisture exposure can significantly affect the flexural capacity. Toutanji [156] reported that CFRP bonded concrete columns shows no significant reduction in strength or ductility after exposure to wet-dry cycles, but the strength of GFRP bonded specimens reduces significantly which is in line with the results obtained by Toutanji and Balaguru [157].

Regarding the bond behavior, Dai and Yokota [158] used 0, 8, and 14 months of wet-dry cycles and observed 50% reduction of bond strength in CFRP-strengthened concrete beams. Karbhari et al. [159] studied the durability of FRP-concrete bond interface under different environmental conditions. The experimental results pointed that water absorption lead to degradation of the interfacial bond performance. Grace and Singh [111] tested 78 large-scale

strengthened RC beams using CFRP plates and fabrics and concluded that moisture affects the bond between FRP and concrete significantly. Wan et al. [160] found 85% reduction of interfacial energy release in CFRP bonded concrete specimens after 8 weeks of water immersion. Tuakta and Buyukozturk [161, 162] investigated the effect of variable moisture conditions on the fracture toughness of CFRP-bonded concrete specimens. Significant reduction of bond strength was during the first periods of water immersion (70% after 8 weeks), followed by a residual value until the end of the tests, was reported. Moreover, it was observed that the bond degradation is not regained upon drying during the wet-dry cycles. The failure mode of the specimens was also changed from cohesive to interfacial debonding with immersion time. Benzarti et al. [163] investigated the effect of surface preparation on the bond degradation of CFRP-strengthened concrete elements in 95% R.H. and 40°C conditions. Reduction of bond strength and changes in the failure mode was observed and reported. Cromwell et al. [164] did not observe any reduction in the bond strength of concrete specimens strengthened with CFRP and GFRP after 10000 h of water immersion. Silva et al. [165] exposed CFRP strengthened concrete elements to cyclic moisture conditions and reported improvement in the bond strength, while the fracture energy was decreased.

As shown above, the testing procedures are rather different in terms of exposure and specimens, and the results are partly inconsistent. Still, the majority of the results indicate a significant loss in bond strength for FRP-strengthened concrete elements subjected to moisture exposure. Differently, the available information for FRP-strengthened masonry elements is very scarce. Aiello and Sciolti [5] and Briccoli Bati and Rotunno [4] reported significant reduction in bond strength of CFRP-bonded masonry specimens after exposure to different wet-dry cycles and durations. Briccoli Bati and Rotunno [4] also observed that the bond strength reached a residual value after the initial degradation. In a recent study, Sciolti et al. [166] reported 26% reduction of bond strength in CFRP-strengthened weak stones (calcernite) after 25 weeks of water immersion. The debonding behavior became more fragile with immersion time. The failure mode of the specimens was cohesive within a thin layer in all the specimens, and the effective bond length remained constant.

2.3.1.2 Temperature exposure

Chajes et al. [151] studied the effects of freeze-thaw and wet-dry cycles on RC beams reinforced with aramid fiber, E-glass fiber, and graphite fiber composites in the tension face of the beams. The freeze–thaw cycles involved immersing the samples in 4% $CaCl_2$ for 16 h in a freezer at –17°C followed by 8 h of thawing at room temperature. The strength losses after 100 freeze–thaw cycles were observed to be 9%, 27% and 21% for the aramid, E-glass, and graphite fiber composite

strengthened beams, respectively. They also showed that wet–dry environment yields in more degradation of beams strength than freeze–thaw exposures. Another study has shown that the CFRP bonded concrete beams performed well up to 200 freeze-thaw cycles [167]. Silva and Biscaia [112] exposed the GFRP bonded concrete beams and blocks to freeze-thaw cycles between –10°C (12 h) to +10°C (12 h) for 1000, 5000, and 10000 h and tested them under flexural and pull out tests respectively after and before exposure. The results showed a 31% decrease in flexural strength and 18% decrease in average bond stresses after exposure, and the failure started at the concrete substrate layer similar to unconditioned specimens. Karbhari and Zhao [154] reported 7.5% decrease in flexural failure load and a more brittle failure of CFRP- and GFRP-strengthened RC beams after exposure to 127 freeze-thaw cycles between –15.5°C (12 h) to +23°C (12 h). Arnsten and Pedersen [168] showed after 56 cycles of freeze-thaw exposure between –22°C (15 h) to +17°C (9 h) with relative humidity of 0 or 80% no significant degradation occurred in flexural strength of the strengthened beams. The decrease in ultimate strength of GFRP-strengthened beams after exposure is again reported in [169].

Other authors focused on the effect of environmental conditioning on the shear bond behavior of FRP bonded specimens. Freeze-thaw cycles have been found to reduce the bond shear strength and peak slip while the force-elongation diagram became nonlinear with a lower peak load [170]. Colombi et al. [171] studied the bond behavior of CFRP-concrete specimens after exposure to 100 and 200 freeze-thaw cycles between –18 to +4°C according to ASTM C666 [172]. They observed that the specimens are not substantially influenced by the duration of the treatment, and the effect of conditioning on the ultimate load is not significant is in opposition to the results obtained by Subramaniam et al. [173]. Subramaniam et al. [173] used 100, 200, and 300 cycles of freeze-thaw between –18°C to +5°C and obtained a 17% decrease in the ultimate load and 35% decrease in the interface fracture energy. Green et al. [174] also did not find significant reduction in the behavior of retrofitted beams after exposure to freeze-thaw cycles. Homam and Sheikh [175] used CFRP- and GFRP- bonded concrete specimens and exposed them to two different freeze-thaw cycles. In the exposure, the specimens were subjected to 50, 100, 200, and 300 cycles of –18°C to +4°C while the specimens were submerged in water, and in the second method, the specimens were subjected to 28, 56, 112, and 336 cycles between –20°C to +40°C with the rate of 4 cycles/day in a dry chamber. In the worst case a drop of 7% in strength of GFRP-bonded specimens after 336 cycles of dry exposure was observed. Cromwell et al. [164] observed 6% and 4% of degradation in flexural strength of CFRP- and GFRP-strengthened beams after 360 cycles of freeze-thaw exposure. Yun and Wu [176] reported a reduction of bond stiffness, bond strength, fracture energy and maximum slip in the CFRP-concrete joints after exposure to freeze-thaw cycles. The effective bond

length was increased with exposure cycles and the failure mode remained cohesive in all the specimens. Silva et al. [165] reported a significant loss of bond strength and fracture energy in CFRP- and GFRP-strengthened concrete elements after exposure to freeze-thaw cycles. Myers et al. [150] used a combined exposure test to simulate the yearly environmental condition of US and observed degradation in bond strength. Gamage et al. [177] subjected CFRP-bonded concrete specimens to 1800, 2250 h of temperature cycles (4.5 h each cycle) between +20°C (1 h) to +50°C (1.25 h) while the specimens were loaded to different sustained loads varying between 0 to 50% of ultimate load.

Again, the results for concrete are rather diverse and partly inconsistent. As for FRP-masonry systems, Desiderio and Feo [6] exposed CFRP-bonded masonry specimens to 50 and 105 freeze thaw cycles between –18°C and +30°C following ASTM C666 [172] standard. They observed a decrease in bond stress and ultimate load after exposure. The governing failure mode was also observed to change from failure in masonry (cohesive) to FRP-masonry interface failure (adhesive). Briccoli Bati and Rotunno [4] also observed a decrease in shear bond strength of the specimens after exposure to freeze-thaw cycles. They used different specimens and exposed them to 12, 24, 48, and 96 freeze-thaw cycles between –8°C (for 6 h) and +50°C with (for 6 h) and observed continuous decrease in shear strength with increasing the cycles, which eventually ended in a 50% decrease after 96 cycles.

2.3.2 Numerical modeling

The majority of the performed studies on numerical modeling of degradation and service life predictions have been carried out for concrete or composite elements separately, and very few studies can be found focused on computational modeling of FRP-strengthened masonry or concrete elements. Generally, the approaches can be categorized into mechanistic, non-mechanistic, correlation and extrapolation [178].

Mechanistic approaches are based on modeling all the degradation mechanisms including mass transfer and chemical and physical reactions. Non-mechanistic approaches relate the materials strength to the degradation agent level. The correlation approaches include a simple expression relating the strength degradation with physical or chemical changes in the adhesive (e.g. moisture level, swelling, etc.), [178]. These models require a large database of experimental results and the correlation is usually valid for the investigated cases. The extrapolation approaches include predictive models aiming at relating the accelerated ageing tests to real exposure conditions. The mechanistic and non-mechanistic approaches seem to be most suitable for modeling environmental degradation of materials and are briefly explained next.

2.3.2.1 Mechanistic approaches

Mechanistic approaches involve predicting the degradation based on the active kinetic and mechanisms due to environmental attack. The degradation mechanisms are related to the chemical reaction of the environmental agents with the adhesive and the substrate. The relation between these mechanisms, the degrading agent amount and the material mechanical properties is thus necessary to be utilized in predictive modeling. The complexity of these models is high, but they can be a useful tool for accurately predicting the degradation and service-life modeling of materials. The steps required in these approaches can be summarized as [179-181]: (i) solving moisture, temperature, carbonation and other transfer problems by using proper diffusion models and modeling the concentration of each agent in the material after exposure to specific value and time; (ii) numerical modeling of physical and chemical actions and reactions due to concentration of degrading agents in the material; (iii) obtaining the stresses, strains or damage due to the physical and chemical actions; (iv) establishing a link between structural mechanics and thermo-hydro physics in terms of the mechanical performance of materials through constitutive modeling in both space and time.

It is worth noting that the moisture and heat transfer in porous media is a coupled problem that should be considered in the governing equations. Many studies can be found in the literature in which the moisture and heat transfer problems in porous media have been studied. Among them, the most important ones are the studies performed by Philip and De Vries [182] and Luikuv [183], in which the temperature and moisture content were used as driving potentials. The model derived by Philip and De Vries [182] considered the moisture movement in both vapor and liquid states using Fick's and Darcy's laws, respectively.

Also, it is noted that the moisture content profile is discontinuous at the interface between two different porous media, due to their different hygroscopic behavior. As a consequence, usage of these models is rather difficult [184]. Moisture diffusion analysis of FRP-bonded specimens across the interface between concrete or masonry and epoxy still remains a challenge [185-189]. This restricts the use of Fick's diffusion law. When the moisture moves across layered systems, the moisture potential must be continuous at the layer boundaries for isothermal diffusion process [190]. In a multilayered structure constructed with distinct permeable materials, the moisture content state variable is discontinuous at the adjacent material interface. In such cases, the relative humidity in the environment can be used as the common moisture potential in moisture diffusion equation [185-189].

Another important issue to deal with is the selection of an appropriate approach for modeling damage. Cracking is in fact the most important damage index associated with mass transport inside the targeted structures. Cracks are assumed to be normal to the maximum principal stress direction, occurring when the tensile principal stress exceeds the tensile strength of the material. After crack initiation, tension softening on progressive crack planes is taken into account in the form of fracture mechanics [179]. In cases in which mechanical actions on the structure are dominant, multidirectional cracks intersect orthogonally, but in cases where both mechanical and ambient weather actions are applied, principal stress axes can drastically rotate and non-orthogonal cracking easily takes place in the representative element volume [179].

2.3.2.2 Non-mechanistic approaches

In non-mechanistic approaches, see e.g. [191], besides modeling the degradation mechanisms and chemical reactions, the degradation of materials is related to the degrading agent amount. A general assumption in these modeling approaches is that the degradation is instantaneous. The agent dependent mechanical properties (usually moisture-dependent or temperature-dependent) coupled with numerical transfer models can then be used for predicting the material performance. This can be incorporated with Cohesive Zone Models (CZM) for simulating the durability in bonded systems.

CZM, which was originally introduced in [192-194], has been used to model the fracture behavior and durability in adhesively bonded joints. This model is particularly useful in situations where the crack propagation and initiation are going to be modeled in a single analysis. A traction-separation law is used to model the damage initiation and evolution in the fracture process zone [195]. The main parameters that define this response are the cohesive fracture energy and critical traction of the adhesive in each fracture mode [196]. The underlying concept is that, as the moisture diffusion weakens the bond strength through reversible and irreversible mechanisms, the cohesive properties degrade based on the moisture concentration level. Therefore, moisture-dependent cohesive properties are needed to accurately predict the failure behavior using this approach [197]. This model has also been used for modeling the fatigue induced degradation in joints by adopting a damage evolution law which accounts for the irreversible accumulation of damage through the cyclic process [198].

Ouyang and Wan [118, 185] studied the changes in fracture energy of the FRP-bonded concrete specimens under peeling load after moisture exposure. They found a relation between the fracture energy of the bond and the interfacial relative humidity which resulted in proposing a moisture dependent bond-slip law for numerical modeling purposes, see Figure 2-5. In another

study, Nguyen et al. [199] studied the stresses and displacements of thin masonry walls after exposure to fire by using a finite element model. The temperature dependency of the mechanical and thermal properties of the wall constituents were considered in the model using the available experimental data.

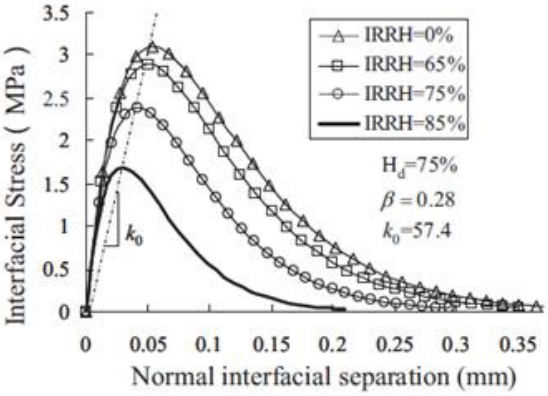

Figure 2-5: Effect of moisture on bond behavior, Ouyang and Wan [118, 185]

2.3.2.3 Other approaches

A new model has been developed by Freddi and Frémond [200] in order to predict the durability of adhesively bonded joints made of concrete. The model takes into account both bulk and interfacial damaging behavior and their interactions. A simplified version of this model has been presented in [201, 202], based on the principle of virtual power for modeling the bond durability in FRP-concrete systems. The process of damage is caused by microscopic motions, which is taken into account in the virtual power of the interior forces. This contribution is assumed to depend, besides on the strain rate (velocity discontinuity for the interface), on the damage velocity and its gradient (damage velocity discontinuity for the interface). The damage parameters were calibrated for obtaining the best fit with experimental results.

Gamage et al. [203] tried to simulate the experimental bond degradation of FRP-bonded concrete specimens through finite element modeling. For modeling the degradation, a thin layer of concrete with different meshing sizes and material properties on the top layer of the model between the concrete and epoxy elements was used. The properties of this thin layer were calibrated with experimental results to have the same strain distributions and failure modes in the numerical model.

Silva and Biscaia [107] used an interface law for modeling the bond degradation in FRP-strengthened concrete elements. The interface law was calibrated for each ageing condition with the experimental results and the data obtained from the strain gauges attached to the specimens.

Hu et al. [204] used a CZM bilinear traction-separation law for simulating the joints progressive damage and environmental degradation, see Figure 2-6. An environmental damage factor was introduced in the adopted model to represent the effect of cyclic temperature on the bond degradation. The damage factors were calibrated so that the best fit with the experimental results are obtained.

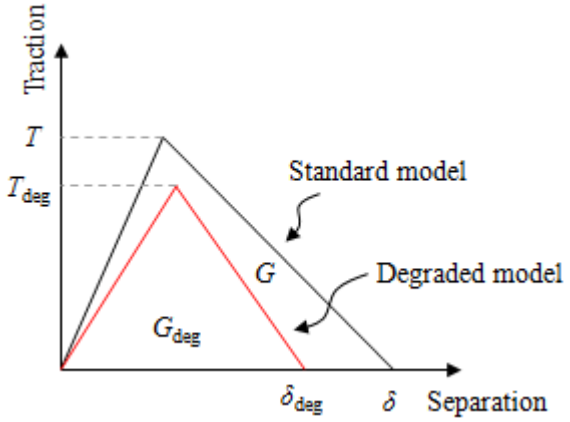

Figure 2-6: Hu et al. [204] bond degradation model.

2.4 Predictive degradation models

Service life prediction of structural components and modeling their degradation may be the most important aspect for practical application in durability problems. In fact, the main reason for durability investigations is to predict the service life of the component, which can be defined as a specific loss of strength or other mechanical or chemical properties, or as modeling the behavior of the component through time. The degradation process of the component due to exposure to environmental conditions should thus be well known so that it can be numerically or experimentally simulated. In other words, it can be said that the durability is a qualitative term which can be quantified by predicting the service life.

Several researchers have been trying to predict the service life of materials or structural components with different methods. A brief review of service life prediction models is presented next. Despite the challenges encountered in practice, development of models for determination of service life is in continuing progress. There are a number of factors that provide difficulties in the model developments: (i) the rate of degradation may change with time. The degrading mechanism may also change with time, temperature and moisture conditions; (ii) establishment of a link between accelerated ageing tests and real exposure conditions is a very complicated task; (iii)

statistical variability may increase with time introducing difficulties in interpretation of the results and extraction of the key mechanisms; (iv) besides the strength degradation, increment of strength with time may also be observed due to post-ageing, curing or relief of residual stresses.

2.4.1 Arrhenius model

The Arrhenius equation is one of the most-known models for lifetime predictions and is commonly used to predict the combined effects of temperature and time [136]. This model has been used in many fields including pharmaceutical, insulation, adhesives and batteries, see Nelson [205]. It is particularly useful for the accelerated testing of polymers as it allows short-term tests conducted at elevated temperatures for assessment of long-term exposure at lower temperatures, being given by:

$$\frac{dP}{dt} = A.\exp(-\frac{E}{RT}) \tag{2.18}$$

where *dP/dt* is the reaction factor (or degradation rate) for the process, *E* is the activation energy, *R* is the universal gas constant (8.3145 KJ $kmol^{-1}$ K^{-1}), and *T* is the absolute temperature at which the test is performed (in Kelvin). This equation can be rewritten in the form of Kinetic Rate Theory as:

$$P = B.\exp(-\frac{E}{RT})\ln t + P_0 \tag{2.19}$$

where P_0 is the initial material property and *B* is the integration constant. The key assumptions in simple application of the Arrhenius model are [136]: (i) the same process controls the degradation at both elevated and in-service temperatures and (ii) the degradation rate is directly related to a single chemical reaction.

As the temperature level is required for using this model, usually an average value of temperature is used to calculate the reduction factor in case of long exposure periods or for accelerated cyclic tests. Purnell [136] showed that using this average value can lead to severe errors, in particular in underestimating degradation rate. Hence, varied temperature regimes can be collapsed to a single thermodynamic equivalent temperature [136] or the life time of the material can be divided into small time steps over which temperature and humidity is assumed constant [206].

2.4.2 Time-Temperature Superposition (TTS) model

This model indicates that the changes of material properties through time at different temperatures are related to each other by a time shift. Modeling of any degradation process requires information on the change of material properties with time, and the rate of change of those properties with the

level of temperature. A number of semi-empirical relationships (linear and logarithmic) for property degradation have been suggested with the following general form [207, 208]:

$$P(t,T) = P(\infty,T) + [P(0,T) - P(\infty,T)]e^{[-k(T).t^n]} \quad (2.20)$$

where P is the material property (like strength or stiffness), T is the ageing temperature, t is the ageing time, and n is an experimentally determined constant. The strength decays exponentially with time to an asymptotic value. Assuming that only one time-dependent process is occurring, TTS is implemented by shifting a series of curves (time-dependent material property), obtained at a series of temperatures, to form a master curve. The Arrhenius equation can be used in determining the shift factor required to align the degradation trends at a variety of temperatures.

2.4.3 Time-Temperature-Moisture Superposition (TTMS) model

An alternative approach is to plot the material property data against time for one temperature-moisture level with the data represented by one of the following empirical relations:

$$\log P(t,T) = A(T) - B(T).t \quad (2.21)$$

$$P(t,T) = P(0,T)e^{[-k(T).t^n]} \rightarrow P(\infty,T) = 0 \quad (2.22)$$

where B is the degradation rate, and A is a constant. It is also possible to relate the rate of degradation with the rate of moisture uptake (i.e. diffusivity D). Using the Arrhenius relation, the diffusivity can be obtained as a function of absolute temperature T:

$$D = D_\circ \exp^{-E/RT} \quad (2.23)$$

where D_0 is a constant, and R is the ideal gas constant.

Phani and Bose [209] simplified the time-temperature superposition model for predicting the flexural response of CSM laminates. They observed that the flexural strength of the laminates at time t can be obtained as:

$$\frac{P - P_\infty}{P_0 - P_\infty} = \exp\left(\frac{-t}{\tau}\right) \quad (2.24)$$

where P_∞ is the final flexural strength and τ is a parameter dependent on the temperature following an Arrhenius model. Therefore, the temperature in this model only influences the rate constant ($1/\tau$). Strength and stiffness degradation due to the effects of hygrothermal ageing can also be approximated using a simple algebraic relationship of the following form [210]:

$$\frac{P}{P_\circ} = \left(\frac{T_{gw} - T}{T_{gd} - T_\circ}\right)^n \quad (2.25)$$

where P denotes the material property at the test temperature T, P_0 is the initial property value of the dry material at room or reference temperature T_0, and T_{gd} and T_{gw} are the glass transition temperatures of the dry and the conditioned (wet) material. The exponent n is a constant empirically derived from experimental data (proposed equal to 0.5 in [211]). This relationship provides a rational solution only when $T_{gd} > T_0$, and $T_{gw} > T$. Since this relation is originally proposed for epoxy resins, predicting the hygrothermal degradation of FRP composites can be satisfactory only for matrix dominated properties (such as shear and transverse flexural strength). For fiber dominated properties, a micromechanics approach may be used adapting this formula to account for the effect of matrix changes in the composite material behavior. A more general form of this equation which also includes cyclic fatigue effects on the strength degradation is [210]:

$$\frac{P}{P_\circ} = \left(\frac{T_{gw} - T}{T_{gd} - T_\circ}\right)^n - k \log N \tag{2.26}$$

where K is obtained by curve fitting of experimental results and N is the number of cycles. In case of lack in experimental data, the wet glass transition temperature can be obtained as [210]:

$$T_{gw} = (AM^2 + BM + C)T_{gd} \tag{2.27}$$

where M is the moisture content (%), and A, B and C are constants obtained from curve fitting of experimental data. Based on experimental observations, Chamis and Murthy [210] found these parameters equal to 0.005, –0.1 and 1, respectively. The following relation has also been suggested for predicting the wet T_g [212]:

$$T_{gw} = T_{gd} - gM \tag{2.28}$$

where g is the temperature shift (in K) per unit absorbed moisture. In another study, Kelley and Bueche [213] developed a model for modeling the plasticization effect of a diluent on polymers based on the relative increase in free volume:

$$T_g = \frac{A_p V_p T_{gp} + A_d (1 - V_p) T_{gd}}{A_p V_p + A_d (1 - V_p)} \tag{2.29}$$

where T_{gp} and T_{gd} are the glass transition temperatures of the dry polymer and diluent (water in this case), respectively. V_p is the volume fraction of the polymer, A_p and A_d are the volumetric expansion terms for the polymer and water. The volume fraction of polymer at time t can be obtained as:

$$V_p = \frac{1}{1 + 0.01 M_t \rho \dot{V}} \tag{2.30}$$

where $\dot{V}$ is the specific volume of water (=1 cc/g) and ρ is the water density. The T_g of water is often assumed equal to 0°C. The empirical values of A_p and A_d are 1.253×10^{-4} K^{-1} and 1.5×10^{-3} K^{-1},

respectively [98]. The Fox equation has also been used for estimating the wet glass transition temperature [214]. According to this equation, the wet T_g can be obtained as:

$$\frac{1}{T_g} = \frac{w_1}{T_{gd}} + \frac{w_2}{T_{gp}} \tag{2.31}$$

where w_1 and w_2 are the mass fractions of water and polymer, respectively.

For the composite materials, the changes of T_g due to moisture absorption (or in general a diluent) as follows [215]:

$$T_g = \frac{\alpha_m T_{gm}(1-V_f) + \alpha_f V_f T_{gf}}{\alpha_m (1-V_f) + \alpha_f V_f} \tag{2.32}$$

where T_{gm} and T_{gf} are the glass transition temperatures of fiber and matrix respectively α_m and α_f are the thermal expansion coefficients and V_f is the fiber volume fraction.

2.4.4 Crack growth rate model

Purnell et al. [216] proposed a mechanistic model for accelerated testing of glass reinforced concrete materials assuming that the main degrading mechanism is propagation of fiber surface flaws. The strength degradation with time in this model is obtained as:

$$\frac{\sigma_t}{\sigma_\circ} = \frac{1}{\sqrt{1+k_1 t}} \tag{2.33}$$

where σ_t is the tensile strength at time t, σ_0 is the initial tensile strength. k is the flaw size rate (assumed linear) and can be obtained as follows:

$$k_1 = \frac{1}{a_\circ} k_c k_T C \exp\left[\frac{-E}{RT}\right] \tag{2.34}$$

where the terms k_c and k_T relate the proportionality of flaw growth rate, da/dt, to hydroxyl concentration, C, and the proportionality of induced stress to temperature, respectively. The model assumes that the stress required for propagation of surface flaw rate is proportional to the concentration of hydroxyl ions, C, responsible for hydrolytic attack on glass. Moreover, the crack propagation rate follows an Arrhenius model. However, further studies suggested that the strength loss rate may decrease with time [217]. Based on the fact that this rate change is the result of change in chemical reaction rate (being diffusion controlled), square-root model was proposed:

$$\frac{\sigma_t}{\sigma_\circ} = \frac{1}{\sqrt{1+\sqrt{k_2 t}}} \quad or \quad \frac{\sigma_t}{\sigma_\circ} = \frac{1}{\sqrt{\sqrt{1+k_{2a} t}}} \tag{2.35}$$

A non-linear flaw progression rate has also been used, given by:

$$\frac{\sigma_t}{\sigma_\circ}=\frac{1}{\sqrt{1+(k_3 t)^n}} \quad or \quad \frac{\sigma_t}{\sigma_\circ}=\frac{1}{\sqrt{(1+k_{3a} t)^n}} \tag{2.36}$$

2.4.5 Moisture level dependent models

Some researchers proposed degradation models based on the moisture content of the materials. Nissan [218] proposed a degradation model introducing two different regimes for degradation. In this model, a critical moisture levels, w_c, is defined, below which the moisture forms hydrogen bonds with the polymer network similar to the formation of an adsorption monolayer. Above this value, additional water molecules form hydrogen bonds with broken polar bonds and adjacent water molecules. In this model, the change of the Young's modulus with moisture content is defined as follows:

$$\begin{aligned} P &= P_\circ \exp[-\frac{1}{3}.\frac{w}{W}] \quad w < w_c \\ P &= P_\circ \exp[\frac{1}{3}.\frac{w_c}{W}(CI-1)]\exp[-\frac{CI}{3}.\frac{w}{W}] \quad w > w_c \end{aligned} \tag{2.37}$$

where W is the theoretical quantity of water molecules required for each polar group on the sorbent to be in a hydrogen bond with a single water molecule, CI is an index representing the number of hydrogen bonds established by a single water molecule.

Papanicolaou et al. [219] proposed an exponential decay model for obtaining the material property as a function of water content:

$$\frac{P_\infty - P_t}{P_\infty - P_0}=\exp[\frac{-P_\infty}{P_0}M_t] \tag{2.38}$$

where P_∞ denotes the material property at saturation level, P_t is the property value at time t, P_0 is the property value of dry material and M_t is the water content at time t. Nakamura et al. [220, 221] suggested the following relation for obtaining the joint strength as a function of water uptake:

$$\frac{P}{P_0}=1-\alpha\frac{M_t}{M_\infty} \tag{2.39}$$

here, α is a fitting parameter representing the ratio of absorbed water that contributes to bond breakage, confirming again the existence of the critical water content. Abanilla et al. [98] used a similar degradation model for predicting the short-beam shear strength of CFRP laminates:

$$\frac{M_t}{M_\infty}=m\frac{1-P_t}{P_0} \tag{2.40}$$

Ouyang and Wan [185] proposed an analytical model for deterioration of interfacial fracture energy with moisture attack. They proposed that interfacial fracture energy is related to the interfacial relative humidity:

$$G_f(H) = G_{f0}\left(1 - \frac{1-\beta}{1+[1-H(x,y,t)/(1-H_d)]^n}\right) \quad (2.41)$$

where $H(x,y,t)$ is the interfacial relative humidity at (x,y) coordinate at the interface at time t, G_{f0} is the initial fracture energy, $G_f(H)$ is the interfacial fracture energy in wet conditions and β is a parameter equal to G_{fR}/G_{f0}. H_d defines the deterioration rate of the interfacial energy and is equal to the interfacial fracture energy in which it is reduced to half value of (G_{f0}- G_{fR}). G_{fR} is the final fracture energy at H=100%. In another study, Tuakta and Büyüköztürk [162] proposed an exponential decay model for degradation of bond in FRP-concrete systems under continuous moisture exposure:

$$G_f = Ae^{-b(C/C_{th})} \quad (2.42)$$

where G_f is the interfacial fracture energy, A and b are parameters to be fitted with experimental results, C is the interfacial moisture content at the time of investigation and C_{th} is the threshold moisture content defined as the moisture content beyond which no additional degradation is observed. They observed that this value for FRP-concrete systems is 1.29% and 2.71% at room and high temperatures, respectively. Assuming a constant rate of degradation for any wet-dry cycles, they have proposed the following relation for bond degradation modeling under cyclic moisture conditions:

$$\frac{dG_f}{dN} = q(C/C_{th})^n \quad (2.43)$$

where G_f is the interfacial fracture energy obtained from Eq. (2.42), N is the number of cycles and parameters q and n are obtained from experimental fitting, see Table 2-1. According to this model, the required number of wet-dry cycles for the fracture energy to approach a residual value can be obtained as:

$$N_{th} = \frac{G_{f0} - G_{th}}{q(C/C_{th})^n} \quad (2.44)$$

Table 2-1: Fitted parameters for peel and shear fracture tests [162].

Parameter	Peel test		Shear test	
	23°C	50°C	23°C	50°C
A	647.97	587.09	1040.40	1013.50
b	1.24	1.30	0.49	0.73
C_{th}	1.29	2.71	1.29	2.71
q	223.73	190.85	218.29	406.42
n	0.83	0.78	0.48	0.63

2.4.6 Metric based model

Temperature, time, moisture and corrosive substances can chemically degrade the matrix by chemical reactions. Although modeling all the degrading mechanisms is a complex task, the degradation can be modeled using degradation metrics, α_i [222]. Therefore, the change in the material properties can be obtained as:

$$\frac{P}{P_\circ} = \sqrt{\frac{T_g - T}{T_g - T_0}}(1 + p\alpha_i^q) \tag{2.45}$$

where T_0 is the reference temperature and p and q are empirical parameters. The progression of reaction, $d\alpha/dt$, can be described with an Arrhenius model:

$$\frac{\partial \alpha_t}{\partial t} = k_i(1-\alpha_i)^{n_i} c_s^{m_{si}} \exp\left(\frac{-E_i}{RT}\right) \tag{2.46}$$

where, k_i is the reaction rate, E_i is the activation energy, c_s is the concentration of diffusing substance and n_i and m_{si} are parameters to be obtained experimentally.

2.4.7 Multifactor interaction method

Chamis [223] proposed a model for simulation of thermo-mechanical fatigue of composite laminates based on probabilistic simulations, see Figure 2-7:

$$\frac{P}{P_\circ} = \left(\frac{T_{gw} - T}{T_{gd} - T_\circ}\right)^l \left(1 - \frac{\sigma}{S_f}\right)^m \left(1 - \frac{\sigma_T}{S_f t_f}\right)^n \left(1 - \frac{\sigma_M N_M}{S_f N_{Mf}}\right)^p \left(1 - \frac{\sigma_T N_T}{S_f N_{Tf}}\right)^q \tag{2.47}$$

The definition of the parameters included in this equation is presented in Figure 2-7. In this model, all physical effects are accounted in one simple formula. Each term in this equation describes a specific effect with a degradation rate. The concept of this model is that the complex behavior of any material is assumed to be a surface in space and the shape of this surface is defined by different vectors representing each physical effect (thermal, mechanical, chemical, etc.), see Figure 2-7.

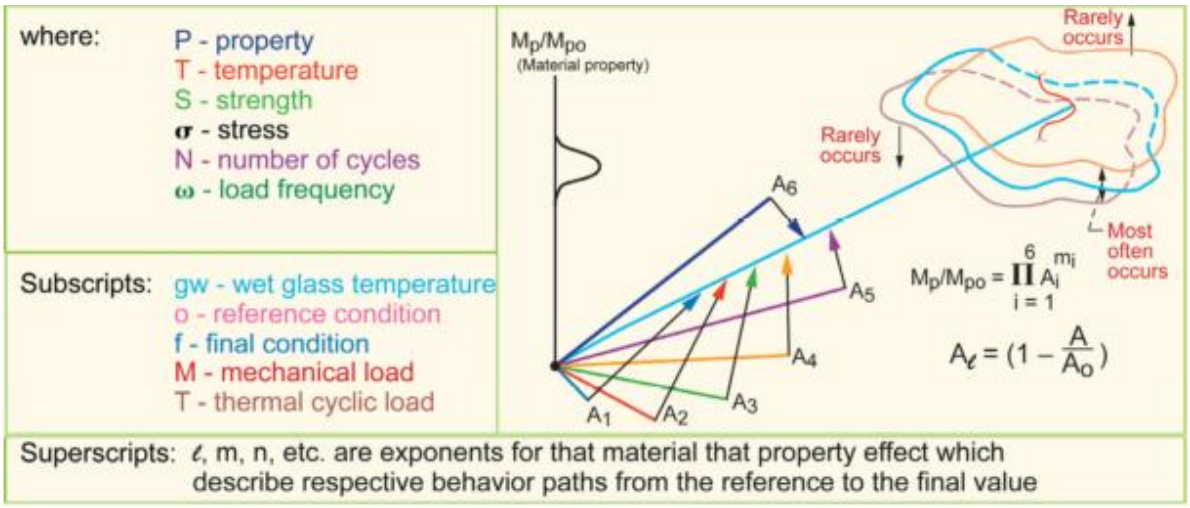

Figure 2-7: Multi-factor interaction model

2.5 Nondestructive techniques

Despite the extensive experimental and theoretical investigations conducted on the bond behavior between composite materials and concrete/masonry substrates, development and utilization of non-destructive methods to monitor the bond quality condition or active fracture mechanisms during the debonding have received less attention.

Visual inspection and hammer tapping are the most widely used in-situ non-destructive testing methods for bond monitoring in FRP-strengthened elements, while several other methods are being applied and developed such as digital image correlation (DIC), infrared (IR) thermography, ultrasonic testing, shearography or acoustic emission (AE) testing. A brief description of these techniques is presented in this section.

2.5.1 Digital image correlation

Several interferometric and white-light optical methods, such as DIC, have been proposed and developed in experimental solid mechanics for displacement or strain measurements over an entire region of interest (ROI) [45, 224]. However, only a few studies can be found using these techniques for investigating the interfacial bond behavior, see e.g. [48, 49, 225]. These techniques contrast with conventional strain gauges or extensometers by the fact that they provide full-field data and are contact-free.

The DIC technique provides full-field displacements of an object by comparing the similarity between images recorded (with a digital camera), at least, at two different mechanical states. The strain field can then be obtained from the derivation of the displacement field measured

with DIC. The surface of interest must have a speckled pattern, which is typically obtained by spray or airbrush painting. A suitable balance between region of interest (ROI) and average size of white-to-dark spots must be achieved in order to enhance the displacement spatial resolution (small aperture) associated to the DIC measurements.

This technique can be used during debonding tests for obtaining the distribution of strains on the FRP surface and investigating the three-dimensional aspects of the bond behavior (such as transversal strains or the changes of bond-slip behavior along FRP width) [225]. The full-field strain distribution can be used for the characterization of bond-slip laws to be used in numerical modeling approaches [226].

2.5.2 Shearography

Shearography is one of the few interferometric methods that directly provides the full-field strain distribution on the surface under investigation [227, 228]. This method can also be used to detect internal defects and flaws. Any defect or flaw, unless very far from the surface, induces surface strains on the objects, which make it detectable. This method has been widely used to detect defects in composites and tires [228]. Application of this method for the detection and localization of interfacial bond defects in FRP-strengthened concrete elements has recently received attention, see e.g. [229, 230].

In this technique, the light waves reflected from the object's surface are recorded with a Charge Coupled Device (CCD) camera as a pair of laterally sheared images. The interference between the image pairs produces a random interference pattern. The comparison between the patterns obtained at different mechanical states produces a fringe pattern, called shearogram, presenting the derivative of the surface displacements [231]. A major drawback of this method, much alike all speckle interferometric methods, is that excessive rigid body motion produces de-correlation of speckle patterns resulting in a reduction the visibility of the fringe [228].

2.5.3 IR thermography

The IR thermography method has been extensively used in the last years for detection and evaluation of defects in FRP bonded components [230, 232, 233]. Applications are mostly focused on the qualitative assessment and the localization of the defects. However, once the defects have been located, it is interesting to characterize them quantitatively in order to evaluate the performance of the structure [234].

IR thermography is based on the principle that the heat flux is transmitted at different rates in materials with different thermal properties [234]. In an FRP-strengthened element, any defect or

delamination in the interfacial region changes the thermal properties in that area. Therefore, if a heat flux is applied to the surface of a FRP-bonded element, the heat will be transferred with a different rate in the defected areas with respect to the perfectly bonded regions. This leads to the appearance of hot or cold spots in thermal images depending on the heat observation method [232].

2.5.4 Ultrasonic testing

Ultrasonic methods have been widely used for the evaluation of concrete [235]. These methods have also been used for investigating the deterioration in FRP-strengthened concrete structures [236] or characterization of the bond in adhesive bonded elements [237]. Detection of interfacial delamination or defects with these techniques has been reported in [238, 239]. The method is based on the transmission of ultrasonic waves through the material. The defect depth can be calculated from the required time to receive the reflected echo. Alternatively, an ultrasonic tomography can be performed in a direct (sender and receiver on opposite sides of the specimen) or indirect (on the same side of the specimen) manner. Thereby, the ultrasonic wave velocity is correlated to the material density and voids are detected as areas with high wave transmission resistance.

2.5.5 Acoustic Emission (AE) technique

Acoustic Emissions (AE) are high-frequency transient elastic waves that are emitted within the material during local stress redistributions occurring during crack initiation and growth. These emissions are detected on the material's surface by means of piezoelectric transducers, pre-amplified, filtered and amplified before they are sent to the data logger. Background noise is eliminated using a minimum amplitude threshold.

The recorded acoustic emissions hold information on the fracture process which produced them. Basic AE hit counting, taking into account the cumulative or average number of AE hits or emitted AE energy, has successfully been used for damage assessment in rock, concrete and masonry [240-242].

Limited results are reported in literature regarding the analysis of debonding phenomena in externally strengthened masonry and concrete components by means of the acoustic emission technique. AE monitoring during FRP debonding from concrete beams and slabs was studied by Carpinteri et al. [243], who detected the propagation of flexural cracks in an FRP-strengthened beam and by Degala et al. [244], who observed the progressive debonding of CFRP strips from concrete slabs and differentiated between CFRP debonding and concrete failure (flexural, compressive or shear failure) by looking at the relative intensity of the AE signals. Shear behavior of strengthened masonry walls was analyzed with the acoustic emission technique by Masera et al.

[245] who observed decrease of the signal peak frequency upon failure of the masonry specimens. Here, the debonding mechanism itself will be the object of investigation.

Chapter 3

Experimental plan and test methods

The experimental program and test methods followed in this thesis are described in the present chapter. A scheme of the experimental plan is shown in Figure 3-1. The main aim of this plan is to investigate the effects of environmental conditions on the bond behavior in FRP-strengthened masonry. Accelerated ageing tests are performed to simulate different environmental conditions. The changes in the material mechanical properties and the bond behavior with exposure time are monitored periodically by performing qualitative and quantitative laboratory tests. Advanced measurement techniques are adopted for investigating the fracture propagation and degradation in the bond between FRP and masonry, as explained in Chapter 6.

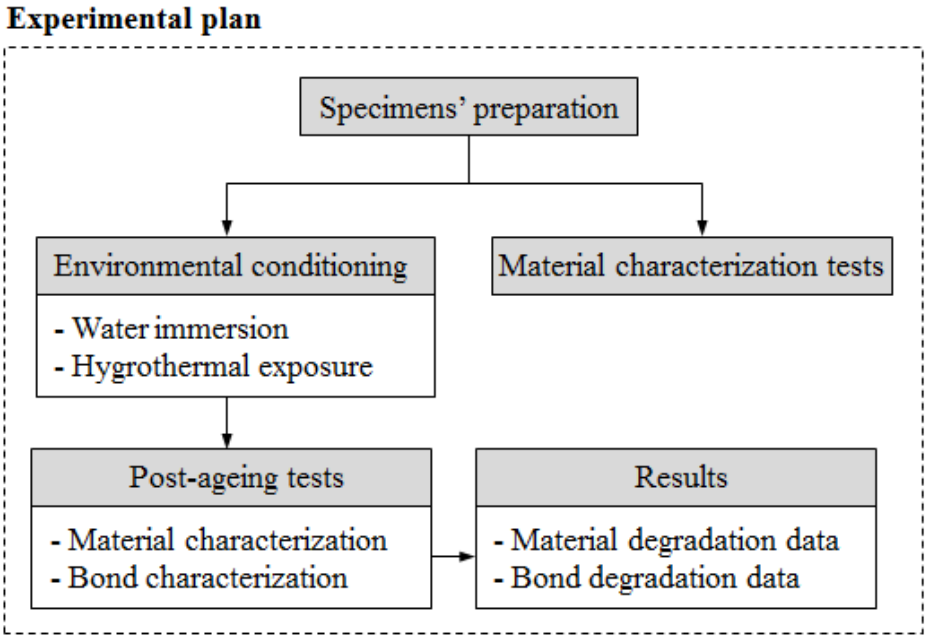

Figure 3-1: Experimental plan.

3.1 Materials

Two types of solid cay bricks are used in this study as substrate, hereafter denoted by brick type 1 and 2. Both brick types have dimensions of 200x100x50 mm^3. The brick type 1 is a handmade brick produced in Galveias (Portugal) with low compressive strength, selected as representative of historical Portuguese masonry bricks. These bricks are used in the preparation of the specimens for water immersion tests (Chapter 4). Physical and mechanical properties of these bricks are detailed in Fernandes and Lourenço [246]. Their compressive strength is reported as 9.2 MPa with 20.9 % porosity and 11.2 % water absorption after 24 hours water immersion [246]. The bricks type 2, used for accelerated hygrothermal exposure tests (chapter 5), are produced for the present work given the difficulty in obtaining the bricks type 1.

Glass Fiber Reinforced Polymer (GFRP) is used as the composite material for external strengthening of the bricks. GFRP composites, compared with other conventional FRP materials, have lower axial stiffness that makes them more suitable for masonry structures [59]. GFRPs have been extensively used for externally bonded reinforcement (EBR) of masonry structures, but issues such as durability and compatibility with masonry substrates are still under investigation. The GFRP composites are prepared with commercially available unidirectional E-glass fibers (MapeWrap G UNI-AX 900/60) and a compatible two-part epoxy resin (MapeWrap 31) as the matrix, following the wet lay-up procedure. A two-part epoxy primer (MapeWrap primer 1) is also used for preparation of the bricks' surfaces before application of FRP composite. The mechanical and physical properties of the composite components provided by the supplier are presented in Table 3-1.

Table 3-1: Material properties provided by the manufacturer.

E-Glass fibers		
Density	ρ (kg/dm^3)	2.62
Weight	(g/m^2)	900
Fabric equivalent thickness	t_{eq} (mm)	0.48
Tensile strength	f_{tf} (MPa)	2560
Tensile elastic modulus	E_f (GPa)	80.7
Tensile maximum strain	ε (%)	3-4
Thickness	t (mm)	0.17
Epoxy resin		
Brookfield viscosity	(mPa.s)	7000
Tensile strength	f_{tm} (MPa)	40
Tensile maximum strain (28 days)	ε (%)	1.80
Primer		
Brookfield viscosity	(mPa.s)	300

3.2 Specimens

Two different types of specimens are used in this study: (a) specimens for characterization tests of the different materials and (b) specimens for characterization tests of interfacial bond.

The specimens prepared for material characterization tests consist of: brick specimens, see Figure 3-2 (a, b); epoxy dog-bone shape specimens, see Figure 3-2 (c); primer dog-bone shape specimens, see Figure 3-2 (c); GFRP coupons, see Figure 3-2 (d). The procedures followed for preparation of these specimens are explained in Sec. 3.3 for each test method separately.

Two types of specimens are prepared for bond characterization tests: pull-off test specimens, see Figure 3-3 (a); and shear debonding test specimens, see Figure 3-3 (b). The preparation procedure for these specimens is presented in Sec. 3.4.1.

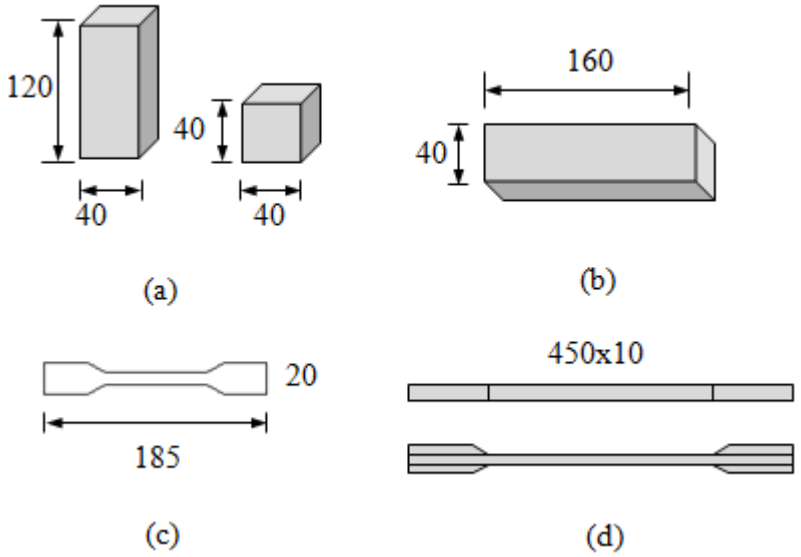

Figure 3-2: Specimens for material characterization tests (dimensions in mm).

3.3 Mechanical characterization

The experimental tests performed for characterization of mechanical properties of constituent materials are presented in this section. Five specimens are tested in each test method and the average results are presented. A summary of the obtained mechanical properties can be found in Table 3-2.

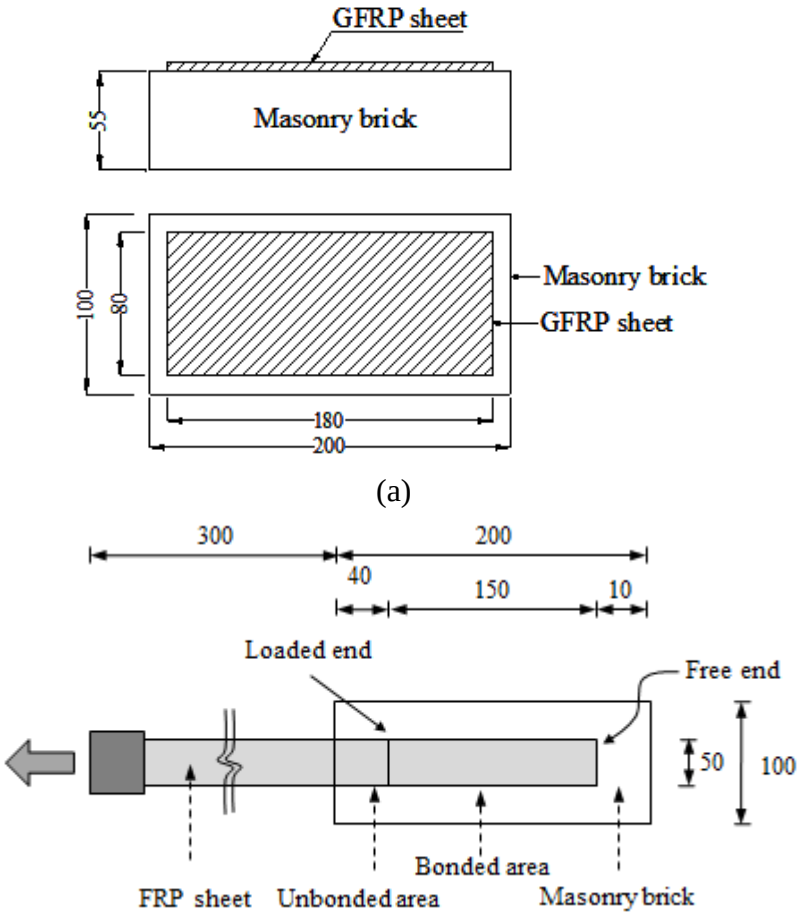

Figure 3-3: Specimens for bond characterization tests (dimensions in mm): (a) pull-off test specimen; (b) shear debonding test specimen.

Table 3-2: Material properties of the materials.

Clay brick type 1		Average	CoV(%)
Compressive strength	f_{cb} (MPa)	8.0	11.0
Clay brick type 2			
Compressive strength	f_{cb} (MPa)	14.3	4.0
Epoxy resin			
Tensile strength	f_{te} (MPa)	53.8	9.7
Elastic modulus	E_{te} (GPa)	2.5	9.5
Ultimate deformation	ε (%)	2.6	10.4
Primer			
Tensile strength	f_{tp} (MPa)	55.3	11.1
Elastic modulus	E_{tp} (GPa)	2.9	6.1
Ultimate deformation	ε (%)	2.1	14.5
GFRP coupon			
Tensile strength	f_{tf} (MPa)	1250.0	15.0
Elastic modulus	E_{tf} (GPa)	79.2	6.8
Ultimate deformation	ε (%)	1.9	20.2

3.3.1 Brick

The compressive strength of the bricks is obtained according to standards EN 772-1 (2002) [247] and UNI EN 8942-3 (1986) [248]. Water absorption tests have also been performed on the brick specimens and the results are presented.

3.3.1.1 Compressive strength

Compression tests are performed on 40×40×40 mm^3 cubic brick specimens. The specimens are extracted from the internal volume of the bricks as shown in Figure 3-4 (three specimens from each brick). The top and bottom surfaces of the bricks are regularized initially with a grinding machine. The specimens are then extracted with the aim of an electric masonry saw.

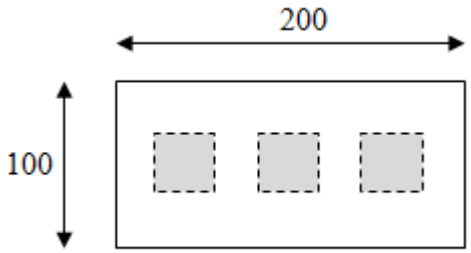

Figure 3-4: Cutting scheme of the brick specimens (dimensions in mm).

The small specimens are loaded perpendicular to the flatwise direction, see Figure 3-5, with a LLOYD 50kN testing machine. As shown in Figure 3-6 (a), a steel plate with a spherical seat is placed on top of the specimen for facilitating the load application and preventing any effects due to the specimen's imperfections. Additionally, in order to minimize the friction effect on the boundaries of the specimen, a pair of Teflon sheets with a thin layer of oil between them is placed between the surface of the platens and the specimen, see Figure 3-6 (b).

Due to the small dimensions of the specimens, no measurement device was mounted on the specimens and the specimen's deformation is monitored with the control displacement transducer (LVDT) mounted on the actuator.

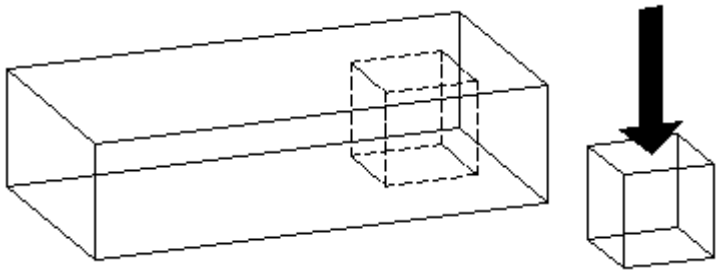

Figure 3-5: Direction of load application in compressive tests.

(a) (b)

Figure 3-6: Laboratory set-up for compressive tests: (a) test set-up; (b) specimen preparation.

The compressive strength of the brick type 1 is 9.2 MPa (CoV=11.0%) [246]. The average compressive strength of the brick type 2 was obtained equal to 16 MPa (CoV=4.0%). According to ASTM C39-12a, when the height-to-length ratio of the specimens is lower than two, the compressive strength values should be corrected. Since the brick specimens are cubic (height-to-length ratio equal to 1), a reduction factor of 0.87 is proposed in this standard leading to compressive strengths of 8.0 MPa and 14.3 MPa for bricks type 1 and 2, respectively. Figure 3-7 presents the typical stress-strain behavior and failure modes of the tested specimens.

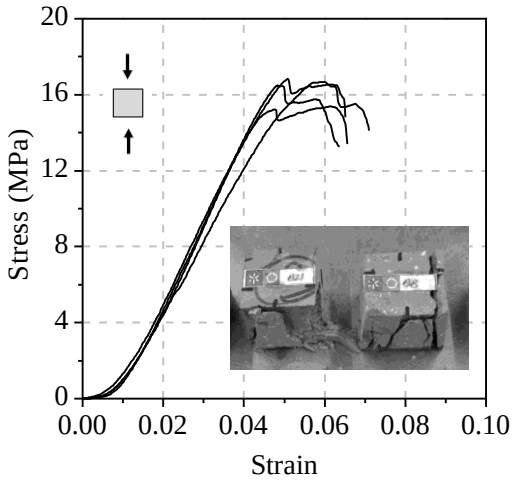

Figure 3-7: Brick type 2 typical compressive behavior.

3.3.2 Epoxy resin and primer

Mechanical properties of the epoxy resin and primer are determined by performing tensile tests on dog-bone shape specimens, see Figure 3-2 (c). Although seven days are proposed for curing of the epoxy resin in the technical datasheet provided by the manufacturer, the specimens were cured for 60 days at room temperature. Previous studies have shown that curing times much longer than the

period proposed by the suppliers are necessary for complete curing of cold-cured epoxy resins [104, 249]. Cross-linking reactions are still in progress before complete curing of the epoxy resin, meaning that the material is not in a stable condition and with its maximum mechanical properties. In order to accurately investigate the effect of water on the properties of epoxy resin, it is necessary to separate the water degrading effects and epoxy resin cross-linking reactions.

The recommendations provided by the supplier and ISO 527-1 (2012) [250] are followed for preparation of the specimens and performing the tensile tests. Type A specimens are selected from ISO 527-1 (2012) for preparation of the samples in this study. Both primer and resin have the same mixing time, curing time and working temperature according to the technical sheets. The specimens preparation is performed at around +20℃ (within the proposed working temperature range of +10℃ to +30℃). The specimens preparation procedure is illustrated step by step in Figure 3-8. The epoxy resin and primer are prepared by mixing two materials parts (both were two-part materials) appropriately until obtaining a homogenous paste. The paste is then poured into a silicone mold with special care to minimize the air voids in the specimens. A steel roller is used for removing the excessive epoxy/primer from the molds. The specimens are taken out from the molds after two days curing in the laboratory conditions, having average final dimensions of 185×20×4 mm^3.

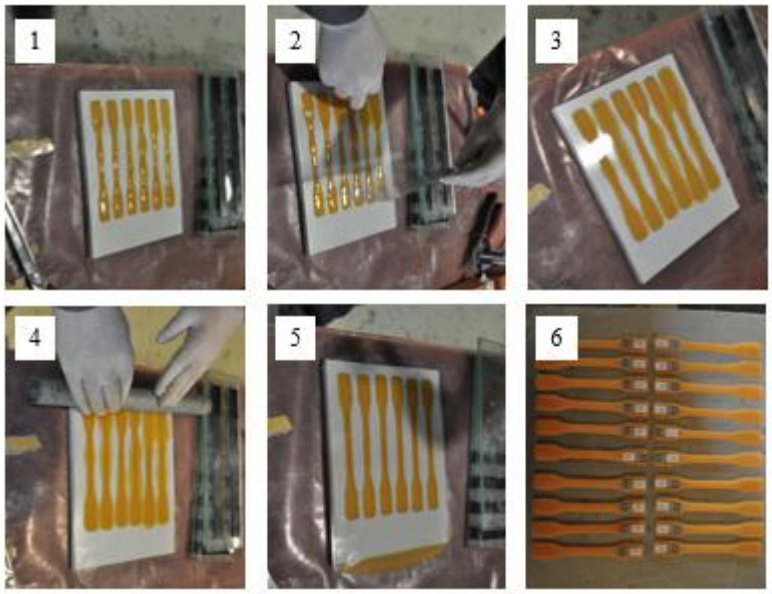

Figure 3-8: Preparation of epoxy resin and primer specimens.

The glass transition temperature (T_g) of the epoxy resin is obtained by means of differential scanning calorimetry (DSC) method. The specifications proposed by ASTM E1356-08 [251] are followed for performing the tests. In this method, the rate of heat absorption or emission from a specimen with temperature increment is measured. The T_g, defined as the temperature in which the

specific heat of the material is changed, is determined from the heat flow-temperature curve obtained from the DSC tests [252]. Here, the thermal scans are carried out between 40°C and 200°C with a heating rate of 10°C/min. The typical heat flow-temperature curve obtained from the DSC tests is shown in Figure 3-10. The average T_g was +70°C (the mean value of four tests).

3.3.2.1 Tensile strength

The tests are carried out in accordance with ISO 527-1 (2012) [250] and ASTM D638-10 [253] with a LLOYD 50kN testing machine, see Figure 3-10. The tests are driven displacement control at a rate of 1 mm/min. Deformation of the specimens is monitored by a clip gauge placed on the middle of the specimens. The tensile stress is determined as the recorded force divided by average cross sectional area measured at three sections of the specimens. The elastic modulus is then calculated as the initial slope of the stress-strain curve.

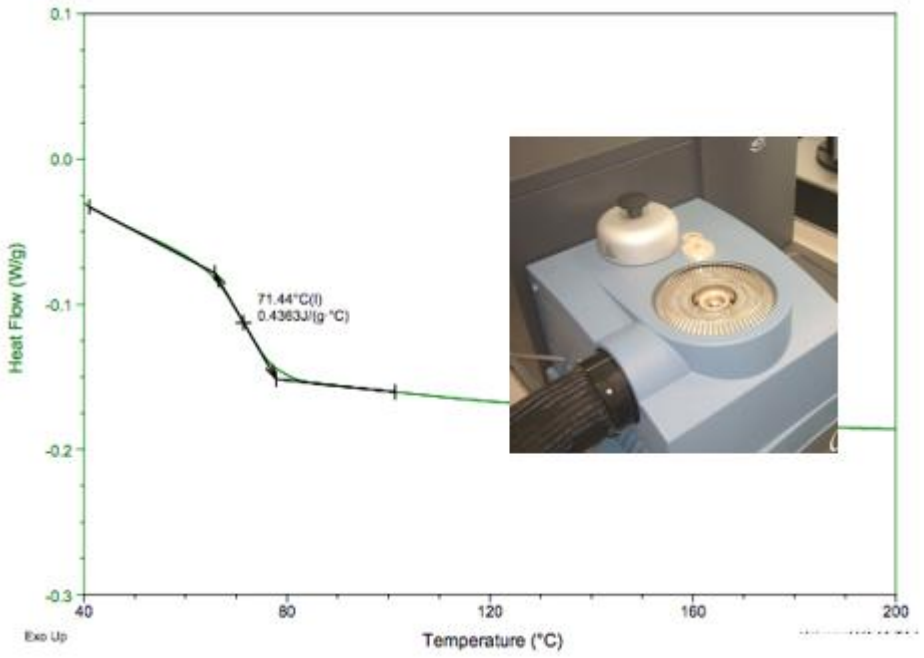

Figure 3-9: Typical heat flow-temperature curve obtained from DSC tests.

Figure 3-10: Laboratory set-up for epoxy/primer tensile tests.

The average tensile strength of epoxy resin is obtained as 55.3 MPa (CoV=4.1%) with elastic modulus of 2.5 GPa (CoV=9.5%). The primer has an average tensile strength of 54.0 MPa (CoV=7.0%) with elastic modulus of 2.4 GPa (CoV=6.1%). The typical stress-strain curves of the specimens together with the observed failure modes are shown in Figure 3-11.

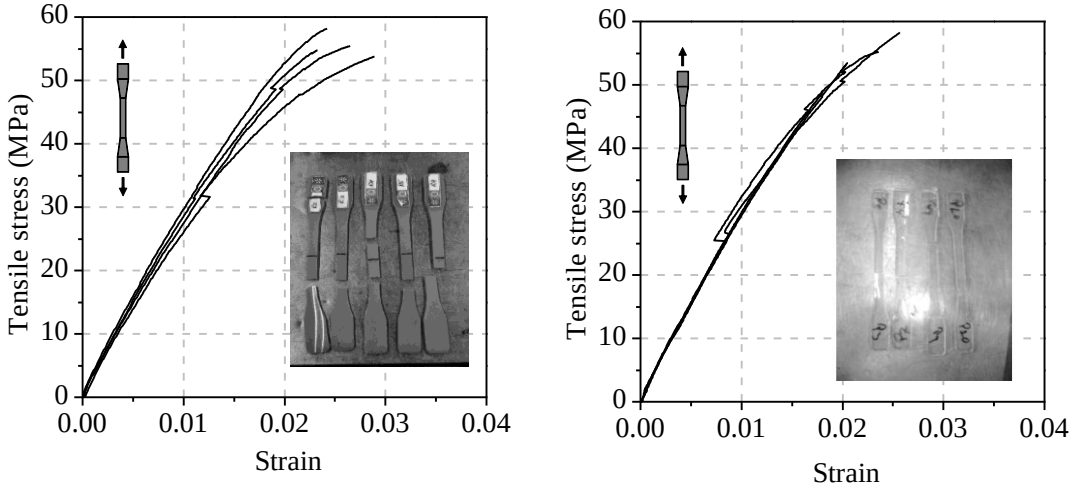

Figure 3-11: Typical tensile behavior of: (a) epoxy resin; (b) primer.

3.3.3 GFRP composite

Regarding the composite materials, the specimens preparation, tensile tests and analysis of the results are conducted following the recommendations of ISO 527-1 (2012) [250] and ASTM D3039-08 [254]. The mechanical properties are obtained in terms of tensile strength, f_{tf}, and elastic modulus, E_f.

The GFRP coupons are prepared following the wet lay-up procedure according to the code specifications. Since the glass fibers used in this study consist of bundles with a large number of

filaments, specimen type B in ISO 527-1 (2012) [250] is selected for preparation of the coupons. The procedure followed for preparation of the specimens is illustrated step by step in Figure 3-12, see ISO 527-1 (2012) [250] for detailed explanation. The average final dimensions of the specimens are 300×15×2×mm^3 with gauge length of 150 mm.

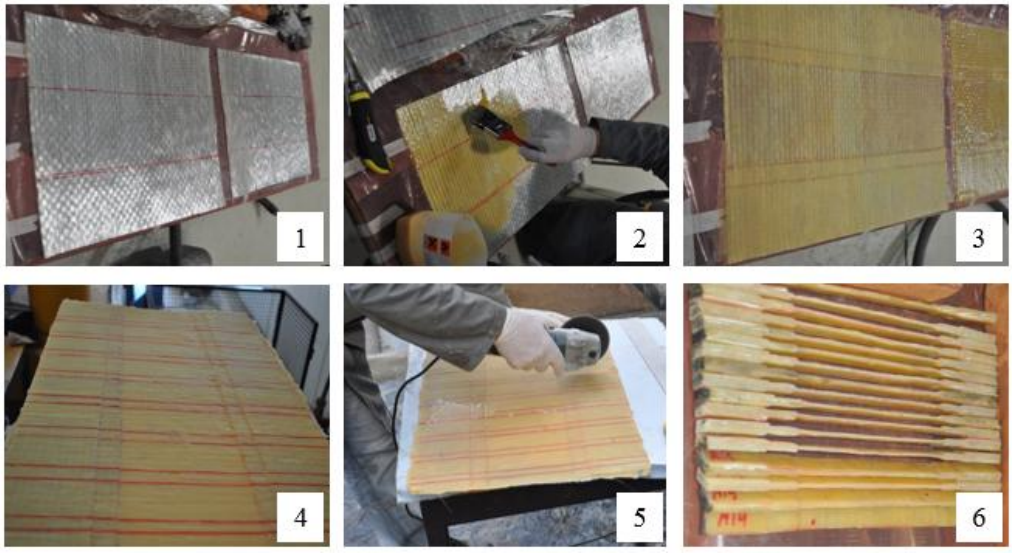

Figure 3-12: Preparation of GFRP coupon specimens.

3.3.3.1 Tensile strength

The tests are carried out in accordance with ISO 527-1 (2012) [250] and ASTM D3039-08 [254] with a LLOYD 50kN testing machine. The tests are driven displacement control at a rate of 1 mm/min. Deformation of the specimens is monitored by a clip gauge placed on the middle of the specimens. The test setup is shown in Figure 3-13.

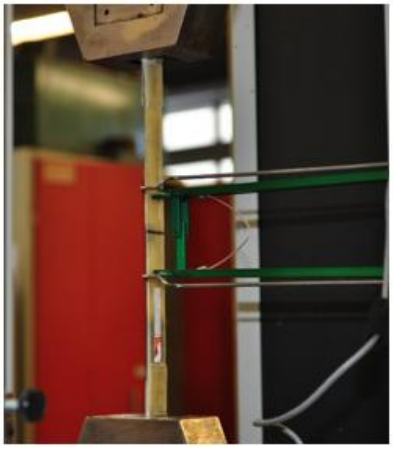

Figure 3-13: Laboratory set-up for GFRP tensile tests.

According to ASTM D3039-08 [254], the tensile stress can be obtained as the recorded force divided by the average cross sectional area and the elastic modulus is the slope of the stress-strain curve in the strain range between 1000 to 3000 microstrains. ACI 440.3R-04 [255] proposes that the tensile stress can also be obtained as the recorded force divided by equivalent fiber area. Equivalent fiber area is defined as the width of the specimens multiplied by fiber equivalent thickness given in technical data sheets. As in the wet lay-up procedures, the specimens' thickness is not usually uniform though the specimen, the latter seems to provide more realistic results. Normalizing the mechanical properties to thickness can also provide an accurate baseline for comparison purposes in wet lay-up specimens [164, 256].

Throughout this study, the changes in tensile strength and elastic modulus of GFRP coupons are normalized to the specimens thickness in accordance with ASTM D7565-10 [256]. However, for initial characterization of the material properties, the method based on equivalent fiber area, proposed in ACI 440.3R-04 [255] is also used. The typical stress-strain curves obtained from tensile tests on GFRP coupons are shown in Figure 3-14 for both methods.

The average tensile strength of GFRP coupons is 1250.0 MPa (CoV=15%) with elastic modulus of 79.2 GPa (CoV=6.8%). The typical failure mode of the specimens is shown in Figure 3-14 (failure modes type XGM and SGM according to ASTM D3039-08 [254]).

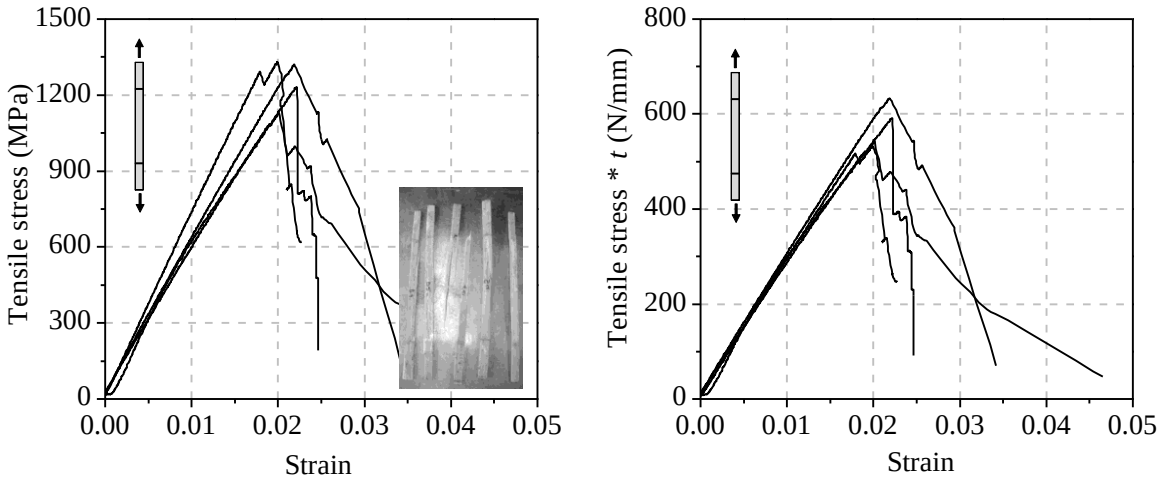

(a) (b)

Figure 3-14: Typical tensile behavior of GFRP coupons: (a) based on equivalent fiber area; (b) based on stresses normalized to thickness.

3.4 Water absorption tests

3.4.1 Bricks

Bricks water absorption tests are performed based on the gravimetric sorption method according to ASTM C 67-12 [9]. Full size bricks are used for performing the tests as suggested in the standard. The specimens are immersed in water at 23℃ after initial drying. Five specimens are then taken from the water periodically, wiped and weighed to measure the absorbed water with time. The difference between the initial weight and the weight after immersion represents the moisture mass uptake, see Eq. (3.1). This procedure is repeated until having water absorption lower than 1% of the dry weight in three sequential measurements.

$$M_t = \frac{W_t - W_0}{W_0} \times 100 \tag{3.1}$$

where, M_t is the moisture uptake content at time t, open porosity, W_t is the specimen's weight at time t, W_0 is the dry weight of the specimen. The average moisture uptake behavior of the brick specimens through time is presented in Figure 3-15. The brick type 1 absorbed 10.3% mass of moisture upon saturation while this value is 9.3% for the brick type 2. This absorbed water is corresponding to 17% and 17.9 % open porosity in bricks type 1 and 2, respectively. The open porosity of the bricks is reasonably high, even if higher values are normal in hand-made bricks [257]. Open porosity, f, is defined as the voids volume in which the water can penetrate due to immersion:

$$f = \frac{W_s - W_d}{V\rho_w} \tag{3.2}$$

where, W_s is the saturated weight, W_d is the dry weight, V is the volume of the specimen and ρ_w is the water density.

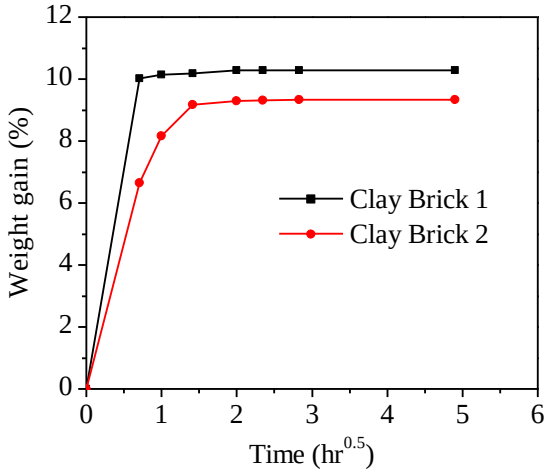

Figure 3-15: Moisture uptake behavior of brick specimens.

3.4.2 Epoxy and GFRP

Water absorption tests for epoxy and GFRP are performed according to ASTM D 570-98 (2010) [258]. The specimens are immersed in deionized water at 23℃ after initial drying. Five specimens are then taken from the water periodically, wiped and weighed to measure the absorbed water with time. The difference between the initial weight and the weight after conditioning represents the moisture mass uptake. This procedure is repeated until having water absorption lower than 1% of the dry weight in three sequential measurements. The average moisture uptake behavior of epoxy resin and GFRP coupon is presented in Figure 3-16. In general, the epoxy resin absorbed 1.6% mass of moisture upon saturation, while GFRP coupons absorbed 3.7%.

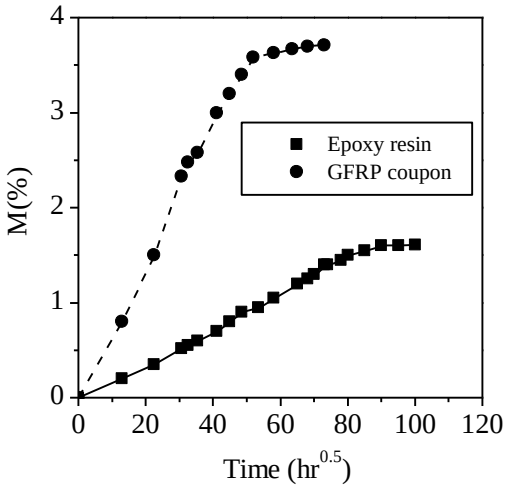

Figure 3-16: Moisture uptake behavior of epoxy and GFRP.

Assuming a Fickian moisture uptake behavior, the moisture diffusion coefficient of epoxy resin and GFRP can be obtained. According to the Fick's second law, the moisture uptake in a one-dimensional space can be modeled with the following differential equation:

$$\frac{\partial C}{\partial t} = -D\frac{\partial^2 C}{\partial x^2} \tag{3.3}$$

This equation provides the moisture concentration, C, at a distance x from the contact surface as a function of time t and moisture diffusion, D. The analytical solution to this equation is:

$$M_t = M_\infty[1 - \frac{8}{\pi^2}\sum_{n=0}^{\infty}\frac{\exp[(2n+1)^2\pi^2(\frac{-Dt}{h^2})]}{(2n+1)^2}] \tag{3.4}$$

where, M_∞ is the equilibrium moisture content at saturation point, and h is the specimen's thickness. Eq. (3.4) can be approximated for short-term exposures ($Dt/h^2<0.04$) as:

$$\frac{M}{M_\infty} = \frac{4}{h}\sqrt{\frac{Dt}{\pi}} \tag{3.5}$$

while for long-term exposures ($Dt/h^2>0.04$), Eq. (3.4) reduces to:

$$\frac{M}{M_\infty} = [1 - \frac{8}{\pi^2}\exp(\frac{-Dt}{h^2}\pi^2)] \tag{3.6}$$

The moisture diffusion coefficients can be determined as the initial slope of the water uptake curve as follows, see Figure 3-17:

$$D = \pi(\frac{h}{4M_\infty})^2(\frac{M_2 - M_1}{\sqrt{t_2} - \sqrt{t_1}})^2 \tag{3.7}$$

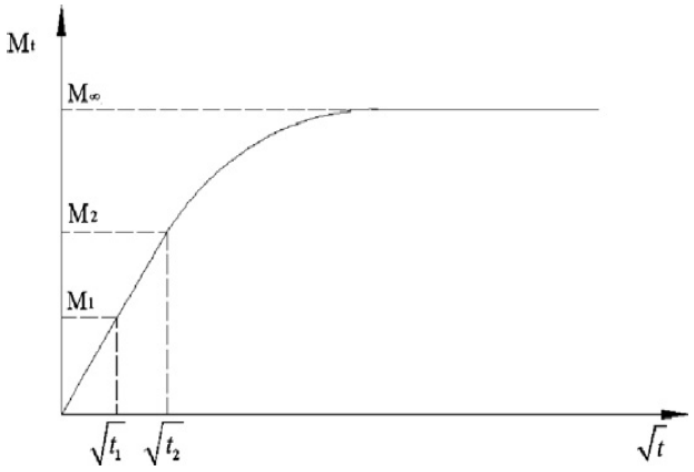

Figure 3-17: Fickian diffusion.

The diffusion coefficient for epoxy resin is obtained as 8.85×10^{-8} mm^2/sec, in line with [113, 259]. Water absorption rate and the amount of absorbed water upon saturation in epoxy resins depend on different parameters such as formulation, curing conditions, environment temperature and humidity [104]. A wide range of equilibrium water content and moisture diffusion coefficients can be found in the literature. In [90, 259] a water content range from 0.4% to 1.9% was observed at saturation, with a moisture diffusion coefficient of 1.19×10^{-9} mm^2/sec. In [104], a water content range from 4.7% to 8.7% was observed, with a moisture diffusion coefficient about 10^{-10} mm^2/sec. The calculated diffusion coefficient for GFRP is 2.1×10^{-7} mm^2/sec, in line with [113, 259]. It can be observed that the equilibrium moisture content and moisture diffusion coefficient of the composite specimens are higher than of the epoxy resin. This difference is due to the imperfect interfaces that are in contact with water in the composite specimens [104].

3.5 Bond characterization

For characterization of the bond behavior single-lap shear bond and pull-off tests are performed. Pull-off tests are only used in water immersion tests (Chapter 4). The specimens preparation and test procedure for each test method are presented in this section. Advanced measurement techniques are also used for obtaining a detailed understanding of the debonding phenomenon as well as developing new methods for bond quality assessment. The detailed explanation of these techniques can be found in Chapter 6.

3.5.1 Specimens preparation

The geometrical details of the specimens are presented in Figure 3-3. The GFRP sheets are applied to the bricks surface following the wet lay-up procedure, see Figure 3-18. The masonry bricks are dried in the oven before application of the GFRP sheets. After cleaning the brick surface, a two-part epoxy primer (MapeWrap Primer 1) is applied to the bricks surface with a bristle roller for preparation of the substrate surface before GFRP application. Finally, a two-part epoxy resin (MapeWrap 31) is used as matrix for the composite material and for adhesion to the masonry substrate. The epoxy resin is applied on the still fresh primer layer as suggested in the technical sheets.

Figure 3-18: Preparation of the specimens for debonding tests.

For the pull-off tests, the GFRP sheets are applied over a 180x80 mm^2 area of the bricks surface as shown in Figure 3-3 (a). As for the pull-out tests, the GFRP sheets with 50 mm width are applied on the brick surface. The bonded length of the GFRP is equal to 150 mm with a 40 mm unbonded part at the loaded end, see Figure 3-3 (b).

3.5.2 Pull-off tests

Pull-off tests are usually performed for evaluating the tensile bond performance as an in-situ test method even if the results obtained represent the local adhesion strength between composite material and the substrate, and are not representative of the global bond behavior. This test method is only used in water immersion tests.

The pull-off tests are performed according to the recommendations of ASTM D4541-09 [260]. A 50 mm diameter partial core is drilled on the test zone with an approximate depth of 5 mm, see Figure 3-19. Then, an aluminum disk is glued over the GFRP surface, inside the drilled zone, with a high strength adhesive. After curing of the adhesive, the disks are pulled monotonically at a constant rate of about 20 kPa/s so that failure occurred within one minute. The tests are carried out using a portable Proceq DYNA Z15 instrument.

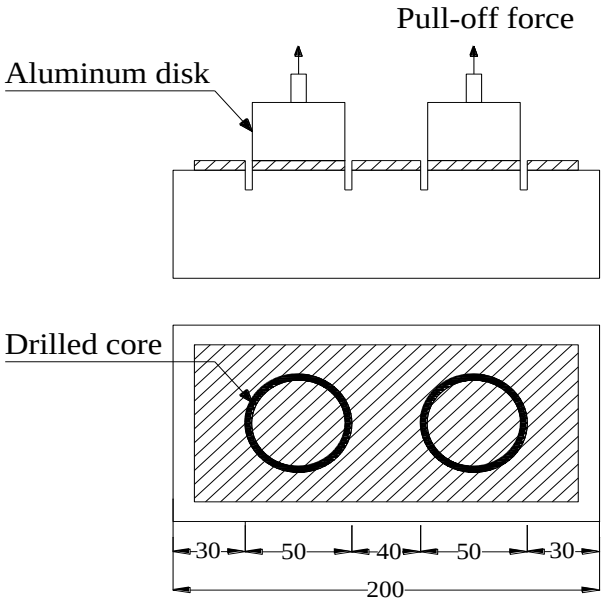

Figure 3-19: Pull-off tests setup.

3.5.3 Shear debonding tests

Single-lap shear bond tests are performed on the conditioned specimens to assess the changes in the shear bond behavior. The tests are performed using a closed-loop servo-controlled testing machine with maximum load capacity of 50 kN. A rigid supporting steel frame is used to support the specimens appropriately and avoid misalignments in load application. The specimens are placed on the steel frame and firmly clamped to it as shown in Figure 3-20 (a). The specimens are pulled monotonically with a speed rate of 5μm/sec. Tests are driven under displacement control with

reference to the LVDT placed at the loaded end of the FRP composite. The resulting load is measured by means of a load cell. The relative slip between the GFRP and the masonry substrate is measured with the LVDTs glued along the bonded length, see Figure 3-20 (b). Two LVDTs are glued at the loaded end, two in the middle of the bonded length, and one at the free end of the FRP sheet.

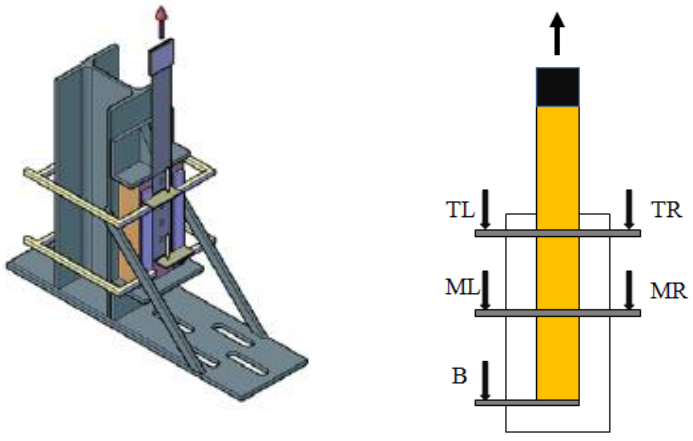

(a) (b)

Figure 3-20: Single-lap shear bond tests: (a) test setup (perspective); (b) specimen instrumentation (front view).

3.6 Environmental exposures

3.6.1 Water immersion

This exposure is intended to investigate the influence of moisture on the bond behavior in FRP-strengthened masonry components. The test specimens are immersed in deionized water for 24 weeks. A water tub placed in a temperature controlled environment (23℃, 60% R.H.) is used for performing the tests.

3.6.2 Hygrothermal conditions

This exposure is aimed at investigating the degrading effect of hygrothermal conditions (coupled temperature and humidity exposure) on the bond behavior. The specimens are exposed to three different hygrothermal conditions in a climatic chamber, see Figure 3-21. Since the climatic chamber was only available discontinuously and with different periods, the exposures are performed with different durations.

Figure 3-21: Climatic chamber.

The details of exposure conditions are shown in Figure 3-22. In the first exposure, HT1, the specimens are exposed to 6 h temperature cycles from +10℃ to +50℃ and constant relative humidity of 90%. In each cycle, the temperature is kept constant at +10℃ for 2 h, subsequently increased to +50℃ in 1 h, followed by 2 h constant temperature at +50℃. Then, the temperature is decreased again to +10℃ in 1 h resulting in 6 h cycles of exposure. The +50℃ is relatively a high temperature chosen to accelerate the degradation phenomenon while being far enough from the epoxy resin T_g (70℃). Since environmental conditions can cause reduction of T_g in epoxy resins, the maximum temperature in the thermal cycles should avoid reaching the T_g of the epoxy resin during the tests [88]. The specimens are subjected to a total of 225 cycles of this exposure. The aim of this exposure is to simulate temperature cycles in high relative humidity environments.

Exposure HT2 consists of temperature cycles similar to the HT1 with constant relative humidity of 60%. The aim is to investigate the effect of relative humidity level on the bond degradation (compared to HT1). The specimens are subjected to a total of 820 cycles in this exposure. The aim is to investigate the bond degradation due to temperature cycles in regions with low relative humidity conditions.

In the third exposure, FT, the specimens are exposed to temperature cycles from –10℃ to +30℃ and constant relative humidity of 90%. The aim is to investigate the effect of freeze-thaw conditions on the bond behavior while having the minimum number of changes comparing to the other exposures. Therefore, a similar rate of exposure is used with 20℃ decrement of the maximum and minimum temperatures. The specimens are subjected to a total of 300 cycles during this exposure.

Exposure	T_{min} (°C)	T_{max} (°C)	R.H. (%)
HT1	10	50	90
HT2	10	50	60
FT	-10	30	60

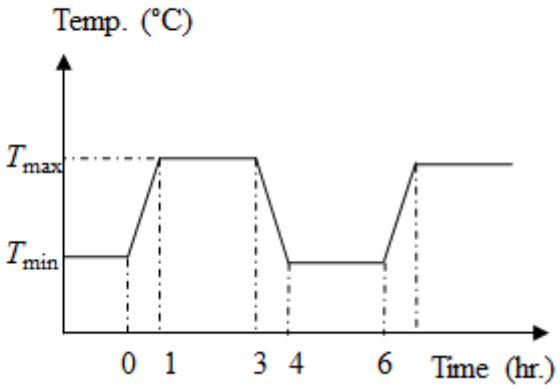

Figure 3-22: Hygrothermal exposure.

3.7 Post-ageing tests

Post-ageing tests are performed periodically during the environmental conditioning, both for mechanical characterization of materials and bond behavior.

In water immersion tests, Chapter 4, the post ageing tests are performed after each month of immersion. The specimens are dried in the laboratory conditions before performing the post-ageing tests, so that the results present solely the irreversible degradations. Mechanical tests are performed on epoxy resin, GFRP coupons and bricks. For the bond characterization, pull-off and pull-out (single-lap shear debonding) tests are performed.

In hygrothermal exposure tests, Chapter 5, the post ageing tests are performed periodically during the exposure. The specimens are taken from the climatic chamber after stabilizing at +50℃ in HT cycles and +30℃ in FT cycles. The specimens are then stabilized in laboratory conditions for four days before performing the post-ageing tests. The tests included mechanical characterization of material properties and single-lap shear debonding test. As no correlation was found between the pull-off and the pull-out tests in water immersion, the pull-off tests are not performed in specimens exposed to hygrothermal conditions.

Chapter 4

Water induced degradations

The experimental results obtained from the water immersion tests are presented and discussed in this chapter. The specimens were immersed in water in a controlled temperature water bath for a total period of 24 weeks. The results are presented next in terms of the changes in material mechanical properties and bond behavior with immersion time. Finally, some analytical models presented in sec. 2.4 have been adopted and used for durability predictions.

4.1 Material properties

4.1.1 Brick

The changes in compressive strength of brick with immersion time are shown in Figure 4-1. The results are presented as the average of five tests for each exposure period. The CoVs of the tests were less than 15% in all exposure periods which seems reasonable for testing material properties [261].

Significant reduction of compressive strength can be observed, up to 25% after 24 weeks of immersion. This reduction of the compressive strength can be due to the chemical reactions of water with brick components (dissolving effect of water) or due to insufficient firing temperature [105]. Insufficient firing temperature in clay bricks can lead to a low degree of vitrification and a high moisture expansion coefficient [106]. The degree of vitrification is defined as the amount of glass formed in the brick during firing. The water can react with the remaining clay inside the brick resulting in micro-cracking, expansion and, consequently, strength degradation.

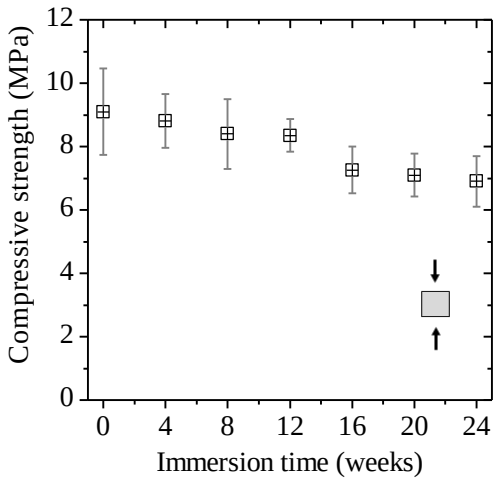

Figure 4-1: Effect of water immersion on bricks compressive strength.

4.1.2 Epoxy resin

The changes in the mechanical properties of epoxy resin, namely Young's modulus and tensile strength, are presented in Figure 4-2. The results are presented as the average of five tests for each exposure period. The CoVs of the tests were less than 10% for the tensile strength and less than 16% for the elastic modulus in all exposure periods which is reasonable for testing material properties [261].

A strong reduction of mechanical properties is observed upon immersion time. The Young's modulus and tensile strength are decreased 40% and 25% after 24 weeks of immersion, corresponding to 1.2% of water absorption. It seems that the elastic modulus has reached a constant value after 12 weeks of immersion. However, the tensile strength decreases continuously during the 24 weeks of exposure. The degradation of epoxy resins due to water absorption varies with the type of epoxy resin [98, 104, 160, 161]. Tuakta and Büyüköztürk [161] reported 7% reduction of elastic modulus and 22% reduction of tensile strength in epoxy resin for 1.2% mass water absorption. In another study, Sciolti et al. [104] reported 32% reduction of tensile strength and 45% reduction of elastic modulus after 24 weeks of water immersion corresponding to 4% mass water absoprtion. The observed reduction in mechanical properties is due to the plasticization and possibly hydrolysis of epoxy resin [129, 262, 263]. The absorbed water acts as a plasticizer, which usually reduces the T_g and mechanical properties. The decrease in the T_g reflects the degree of plasticization and occurrence of the water/resin interactions [249], but this reduction can be partially regained upon drying [96]. For long exposure periods, the possibility of resin degradation increases because hydrolytic reactions or chain scission may also occur, and these can strongly affect the resin performance [249].

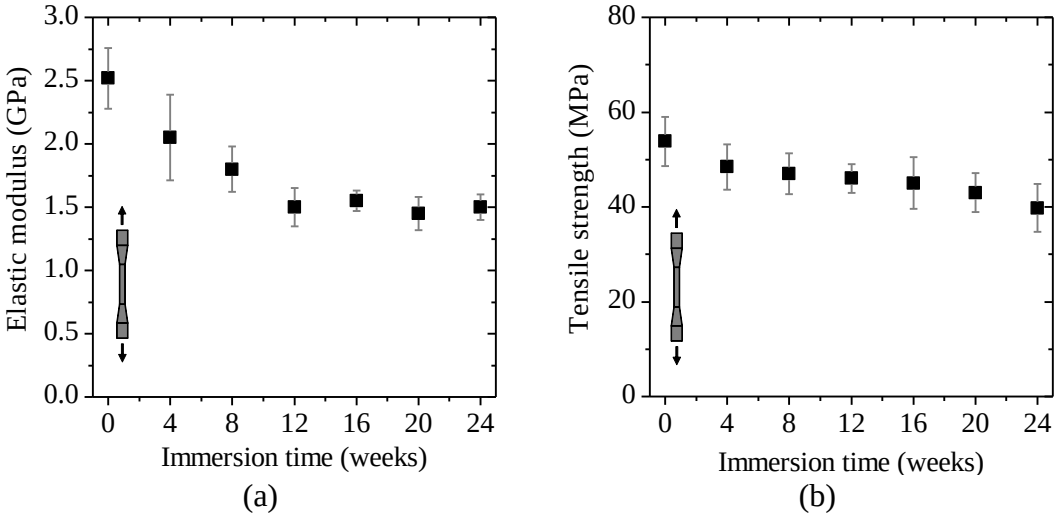

Figure 4-2: Effect of water immersion on epoxy resin: (a) elastic modulus; (b) tensile strength.

4.1.3 GFRP

The changes in mechanical properties of GFRP coupons due to water immersion are presented in Figure 4-3. The results are presented as the average of five tests for each exposure period. The CoVs of the tests were less than 16% in all exposure periods.

Again, Young's modulus and tensile strength decrease significantly. The Young's modulus reached a plateau after 16 weeks of immersion with 38% degradation. The tensile strength decreased about 40% after 24 weeks of exposure corresponding to 3.67% water uptake. Severe deterioration of mechanical properties of GFRP (50% reduction in tensile strength) has also been reported in [264]. Mechanical properties of fiber reinforced polymers are usually fiber dominated. Since fibers are protected with epoxy resin no degradation is expected due to water attack. However, the formation of voids and non-uniformities in the specimens prepared following the wet lay-up procedure increases the vulnerability of the composite material to moisture uptake [98]. The observed degradation in mechanical properties of GFRP coupons can be attributed to the degrading effect of water in the epoxy and epoxy/fiber interface. Moreover, the water can attack fibers which results in corrosion and fiber/epoxy bond degradation [129].

On the other hand, the resin layers between fibers may not be polymerized completely at earlier times. Polymerization and curing take place over an extended period of time and can be accelerated due to moisture uptake resulting in an initial increase of the composite material's performance [104]. This post-curing behavior can offset the degrading effect of water attack. Since the specimens were cured for two months before moisture conditioning, it is assumed that the polymerization has fully occurred. Therefore, the results present solely the strength degradation due to water immersion.

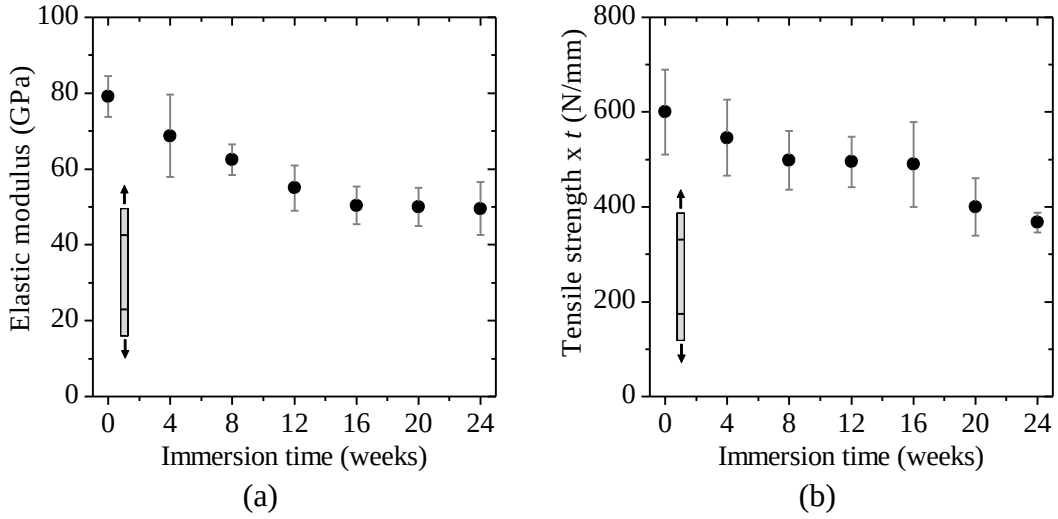

Figure 4-3: Effect of water immersion on GFRP: (a) elastic modulus; (b) tensile strength.

4.2 Bond behavior

4.2.1 Pull-off tests

The changes in the pull-off bond strength of the specimens are presented in Figure 4-4 for all the tested specimens. The mean values are obtained from the average of six tests. Some scatter is found which is common in this type of test [265]. A large and progressive reduction of bond strength can be observed in the specimens with time. The pull-off bond strength has been reduced 56% after 24 weeks of immersion. However, the failure mode remained cohesive in all immersion periods with reduction of the thickness of the detached brick layer. The thickness of the detached brick layer, being thick initially, was reduced until reaching the primer impregnated layer of the brick. The results obtained from the pull-off tests depend on the local condition of the specimens and they cannot be directly used to evaluate the bond behavior, as stated before.

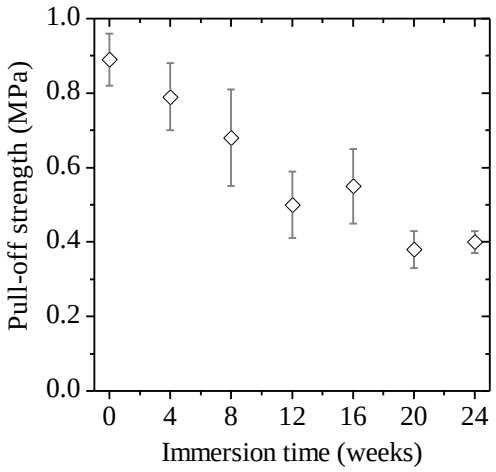

Figure 4-4: Effect of water immersion on the pull-off bond strength.

4.2.2 Debonding tests

Typical load-slip curves (envelope and average) obtained from experimental tests for different immersion times are shown in Figure 4-5. It can be observed that the bond stiffness and strength are degraded in time. Moreover, a relatively less brittle behavior can be observed in the immersed specimens, when compared to the reference specimens. The load-slip behavior of the specimens after 24 weeks of immersion exhibits 1.4 mm of slip at the deboning point. In comparison, debonding has been occurred at 0.6 mm slip in the reference specimens. An opposite behavior was reported in [166] for CFRP-strengthened calcernite stones, where a more brittle bond behavior was found in the specimens after water immersion.

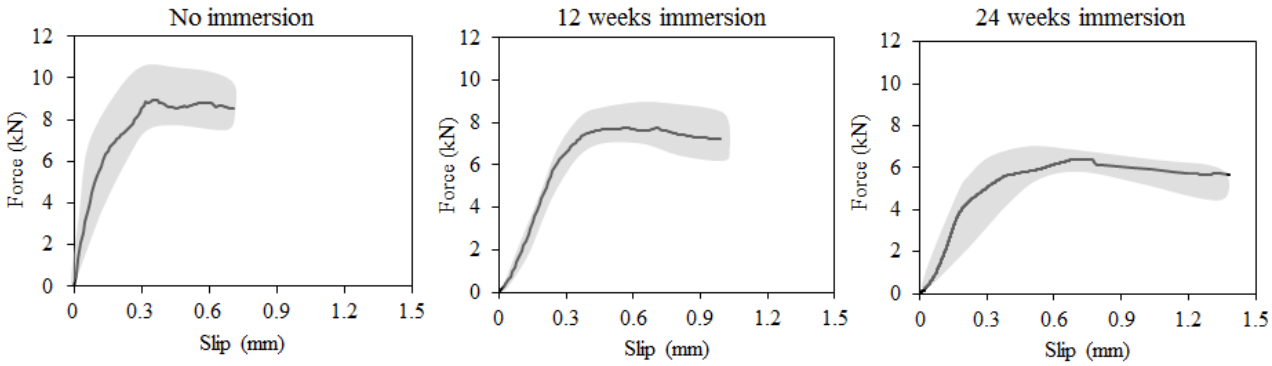

Figure 4-5: Envelope and average load-slip curves obtained from debonding tests.

A comparison between the slip values captured by the LVDTs at the loaded end and middle of the bonded length, see Figure 4-6, shows that the slip at the middle is negligible in the reference specimens. In the specimens with 12 weeks of immersion, the slip at the middle is negligible initially, but it increases after the peak bond strength until complete debonding. In the specimens with 24 weeks of immersion, the slip at the middle starts to increase before reaching the maximum bond strength and it continues until complete debonding. This phenomenon, being the result of stiffness reduction in the GFRP and epoxy resin, shows an increase of effective bond length in the specimens with time due to water immersion. The effective bond length is defined as the minimum length along which the strains and stresses are transferred to the substrate. Changes in effective bond length due to water immersion, even if not considered in current design procedures, can cause unsatisfactory failure modes in the strengthened specimens. However, more precise instrumentation such as strain gauges or digital image correlation techniques is necessary for accurate measurement of the changes in the effective bond length.

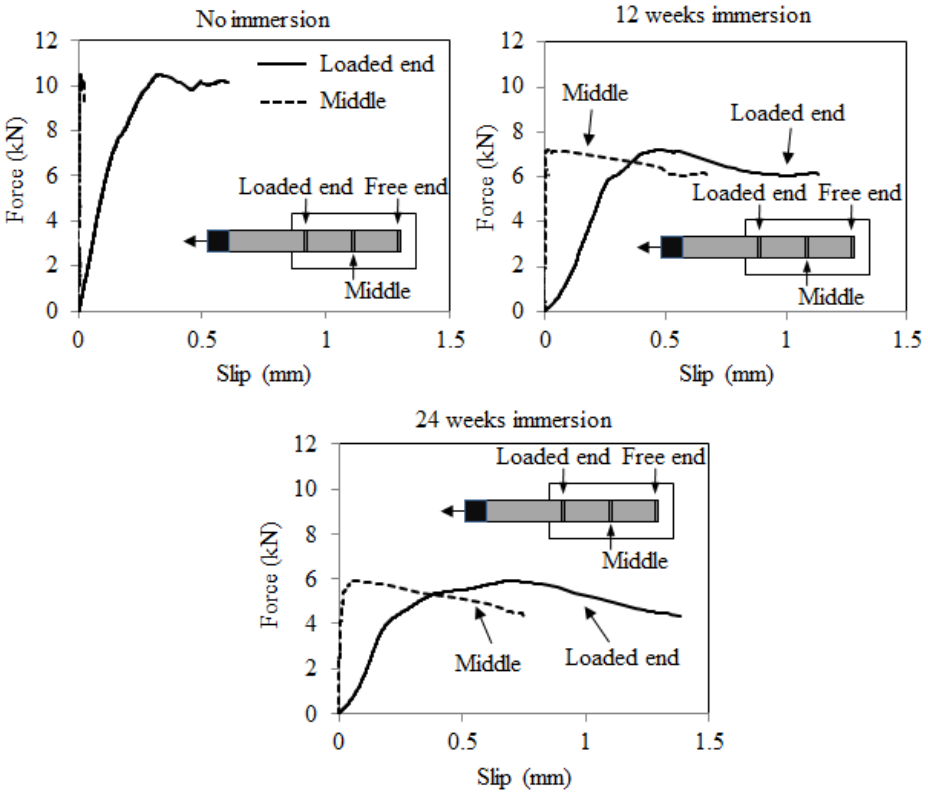

Figure 4-6: Typical load-slip behavior at the loaded end and middle bonded length, through time.

The changes in the debonding strength and stiffness with immersion time are presented in Figure 4-7. The results shown provide the average of five tested specimens for each immersion period. The bond strength decreased slightly in the first 12 weeks of immersion (about 16%). The rate of degradation increased after 12 weeks of immersion reaching 35% reduction of bond strength after 20 weeks of exposure. It seems that the degradation is less dependent on time after 20 weeks of immersion and the bond strength might have reached a residual value. However, performing water immersion tests for longer periods is necessary for obtaining a clear insight into the degradation pattern upon time. A similar residual bond strength has been reported in [166] after 8 weeks of immersion for CFRP strengthened calcernite stones. Water at the bond interface replaces the brick/adhesive contact resulting in a weaker boundary layer. The free surface energy at the water/epoxy interface and brick/epoxy interface is much lower than the one at the brick/epoxy. Therefore, the presence of water at the interface decreases the free surface energy of adhesion, resulting in lower fracture energy and bond strength degradation values [160].

The bond stiffness, defined as the initial slope of the bond-slip curves, has decreased significantly in the first eight weeks (about 60%). Afterwards, the rate of degradation in the bond stiffness decreased, reaching 80% reduction in the end of the experimental program. This reduction in the bond stiffness can be attributed to the stiffness reduction in epoxy resin, GFRP, and FRP/brick bond. In comparison, the stiffness was observed to remain unaffected with immersion

time in CFRP-strengthened calcernite stones [166] and concrete specimens strengthened with CFRP laminates [118, 186]. In general, it seems that degradation diminishes with time for bond strength and stiffness. This phenomenon, being an evidence of reaching a thermodynamic balance, has also been reported in [161, 186].

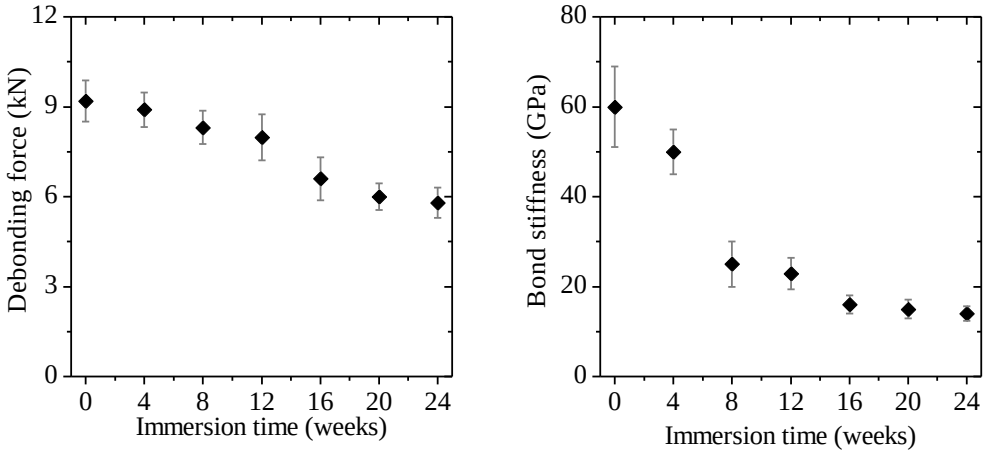

Figure 4-7: Debonding behavior under continuous water immersion: (a) strength; (b) stiffness.

A comparison between the observed degradation in debonding force and pull-off strength is presented in Figure 4-8. In this graph, the changes in the bond properties are presented as normalized to the initial values. The results shows that rate of degradation in the pull-off strength is more than, and different from, the degradation in debonding force. As explained before, this difference is due to the fact that pull-off tests provide information on the local adhesion normal to the surface of the specimens (fracture mode I). However, the results obtained from the debonding tests are representative of the global bond behavior parallel to the specimens' surface (fracture mode II).

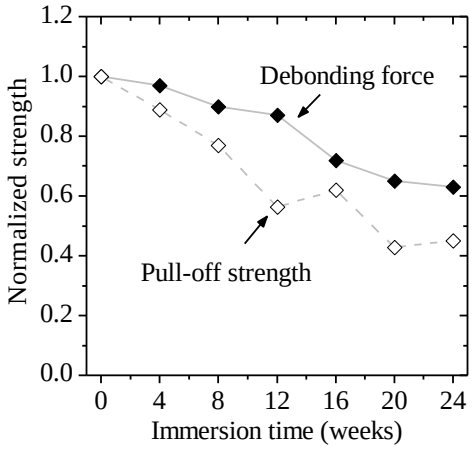

Figure 4-8: Comparison between pull-off and debonding test results.

A drawback of strength-based approaches in investigating the environmental effects on the bond behavior, as done in Figure 4-7, is that the results depend on the geometrical characteristics of the specimens. Considering the debonding as a local failure that involves crack propagation, fracture mechanics approaches seem to be more appropriate [161]. In fracture-based approaches, the degradation parameter is usually the bond fracture energy or the critical energy release rate. For generalizing the results presented, the changes in the fracture energy due to moisture ingress is determined according to CNR DT200 [1], as:

$$G_f = \frac{P_{\max}^2}{b_f^2 (2E_f t_f)} \tag{4.1}$$

where $P_{\max}$ is the debonding strength, b_f is the FRP width, E_f is the FRP elastic modulus, and t_f is the FRP thickness. The average bond fracture energy value reaches 0.45 N/mm for the reference specimens. Changes in the fracture energy of the specimens due to hygrothermal conditions are presented in Figure 4-9. It can be observed that in the first 12 weeks of exposure there is no degradation in the interfacial fracture energy. However, significant degradation occurs after 12 weeks and it continues until 20 weeks of immersion. It seems that after 20 weeks of immersion, the fracture energy has reached a residual value with 40% degradation comparing to its initial value. A similar degradation trend has also been reported by Ouyang and Wan [186], although they observed that the reduction in the mode I fracture energy in FRP-strengthened concrete specimens starts after two weeks of water immersion.

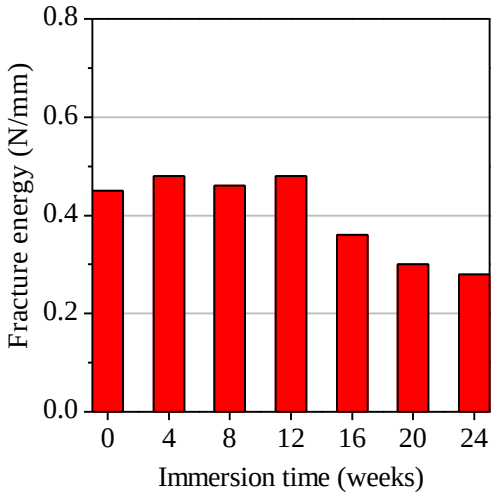

Figure 4-9: Changes in the average interfacial fracture energy with immersion time.

Assuming that the FRP width and thickness are constant during the water immersion tests, the debonding force is directly related to the square root of interfacial fracture energy and FRP elastic modulus, see Eq. (4.1). Therefore, the participation of each factor in degradation of debonding force can be obtained by plotting the changes in the normalized square root of fracture energy and FRP elastic modulus, see Figure 4-10. It can be concluded, from this graph, that in the first 12 weeks of exposure, the observed degradation in the debonding force is due to the degradation in the stiffness of GFRP composite. After 12 weeks of exposure, the stiffness of GFRP does not change significantly. On the contrary, the degradation of interfacial fracture energy occurs in this period which makes it the governing degradation mechanism after 12 weeks of exposure.

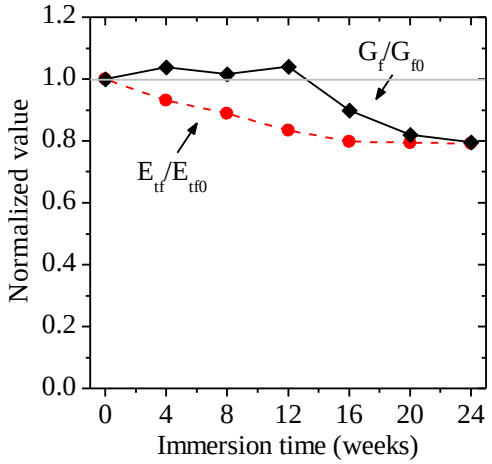

Figure 4-10: Degradation mechanisms in the bond behavior.

Regarding the failure mode, a cohesive failure mode was mainly observed in the specimens in all exposure periods, see Figure 4-11. However, the thickness of the detached layer decreased with time up to a thin layer equal to the primer impregnated thickness. As stated above, the fracture surface has moved to the brick/primer interface with the increase of water content at the interface, as reported in [160, 166, 186].

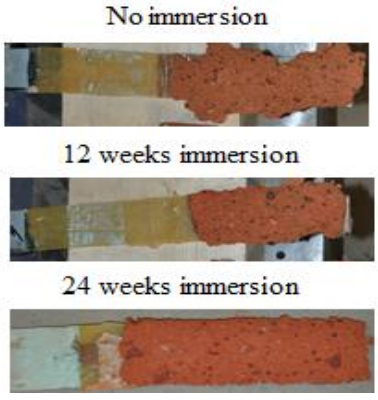

Figure 4-11: Failure mode of the specimens in shear bond tests.

4.3 Durability predictions

The observed degradation in the bond behavior and material properties has been modeled with the predictive decay models. Prediction of materials degradation and changes in the performance of structural components during the service life of the structures is of crucial importance for design and health assessment procedures. The detailed analysis procedures and predictions of each model are detailed in this section. Suitable life prediction models, addressed in sec. 2.4, are used for this purpose.

4.3.1 Arrhenius rate degradation model

Since the water immersion tests are performed only at 23°C, the Arrhenius reaction model is independent of the temperature. The kinetic rate equation, Eq.(2.19), can therefore be rewritten as:

$$P = C \ln t + P_0 \tag{4.2}$$

where, C is:

$$C = B.\exp(\frac{E}{RT}) \tag{4.3}$$

In general, the parameter C includes the activation energy and temperature effects. However, as explained, this parameter is constant in this study and can be derived by performing a linear regression analysis. For applying this model to the results obtained from the water immersion tests, the strength degradation in epoxy resin, GFRP coupons and bond is plotted against the logarithm of time (in days) in Figure 4-12 and Figure 4-13. The straight lines in these figures represent the fitted curves obtained from linear regression analysis, also tabulated in Table 4-1. Since the natural logarithm of time at zero days is mathematically undefined, “0 day” for the unconditioned specimens has been replaced by “1 day” in the calculations.

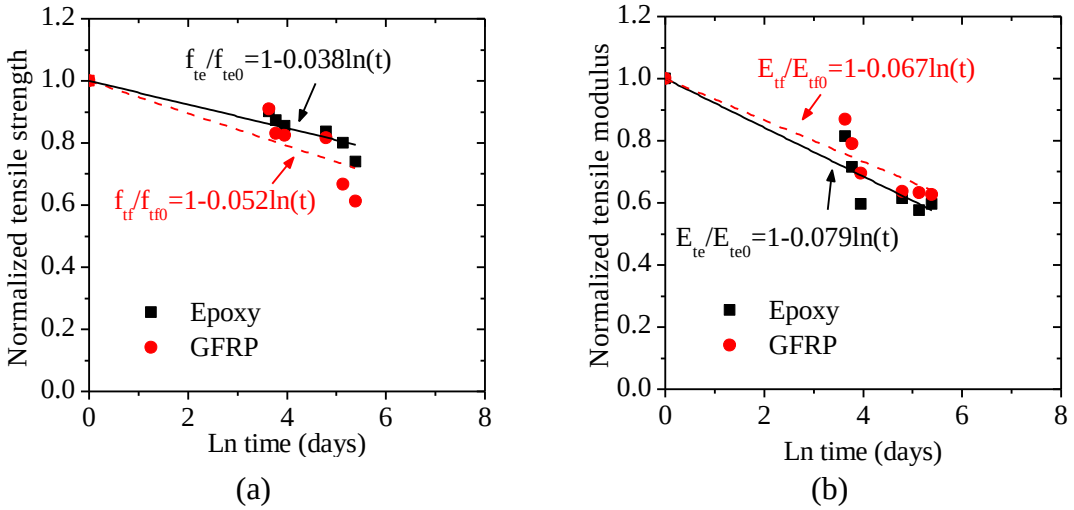

Figure 4-12: Arrhenius model for epoxy and GFRP: (a) tensile strength; (b) elastic modulus.

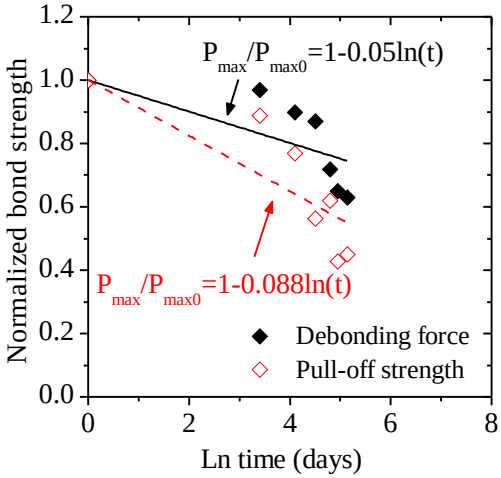

Figure 4-13: Arrhenius model for debonding force.

Table 4-1: Arrhenius type prediction models.

Specimen/property	Fitted model	R^2
Epoxy resin/tensile strength	$P/P_0=1-0.038\times\ln(t)$	0.87
Epoxy resin/elastic modulus	$P/P_0=1-0.079\times\ln(t)$	0.87
GFRP/tensile strength	$P/P_0=1-0.052\times\ln(t)$	0.70
GFRP/ elastic modulus	$P/P_0=1-0.067\times\ln(t)$	0.85
GFRP-brick/debonding force	$P/P_0=1-0.05\times\ln(t)$	0.60
GFRP-brick/pull-off strength	$P/P_0=1-0.088\times\ln(t)$	0.71

The percent error in the predictions for each material is presented in Table 4-2 to Table 4-4. For the epoxy resin, the accuracy of the model for predicting the tensile strength is relatively good, with errors up to 7.5% and an average error of 5.4% (in absolute value), see Table 4-2. The model presents larger error for predicting the elastic modulus (up to 15.6%, average of 2.5%) with the maximum error being at 4 and 12 weeks of exposure. These errors can be due to the post-curing of the epoxy resin. In reality, the mechanical performance of epoxy resin may increase in the first periods of exposure due to the post-curing effects and therefore the mechanical degradation is balanced. Isolation of this effect from the experimental results is a complex task and has not been done in this study. Arrhenius model can only model degradations and do not consider the post-curing behavior of the material. This leads to large errors in the first periods of exposure, but the error decreases with exposure time when the post-curing effects diminish. For the GFRP, the error range is up to 17.5% (average of 7.6%) and 12.9% (average of 5.2%) for the tensile strength and the elastic modulus, respectively. The error in prediction of the debonding force is up to 15.9%

(average of 9.9%) and for the pull-off strength is up to 27.9% (average of 14.8%), indicating the poor fitness of the model for the latter case.

It should also be noted that the comparisons are made between the predictions and average experimental results. The model predictions are plotted against experimental results with the corresponding standard deviations in sec 4.3.5 below. The scatter of experimental results minimizes the actual error in many cases. However, it will be shown that even with considering the experimental scatter, the prediction for pull-off strength and debonding force are relatively poor.

Table 4-2: Arrhenius model error for predicting the mechanical properties of epoxy resin.

Immersion time (days)	f_{te}/f_{te0}	Err. (%)	E_{te}/E_{te0}	Err. (%)
1	1.00	0.0	1.00	0.0
30	0.86	-4.3	0.71	-12.4
60	0.86	-2.0	0.70	-1.9
90	0.85	-0.6	0.69	15.6
120	0.82	-2.2	0.62	1.1
140	0.80	0.7	0.59	3.3
170	0.80	7.5	0.57	-3.6
Average Err.		5.4		2.5

Table 4-3: Arrhenius model error for predicting the mechanical properties of GFRP.

Immersion time (days)	f_{tf}/f_{tf0}	Err. (%)	E_{tf}/E_{tf0}	Err. (%)
1	1.00	0.0	1.00	0.0
30	0.81	-10.9	0.76	-12.9
60	0.80	-3.2	0.75	-5.5
90	0.79	-3.7	0.74	5.8
120	0.75	-8.0	0.68	6.7
140	0.73	9.9	0.66	3.8
170	0.72	17.5	0.64	2.0
Average Err.		7.6		5.2

Table 4-4: Arrhenius model error for predicting the bond behavior.

Immersion time (days)	Debonding force		Pull-off strength	
	P_{max}/P_{max0}	Err. (%)	P_{max}/P_{max0}	Err. (%)
1	1.00	0.0	1.00	0.0
30	0.82	-15.7	0.68	-23.6
60	0.81	-9.9	0.67	-13.3
90	0.80	-7.8	0.65	15.7
120	0.76	5.6	0.58	-6.7
140	0.74	14.3	0.55	27.9
170	0.73	15.9	0.53	16.5
Average Err.		9.9		14.8

4.3.2 Time-Temperature-Moisture superposition model

Again, since the water immersion tests have been performed in only 23°C, temperature dependent variables in these models become constant. For the Phani and Bose [209] model, explained in sec. 2.4.3, the changes in the mechanical properties of the materials are plotted against time (in days) in Figure 4-14 and Figure 4-15. Eq. (2.24) is then fitted to the experimental data by performing a regression analysis. The obtained prediction models are also tabulated in Table 4-5. The high values of R^2 for the prediction curves show the suitability of the exponential degradation models for this problem.

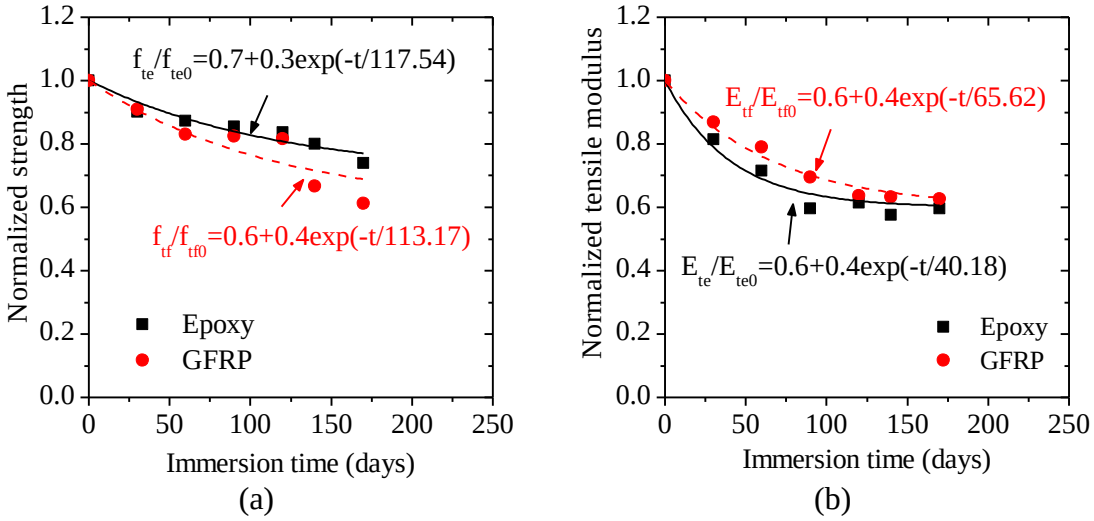

Figure 4-14: Exponential model for predicting the degradation in epoxy resin and GFRP: (a) tensile strength; (b) elastic modulus.

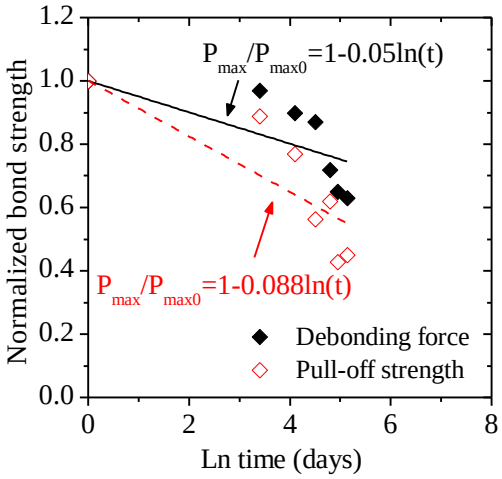

Figure 4-15: Exponential model for model for predicting the degradation in debonding force.

Table 4-5: Exponential fitted prediction models.

Specimen/property	Exponential relationship	R^2
Epoxy resin/tensile strength	P/P_0=0.7+0.3exp(-t/117.54)	0.92
Epoxy resin/elastic modulus	P/P0=0.6+0.4exp(-t/40.18)	0.97
GFRP/tensile strength	P/P0=0.6+0.4exp(-t/113.17)	0.85
GFRP/elastic modulus	P/P0=0.6+0.4exp(-t/65.62)	0.98
GFRP-brick/debonding force	P/P0=0.45+0.6exp(-t/163.72)	0.90
GFRP-brick/pull-off	P/P0=0.45+0.6exp(-t/70.57)	0.90

The percent error in the predictions for each material is presented in Table 4-6 to Table 4-8. For the epoxy resin, the accuracy of the model for predicting the tensile strength is relatively good, with errors up to 4.3% (average of 2.1%), see Table 4-6. The model presents larger errors for predicting the elastic modulus (up to 8.1%, average of 3.3%) with the maximum errors being at 8 and 12 weeks of exposure. For the GFRP, the error range is up to 12.7% (average of 5.1%) and up to 4.5% (average of 2.2%) for the tensile strength and elastic modulus, respectively. The error in prediction of the debonding force is up to 8.7% (average of 5.1%) and for the pull-off strength is up to 24.6% (average of 10.5%), again indicating the poor fitness of the model for pull-off strength prediction.

In general, the exponential decay model has a reasonable accuracy in predicting the degradation of bond and material properties. However, it should be noted that the predictions are made for short periods of exposure and using them long-term predictions may be misleading unless extensive long-term experimental tests are performed.

Table 4-6: Model error for predicting the mechanical properties of epoxy resin.

Immersion time (days)	f_{te}/f_{te0}	Err. (%)	E_{te}/E_{te0}	Err. (%)
0	1.00	0.0	1.00	0.0
30	0.93	3.7	0.79	-2.4
60	0.88	0.9	0.69	-3.1
90	0.84	-1.7	0.64	8.1
120	0.81	-3.3	0.62	0.9
140	0.79	-0.9	0.61	6.5
170	0.77	4.3	0.61	1.8
Average Err.		2.1		3.3

Table 4-7: Model error for predicting the mechanical properties of GFRP.

Immersion time (days)	f_{tf}/f_{tf0}	Err. (%)	E_{tf}/E_{tf0}	Err. (%)
0	1.00	0.0	1.00	0.0
30	0.91	-0.1	0.86	-1.3
60	0.84	0.9	0.76	-3.4
90	0.78	-5.2	0.70	1.2
120	0.74	-9.4	0.67	4.5
140	0.72	7.6	0.65	2.6
170	0.69	12.7	0.63	0.7
Average Err.		5.1		2.0

Table 4-8: Model error for predicting the bond behavior.

Immersion time (days)	Debonding force		Pull-off strength	
	P_{max}/P_{max0}	Err. (%)	P_{max}/P_{max0}	Err. (%)
0	1.05	5.0	1.05	5.0
30	0.95	-1.8	0.85	-4.7
60	0.87	-3.5	0.71	-7.7
90	0.80	-8.2	0.62	10.0
120	0.74	2.8	0.56	-9.5
140	0.71	8.7	0.53	24.6
170	0.66	5.4	0.50	11.9
Average Err.		5.1		10.5

For using the model proposed by Chamis [210], Eq.(2.25), it is necessary to have the changes in the T_g of the polymer with water uptake. Since the T_g of the epoxy resin is only characterized at the dry state in this study, its changes are modeled with the aim of predictive models presented in sec. 2.4.3, see Eqs. (2.27, 2.29, 2.31).

The input parameters and calculation details for obtaining the wet T_g during the water immersion tests are presented in Table 4-9 to Table 4-12. It can be observed that, besides the Fox equation, the two other models give similar results for the wet T_g. Therefore the average of the T_g values obtained from the models proposed by Chamis [210] and Kelley and Bueche [213] are used hereafter.

Table 4-9: Input parameters for calculating the wet T_g.

Kelley and Bueche model			*Fox equation*			*Chamis model*	
$V°$	1	cm^3/gr	T_{gp}	-203.15	K^{-1}	A	0.005
ρ	1	gr/cm^3	T_{gd}	-273.15	K^{-1}	B	-0.1
A_p	1.25E-04	K^{-1}				C	1
A_d	1.50E-03	K^{-1}					
T_{gp}	-203.15	K^{-1}					
T_{gd}	-273.15	K^{-1}					

Table 4-10: Calculation details for obtaining the wet T_g with Chamis model (Eq. 2.27).

Immersion time (days)	W (%)	T_g (C^{-1})
0	0.00	70.00
30	0.52	66.45
60	0.60	65.93
90	0.80	64.62
120	0.95	63.67
140	1.00	63.35
170	1.10	62.72

Table 4-11: Calculation details for obtaining the wet T_g with Kelley and Bueche model (Eq. 2.29).

Immersion time (days)	W (%)	$\Delta V_t/V_0$	V_p	T_g	
				(K^{-1})	(C^{-1})
0	0.00	0.0000	1.0000	-203.15	70.00
30	0.52	0.0052	0.9948	-207.25	65.90
60	0.60	0.0060	0.9940	-207.84	65.31
90	0.80	0.0080	0.9921	-209.27	63.88
120	0.95	0.0095	0.9906	-210.30	62.85
140	1.00	0.0100	0.9901	-210.63	62.52
170	1.10	0.0110	0.9891	-211.30	61.85

Table 4-12: Calculation details for obtaining the wet T_g with Fox equation (Eq. 2.31).

Immersion time (days)	W (%)	w_1	w_2	T_g	
				(K^{-1})	(C^{-1})
0	0.00	0.0000	1.0000	-203.15	70.00
30	0.52	0.0052	0.9948	-203.42	69.73
60	0.60	0.0060	0.9940	-203.46	69.69
90	0.80	0.0079	0.9921	-203.56	69.59
120	0.95	0.0094	0.9906	-203.64	69.51
140	1.00	0.0099	0.9901	-203.67	69.48
170	1.10	0.0109	0.9891	-203.72	69.43

Having the wet T_g, the Chamis [210] model, Eq. (2.25) can be used for predicting the degradation of material properties due to water immersion. The model has only been used for predicting the degradation in epoxy resin. The changes in mechanical properties of the epoxy resin together with the prediction model are shown in Figure 4-16. The model has been used with two different n values of 0.5 (proposed by Chamis [210]), 0.9. It can be observed that the model with n=0.5 does not have a good accuracy, while when n=0.9 is selected reasonable results are obtained for the epoxy tensile strength. However, it seems higher values of n is required for predicting the degradation in elastic modulus.

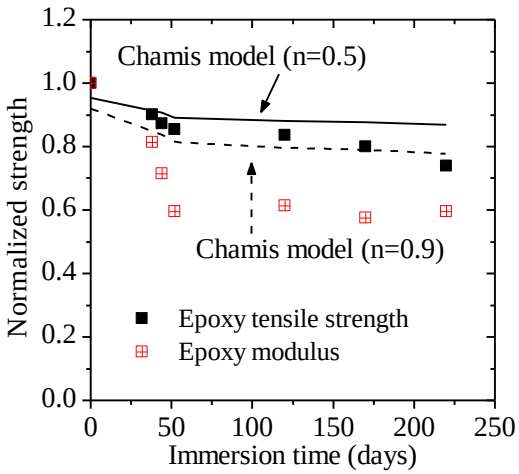

Figure 4-16: Chamis [210] model for predicting the degradation epoxy resin.

The poor fitness of the model can be due to the fact that the wet T_g is obtained with simplified predictive models. Moreover, this model assumes the same degradation trends for both the tensile strength and the elastic modulus which is in opposition to the experimental observations in this study.

4.3.3 Moisture level dependent model

The degradation model proposed by Nakamura et al. [220], Eq.(2.39), is used only for predicting the degradation in mechanical properties of epoxy resin and GFRP materials. For the bond behavior, since the specimens' weight is governed by the brick water absorption, the model cannot accurately predict the observed degradation. The brick is a porous material and it absorbs a large amount of water during the first days of water immersion which leads to the saturation condition quickly (usually in one day). Thereafter, the changes in the specimen's weight are rather small and therefore this degradation model predicts very small degradation in the bond behavior in contrary to the experimental observations. For modeling the bond degradation, using time-dependent models, exponential decay models, or models based on the interfacial relative humidity, e.g. Ouyang and Wan [185], are more suitable. In the latter case, laboratorial or on-site measurement of the interfacial relative humidity is a complicated task. In addition, numerical modeling of the interfacial relative humidity requires simplified assumptions for the boundary conditions and transfer phenomenon.

The change of the materials mechanical properties is plotted against moisture level (M_t/M_u) in Figure 4-17. Eq. (2.39) is then fitted to the experimental data and the obtained prediction models are also tabulated in Table 4-13.

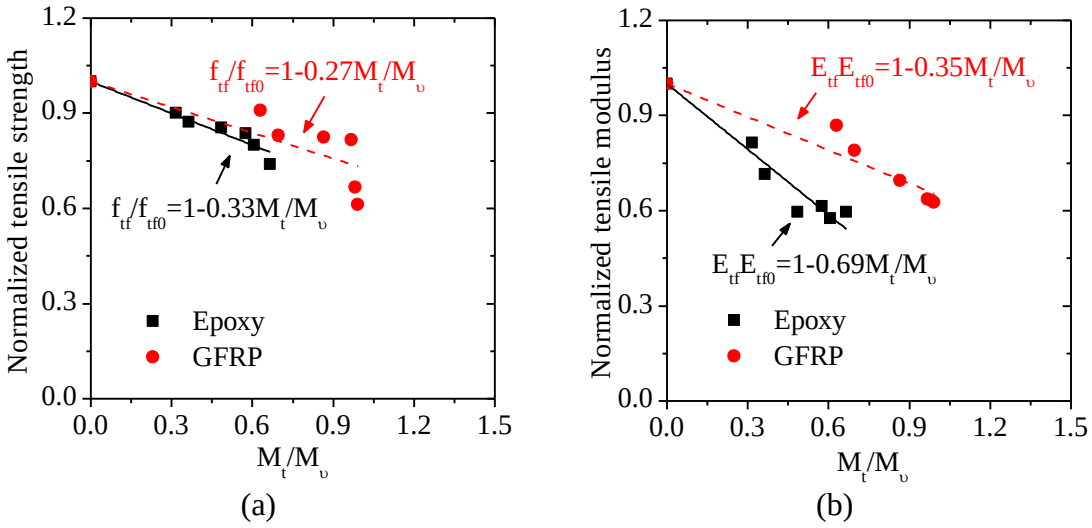

Figure 4-17: Moisture dependent model for predicting the degradation in epoxy resin and GFRP: (a) tensile strength; (b) elastic modulus.

Table 4-13: Moisture dependent prediction models.

Specimen/property	Fitted model	R^2
Epoxy resin/tensile strength	$P/P_0=1.0-0.33M_t/M_\infty$	0.93
Epoxy resin/elastic modulus	$P/P_0=1.0-0.69M_t/M_\infty$	0.93
GFRP/tensile strength	$P/P_0=1.0-0.27M_t/M_\infty$	0.67
GFRP/elastic modulus	$P/P_0=1.0-0.35M_t/M_\infty$	0.90

With the exception of the predictions for the GFRP tensile strength (R^2=0.67), the predictions have generally excellent accuracy (R^2>0.90). The percentage error of predictions for each material is presented in Table 4-14 and Table 4-15. For epoxy resin, the error for the tensile strength is up to 5.5% with average of 1.7%, while for the elastic modulus is up to 11.8% (average of 4.7%), see Table 4-14. For the GFRP coupons, the error range is up to 19.6% (average of 8.2%) and up to 10.2% (average of 3.8%) for the tensile strength and the elastic modulus, respectively.

Table 4-14: Model error for predicting the mechanical properties of epoxy resin.

Immersion time (days)	f_{te}/f_{te0}	Err. (%)	E_{te}/E_{te0}	Err. (%)
0	1.00	0.0	1.00	0.0
30	0.90	-0.5	0.78	-3.8
60	0.88	0.8	0.75	4.9
90	0.84	-1.7	0.67	11.8
120	0.81	-3.2	0.60	-2.0
140	0.80	0.1	0.58	1.1
170	0.78	5.5	0.54	-9.3
Average Err.		1.7		4.7

Table 4-15: Model error for predicting the mechanical properties of GFRP.

Immersion time (days)	f_{tf}/f_{tf0}	Err. (%)	E_{tf}/E_{tf0}	Err. (%)
0	1.00	0.0	1.00	0.0
30	0.83	-8.8	0.78	-10.2
60	0.81	-2.2	0.76	-4.3
90	0.77	-7.1	0.70	0.4
120	0.74	-9.5	0.66	3.8
140	0.74	10.3	0.66	4.0
170	0.73	19.6	0.65	4.3
Average Err.		8.2		3.8

4.3.4 Proposed model

The available models can simulate the mechanical degradation of epoxy resin and GFRP composite with reasonable accuracy. Among the investigated models, the exponential decay (Table 4-5) and moisture dependent (Table 4-13) models have the highest accuracy for predicting the mechanical properties of epoxy resin and GFRP and are proposed for prediction purposes.

Models for predicting the degradation of the bond behavior are scarce. Based on the experimental observations, a degradation model is proposed in this section for predicting the bond performance in FRP-strengthened masonry.

The degradation of the bond behavior observed in the experimental tests is very similar to the typical degradation curve of the bonded systems attacked by interfacial degradation and

plasticization [119], see Figure 2-4. Therefore, the model is proposed based on the three degradation stages explained by Bowditch [119], see sec. 2.2.1.

The model assumes no degradation in the bond behavior until reaching a critical water limit, after which the degradation starts. The degradation then continues until the solubility limit. After this limit the degradation rate is very slow and the system reaches a residual strength. The proposed model can be explained as follows, see Figure 4-18:

debonding force:

$$\begin{cases} P/P_{max} = 1 & for \quad t < t_l \\ P/P_{max} = 0.61 + 0.59\exp(-t/72) & for \quad t < t_l \end{cases} \tag{4.4}$$

pull-off strength:

$$\begin{cases} P/P_{max} = 1 & for \quad t < t_l \\ P/P_{max} = 0.43 + 0.92\exp(-t/64) & for \quad t < t_l \end{cases} \tag{4.5}$$

where t is the time in days, t_l is the time lag for starting the degradation. The time lag for starting the degradation is a combination of: (a) the time required for the interfacial water content to reach a critical value and (b) the time required for the chemical reactions and degradation to occur. Quantification of these factors requires an extensive experimental and numerical investigation and is out of the scope of this study. According to the experimental results in the present study this limit is reached after 4 weeks of water immersion.

Having the model for degradation of debonding force (Eq. 4.4) and the GFRP elastic modulus (Table 4-5), the degradation of bond fracture energy, required for numerical purposes, can be obtained according to Eq. (4.1).

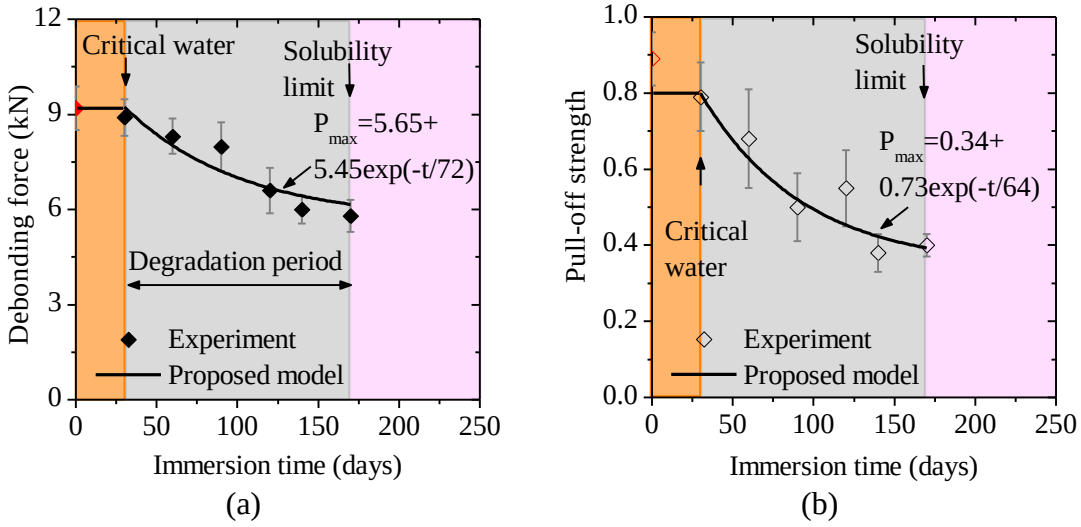

Figure 4-18: Proposed model for degradation in: (a) debonding force; (b) pull-off strength.

4.3.5 Comparison between the adopted models

A comparison is made here between different degradation models and the experimental results, see Figure 4-19 to Figure 4-21. For the epoxy resin and GFRP, it can be observed that when the scatter of the experimental results is considered, all the models have reasonable accuracy. For the bond behavior, both the exponential model and the proposed models (Eqs. 4.4, 4.5) have a reasonable accuracy, although the proposed model follows the average experimental results perfectly. The Arrhenius model shows less accuracy in predicting the bond degradation.

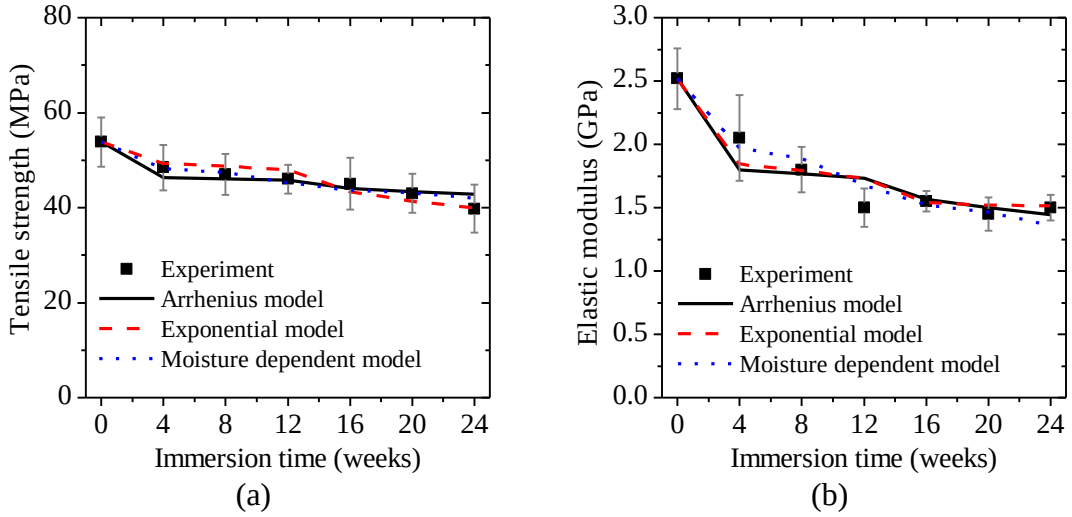

Figure 4-19: Comparison between experimental results and prediction models for epoxy resin: (a) tensile strength; (b) elastic modulus.

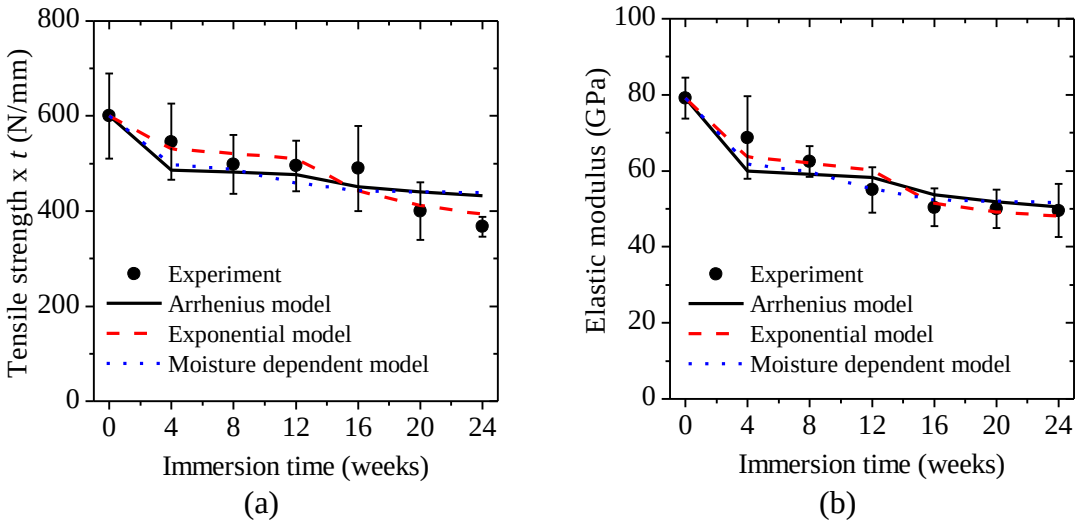

Figure 4-20: Comparison between experimental results and prediction models for GFRP: (a) tensile strength; (b) elastic modulus.

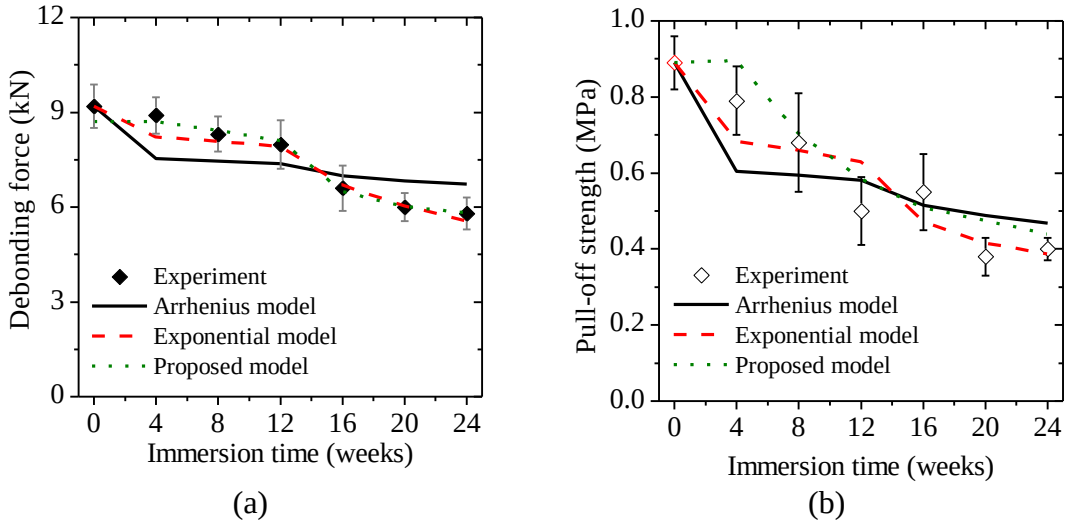

Figure 4-21: Comparison between experimental results and prediction models for bond behavior: (a) debonding force; (b) pull-off strength.

The long-term performance of bond and material mechanical properties are simulated with the models, see Table 4-16 and Table 4-17. The predictions are made for 50, 125 and 200 years as the usual seismic strengthening objectives for historical masonry. It seems that the exponential model has reached a residual value giving the same degradation level for all exposure periods. The Arrhenius model gives much higher degradation levels for epoxy and GFRP elastic modulus and also the bond pull-off strength comparing to the exponential model. For the bond strength, 49% and 54% reductions after 50 and 125 years is obtained with the Arrhenius model and the exponential model leads to 49% reduction for both exposure periods.

Table 4-16: Long-term predictions of Arrhenius model.

Material	Properties	Duration (years)		
		50	125	200
Epoxy	f_{te}/f_{te0}	0.63	0.59	0.57
	E_{te}/E_{te0}	0.22	0.15	0.12
GFRP	f_{tfe}/f_{tfe0}	0.49	0.44	0.42
	E_{tfe}/E_{tfe0}	0.34	0.28	0.25
Bond	$P_e/P_{0\ (shear)}$	0.51	0.46	0.44
	$P_e/P_{0\ (pull\text{-}off)}$	0.14	0.06	0.01

Table 4-17: Long-term predictions of exponential model.

Material	Properties	Duration (years)		
		50	125	200
Epoxy	f_{te}/f_{te0}	0.7	0.7	0.7
	E_{te}/E_{te0}	0.6	0.6	0.6
GFRP	f_{tfe}/f_{tfe0}	0.6	0.6	0.6
	E_{tfe}/E_{tfe0}	0.6	0.6	0.6
Bond	$P_e/P_{0\ (shear)}$	0.45	0.45	0.45
	$P_e/P_{0\ (pull\text{-}off)}$	0.45	0.45	0.45
Bond (proposed)	$P_e/P_{0\ (shear)}$	0.61	0.61	0.61
	$P_e/P_{0\ (pull\text{-}off)}$	0.43	0.43	0.43

4.4 Conclusions

The results of an experimental investigation on water induced degradation in the bond between GFRP composites and masonry bricks were presented, demonstrating that:

- Water immersion leads to a reduction of mechanical properties of material constituents. Compressive strength of masonry bricks reduced 25% after 24 weeks of water immersion. A similar reduction was also observed in the tensile strength of epoxy resin. However, the reduction in tensile strength of GFRP fabric was 40% at the end of ageing, which is due to the reduction in the mechanical properties of epoxy resin and the degradation of epoxy/fiber interfaces. The elastic modulus of epoxy resin and GFRP fabric also decreased with time, about 40% after 24 weeks of water immersion.
- The pull-off strength of the specimens decreased significantly (about 60%) after 24 weeks of immersion. However, the results obtained from pull-off tests are not completely consistent with the shear bond tests, where a different degradation trend was observed. The failure mode remained cohesive during the tests but the fracture surface moved from the brick to the brick/primer interface.
- Shear bond tests showed that the ductility of the bond behavior increases with immersion time in the tested specimens. The bond strength and stiffness were observed to decrease, while the debonding slip increased. It was observed that the degradation in the bond strength and stiffness diminishes with time and possibly a residual value is obtained after a certain immersion time. However, performing water immersion tests for longer periods is necessary for having a clear idea about the degradation trend upon time. A similar degradation was

also observed in interfacial fracture energy. The failure mode was cohesive in all the specimens, with the fracture surface inside the brick. However, the fracture surface moved towards the brick/primer interface with time.

- Available predictive models were used for modeling the observed degradation in the material properties and bond behavior. It was observed that the moisture dependent and exponential degradation models predict the degradation in mechanical properties of epoxy resin and GFRP with a reasonable accuracy, and therefore are proposed to be used for numerical purposes. For the bond behavior a degradation model is proposed based on the typical degradation trend of bonded systems. It was observed that the proposed model perfectly follows the experimental trend (for the short-term tests performed here). Based on the proposed predictive models, the long-term performance of the bond behavior and material properties were simulated leading to 49% reduction of bond strength after 50 years. However, special care should be taken for extending the short-term degradation models for long-term predictions, as a fully validated predictive model requires performing extensive long-term experimental tests.

Chapter 5

Hygrothermal induced degradations

The experimental results obtained from the post-ageing tests on the specimens exposed to hygrothermal conditions are presented and discussed in this chapter. The results are presented in terms of the degradation of material mechanical properties and bond between GFRP and bricks. Finally, some of the analytical models presented in sec. 2.4 have been adopted and used for durability predictions.

5.1 Material properties

5.1.1 Brick

The changes in the compressive strength of bricks due to the hygrothermal exposures are shown in Figure 5-1 and Figure 5-2. The change in the bricks compressive strength is negligible in all exposure conditions with a low CoV (maximum 10%). The results show the good resistance of the bricks to the environmental exposures considered in this study.

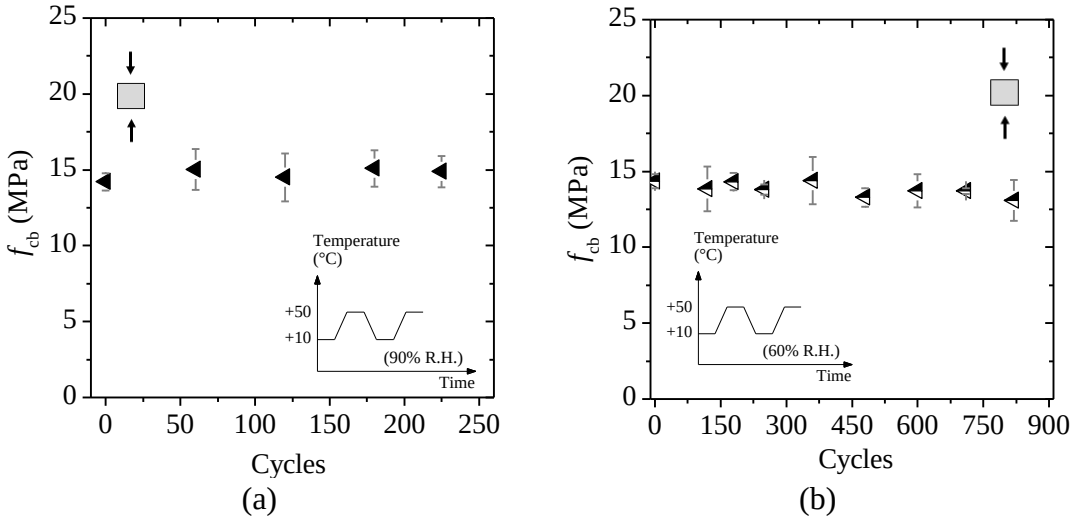

Figure 5-1: Degradation of bricks compressive strength due to exposures: (a) HT1; (b) HT2.

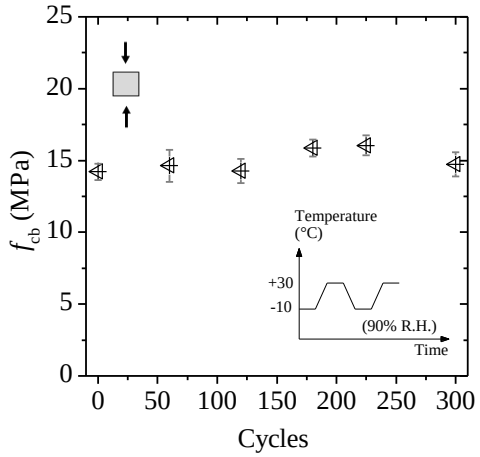

Figure 5-2: Degradation of bricks compressive strength due to FT exposure.

5.1.2 Epoxy resin

The changes in mechanical properties of epoxy resin, namely elastic modulus and tensile strength, are presented in Figure 5-3 to Figure 5-5. A similar degradation is observed in elastic modulus and tensile strength, see Figure 5-7. For the elastic modulus, the degradation after 225 cycles is 7%, 7% and 3% for exposures HT1, HT2 and FT, respectively. Meanwhile for the tensile strength HT1 induced 20% reduction after 225 cycles of exposure being two times more than the corresponding degradation due to HT2 and FT (10% reduction in both exposures). The total observed degradation in epoxy tensile strength is 14% and 8% in HT2 and FT exposures, respectively. The results show that the epoxy resin used in this study has less durability in high humid environments (exposure HT1), although longer cycles of exposure are needed for a clear conclusion for exposures HT1 and FT. The CoVs of the tests in all exposures were in the range of 2% to 13% which seem reasonable for testing material properties [261].

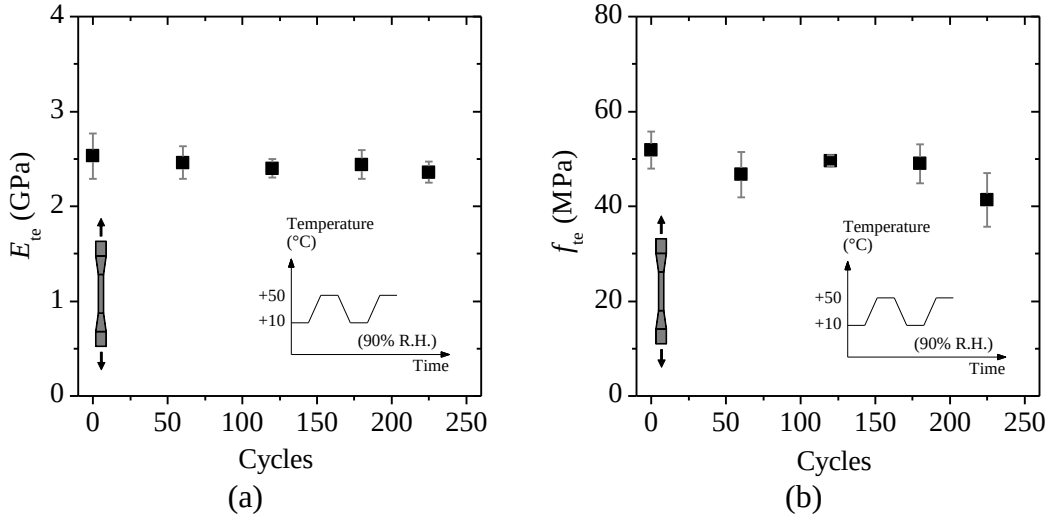

Figure 5-3: Effect of exposure HT1 on epoxy resin: (a) elastic modulus; (b) tensile strength.

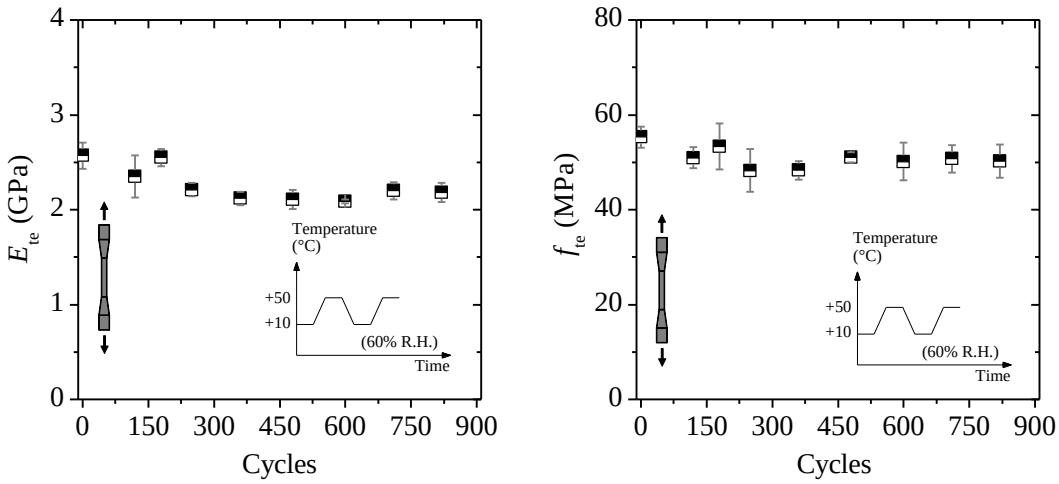

Figure 5-4: Effect of exposure HT2 on epoxy resin: (a) elastic modulus; (b) tensile strength.

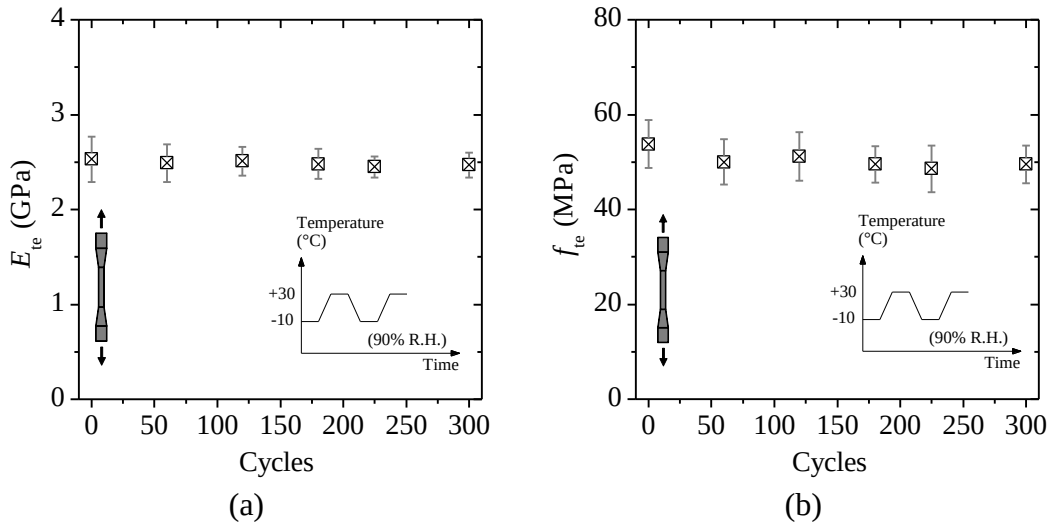

Figure 5-5: Effect of exposure FT on epoxy resin: (a) elastic modulus; (b) tensile strength.

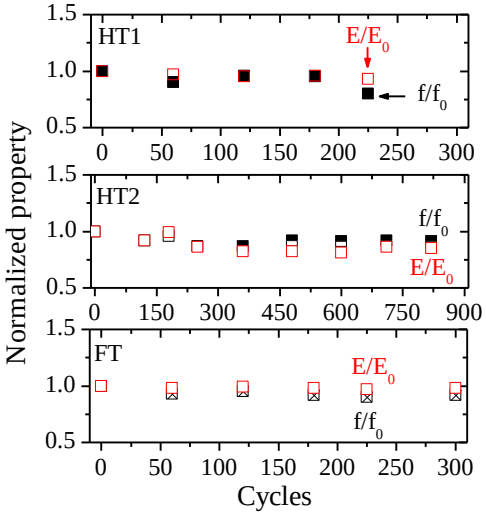

Figure 5-6: Comparison between degradation of elastic modulus and tensile strength.

To provide a clearer baseline for comparison, the observed degradation in all exposure conditions is plotted in the same graph in terms of normalized property against square number of cycles (N^2), see Figure 5-7. The mechanical properties are normalized to the unconditioned mechanical property and, due to the cyclic nature of the considered exposures, the exposure cycles are presented in a logarithmic scale. The observed reduction in mechanical properties can be due to different degradation mechanisms.

Exposure HT2 consists of thermal cycles in a low relative humidity environment (60% R.H.). The active degrading mechanisms in this exposure include thermal fatigue, thermal ageing and epoxy post-curing. Exposure to high temperatures below the epoxy T_g results in an increment of moisture diffusion coefficient and epoxy post-curing [129]. While the former leads to higher moisture uptake and consequently higher mechanical degradation, the latter can cause an improvement in the mechanical properties. On the other hand, thermal cycles can induce thermal fatigue in the specimens. The results show that the balanced effect of these mechanisms has resulted in a small degradation in the mechanical properties of the epoxy resin used in this study. The relatively constant weight of the specimens during the exposure shows that water absorption was negligible and therefore moisture attack was not the main degrading mechanism in this exposure.

In exposure HT1, thermal cycles are combined with high relative humidity conditions (90% R.H.) representing a wet environment. Therefore, in this exposure moisture degradation mechanisms are added to the active degrading mechanisms in exposure HT2. Moisture exposure causes plasticization and hydrolysis of epoxy resin [129, 262, 263]. The water absorbed by the epoxy resin acts as a plasticizer, and the result of plasticization is usually a reduction of T_g and mechanical properties of epoxy resin [249]. In long exposure periods, the possibility of resin degradation increases while hydrolytic reactions or chain scission may also occur, which can strongly affect the resin performance [249]. The observed increase in the degradation rate after 120 cycles of HT1 exposure can be due to this fact. The moisture additional induced degradation in the mechanical properties of epoxy resin can be clearly observed in Figure 5-7. Moisture attack has resulted in earlier initiation and higher levels of degradation. Although, as also stated before, extending the exposure HT1 and FT to longer periods is necessary for a clear conclusion.

Exposure FT induces thermal cycles with high relative humidity conditions in low temperatures. The difference of this exposure with exposure HT1 is that the specimens are additionally exposed to freeze conditions which, depending on the porosity of the material, may cause additional degradation in the specimens. On the other hand, since the moisture uptake during

the freezing period is negligible, the specimens absorb less water comparing to the exposure HT1. This results in less moisture induced degradations in the specimens. The balanced effect of all active mechanisms resulted in less reduction of mechanical properties comparing to exposure HT1, see Figure 5-7.

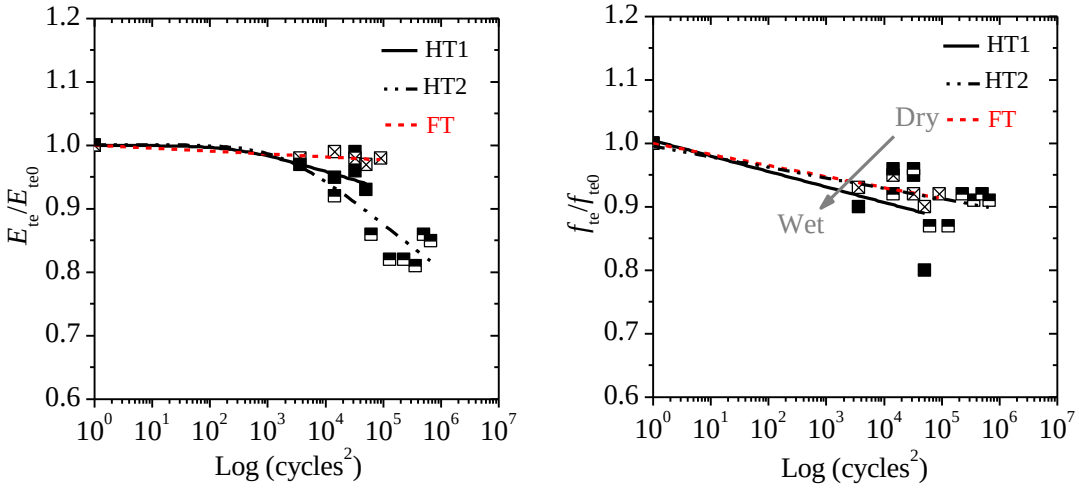

Figure 5-7: Epoxy degradation due to different exposures: (a) elastic modulus; (b) tensile strength.

5.1.3 GFRP

The changes in mechanical properties of GFRP coupons together with the scatter of the experimental results are presented in Figure 5-8 to Figure 5-10. Again, a relatively similar degradation trend is observed in elastic modulus and tensile strength, with exposure HT1 inducing the most degradation in the specimens, as expected. The elastic modulus and tensile strength of GFRP decreased 23% and 22%, respectively, after 225 cycles of HT1 exposure corresponding to 9% and 13% reductions in HT2, and 14% and 7% in FT exposure. The total observed reduction for the elastic modulus and the tensile strength was 22% and 13% in HT2 exposure showing that the degradation in HT2 exposure has reached a residual value. However, reaching a residual value in HT1 and FT exposure cannot be easily concluded at this stage. The CoVs of the experimental results in both exposures were in the range of 5% to 12% which are again typical for testing material properties [261].

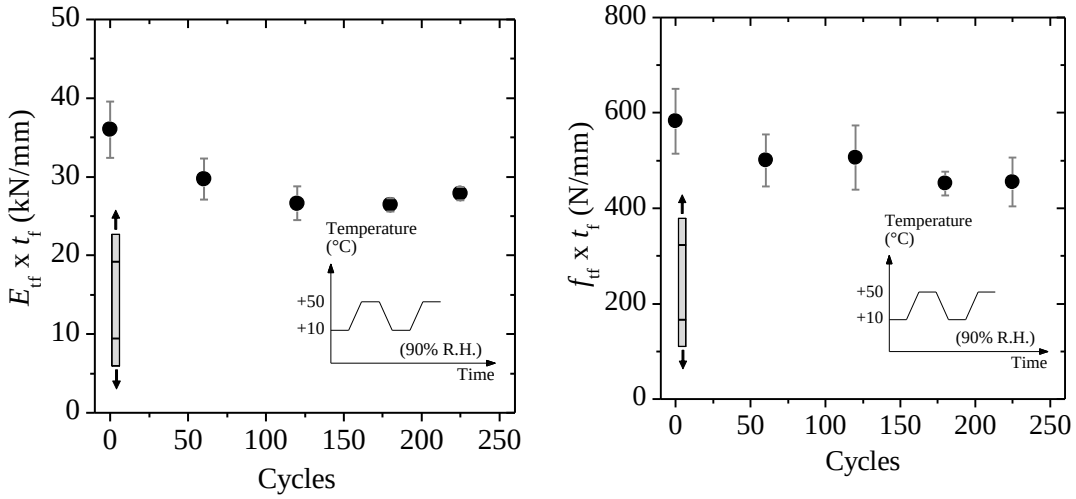

Figure 5-8: Effect of HT1 exposure on GFRP coupons: (a) elastic modulus; (b) tensile strength.

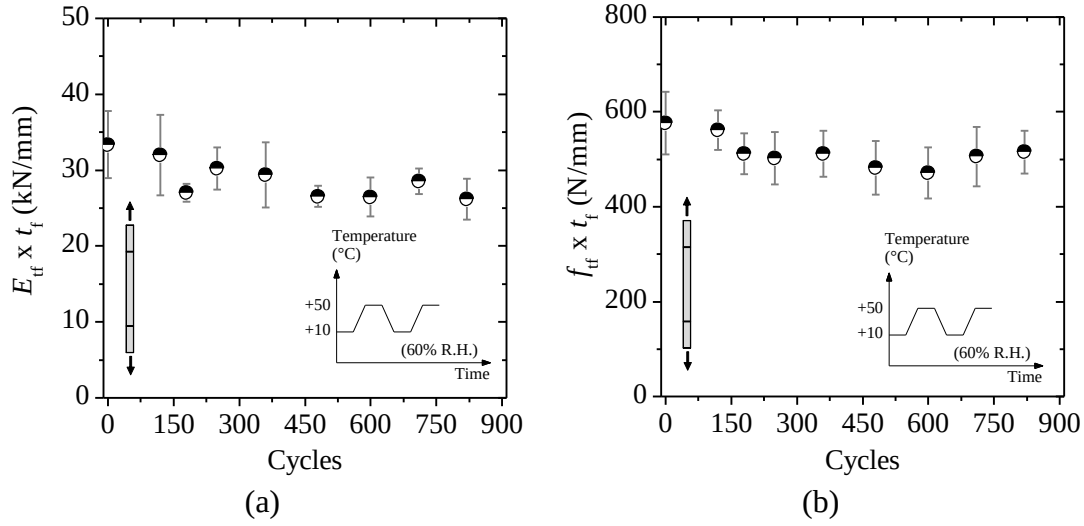

Figure 5-9: Effect of HT2 exposure on GFRP coupons: (a) elastic modulus; (b) tensile strength.

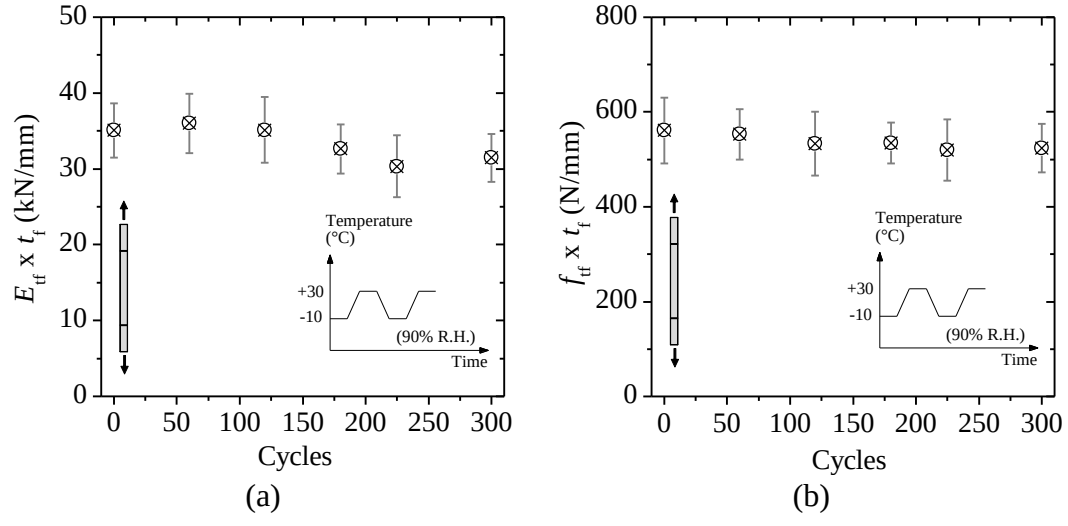

Figure 5-10: Effect of FT exposure on GFRP coupons: (a) elastic modulus; (b) tensile strength.

The observed degradation can be attributed to different degrading mechanisms. Exposure to temperature cycles, besides the above mentioned effects on the matrix, may cause interfacial micro-cracking due to the difference between thermal expansion coefficients of glass fibers and epoxy resin [266, 267]. The thermal expansion coefficient of E-glass fibers is around 5×10^{-6}/℃, while for the epoxy resin is in the range of $3\sim5\times10^{-5}$/℃ [1]. This one-order magnitude difference of thermal expansion coefficient produces large interfacial thermal strains at the fiber/epoxy interfaces. In conclusion, the observed degradation in the specimens in HT2 conditions can be a combination of epoxy post-curing, induced thermal fatigue, and the thermal mismatch between epoxy resin and glass fibers. In wet environments (HT1 and FT exposure), GFRP coupons absorb moisture which causes degradation in the epoxy resin properties, as described before. Moreover, the water attacks glass fibers resulting in degradation of their mechanical properties and surface energy. The fiber/epoxy interface may also degrade due to the degradation of fiber and epoxy resin and also the produced osmotic pressure at the interface [88]. This has resulted in more degradation in the specimens exposed to HT1 conditions comparing to the specimens exposed to HT2 conditions, see Figure 5-11. Meanwhile, the degradation observed in specimens exposed to FT conditions is less than HT1 exposure conditions. This difference can be due to the lower moisture uptake of the specimens in FT exposure, as explained before. Moreover, it has been reported that the thermal expansion coefficient of epoxy resins is much lower at low and negative temperatures [268]. This reduction of epoxy thermal expansion coefficient makes it closer to the glass fibers thermal expansion coefficient resulting in less severe thermal mismatch problem at negative temperatures.

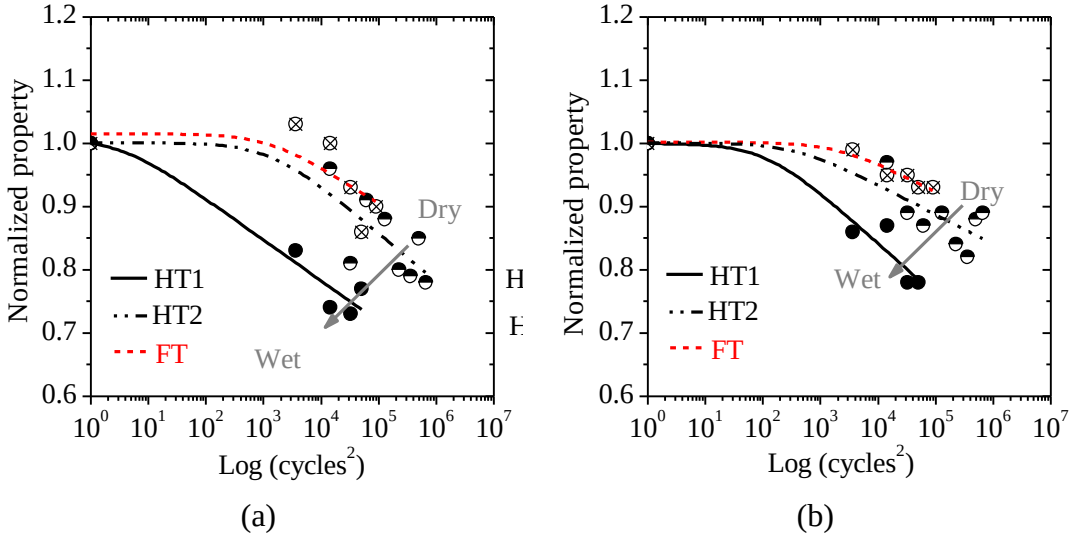

Figure 5-11: Effect of exposures on GFRP properties: (a) elastic modulus; (b) tensile strength.

5.2 Bond behavior

The changes in the bond behavior due to environmental conditions have been investigated qualitatively (using visual inspection and IR thermography) and quantitatively (using shear debonding tests). The observations and detailed discussion of the results are presented next.

5.2.1 Visual inspection

All specimens have been visually inspected periodically, before performing the debonding tests, for investigating the existence of visible interfacial damage or FRP delamination. Although due to the transparency of the epoxy resin, FRP delamination was observable with visual inspection, IR thermography tests have also been performed on some specimens for a better characterization, see Chapter 6. In general, progressive FRP delamination was observed in the specimens as the exposure cycles increased. The delaminations, being at the FRP/brick interface, were generally larger in specimens subjected to HT1 cycles. Figure 5-12 and Figure 5-13 present the average reduction of bonded area, due to FRP delamination, normalized by the initial bonded area with exposure time. The values are presented as the average of the five inspected specimens. One representative specimen in each exposure period is also shown in these graphs.

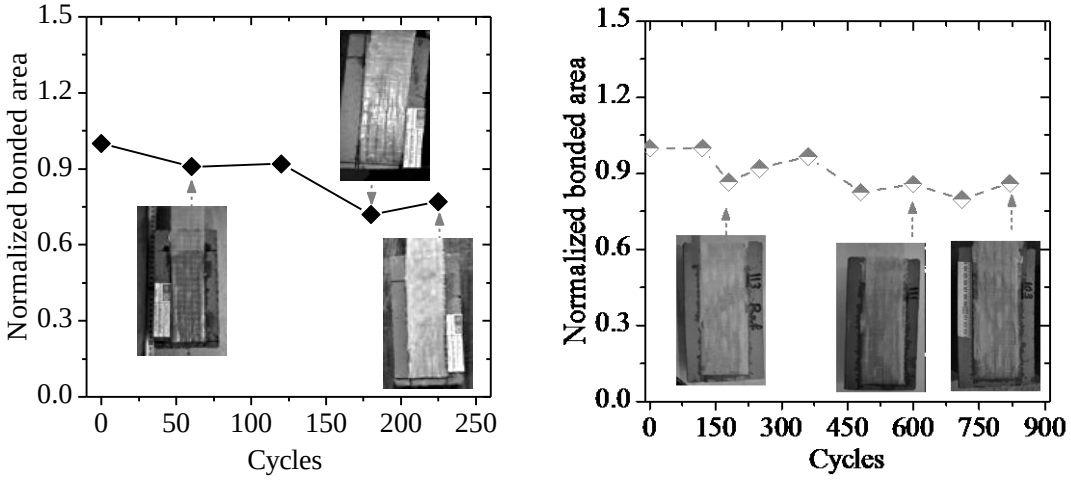

Figure 5-12: Reduction of the bonded area due to exposures: (a) HT1; (b) HT2.

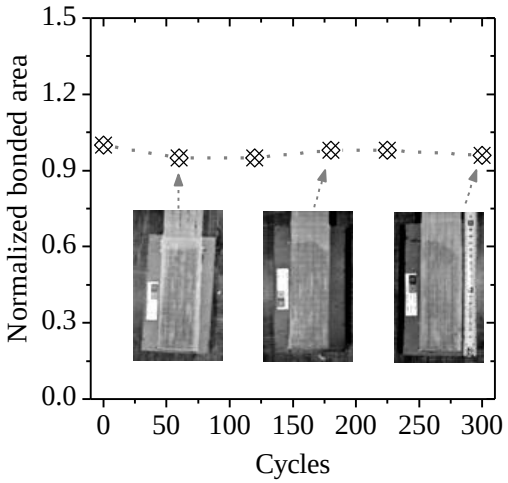

Figure 5-13: Reduction of the bonded area due to FT exposure.

To provide a better baseline for comparison between different exposures, average equivalent debonding length growth with exposure cycles is plotted in the same graph for all exposure conditions, see Figure 5-14. The equivalent debonding length is obtained as the debonded area divided by FRP width. This parameter, while providing a clear idea of the debonding progress, is useful for numerical simulations when two-dimensional models are adopted (as is the case for most situations).

The observed delamination in the specimens can be attributed to the thermal incompatibility between the composite material and the brick used in this study. The thermal expansion coefficient of clay bricks is in order of 5×10^{-6}/℃ [125]. The thermal expansion coefficient of E-glass fibers is similar to the one from the bricks, while for epoxy resin it is in the range of $30\sim54\times10^{-6}$/℃ [1]. This large difference of thermal expansion coefficient, between epoxy resin and glass fibers/bricks, produces interfacial thermal strains at the fiber/epoxy and brick/epoxy interfaces. Cyclic temperature conditions amplify this effect by producing thermal fatigue and may cause FRP delamination from the brick surface during the environmental exposures. On the other hand, it has been observed that the thermal expansion coefficient of epoxy resins is much lower at low and negative temperatures [268]. Therefore, the interfacial strains produced due to thermal incompatibility are lower for the freeze-thaw conditions. This explains the smaller delaminated areas observed in the specimens exposed to the FT conditions in this study. A comparison between exposures HT1 and HT2 shows that the moisture presence has resulted in larger debonded areas in specimens exposed to HT1 exposure, confirming the accelerating effect of moisture on the debonding crack growth rate. The moisture presence has resulted in larger debonded areas in specimens exposed to HT1 exposure.

The observed debonding growth shows the critical effect of water attack on the debonding growth rate. The delamination in the specimens exposed to FT conditions is small with a linear incremental trend. The specimens exposed to HT2 conditions also show a linear debonding growth with a relatively slow rate (similar to FT conditions). However, the debonding growth in the specimens exposed to HT1 conditions is rather large with an exponential incremental rate.

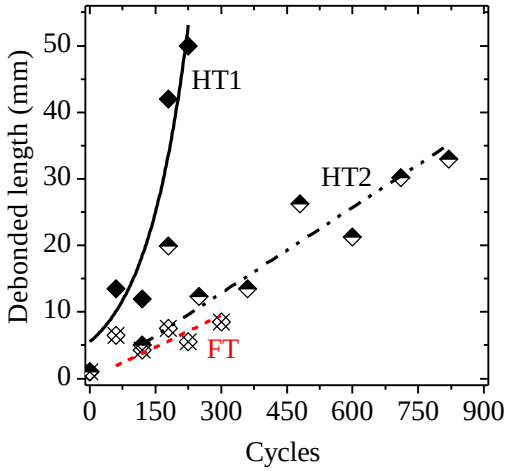

Figure 5-14: Debonded length growth for the specimens with exposure cycles.

5.2.2 Single-lap shear bond tests

The effect of different exposures on the debonding force is presented in Figure 5-15. The debonding force has been progressively decreased with the number of exposure cycles. The debonding force decreased 45%, 20% and 5% after 225 cycles of HT1, HT2 and FT exposures, respectively. The average reduction of debonding force is 13% at the end of both HT2 and FT exposures. Again, it seems that the degradation has reached a residual value in exposure HT2. The lower observed degradation at the end of exposure HT2, 13%, comparing to 20% reduction after 225 cycles can be attributed to the scatter of experimental results. Moreover, the debonding behavior changed from a brittle failure mode to a progressive and less brittle failure mode in exposures HT1 and FT. Similar changes in the bond behavior have also been reported in the literature for the specimens exposed to freeze-thaw and wet-dry cycles, see e.g. [269].

A comparison between the obtained results shows that HT1 exposure induces higher degradation on the specimens used in this study, see Figure 5-16. The observed degradation in the specimens exposed to HT1 can be attributed to the thermal fatigue and mismatch between epoxy/fiber and epoxy/brick. The higher degradation observed in specimens exposed to HT1 is due to the moisture attack to the interfacial bond between FRP composite and brick and also to the constituent materials. The least degradation has occurred in specimens exposed to FT conditions.

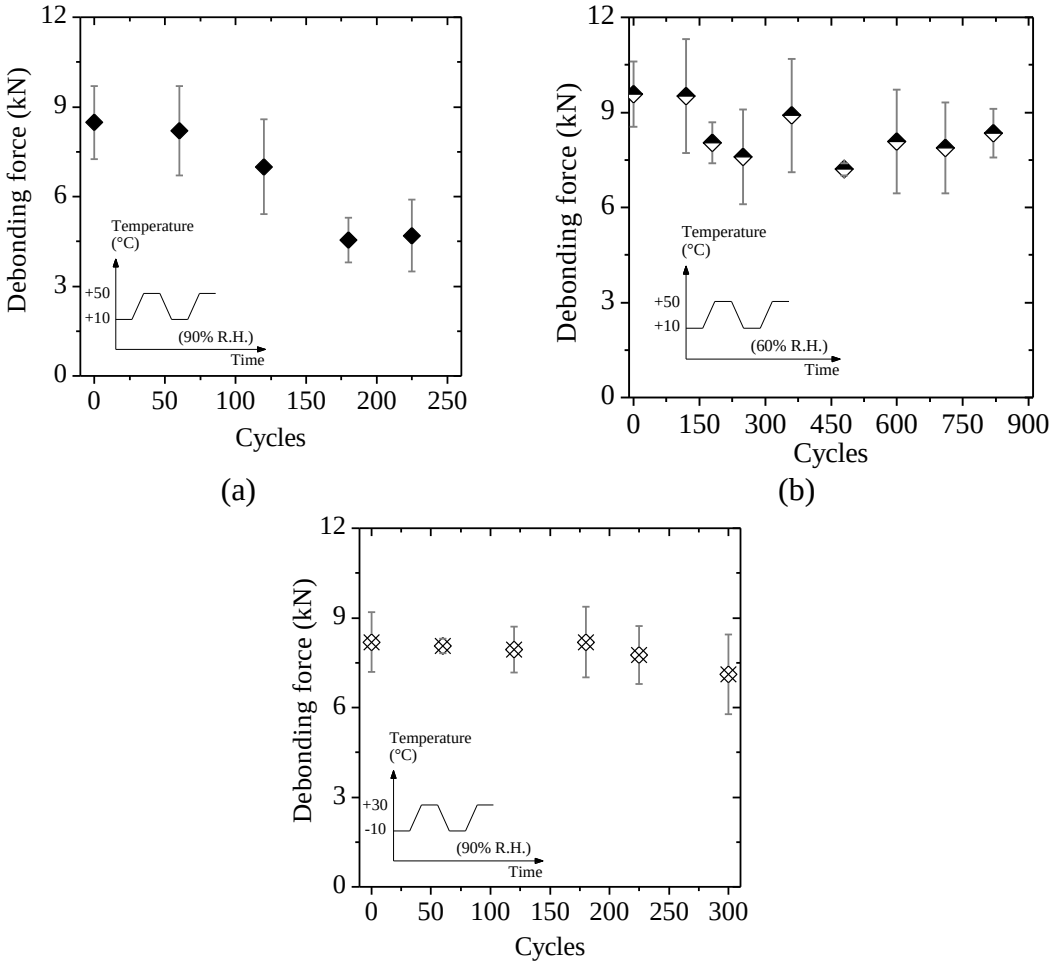

Figure 5-15: Debonding force degradation due to exposure: (a) HT1; (b) HT2; (c) FT.

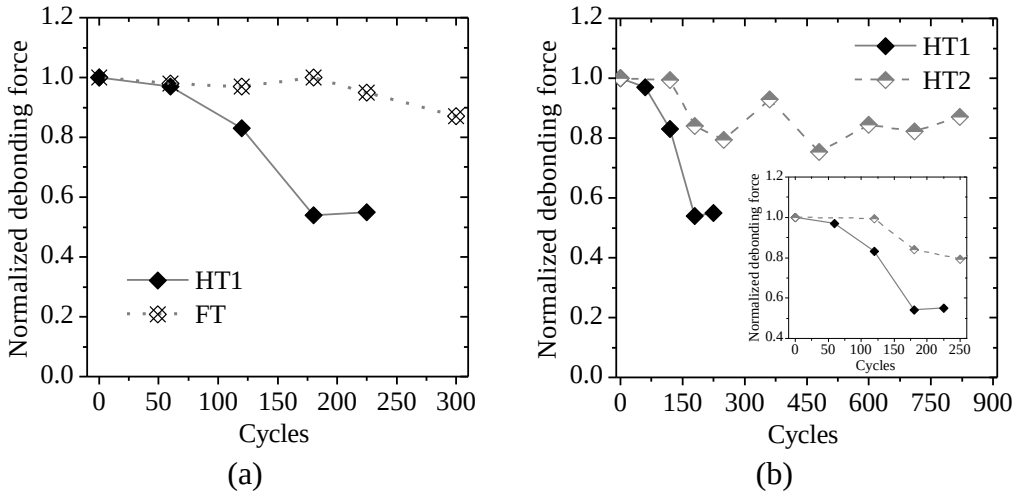

Figure 5-16: Debonding force comparison between: (a) HT1 and FT; (b) HT1 and HT2.

The changes in the debonding fracture energy, obtained according to Eq. (4.1), are plotted in Figure 5-17. The average bond fracture energy value reaches 0.45 N/mm for the reference specimens. The fracture energy has moderate changes due to FT conditions (with a 20% reduction at the end of exposure), while a large degradation is observed in the specimens exposed to HT1 conditions (60% total reduction at the end of exposure), see Figure 5-17(a). It seems that the interfacial fracture energy has reached a residual value in exposure HT2, see Figure 5-17(b). A comparison between HT1 and HT2 exposure, shows that the moisture affects the interfacial fracture energy to a large extent. The interfacial fracture energy in exposure HT1 may have reached a residual value as well, although performing longer exposure periods is necessary for a clear conclusion.

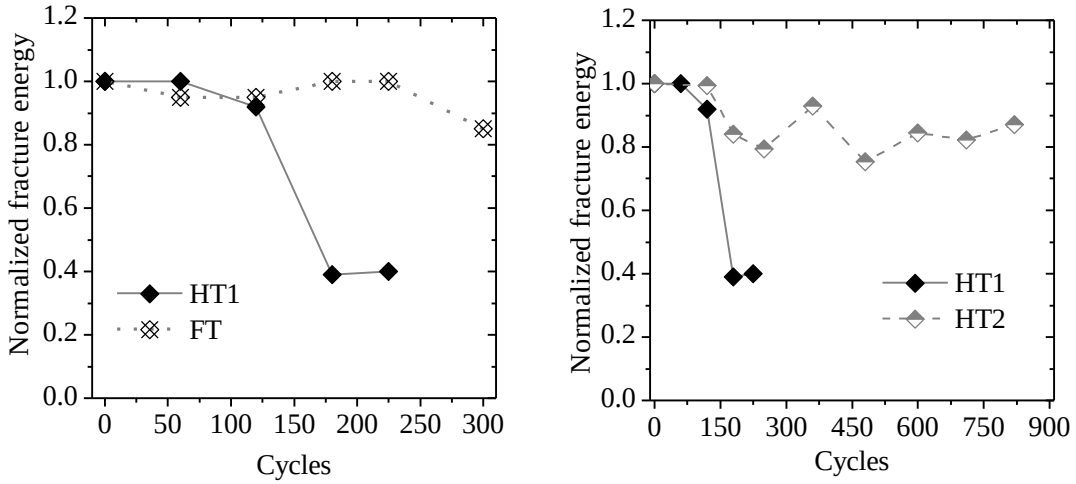

Figure 5-17: Fracture energy comparison between: (a) HT1 and FT; (b) HT1 and HT2.

Assuming that the FRP width and thickness are constant during the hygrothermal exposures, the debonding force is directly related to the square root of interfacial fracture energy and FRP elastic modulus, see Eq. (4.1). Therefore, the participation of each factor in the degradation of the debonding force can be obtained by plotting the changes in the normalized square root of fracture energy and FRP elastic modulus as shown in Figure 5-18 and Figure 5-19.

In exposure HT2, see Figure 5-18(b), the degradation of fracture energy and FRP stiffness has similar effects on the global bond behavior, with the fracture energy having a larger contribution in the bond degradation. The interfacial bond degradation can be attributed to the existing thermal incompatibility inside the composite system and FRP-brick interface. However, when moisture exist in the environment, such as for exposure HT1, the interfacial degradation of the bond has a major effect on the global bond degradation when compared to the FRP elastic

modulus, see Figure 5-18(a). This was expected as moisture is known to cause degradation in the bond strength and fracture energy [166, 186, 262].

In exposure FT, see Figure 5-19, the effect of FRP mechanical properties and interfacial behavior is similar in the observed degradation. The presence of water at the interface region is an important factor in degradation due to the freeze-thaw exposure which is directly related to the porosity of superficial layer of the bricks [171]. Since the surface layer of the bricks used in this study has a low porosity, the observed performance of the system against freeze-thaw conditions was expected. Moreover, as explained before, since the thermal expansion coefficient of epoxy resins decreases at low temperature, a less relevant thermal incompatibility problem is expected in this exposure condition.

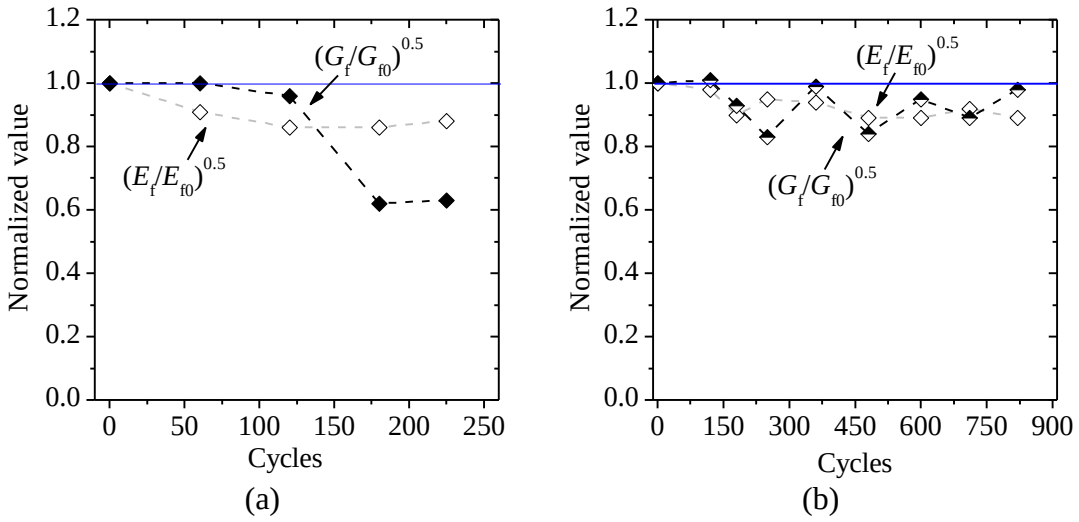

Figure 5-18: Bond degradation mechanisms in: (a) exposure HT1; (b) exposure HT2.

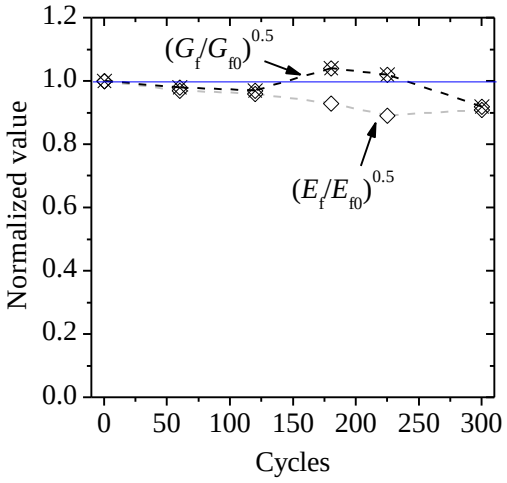

Figure 5-19: Bond degradation mechanisms in exposure FT.

Regarding the failure mode, four different failures were observed in the specimens: (1) cohesive failure within a thick layer of the brick along the bonded length; (2) formation of a brick bulb at the free end (3) cohesive failure within a superficial layer of the brick, next denoted by interfacial cohesive; (4) adhesive failure at the FRP/brick interface, see Figure 5-20. Formation of the brick bulb at the free end occurred within a deep layer of the brick resulting in a similar bond behavior (bond strength and debonding mechanism) to the first failure mode. The results obtained from acoustic emission tests also confirms the similar fracture propagation and energy release between these two failure conditions, see Chapter 6. Therefore, this failure mode has been accounted as cohesive failure hereafter. In both exposures HT1 and FT, a progressive change of failure mode from cohesive to adhesive was observed in the specimens with the increase of exposure cycles, Figure 5-21. Such a change in the failure mode of the specimens, also reported in [270], can be attributed to the observed bond degradation during environmental exposures. On the contrary, no significant change of failure mode was observed in the specimens exposed to HT2 conditions. A comparison between failure modes in the specimens exposed to HT1/FT and HT2 conditions highlights the influence of moisture attack in changing the failure modes to interfacial adhesive failure. The contribution of each failure mode in the debonding behavior is presented in Figure 5-22 for the exposures HT1 and FT (this graph is not presented for exposure HT2 because the failure mode of the specimens did not change during the exposure). These values are obtained by measuring the area corresponding to each failure mode on the failure surface of the specimens after debonding tests. Then, the average values are obtained from the specimens belonging to each exposure period. It can be observed that the contribution of the cohesive failure reduces along time and, meanwhile, adhesive failure governs the behavior.

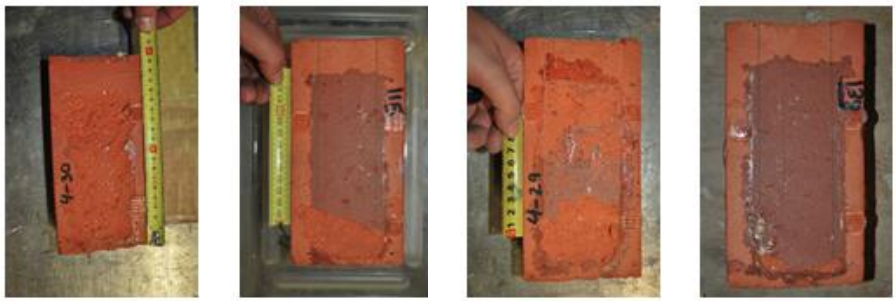

(a) (b) (c) (d)

Figure 5-20: Observed failure modes: (a) cohesive failure with fracture inside the brick; (b) formation of a brick bulb at the free end (c) cohesive-adhesive failure; (d) adhesive failure at the FRP/brick interface.

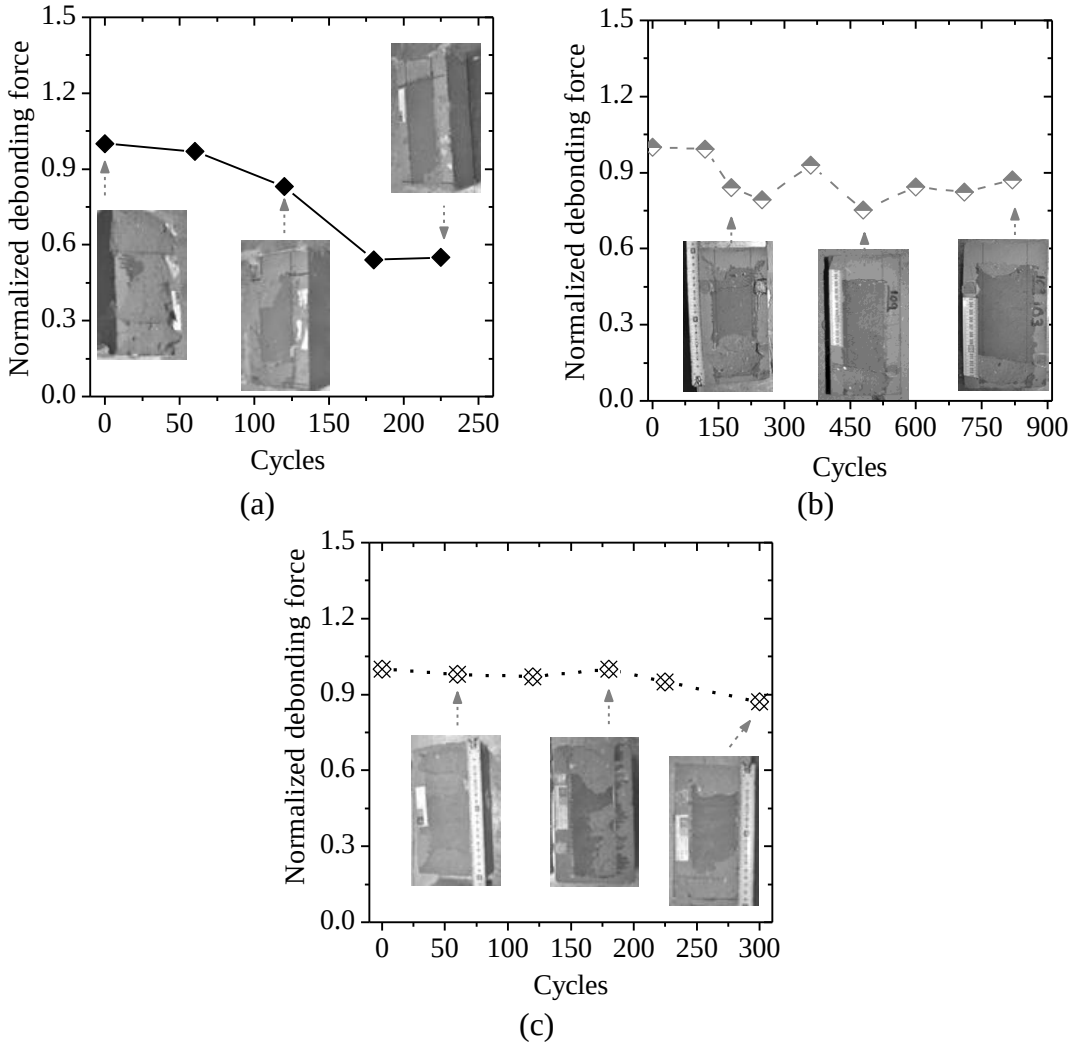

Figure 5-21: Observed failure modes in specimens exposed to: (a) HT1; (b) HT2; (c) FT.

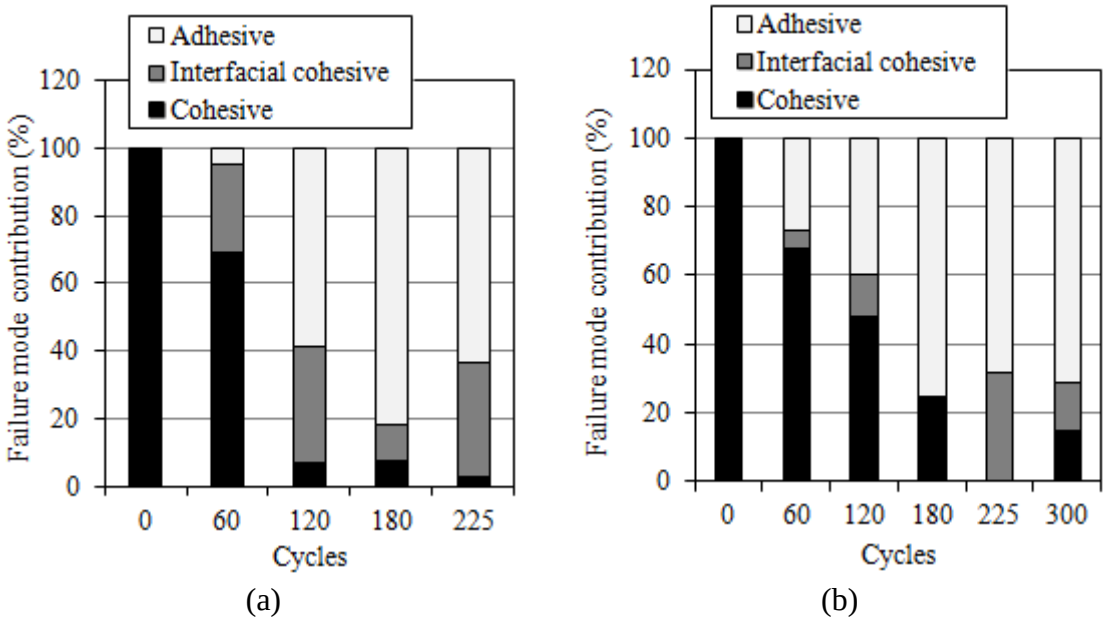

Figure 5-22: Failure modes contribution in exposures: (a) HT1; (b) FT.

5.3 Durability predictions

The observed degradation of the bond behavior and material properties has been modeled with the predictive decay models. The detailed analysis procedures and predictions of each model are detailed in this section. It should be noted that using predictive models in accelerated ageing tests requires a deep knowledge of the active degradation mechanisms and a large experimental database. The experimental results presented here demonstrated the need for performing longer accelerated ageing tests especially for exposures HT1 and FT and therefore the predictions made are limited to the available data. Even though, the use of prediction models can assist in better understanding degradation trends, allow a first comparative study between different exposure conditions and also contribute to development of constitutive models for numerical modeling approaches.

5.3.1 Kinetic rate theory model

For kinetic rate theory model, the strength degradation for epoxy resin, GFRP coupons and bond is plotted against the logarithm of exposure cycles in Figure 5-23 to Figure 5-25. The lines in these figures represent the fitted curves obtained from linear regression analysis, also tabulated in Table 5-1. For the HT2 exposure, the regression analysis is performed for the first 300 cycles so that the accuracy of the model in predicting the degradation until the end of the tests (820 cycles) can be evaluated. Since the logarithm of time at zero days is mathematically undefined, “0 day” for the unconditioned specimens has been replaced by “1 day” in the calculations. In general, the degradation model found for FT and HT2 conditions is similar.

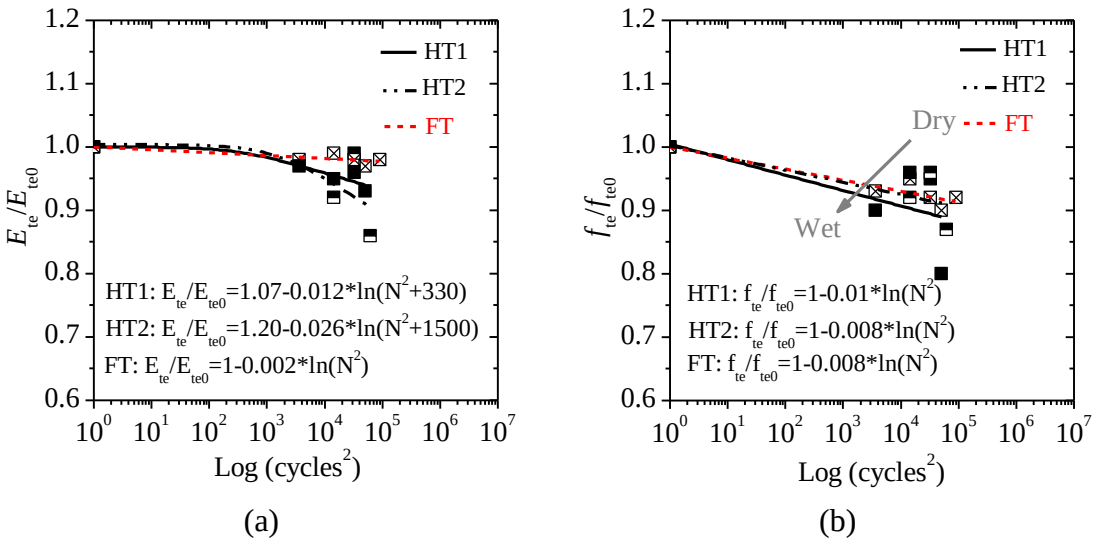

Figure 5-23: Logarithmic degradation model for epoxy: (a) elastic modulus; (b) tensile strength.

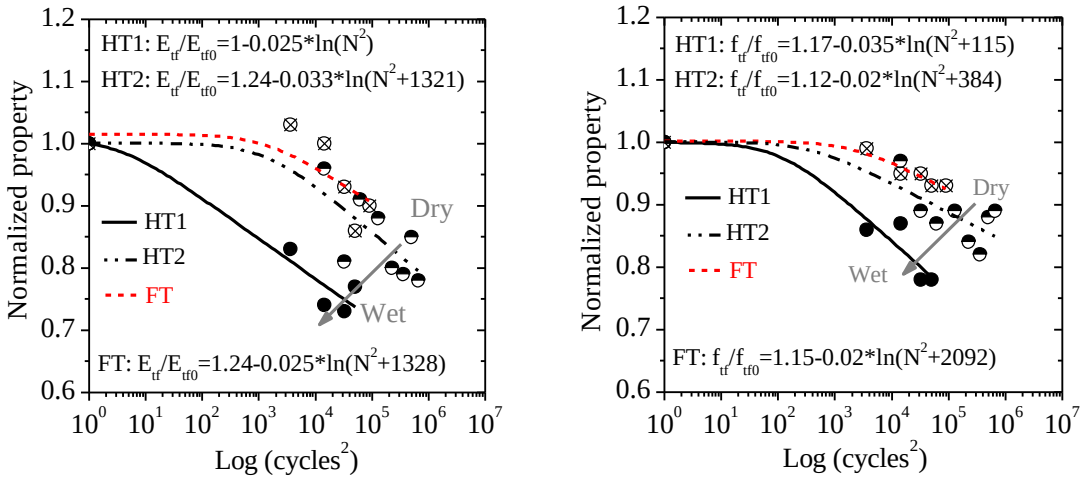

Figure 5-24: Logarithmic degradation model for GFRP: (a) elastic modulus; (b) tensile strength.

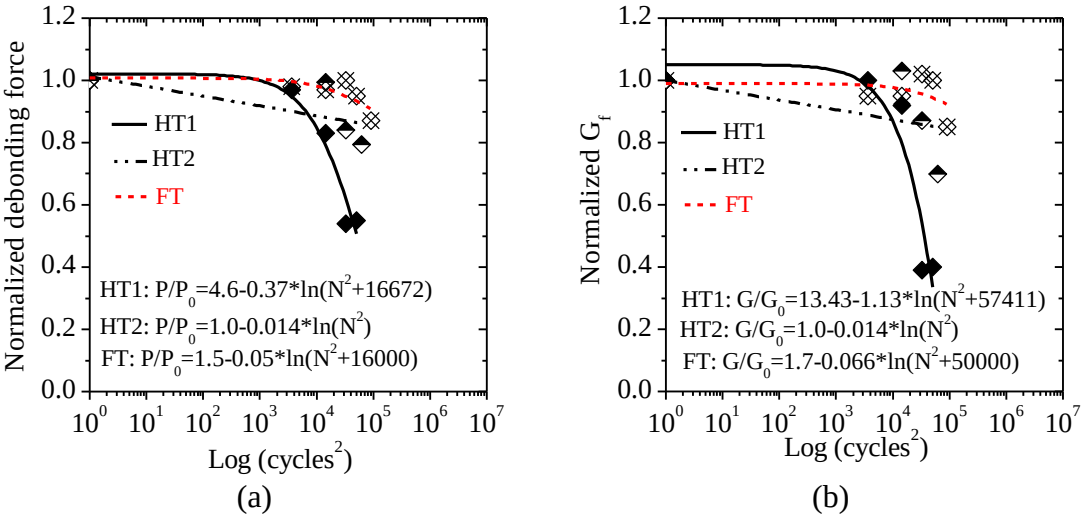

Figure 5-25: Logarithmic degradation model for bond: (a) debonding force; (b) fracture energy.

Table 5-1: Fitted logarithmic degradation modes.

Specimen/property	Exposure	Model
Epoxy resin/tensile strength	HT1	$P/P_0=1-0.01*\ln(N^2)$
	HT2	$P/P_0=1-0.008*\ln(N^2)$
	FT	$P/P_0=1-0.008*\ln(N^2)$
Epoxy resin/elastic modulus	HT1	$P/P_0=1.07-0.012*\ln(N^2)$
	HT2	$P/P_0=1.19-0.026*\ln(N^2)$
	FT	$P/P_0=1-0.002*\ln(N^2)$
GFRP/tensile strength	HT1	$P/P_0=1.17-0.035*\ln(N^2+115)$
	HT2	$P/P_0=1.12-0.02*\ln(N^2+384)$
	FT	$P/P_0=1.15-0.02*\ln(N^2+2092)$
GFRP/elastic modulus	HT1	$P/P_0=1-0.025*\ln(N^2)$
	HT2	$P/P_0=1.24-0.033*\ln(N^2+1321)$
	FT	$P/P_0=1.24-0.025*\ln(N^2+1328)$
GFRP-brick/debonding force	HT1	$P/P_0=4.6-0.37*\ln(N^2+16672)$
	HT2	$P/P_0=1-0.014*\ln(N^2)$
	FT	$P/P_0=1.5-0.05*\ln(N^2+16000)$
GFRP-brick/fracture energy	HT1	$P/P_0=13.43-1.13*\ln(N^2+57411)$
	HT2	$P/P_0=1-0.014*\ln(N^2)$
	FT	$P/P_0=1.7-0.066*\ln(N^2+50000)$

The percent error in the predictions for each exposure is presented in Table 5-2 to Table 5-4. The accuracy of the models is relatively good for all mechanical properties. For the epoxy tensile strength the error range is up to 11.7%, while the error for the elastic modulus is in the up to 7.4%. In general, the maximum error in the tensile strength and the elastic modulus prediction is for HT1 and HT2 exposures, respectively. For the GFRP coupons, the error range is up to 5.7% and up to 12.0% for the tensile strength and elastic modulus, respectively. Here, the maximum error in the tensile strength and the elastic modulus prediction is for HT2 and FT exposures, respectively. Meanwhile, the error in prediction of the debonding force is up to 12.7% and for the bond fracture energy is up to 37.3% with the maximum errors in HT1 exposure.

It can be observed that the predictions for exposure HT2 have reasonable accuracy until the end of the tests, although the model is obtained by fitting the experimental data until 300 cycles of exposure. This shows the suitability of the adopted model for predicting long-term behavior under accelerated ageing conditions, also expected in case of exposure HT1 and FT.

Table 5-2: Logarithmic model error for predicting the degradations in HT1 exposure.

Cycles	Epoxy				GFRP				Bond			
	f_{te}/f_{te0}	Err. (%)	E_{te}/E_{te0}	Err. (%)	f_{tfe}/f_{tfe0}	Err. (%)	E_{tfe}/E_{tfe0}	Err. (%)	P_e/P_0	Err. (%)	G_f/G_{f0}	Err. (%)
0	1.00	0.0	1.00	-0.1	1.00	0.4	0.99	0.0	1.00	0.3	1.05	4.7
60	0.92	2.0	0.97	0.2	0.89	2.7	0.82	-3.7	0.93	-3.8	0.98	-2.1
120	0.90	-5.5	0.96	0.9	0.83	-3.9	0.76	2.8	0.77	-6.4	0.79	-13.7
180	0.90	-5.2	0.95	-1.8	0.80	3.9	0.75	0.8	0.60	12.7	0.54	37.3
225	0.89	11.7	0.94	1.0	0.79	1.2	0.74	-5.7	0.49	-12.0	0.33	-15.6
Average Err.		4.9		0.8		2.4		2.6		7.0		14.7

Table 5-3: Logarithmic model error for predicting the degradations in HT2 exposure.

Cycles	Epoxy				GFRP				Bond			
	f_{te}/f_{te0}	Err. (%)	E_{te}/E_{te0}	Err. (%)	f_{tfe}/f_{tfe0}	Err. (%)	E_{tfe}/E_{tfe0}	Err. (%)	P_e/P_0	Err. (%)	G_f/G_{f0}	Err. (%)
0	1.00	0.0	1.00	0.0	1.00	0.1	1.00	0.3	1.00	0.0	1.00	0.0
120	0.92	0.2	0.94	2.6	0.93	-4.7	0.92	-4.0	0.87	-12.8	0.87	-15.8
180	0.92	-4.9	0.92	-7.4	0.91	2.8	0.89	10.7	0.85	1.8	0.85	-1.9
250	0.91	4.4	0.90	4.9	0.90	3.3	0.87	-3.5	0.85	6.5	0.85	21.5
360	0.91	3.7	0.88	7.1	0.88	-0.3	0.85	-3.4	0.84	-10.2	0.84	-14.8
480	0.90	-2.5	0.87	5.8	0.87	4.5	0.83	4.6	0.83	9.9	0.83	16.3
600	0.90	-1.1	0.86	5.4	0.86	5.7	0.82	3.0	0.82	-2.7	0.82	-8.6
710	0.89	-2.4	0.85	-0.9	0.86	-2.3	0.80	-5.6	0.82	-0.8	0.82	3.1
820	0.89	-1.7	0.84	-0.8	0.85	-4.7	0.79	1.5	0.81	-6.7	0.81	-15.9
Average Err.		2.3		3.9		3.2		4.1		5.7		10.9

Table 5-4: Logarithmic model error for predicting the degradations in FT exposure.

Cycles	Epoxy				GFRP				Bond			
	f_{te}/f_{te0}	Err. (%)	E_{te}/E_{te0}	Err. (%)	f_{tfe}/f_{tfe0}	Err. (%)	E_{tfe}/E_{tfe0}	Err. (%)	P_e/P_0	Err. (%)	G_f/G_{f0}	Err. (%)
0	1.00	0.0	1.00	0.0	1.00	-0.3	1.06	6.0	1.02	1.6	0.99	-1.4
60	0.93	0.6	0.98	-0.1	0.98	-0.9	1.03	0.1	1.01	2.2	0.98	3.6
120	0.92	-3.0	0.98	-1.1	0.96	0.6	1.00	-0.3	0.98	1.5	0.97	2.3
180	0.92	-0.3	0.98	-0.1	0.94	-1.3	0.98	5.3	0.96	-3.9	0.95	-11.7
225	0.91	1.1	0.98	1.0	0.93	0.6	0.97	12.0	0.94	-0.3	0.94	-10.7
300	0.91	-1.2	0.98	0.1	0.92	-1.3	0.95	6.5	0.92	6.1	0.92	9.0
Average Err.		1.0		0.4		0.8		5.0		2.6		6.5

5.3.2 Time-Temperature-Moisture superposition model

An exponential model, similar to the Phani and Bose [209] model explained in sec. 2.4.3, is chosen here for modeling the degradation. The strength degradation in epoxy resin, GFRP coupons and bond is plotted against the exposure cycles in Figure 5-26 to Figure 5-28. The lines in these figures represent the fitted curves obtained from regression analysis, also tabulated in Table 5-5. For the HT2 exposure, the regression analysis is performed for the first 300 cycles so that the accuracy of the model in predicting the degradation until the end of the tests (820 cycles) can be evaluated. Again, in most cases the degradation models for FT and HT2 conditions are similar.

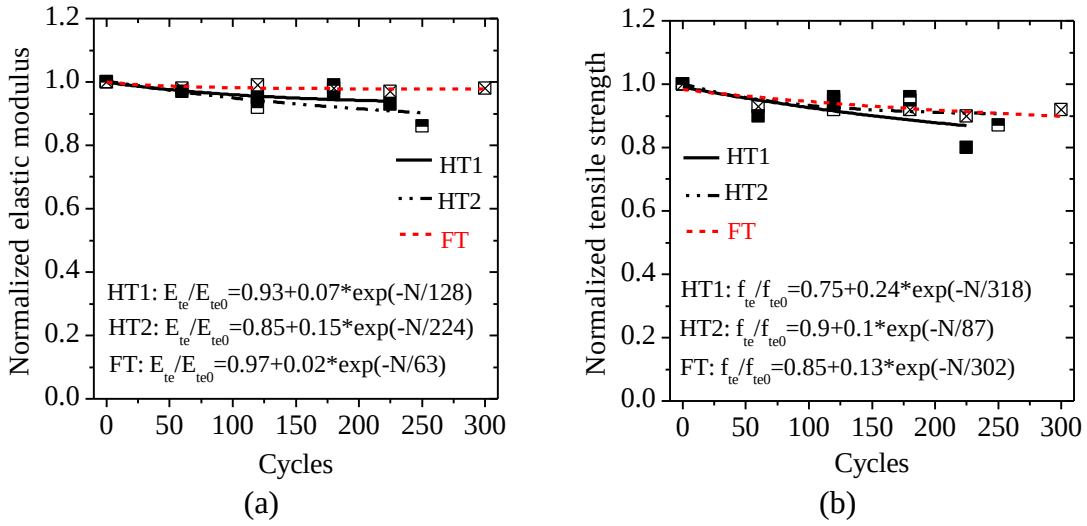

Figure 5-26: Exponential degradation model for epoxy: (a) elastic modulus; (b) tensile strength.

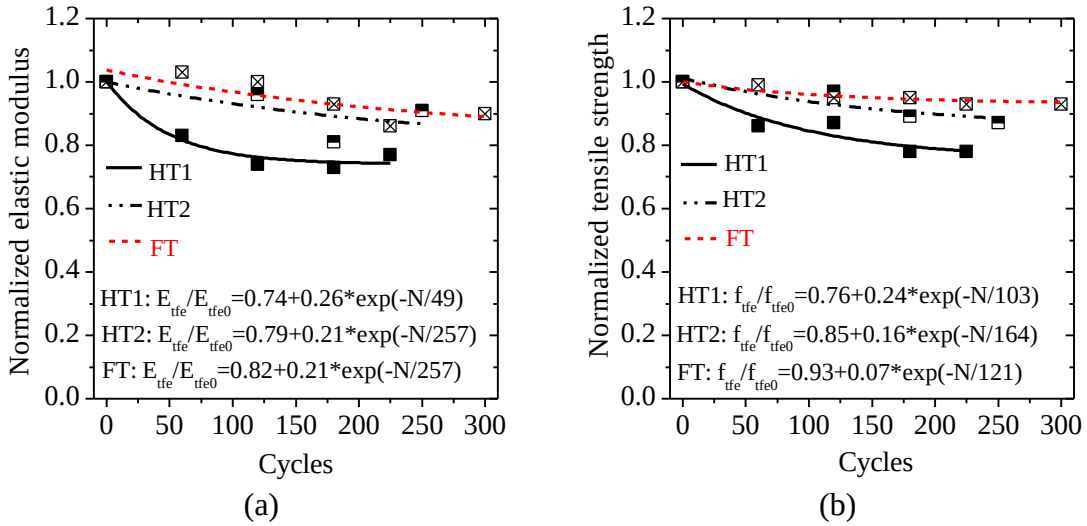

Figure 5-27: Exponential degradation model for GFRP: (a) elastic modulus; (b) tensile strength.

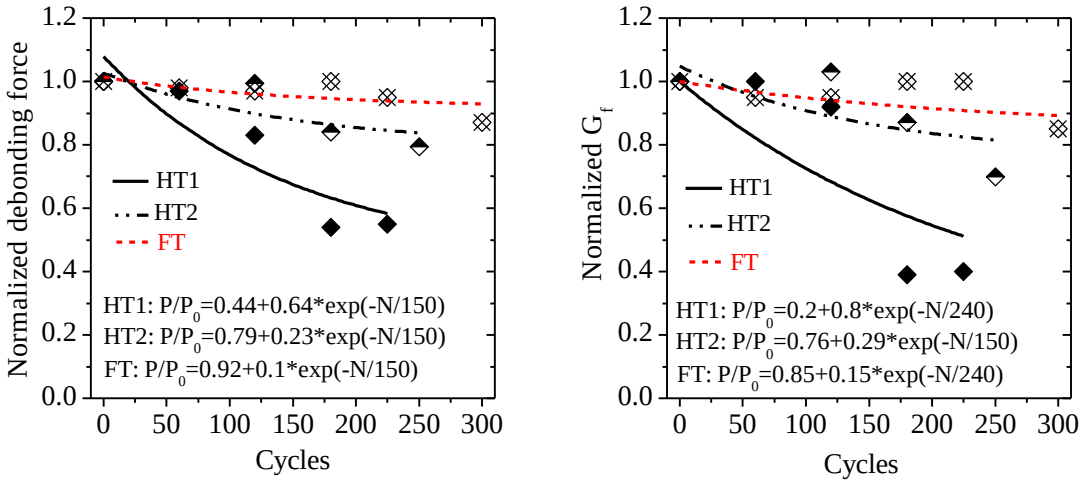

Figure 5-28: Exponential degradation model for bond: (a) debonding force; (b) fracture energy.

Table 5-5: Fitted exponential degradation modes.

Specimen/property	Exposure	Model
Epoxy resin/tensile strength	HT1	$P/P_0=0.75+0.24*exp(-N/318)$
	HT2	$P/P_0=0.9+0.1*exp(-N/87)$
	FT	$P/P_0=0.85+0.13*exp(-N/302)$
Epoxy resin/tensile modulus	HT1	$P/P_0=0.93+0.07*exp(-N/128)$
	HT2	$P/P_0=0.85+0.15*exp(-N/224)$
	FT	$P/P_0=0.97+0.02*exp(-N/63)$
GFRP/tensile strength	HT1	$P/P_0=0.76+0.24*exp(-N/103)$
	HT2	$P/P_0=0.85+0.16*exp(-N/164)$
	FT	$P/P_0=0.93+0.07*exp(-N/121)$
GFRP/tensile modulus	HT1	$P/P_0=0.74+0.26*exp(-N/49)$
	HT2	$P/P_0=0.79+0.21*exp(-N/257)$
	FT	$P/P_0=0.82+0.21*exp(-N/257)$
GFRP-brick/debonding force	HT1	$P/P_0=0.44+0.64*exp(-N/150)$
	HT2	$P/P_0=0.79+0.23*exp(-N/150)$
	FT	$P/P_0=0.92+0.1*exp(-N/150)$
GFRP-brick/fracture energy	HT1	$P/P_0=0.2+0.8*exp(-N/240)$
	HT2	$P/P_0=0.76+0.29*exp(-N/150)$
	FT	$P/P_0=0.85+0.15*exp(-N/240)$

The percent error in the predictions for each exposure is presented in Table 5-6 to Table 5-8. The accuracy of the models is relatively good for all mechanical properties. For the epoxy tensile strength the error range is up to 8.8%, while the error for the elastic modulus is in up to 7.6%.

Again, the maximum error in the tensile strength and the elastic modulus prediction is for HT1 and HT2 exposures, respectively. For the GFRP coupons, the error range is up to 4.8% and 10.5% for the tensile strength and elastic modulus, respectively (being both for HT2 exposure). Meanwhile, the error in prediction of the debonding force is 18.2% and for the fracture energy is up to 46.4%. The error range for the debonding force is in the same range for all the exposure conditions.

Again, it can be observed that the predictions for exposure HT2 have reasonable accuracy until the end of the tests, although the model is obtained by fitting the experimental data until 300 cycles of exposure. The same condition is also expected in case of exposure HT1 and FT.

Table 5-6: Exponential model error for predicting the degradations in HT1 exposure.

Cycles	Epoxy				GFRP				Bond			
	f_{te}/f_{te0}	Err. (%)	E_{te}/E_{te0}	Err. (%)	f_{tfe}/f_{tfe0}	Err. (%)	E_{tfe}/E_{tfe0}	Err. (%)	P_e/P_0	Err. (%)	G_f/G_{f0}	Err. (%)
0	0.99	-1.1	1.00	-0.1	1.00	-0.2	0.99	-0.5	1.08	7.6	1.00	-0.3
60	0.95	5.4	0.97	0.2	0.89	4.1	0.82	-1.1	0.87	-10.1	0.82	-17.7
120	0.91	-4.4	0.96	0.9	0.83	-3.9	0.76	3.0	0.73	-11.9	0.69	-25.6
180	0.89	-6.2	0.95	-1.8	0.80	3.3	0.75	1.7	0.63	18.2	0.58	46.4
225	0.87	8.8	0.94	1.0	0.79	0.8	0.74	-3.9	0.58	5.4	0.51	30.0
Average Err.		5.2		0.8		2.5		2.1		10.6		24.0

Table 5-7: Exponential model error for predicting the degradations in HT2 exposure.

Cycles	Epoxy				GFRP				Bond			
	f_{te}/f_{te0}	Err. (%)	E_{te}/E_{te0}	Err. (%)	f_{tfe}/f_{tfe0}	Err. (%)	E_{tfe}/E_{tfe0}	Err. (%)	P_e/P_0	Err. (%)	G_f/G_{f0}	Err. (%)
0	1.00	-0.1	1.00	-0.1	1.01	0.9	1.00	-0.1	1.02	1.8	1.05	4.8
120	0.93	0.4	0.94	2.6	0.93	-4.8	0.92	-4.0	0.89	-10.1	0.89	-13.4
180	0.91	-5.4	0.92	-7.6	0.90	1.8	0.89	10.5	0.86	2.3	0.85	-2.8
250	0.91	3.7	0.90	4.6	0.88	1.7	0.87	-4.1	0.83	4.9	0.81	17.1
360	0.90	3.2	0.88	6.7	0.87	-2.2	0.84	-4.5	0.81	-12.8	0.79	-19.8
480	0.90	-2.5	0.87	5.7	0.86	2.7	0.82	3.3	0.80	6.2	0.77	8.5
600	0.90	-0.8	0.86	5.8	0.85	4.5	0.81	2.1	0.79	-5.9	0.77	-14.7
710	0.90	-1.9	0.86	0.0	0.85	-2.9	0.80	-6.0	0.79	-3.7	0.76	-3.7
820	0.90	-0.9	0.85	0.7	0.85	-4.7	0.80	1.7	0.79	-9.2	0.76	-21.2
Average Err.		2.1		3.7		2.9		4.0		6.4		11.8

Table 5-8: Exponential model error for predicting the degradations in FT exposure.

Cycles	Epoxy				GFRP				Bond			
	f_{te}/f_{te0}	Err. (%)	E_{te}/E_{te0}	Err. (%)	f_{tfe}/f_{tfe0}	Err. (%)	E_{tfe}/E_{tfe0}	Err. (%)	P_e/P_0	Err. (%)	G_f/G_{f0}	Err. (%)
0	0.98	-2.0	0.99	-1.0	1.00	-0.1	1.03	2.9	1.02	1.9	1.00	-0.1
60	0.96	2.9	0.98	-0.7	0.97	-1.4	0.99	-3.9	0.99	0.3	0.97	2.1
120	0.94	-1.5	0.97	-1.9	0.96	0.6	0.95	-5.0	0.96	-0.5	0.94	-0.7
180	0.92	0.2	0.97	-0.9	0.95	-0.8	0.92	-0.6	0.95	-5.0	0.92	-14.7
225	0.91	0.9	0.97	0.2	0.94	1.5	0.91	5.0	0.94	-0.5	0.91	-13.7
300	0.90	-2.4	0.97	-0.6	0.94	0.2	0.89	-1.2	0.93	7.5	0.89	6.0
Average Err.		1.7		0.9		0.8		3.1		2.6		6.2

5.3.3 Comparison between models and long-term predictions

A comparison is made here between different degradation models and the experimental results in Figure 5-29 to Figure 5-31. It can be observed that when the scatter of the experimental results is considered, reasonable accuracy is achieved and the predictions are in the experimental range for all the cases. Both models seem to be suitable for predicting the degradations for the number of cycles considered. However, using these models for predicting longer exposure periods requires special care and performing longer accelerated ageing tests.

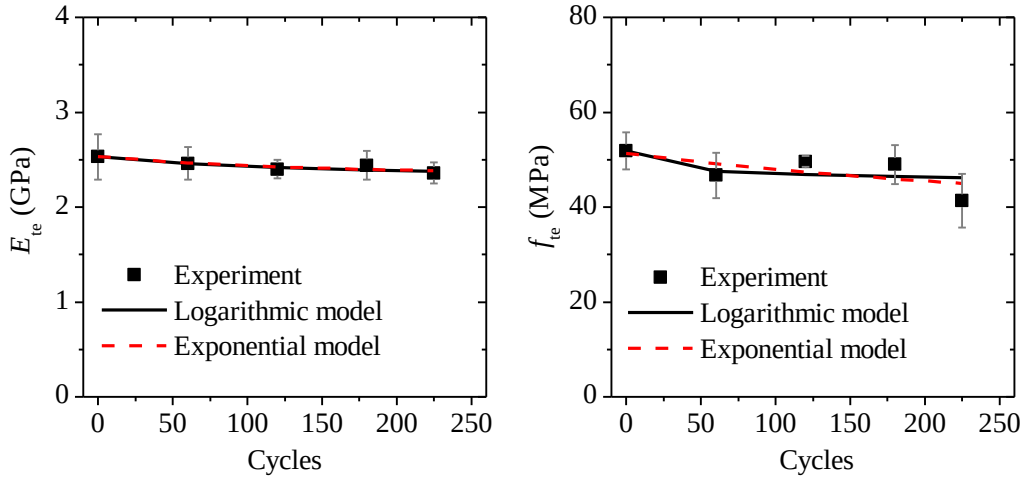

(a)

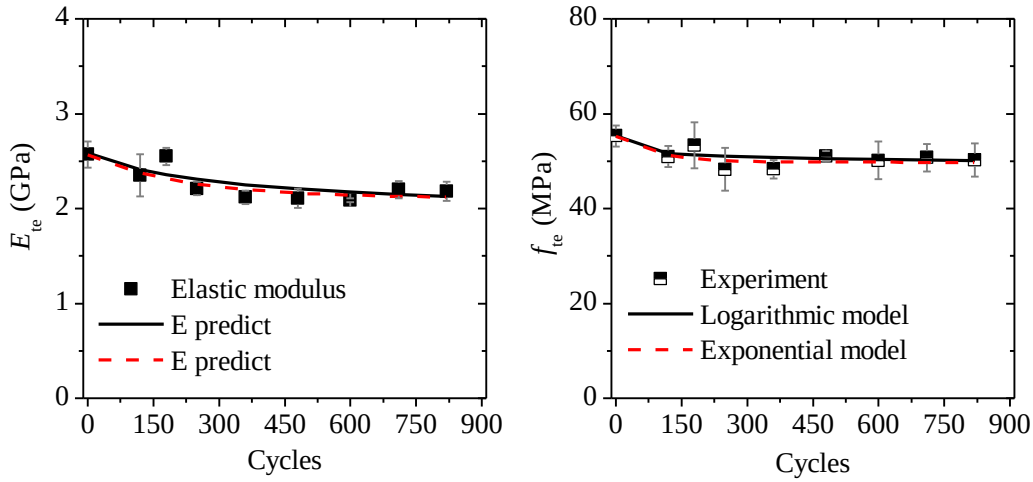

(b)

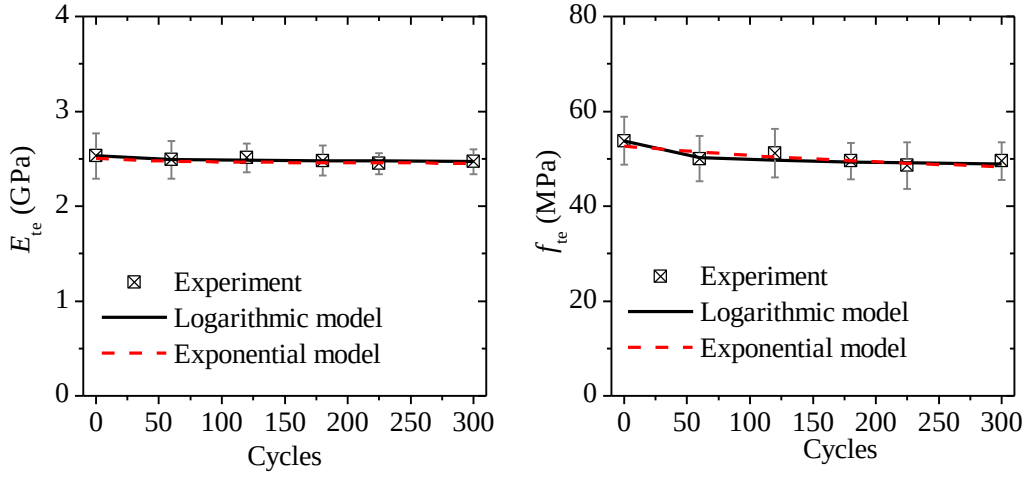

(c)

Figure 5-29: Comparison between experimental results and prediction models for epoxy resin in exposure: (a) HT1; (b) HT2; (c) FT.

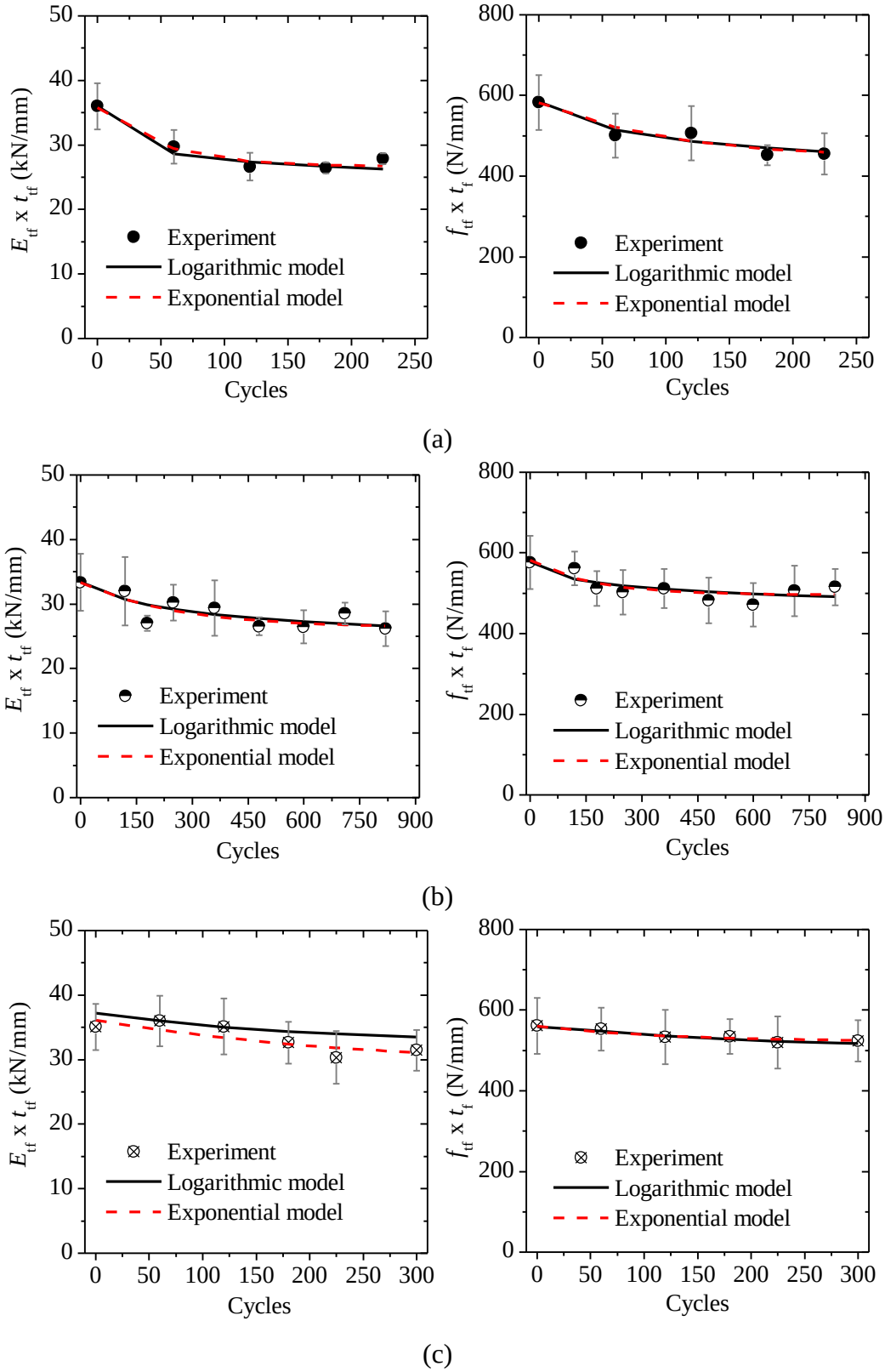

Figure 5-30: Comparison between experimental results and prediction models for GFRP in exposure: (a) HT1; (b) HT2; (c) FT.

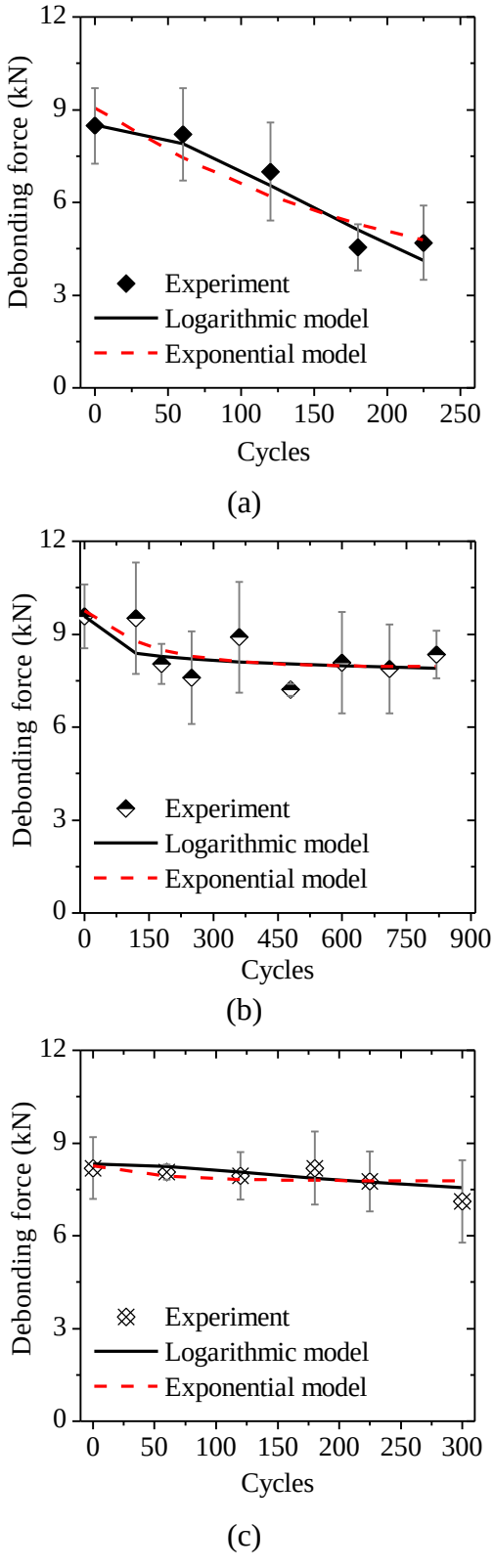

Figure 5-31: Comparison between experimental results and prediction models for debonding force in exposure: (a) HT1; (b) HT2; (c) FT.

The long-term performance of bond and material mechanical properties are simulated with the aim of proposed predictive models for all exposure conditions, see Table 5-9 to Table 5-11. The simulations are presented for wet environments (HT1 exposure), environments with average relative humidity (HT2 exposure), and cold regions (FT exposure). The predictions are made for 50, 125 and 200 years as the usual seismic strengthening objectives for historical masonry. As stated before, establishing a link between real exposure conditions and accelerated ageing tests is a complicated task which requires extensive experimental tests. Here, based on the available information in the literature presented in sec. 2.3.1, it is assumed that each 40 cycles of hygrothermal exposures represent 1 year life of the structure in real exposure conditions. Therefore 2000, 5000 and 8000 cycles of each exposure conditions are assumed equal to 50, 125 and 200 years of structural life in their corresponding environmental conditions.

It can be observed that the models give different values for the residual strength of materials. In general, logarithmic model gives lower values. It seems that the exponential model has reached a residual value giving the same degradation levels for all exposure periods. The logarithmic model predicts 100% degradation of bond in wet environments. For the bond strength 68%, 21% and 5% degradation is predicted with the exponential model for wet environments, environments with average humidity and cold environmental conditions, respectively. These values in logarithmic model are 100%, 20% and 26%. The values obtained with exponential model seem more reasonable, although performing tests with longer periods is necessary for validation of the proposed predictive models.

Table 5-9: Long-term predictions for wet environments.

Material	Properties	Exponential model			Logarithmic model		
		Duration (years)			Duration (years)		
		50	125	200	50	125	200
Epoxy	f_{te}/f_{te0}	0.75	0.75	0.75	0.85	0.83	0.82
	E_{te}/E_{te0}	0.93	0.93	0.93	0.89	0.86	0.85
GFRP	f_{tfe}/f_{tfe0}	0.76	0.76	0.76	0.64	0.57	0.57
	E_{tfe}/E_{tfe0}	0.74	0.74	0.74	0.62	0.57	0.55
Bond	P_e/P_0	0.32	0.32	0.32	0	0	0
	G_f/G_{f0}	0.2	0.2	0.2	0	0	0

Table 5-10: Long-term predictions for environments with average humidity.

Material	Properties	Exponential model			Logarithmic model		
		Duration (years)			Duration (years)		
		50	125	200	50	125	200
Epoxy	f_{te}/f_{te0}	0.9	0.9	0.9	0.88	0.86	0.86
	E_{te}/E_{te0}	0.82	0.82	0.82	0.77	0.72	0.69
GFRP	f_{tfe}/f_{tfe0}	0.86	0.86	0.86	0.82	0.78	0.76
	E_{tfe}/E_{tfe0}	0.79	0.79	0.79	0.74	0.68	0.65
Bond	P_e/P_0	0.79	0.79	0.79	0.8	0.78	0.77
	G_f/G_{f0}	0.75	0.75	0.75	0.83	0.81	0.8

Table 5-11: Long-term predictions for cold regions.

Material	Properties	Exponential model			Logarithmic model		
		Duration (years)			Duration (years)		
		50	125	200	50	125	200
Epoxy	f_{te}/f_{te0}	0.85	0.85	0.85	0.88	0.86	0.86
	E_{te}/E_{te0}	0.97	0.97	0.97	0.97	0.97	0.96
GFRP	f_{tfe}/f_{tfe0}	0.93	0.93	0.93	0.85	0.81	0.79
	E_{tfe}/E_{tfe0}	0.82	0.82	0.82	0.86	0.81	0.79
Bond	P_e/P_0	0.95	0.95	0.95	0.74	0.65	0.6
	G_f/G_{f0}	0.8	0.8	0.8	0.7	0.58	0.51

5.4 Conclusions

The results of an extensive experimental program aimed at investigating the durability of FRP-masonry systems were presented in this study. Accelerated ageing tests were performed following three different hygrothermal conditions consisting of thermal cycles from +10℃ to +50℃ (90% R.H.) called HT1 exposure, +10℃ to +50℃ (60% R.H.) called HT2 exposure, and –10℃ to +30℃ (90% R.H.) called FT exposure. The HT1 exposure was used for simulating the thermal variations in wet environments, while HT2 simulated environments with average relative humidity. Finally, exposure FT was used to simulate freeze-thaw actions in cold regions.

The bond degradation was studied by visual inspection and single-lap shear bond tests. The changes in mechanical properties of material constituents were also investigated. Two different degradation models were finally used to predict the observed degradations due to exposure conditions. Based on the obtained results, the following conclusions can be drawn:

- The hygrothermal exposures did not affect the mechanical properties of bricks. However, epoxy resin and GFRP coupons showed some degradation. Generally, higher degradation levels were observed due to exposing the specimens to HT1 conditions. The degradation level in GFRP coupons were higher than epoxy resin which is due to the epoxy/fibers interfacial degradation. The interfacial degradation can be attributed to the thermal mismatch between epoxy and glass fibers, which induced thermal fatigue and moisture attack. Again, higher degradation levels were observed in the specimens exposed to HT1 conditions.
- FRP delamination was observed at the FRP/brick interface after exposure to environmental conditions. The delamination, being due to the thermal incompatibility between brick and adhesive, was progressively increased with the number of cycles. Moreover, significantly larger FRP delaminations with higher growth rates were observed in the specimens exposed to HT1 conditions. This can be due to the effect of moisture on the debonding growth behavior and adhesive fracture properties.
- A progressive degradation of bond strength and fracture energy was observed in the specimens in all exposure types. However, the degradation in the specimens exposed to HT2 and FT conditions was very small in contrary to the large reductions observed in the specimens exposed to HT1 conditions.
- In both exposure types HT1 and FT, the failure mode changed progressively from cohesive failure in the brick to adhesive failure at the FRP-brick interface with exposure time. However, no significant change of failure mode was observed in the specimens exposed to HT2 conditions.
- Available predictive models were used for modeling the observed degradation in the material properties and bond behavior. It was observed that exponential and logarithmic models can be fairly used for simulating the degradations. The validated models were used for long-term predictions and it was observed that exponential model leads to more reliable results. However, special care should be taken for extending the short-term degradation models for long-term predictions, as a fully validated predictive model requires performing extensive long-term experimental tests.

Chapter 6

Application of advanced NDT techniques

As discussed before, the effectiveness of EBR techniques is intrinsically dependent on the bond behavior between the composite material and the masonry substrate. In this regard, fully understanding the involved strain and stress transfer mechanisms and fracture progress in the interfacial region (bond) is crucial for design and performance assessment. On the other hand, it is known that the environmental conditions can cause bond degradation and FRP delamination in the interfacial region, which affect the performance of the strengthened structure. FRP delamination may also occur due to poor workmanship. Use of non-destructive qualitative and quantitative bond assessment methods seems interesting for detection of delamination or for assessment of the bond degradation in both laboratory tests and on-site structural health monitoring purposes.

Significant progress has been achieved in the last years regarding experimental investigation and computational modeling of the debonding phenomenon and damage in FRP-strengthened masonry elements, see e.g. [34, 39, 59, 226]. However, aspects such as failure initiation, interfacial damage propagation and localization, three-dimensional nature of the bond behavior, effective bond length and strain distributions along the reinforcement as well as nondestructive bond quality monitoring are still open issues. This chapter shows how these aspects can be monitored and characterized by means of three advanced measurement techniques: (a) Digitial Image Correlation (DIC); (b) Infrared (IR) thermography; (c) Acoustic Emission (AE).

Laboratory characterization of the bond behavior is usually performed by means of shear debonding or pull-off tests. In the shear debonding tests, strain gauges are usually attached to the FRP surface for monitoring the distribution of strains along the bonded length during the delamination process. However, the measurements are limited to the location of the strain gauges leading to incomplete understanding of the bond behavior. Use of a full-field measurement technique such as DIC seems to be valuable in better understanding the bond behavior. This method

has been used here for the characterization of the bond behavior in FRP-masonry systems. The applicability of this method and the results obtained from the experimental tests are discussed in Sec. 6.2.

The acoustic emission (AE) technique is used for monitoring the failure initiation and damage propagation at the FRP-masonry interface during experimental testing. Moreover, the correlation between the AE output and bond characteristics such as force-slip behavior, fracture energy, active failure mechanisms and debonding propagation is investigated. The latter provides valuable information for bond behavior assessment and numerical modeling purposes. The tests are also a contribution towards the application of AE techniques for on-site health monitoring of strengthened masonry structures. The basics of the technique and the results obtained are discussed and presented in Sec. 6.3.

The IR thermography technique is used for qualitative and quantitative assessment of the bond degradation in FRP-masonry systems due to environmental conditions. This technique is accepted as an effective method for detection of bond defects and delamination in FRP composites. Once the defects have been located, it is also valuable to characterize them quantitatively in order to judge their severity. A quantitative IR thermography method is adopted and used here for detection of the defects in FRP-strengthened masonry systems. The applicability and accuracy of the adopted method in locating interfacial defects and predicting their sizes are initially validated. Then, the method is used for detecting and quantifying the environmentally induced FRP delamination in the specimens exposed to accelerated ageing conditions. The basics of the technique and discussion of the results are presented in Sec. 6.4.

6.1 Digital image correlation technique

6.1.1 Principles

In the last decades, several interferometric and white-light optical methods have been proposed and developed in experimental solid mechanics for displacement or strain measurements over an entire region of interest (ROI) [45]. These techniques contrast with conventional strain gauges or extensometers by the fact that they provide full-field data and are contact-free. Among these techniques, non-interferometric methods based on image processing, such as the DIC, are increasingly used [224, 271].

The DIC technique provides full-field displacements of a (quasi-)planar object by comparing the similarity between image features recorded, at least, at two different mechanical states. In this technique, the surface of interest must have a textured pattern such that the light intensity reflected

from the surface varies continuously. Such pattern exists either naturally on the material surface or must be created artificially using random patterns, e.g. using spray or airbrush painting. A suitable balance between region of interest and average size of white-to-dark spots must be achieved in order to enhance the displacement spatial resolution (small aperture) associated to the DIC measurements.

With DIC, the displacement field is measured by analyzing the geometrical deformation of the images of the ROI recorded during loading. For this purpose, the initial (undeformed) image is mapped by square facets providing an independent measurement of displacements. The facet size, on the plane of the object, characterizes the displacement spatial resolution. The facet step (*i.e.*, the distance between adjacent facets) controls the total number of measuring points over the ROI and the spatial resolution can be improved by slightly overlapping adjacent facets. Typically, increasing the facet size improves the accuracy of the measurements and lowers the spatial resolution.

To accurately measure the specimen's deformation, the corresponding location of facets is tracked during the test. The tracking or matching process is achieved by searching the extreme location of a pre-defined similarity criterion, commonly called correlation criterion. It has been shown that the zero-normalized sum of squared differences (ZNSSD) is a robust algorithm, since it takes into account the offset and linear scale variations of the light intensity [271], and is given by:

$$C_{ZNSSD}(p) = \sum_{\Omega}\left[\frac{f(x_i, y_i) - f_m}{\sqrt{\sum_{\Omega}[f(x_i, y_i) - f_m]^2}} - \frac{g(x'_i, y'_i) - g_m}{\sqrt{\sum_{\Omega}[g(x'_i, y'_i) - g_m]^2}}\right]^2 \quad (6.1)$$

where Ω is the subset domain, $f(x_i, y_i)$ is the pixel gray level at location (x_i, y_i) in the reference image, $g(x'_i, y'_i)$ is the pixel gray level at (x'_i, y'_i) in the deformed image, and f_m and g_m are the mean gray level values over the subset in the reference and the deformed image, respectively.

A given deformation mapping function must be then chosen. Both first-order and second-order shape functions have been commonly used. Eq. (6.1) is then solved with regard to the mapping parameters (p) using a suitable optimization scheme. Iterative algorithms, e.g. Newton-Raphson or Levenberg-Marquardt methods, can then be used for finding the deformation parameter optimizing the correlation coefficient C_{ZNSSD}.

6.1.2 Measurements

The specimens in the current testing program were prepared by applying a speckle pattern on the ROI, produced by applying a thin coating of white matt followed by a spread distribution of black dots using spray paint, see Figure 6-1. The ARAMIS DIC-2D software by GOM was used in this work [272, 273]. The measurement system was equipped with an 8-bit Baumer Optronic

FWX20 camera coupled with a Nikon AF Micro-Nikkor 200mm *f*/4D IF-ED lens (details in Table 6-1). For mobility and adaptability, the support of the camera was mounted on a Foba ALFAE tripod positioned facing the testing machine.

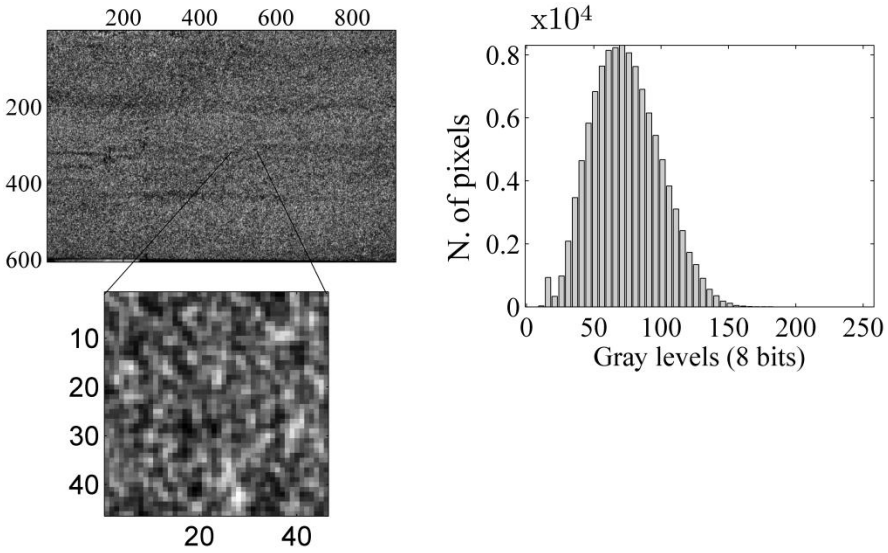

Figure 6-1: Example of a speckle pattern and histogram of a GFRP coupon specimen.

In the test set-up, the optical system was positioned facing the surface of the specimen. A laser pointer is used to guarantee the correct alignment of the camera with regards to the specimen. The working distance (defined as the distance between the target surface and the support of the camera) was set to 1.8 m leading to a conversion factor of 0.037 mm.pixel^{-1}, see Table 6-1. The aperture of the lens was completely open (minimum depth of field) in order to focus the image on the specimen's surface. The lens aperture is then closed to *f*/11 in order to improve the depth of field during the test. The shutter time is set to 5 ms. The light source is finally adjusted in order to guarantee an even illumination of the target surface and to avoid over-exposition.

Regarding the size of the ROI, the optical system (magnification) and the quality of the granulate (average speckle size) obtained by the spray paint, a facet size of 15×15 pixels is chosen in this study. The facet step is also set to 15×15 pixels in order to avoid statistically correlated measurements. The in-plane displacements are then numerically differentiated in order to determine the strains field. The typical resolution of the measurements is in the range of 10^{-2} mm and 0.02-0.04 % for displacement and strain evaluation, respectively.

Table 6-1: Optical system components and measurement parameters.

CCD camera	
Model	Baumer Optronic FWX20 (8 bits, 1624×1236 pixels, 4.4 μm/pixel)
Shutter time	5 ms
Acquisition frequency	1 Hz
Lens	
Model	Nikon AF Micro-Nikkor 200mm *f*/4D
Aperture	*f*/11
Lighting	LEDMHL10 (color temperature: 6000 K)
Working distance	1800 mm
Conversion factor	0.037 mm/pixel
Project parameter – Facet	
Facet size	15×15 pixel^2
Step size	15×15 pixel^2
Project parameter – Strain	
Computation size	7×7 facets
Validity code	55%
Strain computation method	Total
Image recording	
Acquisition frequency	1 Hz

6.1.3 Experimental plan

The experimental program includes tensile and shear bond tests and measurement of strains development on the specimens by means of the DIC technique. Tensile tests are performed on aluminum and GFRP specimens. Aluminum is chosen, as a homogenous and known material in which uniform distribution of strains and deformation are expected during the tensile tests, in order to provide a reference for the results obtained from other materials. Shear bond tests are performed on GFRP-strengthened masonry bricks. The surface deformations and strains in both types of tests are determined with the DIC method.

Tensile test specimens have 450 mm length and 40 mm width, see Figure 6-2. The aluminum plate has a thickness of 2 mm. Three specimens from each material are prepared and tested. Single-lap shear bond tests are performed on GFRP-strengthened brick specimens. The material properties and procedure for preparation of the specimens can be found in Chapter 3.

The test setup used for performing the tensile tests is shown in Figure 6-3 (a). The tests are performed using a universal testing machine with maximum load capacity of 200 kN under displacement control conditions. The specimens are pulled monotonically with a constant velocity of 2 mm/min corresponding to a mean strain rate, $\dot{\varepsilon}$, of 7.5×10^{-5} s^{-1}.

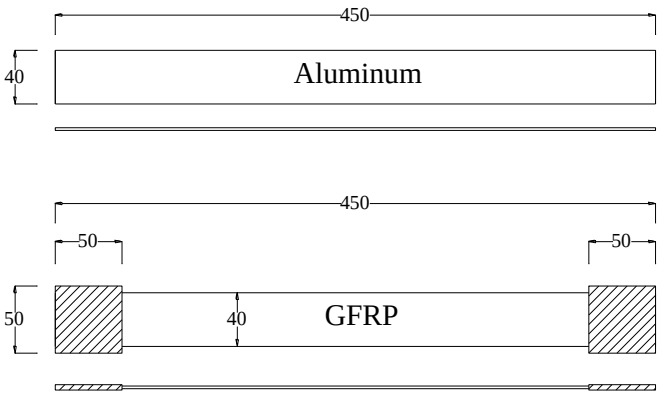

Figure 6-2: Details of the tensile specimens (dimensions in mm).

A testing apparatus with maximum load capacity of 50 kN is used for conducting the single-lap shear bond tests, see Figure 6-3 (b). A supporting frame is used to support the specimens appropriately and avoid misalignments in the load application. The specimens are pulled monotonically, under displacement control, with a velocity of 0.3 mm/min. The resulting load is measured by means of a load cell. The global slip between the GFRP and the masonry substrate is measured by means of two LVDTs mounted at the loaded end.

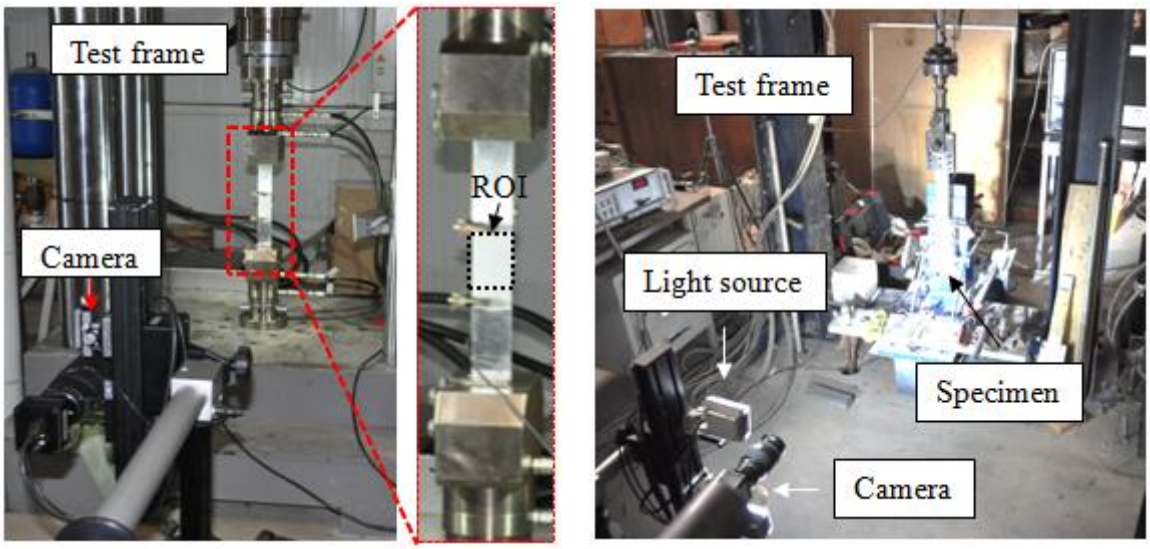

(a) (b)

Figure 6-3: Tests setup: (a) tensile tests; (b) shear bond tests.

6.1.4 Results and discussion

6.1.4.1 Tensile tests

The typical load-displacement behavior of the aluminum plates together with the longitudinal strain distributions measured with the DIC technique are shown in Figure 6-4. Uniform distribution of strains in the ROI can be observed, as expected. This uniformity can be observed clearly in Figure 6-5 where the distribution of strains along a longitudinal and a transverse section on the ROI is presented. The evolution of strains with the load increase and their uniform distribution along the specimen's length and width can be observed. The elastic modulus of the aluminum plate is obtained as the initial slope of the stress-strain curve (from DIC measurements) equal to 60 GPa. The measured strain rate with the DIC technique is 7.5×10^{-5} s^{-1} equal to the applied strain rate during the tests, being an evidence of the measurements accuracy and suitability of the applied speckle pattern and solution algorithms.

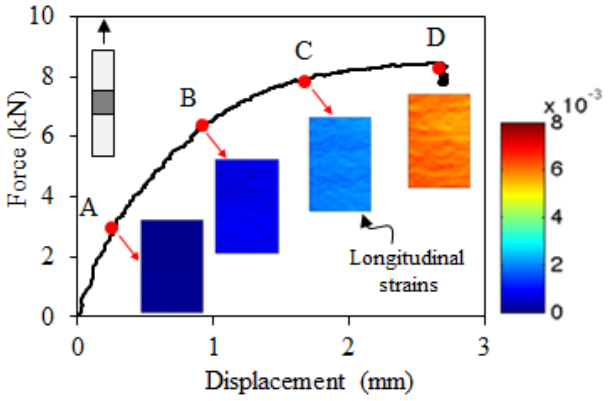

Figure 6-4: Tensile behavior of the aluminum plate
(force-displacement diagram and strains in the ROI).

The typical tensile load-displacement behavior of GFRP coupons together with the longitudinal strain distributions measured with the DIC technique are shown in Figure 6-6. The GFRP coupons show a linear behavior until failure, as expected. It can be observed that the distribution of strains along the GFRP coupon is not as uniform as the aluminum plate. The distribution of longitudinal, ε_x, and transverse strains, ε_y, is presented in Figure 6-7 at two different sections in the ROI for one tested specimen. Large fluctuations of longitudinal and transverse strains can be observed. The non-uniform distribution of fibers and matrix along the specimen's length and width, commonly observed in wet lay-up procedures, can produce such a complex distribution of strains. Moreover, imperfections due to application procedure together with the non-homogenous nature of this composite material can result in the observed strain localizations and fluctuations [274]. This observation becomes clearer when comparing the strains obtained in the

aluminum plate and the GFRP coupon at the same load level, see Figure 6-8. On the other hand, large transversal strains are found in the GFRP specimen, which makes the stress states and failure complex. The observed strain fluctuations and large transversal strains can affect the bond behavior between the GFRP sheet and masonry substrate in strengthened masonry elements, and this should be considered in the interpretation of experimental results. The variation of strains along the specimen's width and length shows that the use of local measurement instruments such as strain gauges may lead to inappropriate observations and conclusions. The elastic modulus of GFRP is obtained as the initial slope of the stress-strain curve equal to 75 GPa. The measured strain rate with the DIC technique is again 7.5×10^{-5} s^{-1} equal to the applied strain rate during the tests, showing the accuracy of the measurements.

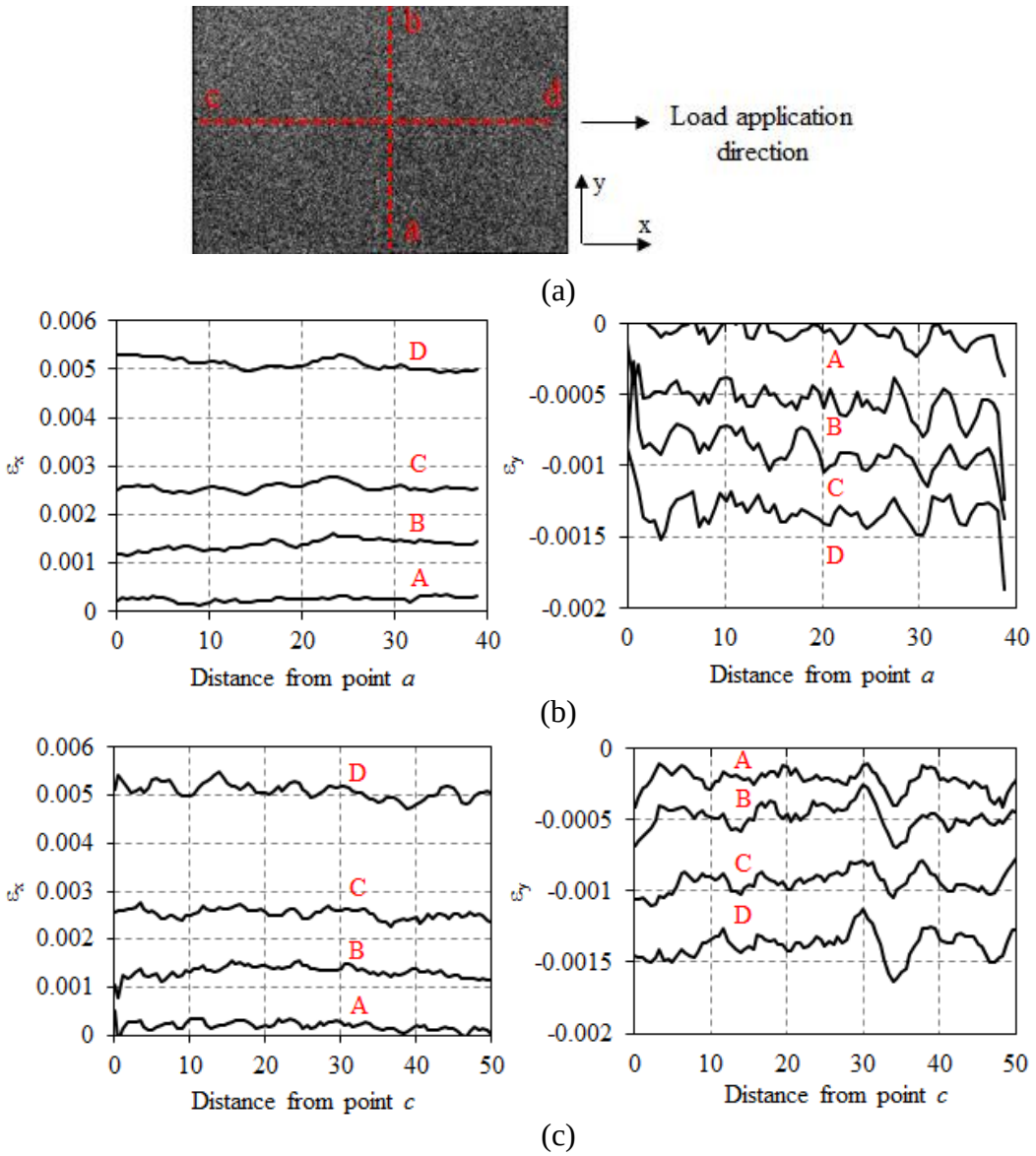

Figure 6-5: Strain profiles in the aluminum plate for different load levels (A to D in Figure 6-4): (a) speckle pattern; (b) strain profiles along line a-b; (c) strain profiles along line c-d.

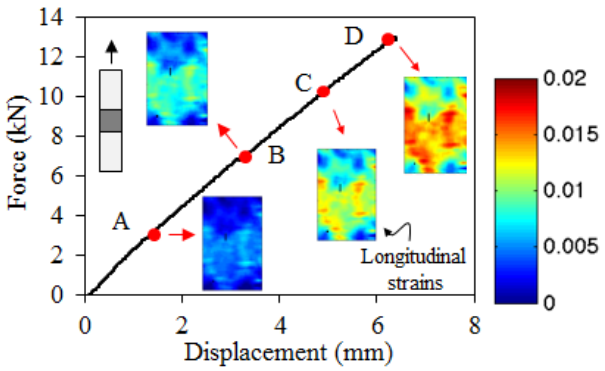

Figure 6-6: Tensile behavior of the GFRP (force-displacement diagram and strains in the ROI).

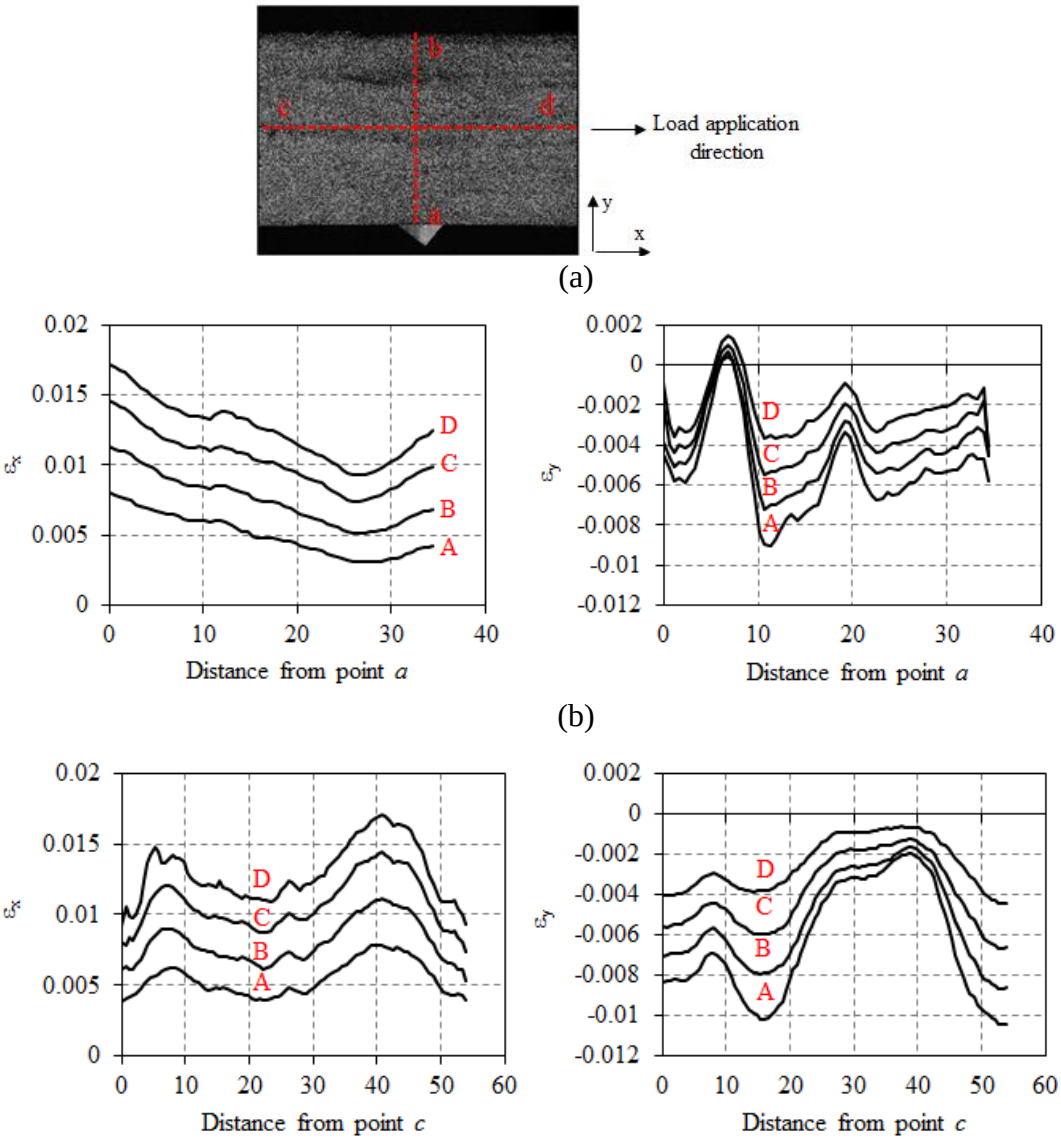

Figure 6-7: Strain profiles in the GFRP coupon at different load levels (A to D in Figure 6-6): (a) speckle pattern; (b) strain profiles along line a-b; (c) strain profiles along line c-d.

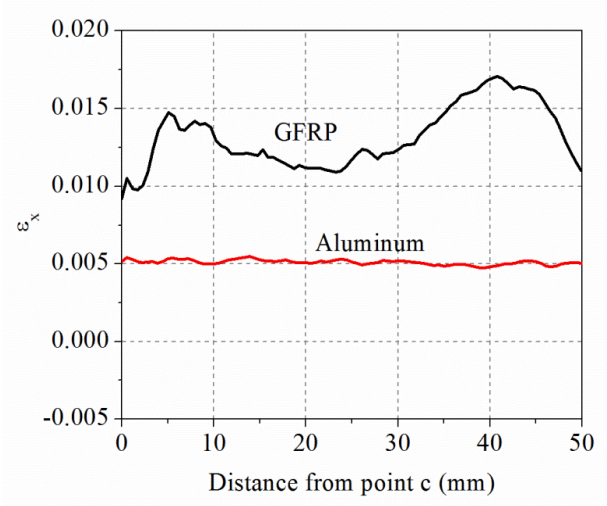

Figure 6-8: Comparison of longitudinal strains along section c-d between GFRP coupon and aluminum plate close to failure (load level D).

6.1.4.2 Debonding tests

The typical force-slip response obtained from experimental tests is shown in Figure 6-9. The distribution and evolution of strains with load increment along the bonded length, determined from the DIC measurements, is presented in Figure 6-10.

The longitudinal strains profiles are shown in Figure 6-11 (b, c) at the FRP middle and edge sections, respectively. It can be observed that the strain distributions are different in these two sections, due to the boundary conditions [275]. Moreover, significant transversal strains appear near the loaded end at high load levels, see Figure 6-11 (d). These observations confirm experimentally the three-dimensional nature of the debonding phenomenon, which is commonly neglected in design procedures and in the discussion of experimental results. It can be observed that the strain values increase suddenly moving forward from point C to D which is due to the initiation of debonding and crack propagation along the FRP bonded length. This is also observable in the force-slip diagram, Figure 6-9, where the stiffness changes at point C. The observed fluctuations in the strain profiles can be partly attributed to the variation of the material properties and bond imperfections.

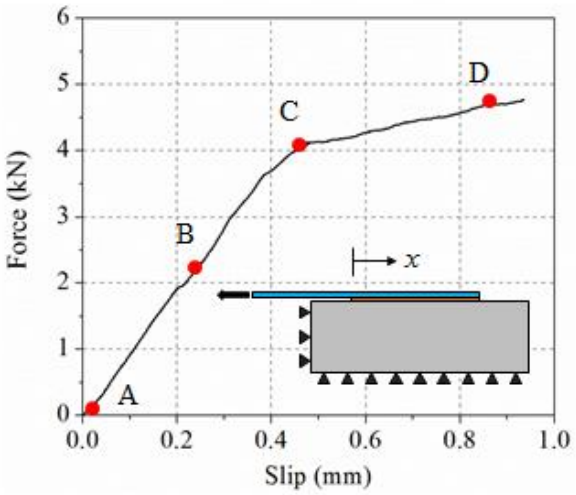

Figure 6-9: Typical force-slip behavior of GFRP-strengthened specimen.

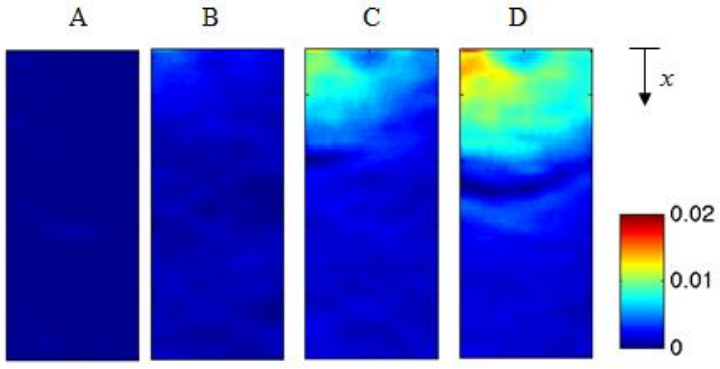

(a)

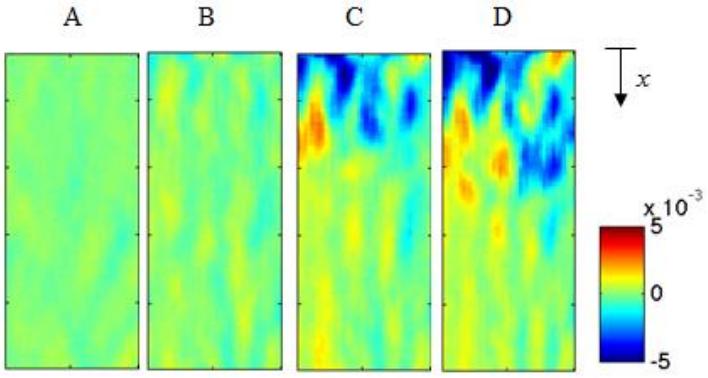

(b)

Figure 6-10: Distribution of strains along the bonded area at different load levels (A to D in Figure 6-9): (a) longitudinal strains; (b) transversal strains.

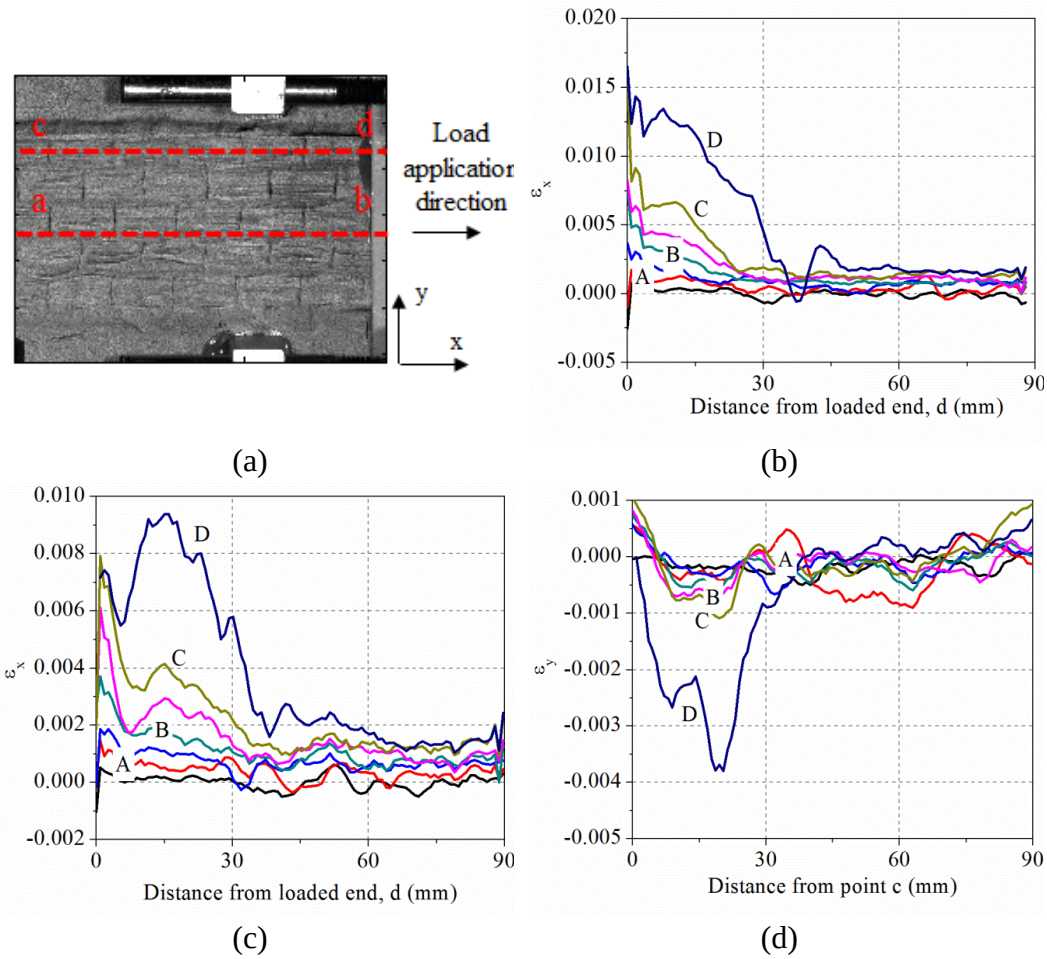

Figure 6-11: Strain profiles in GFRP-strengthened brick specimen: (a) speckle pattern; (b) longitudinal strains along section a-b; (c) longitudinal strains along section c-d; (d) transversal strains along section c-d.

An important parameter that can be obtained from the strain profiles is the effective bond length l_e, defined as the length in which the stresses are fully transferred from the FRP composite to the substrate (i.e. the minimum length to achieve the maximum load) [48]. After the effective bond length, the strain values are negligible and therefore no stresses are transferred to the masonry. For obtaining the effective bond length, the average strain profile at failure (point D in Figure 6-9) is determined, see Figure 6-12, by averaging the strain values over a 10 mm width strip at the middle of the FRP sheet. The average values are used in order to reduce the effect of material variations [48] and it is observed that the effective bond length obtained is not sensitive to the averaging width, as 5, 10 and 15 mm widths were tested. The strain distribution is then approximated with a nonlinear expression by performing regression analysis. It is observed that an expression with the following type can suitably simulate the strain distributions along the bonded length:

$$\varepsilon(x) = A_2 + \frac{A_1 - A_2}{1 + (\frac{x}{x_0})^p} \tag{6.2}$$

where A_2, A_1, x_0, p are the constants to be determined from experimental results and x is the distance from the loaded end. The predicted strain distribution is shown with a solid line in Figure 6-12. It can be seen that the bonded area consists of three main regions, as also observed in [48]. The FRP is fully debonded from the substrate near the loaded end. This is followed by a stress transfer zone, and after that no stress is transferred to the substrate. The length of the stress transfer zone, about 30 mm in this case (average of three tests), is then the effective bond length.

Finally, it is noted that the bond-slip laws in longitudinal and transversal directions can be obtained from the strain profiles [226]. The local bond stress-slip (τ–s) curves can obtained from the experimental strain profiles measured along the FRP reinforcement at different load levels. In fact, the bond stress distribution within the bonded length can be evaluated by imposing the equilibrium condition of a FRP strip with a length *dx* bonded to masonry, assuming an elastic behavior of the reinforcement, as:

$$\tau(x) = t_f E_f \frac{d\varepsilon_f}{dx} \tag{6.3}$$

where $d\varepsilon_f / dx$ is the gradient of FRP strain along the sheet length, E_f is the FRP elastic modulus, and t_f is the FRP thickness. Moreover, the slip at distance *x* from the free end of the specimen can be calculated assuming a zero slip in the free end as:

$$s(x) = \int \varepsilon_f dx \tag{6.4}$$

The local bond-slip behavior of the specimens near the loaded end is obtained by means of Eqs. (6.3) and (6.4) using the strain distributions obtained from the DIC measurements, see Figure 6-13. For this reason, the strain profiles obtained from DIC measurements are approximated with the same nonlinear model for different load levels, Figure 6-12. Then, the obtained mathematical formulation for each load level is used in Eqs. (6.3) and (6.4) for calculating the spatial value of shear stress and slip. For obtaining an average bond-slip behavior, the values are presented for 10, 15, 18, and 20 mm distances from the loaded end. It can be seen that the bond-slip curve follows a tri-linear trend with a plastic branch in the middle, solid line depicted in Figure 6-13. The tri-linear bond-slip behavior observed here has also been proposed for FRP-strengthened brick specimens in [226].

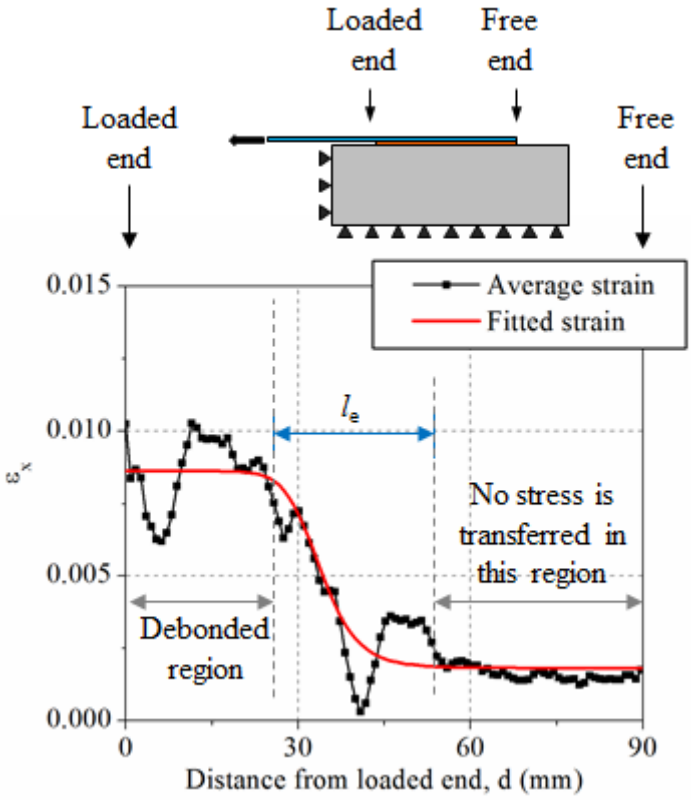

Figure 6-12: Average longitudinal strain along FRP middle section (sec. a-b in Figure 6-11) and the effective bond length l_e.

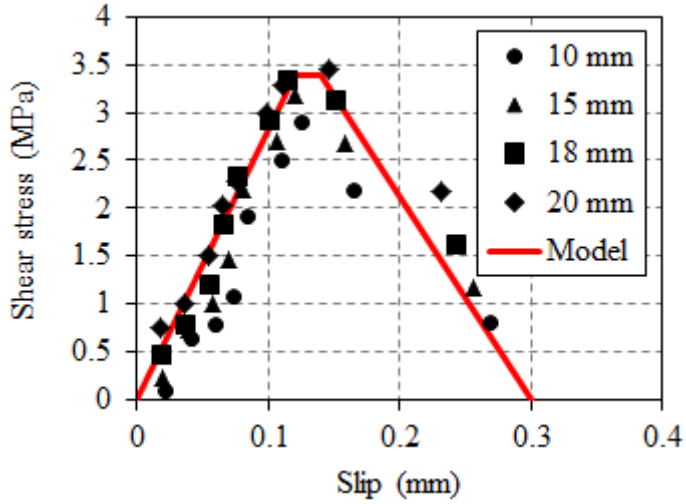

Figure 6-13: Bond-slip behavior of GFRP-strengthened brick.

6.2 Acoustic emission technique

6.2.1 Principles

Acoustic Emissions (AEs) are high-frequency transient elastic waves that are emitted within the material during local stress redistributions such as micro-crack growth. These emissions are detected on the material's surface by means of piezoelectric transducers, pre-amplified, filtered and amplified before being sent to the data logger. The technique has the advantage over other damage detection techniques that it relies on detection of information which is generated by the fracture process itself and allows for on-line damage detection and assessment [276].

A typical AE transient event is presented in Figure 6-14. Background noise is eliminated through setting a minimum amplitude threshold. An AE hit with a predefined duration is recorded when the threshold is exceeded. For each AE hit, a number of parameters (e.g. arrival time, amplitude, count, duration and energy) and the waveform itself are recorded. The amount of detected AE hits and energy is influenced by the hardware used and software settings, thus software defined parameters (e.g. threshold and sampling frequency) should be kept constant for subsequent tests. The detection of acoustic emissions is also sensitive to a number of setup-specific boundary conditions, such as quality of the coupling between sensor and test specimen, attenuation and speed of wave propagation, source-sensor distance, specimen size and homogeneity.

The recorded acoustic emissions hold information on the fracture process that produced them. Basic AE hit counting, taking into account the cumulative or average number of AE hits, or emitted AE energy, has successfully been used for damage assessment in rock, concrete and masonry [240, 277]. Other wave properties, such as amplitude or number of threshold crossings (counts) are also used for parameter-based analysis [240, 278]. It is generally observed that micro-cracks generate a large amount of small amplitude emissions, while AE emissions from macro-cracks are fewer but have higher amplitude. Based on this observation, the b-value is applied in seismic analysis to characterize the fracture process by means of the slope of the amplitude distribution. Instead of the seismic b-value, an improved b-value (Ib-value), in which the number of AE data taken into account is set before calculation, is usually applied for AE applications in concrete and rock [279, 280].

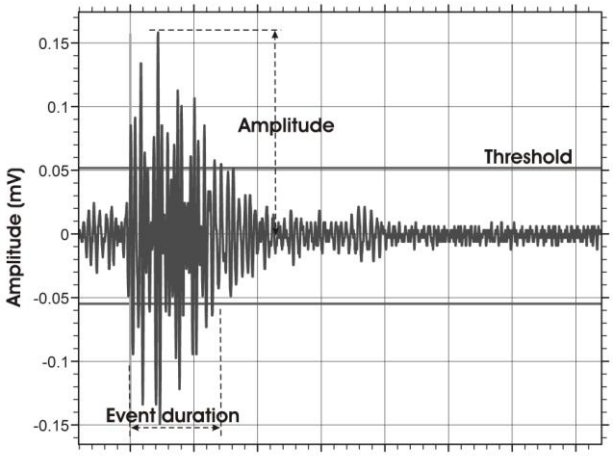

Figure 6-14: Typical AE transient event with indication of wave characteristics.

More advanced signal-based analysis takes into account the complete AE signal allowing characterization of the fracture modes [240, 281]. High sampling rates and the use of broadband AE sensors are required for this technique. But dedicated signal processing and interpretation can become time-consuming for large data sets. Signal-based analysis has limited application in concrete and masonry, due to the high attenuation and disturbance of the AE wave caused by the heterogeneity of the material, especially in case of masonry. As a compromise between both approaches, a simplified signal-based analysis can be applied, using the RA value and frequency to characterize the fracture process. The RA value is calculated from the ratio of the rise time (time interval between triggering time of AE signal and maximum amplitude) and the maximum amplitude. Lower average frequencies and higher RA values indicate a shift from tensile to shear nature of fracture processes [282, 283]. Recent numerical and experimental studies have shown that the reliability of crack classification depends on the homogeneity of the material and the distance between source and sensor [284]. Heterogeneities, such as aggregates in concrete, nucleation of cracks or brick-mortar interfaces in masonry, cause dispersion and consequently alteration of the waveform. As masonry is a highly heterogeneous material, crack characterization should be performed carefully taking into account these issues.

Next, it is shown that average and cumulative AE energy can be applied to characterize debonding phenomenon in strengthened masonry bricks when a limited number of resonance AE sensors are used.

6.2.2 Experimental plan

The experimental study focuses on detection of the interfacial damage during debonding in strengthened masonry bricks by means of the AE technique. The effect of environmental conditions

on the bond fracture process and failure mode is also investigated by performing accelerated ageing tests. Single-lap shear bond tests are performed, before and after environmental exposure, for characterization of the bond behavior. Six specimens in total are tested with AE detection, being three reference specimens and three aged specimens. Specimens' geometry and preparation procedure can be found in Chapter 3. The aged specimens are exposed to 180 cycles of exposure HT2 (temperature cycles of +10°C to +50°C with 60% constant relative humidity), see Chapter 3.

The test setup and procedure for debonding test is explained in Chapter 3, see Figure 6-15. Acoustic emissions were monitored using a 4-channel Vallen AMSY-5 system with 150-500 kHz operation frequency and 5 MHz sampling rate. Four 150 kHz resonance sensors were attached to opposite sides of the bricks by means of hot melt glue, see Figure 6-15 (b). The preamplifier gain was set to 34 dB with a fixed threshold level of 40 dB and pencil lead breaks were used for system calibration [285]. To calculate the AE energy, the AE signal is squared and integrated (the energy unit (eu) is given by $1eu = 10^{-14}V^2s$).

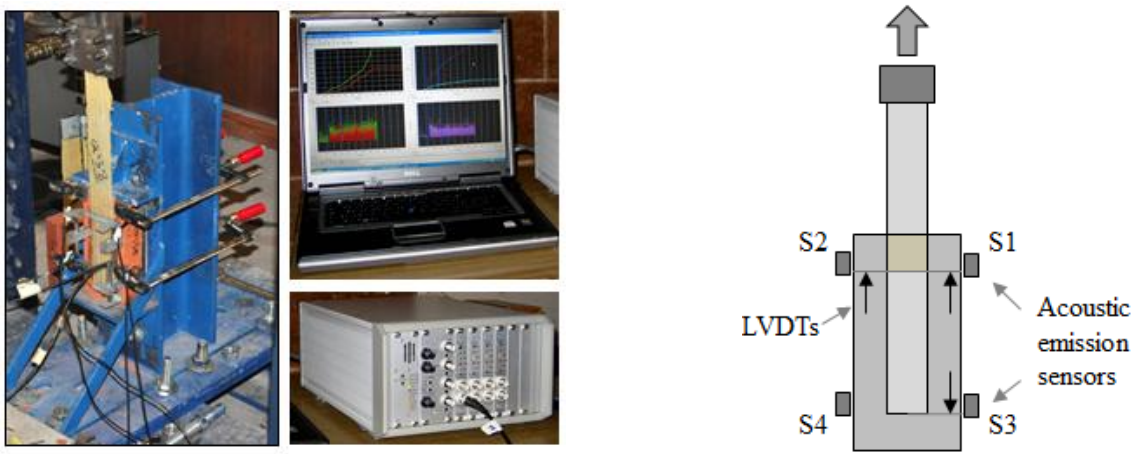

(a) (b)

Figure 6-15: (a) Test setup; (b) test instrumentation.

6.2.3 Results and discussion

6.2.3.1 Debonding behavior

The envelope of the force-slip curves obtained from the experimental tests is shown in Figure 6-16 for the reference and aged specimens. A slight 6% reduction of the average maximum debonding force can be observed in the specimens after exposure to environmental conditions. The initial bond stiffness, defined as the initial slope of the force-slip curves, does not show any relevant change. However, due to the small number of tests and short exposure period, no definitive conclusions can be made about the degradation of the specimens at this stage. The average debonding force for the

reference specimens is 10.0 kN (CoV = 5.3 %), while this value for the aged specimens is 9.4 kN (CoV = 20.6 %).

In terms of failure mode, a change from cohesive failure to adhesive failure is observed in the GFRP-brick specimens. The observed failure modes in the reference specimens are cohesive failure with fracture inside the brick (1 specimen) or a combination of cohesive/adhesive failure (2 specimens), see Figure 6-17 (a, b). The cohesive fracture occurred in a relatively deep layer of the brick (around 10 mm). Moreover, the contribution of the adhesive failure in the specimens with mixed failure mode was relatively small (around 20% of the bonded area). On the other hand, the failure mode in the aged specimens is predominantly adhesive. The fracture surface is at the FRP/brick interface (all three specimens), see Figure 6-17 (c). The adhesive failure is combined with detachment of a brick bulb at the free end in two specimens, see Figure 6-17 (d). The observed change of failure mode after exposure to hygrothermal conditions can be attributed to the degradation of interface properties due to thermal incompatibility problem and induced thermal fatigue on the specimens [91].

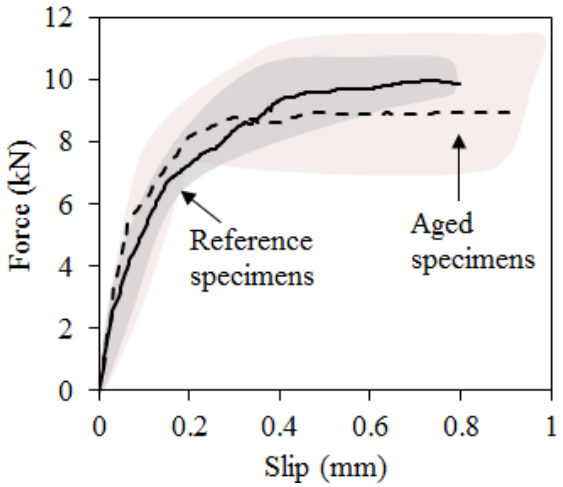

Figure 6-16: Envelope of experimental force-slip behavior in the reference and aged specimens.

(a) (b) (c) (d)

Figure 6-17: Observed failure modes: (a) cohesive; (b) cohesive-adhesive; (c) adhesive at the FRP/brick interface; (d) adhesive with a brick bulb at the free end.

6.2.3.2 Characterization of damage by means of AE output

Typical AE results obtained from the debonding tests on GFRP-strengthened brick specimens are shown in Figure 6-18. The results are presented for a reference specimen with mixed cohesive/adhesive failure mode, in terms of cumulative AE energy and hits together with the force and slip development during the tests. The cumulative AE energy to hit ratio, called *E*/*h* hereafter, is also investigated and the results are presented.

Generally, the debonding phenomenon can be divided into three main regions: elastic range, micro-cracking range, macro-cracking and fracture range. In the elastic range, the system deforms without any crack generation and AE activities. The displacement measured at this stage is small being due to the elastic deformation of the FRP composite. As the applied force increases, micro-cracks appear in the interfacial region and they can be distinguished by initiation of AE activity with low emitted energies, e.g. after 100 sec of the test in Figure 6-18 (a, b). Since the fracture energy release due to the formation of micro-cracks is relatively small, low values of AE energies are expected in this region, see Figure 6-18 (a). The rate of detected AE hits is higher than the AE energy rate at this stage, resulting in a descending E/h, which indicates the formation of micro-cracks, see Figure 6-18 (c). As the debonding progresses, macro-cracks are formed and propagated along the interface with higher fracture energy being released. Therefore, higher AE energy is detected in this region. The cumulative AE energy increases with a stepwise pattern in which each sudden jump of energy can be correlated to a sudden fracture energy release and can thus be attributed to macro-fracture events, see Figure 6-18 (a, d). A sudden release of a high amount of AE energy can also be observed at the moment of full debonding, coinciding with the end of the test. The *E*/*h* ratio, Figure 6-18 (c), shows that each stage of the progressive debonding starts with a high rate of energy release (observed as a sudden jump in the *E*/*h* curve) and continues with a descending rate until the end of each stage. The sudden jumps in *E*/*h* curve, in macro-fracture range, are due to the formation of macro-cracks with high energy release. Figure 6-18 (d) shows a clear correlation between slip increment and cumulative AE energy. This correlation can be used for predicting the FRP slip or debonding fracture energy in FRP-strengthened masonry elements, as will be explained in Sec. 6.3.3.4.

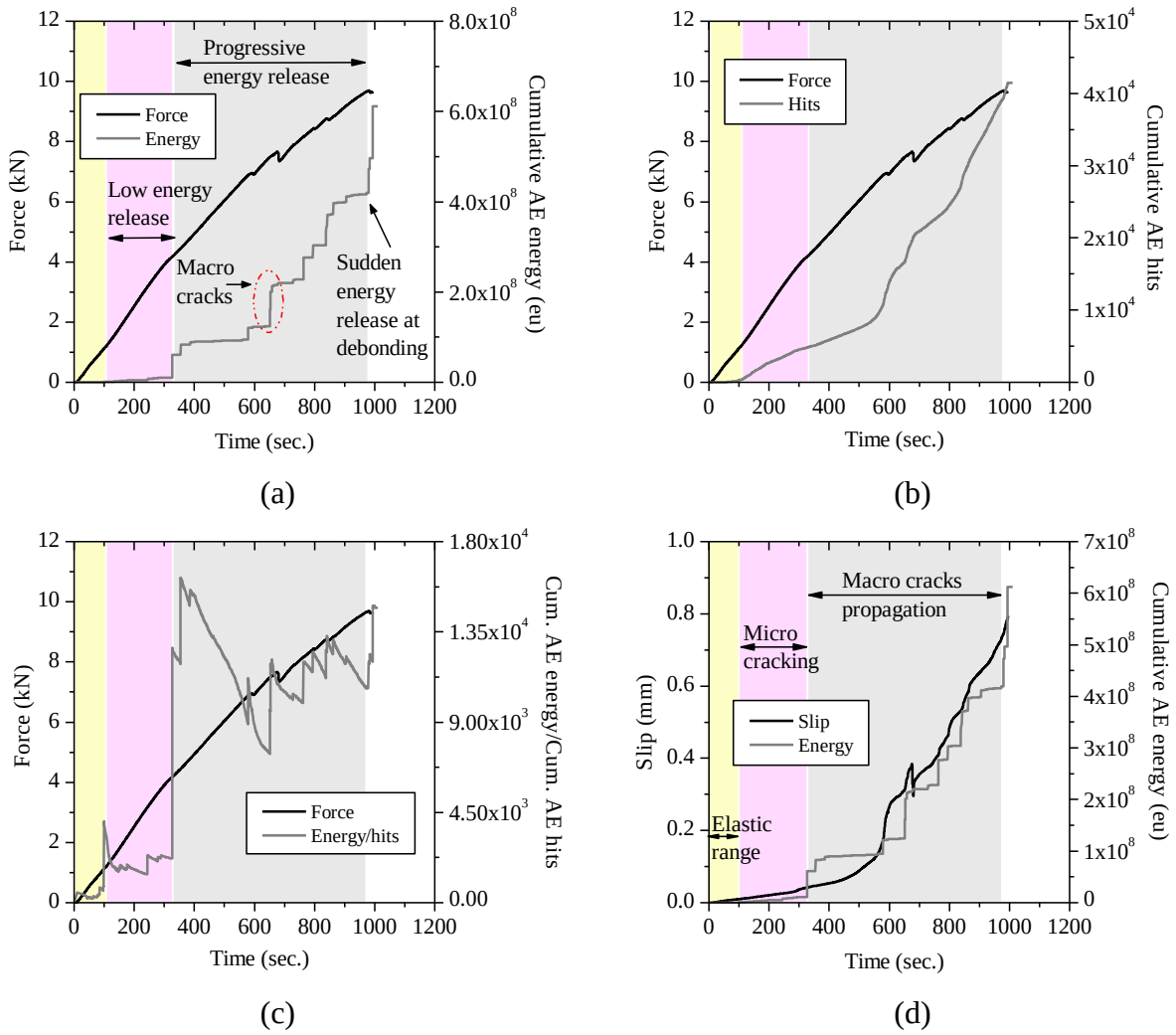

Figure 6-18: Typical AE results in reference specimens: (a) force-cumulative AE energy; (b) force-cumulative AE hits; (c) force-energy/hits, E/h; (d) slip-cumulative AE energy.

The effect of failure mode on the AE outputs is investigated in Figure 6-19. A clear distinction is found between AE outputs of specimens with different failure modes. It can be observed that in the specimen with cohesive debonding the AE energy remains relatively low throughout the test, accompanied by a sudden and large amount of AE energy release and increase of *E*/*h* ratio when the debonding occurs at the end of the test, see Figure 6-19 (a). The observed behavior confirms the brittle and sudden nature of the cohesive debonding. Fewer peaks are observed in the *E*/*h* curve compared to the specimen with cohesive/adhesive debonding. At the end, a macro-crack with a high amount of energy release has suddenly occurred, leading to the complete debonding of the FRP. On the contrary, in the specimen with cohesive/adhesive failure a progressive release of energy is observed during the test. The high rate of energy detection shows the high number of active cracks and progressive failure during the tests. In the specimen with adhesive debonding mode, Figure 6-19 (b), increasing detection of AE energy is observed until the

complete debonding. However, the magnitude of the detected energy is much lower than the ones detected in the specimens with cohesive failure mode. This large difference is due to the different nature and fracture properties of brick and FRP/brick interface. The specimen with adhesive failure combined with formation of a brick bulb at the free end shows a similar AE energy emission similar to the specimen with pure adhesive failure. However, a large amount of energy is released in this specimen before debonding due to the brick bulb fracture at the free end.

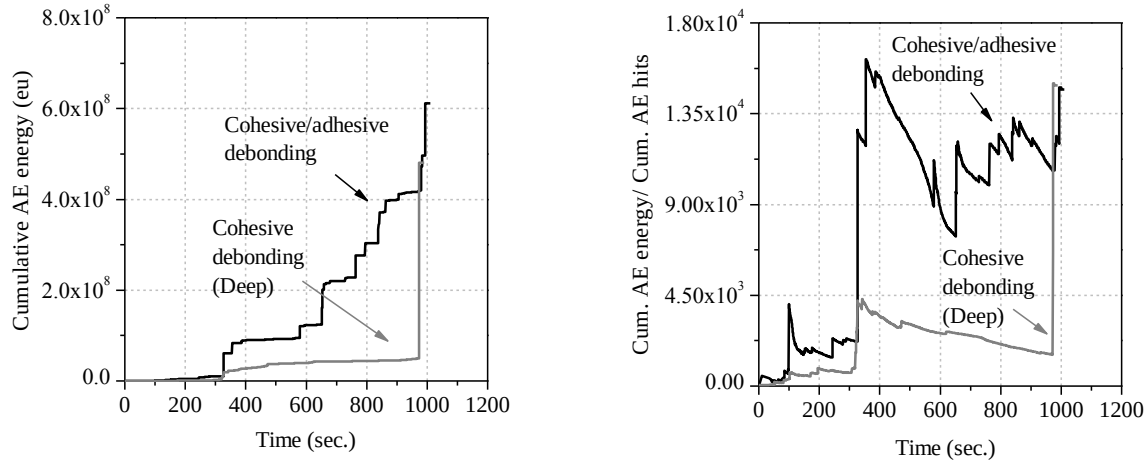

(a)

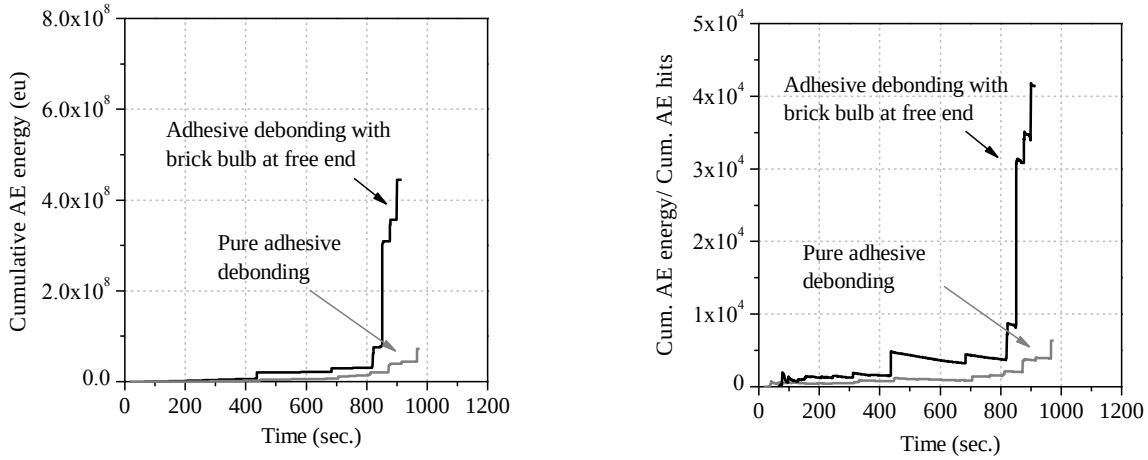

(b)

Figure 6-19: Comparison of different failure modes: (a) cohesive; (b) adhesive.

6.2.3.3 Remarks on other methods for failure characterization analysis

In the previous section, the AE energy release rate was used for failure mode analysis and a correlation was found between the AE energy outputs and the debonding behavior. As indicated in before, other methodologies have been developed in the literature for discrimination between different fracture modes and may be of interest in debonding tests. A review of the applicability of these methods is presented and discussed in this section. RA value and frequency analysis are not

carried out for the presented data. The reason is that the tests were performed with resonance sensors and the test specimens were not isotropic. Distortion of the frequency spectra and of the waveforms strongly affects the accuracy of the results in these analysis techniques.

An Ib-value (Improved b-value) analysis is performed on the obtained data from AE detection. The Ib-value is the ratio between weak (low amplitude, micro-cracking) and strong (high amplitude, macro-cracking) events. It is calculated as the slope of the cumulative distribution of the amplitudes of a preset number of hits. In general, the fracture shifts from micro- to macro-cracking upon monotonic stress increase and the Ib-value decreases. The graphs presented in Figure 6-20 are calculated according to the formula proposed by Shiotani [279] and applied e.g. by Aggelis [282]:

$$Ib = \frac{\log_{10} N(\mu - \alpha_1.\sigma) - \log_{10} N(\mu + \alpha_2.\sigma)}{(\alpha_1 + \alpha_2).\sigma} \quad (6.5)$$

here, σ is the standard deviation and μ is the mean value of the amplitudes of a group of AE hits. Usually, a group of 50 or 100 hits is chosen (the latter is chosen here). The Ib-value is updated after every 10 new hits and α_1 and α_2 are constants related to the minimum and maximum amplitude level. For each subsequent group of AE hits, the cumulative amplitude distribution is applied and the logarithm of the cumulative value corresponding to the lower and upper amplitude values (μ-$\alpha_1\sigma$) and (μ+ $\alpha_2\sigma$) is taken.

Figure 6-20 presents the evolution of the Ib-value calculated for the GFRP-strengthened brick specimens with different failure modes. In general, the graphs have many peaks and the average Ib-value does not decrease towards the end of the test as is generally observed in compression and bending tests [282]. This can be explained by the nature of the fracture process under analysis, which is not a general shift from micro to macro-cracking. Since the bonded area fails progressively, a sequence of stress buildup (micro-cracking) and debonding (macro-cracking) occurs. This results in high and low amplitude hits occurring almost at equal density throughout the test.

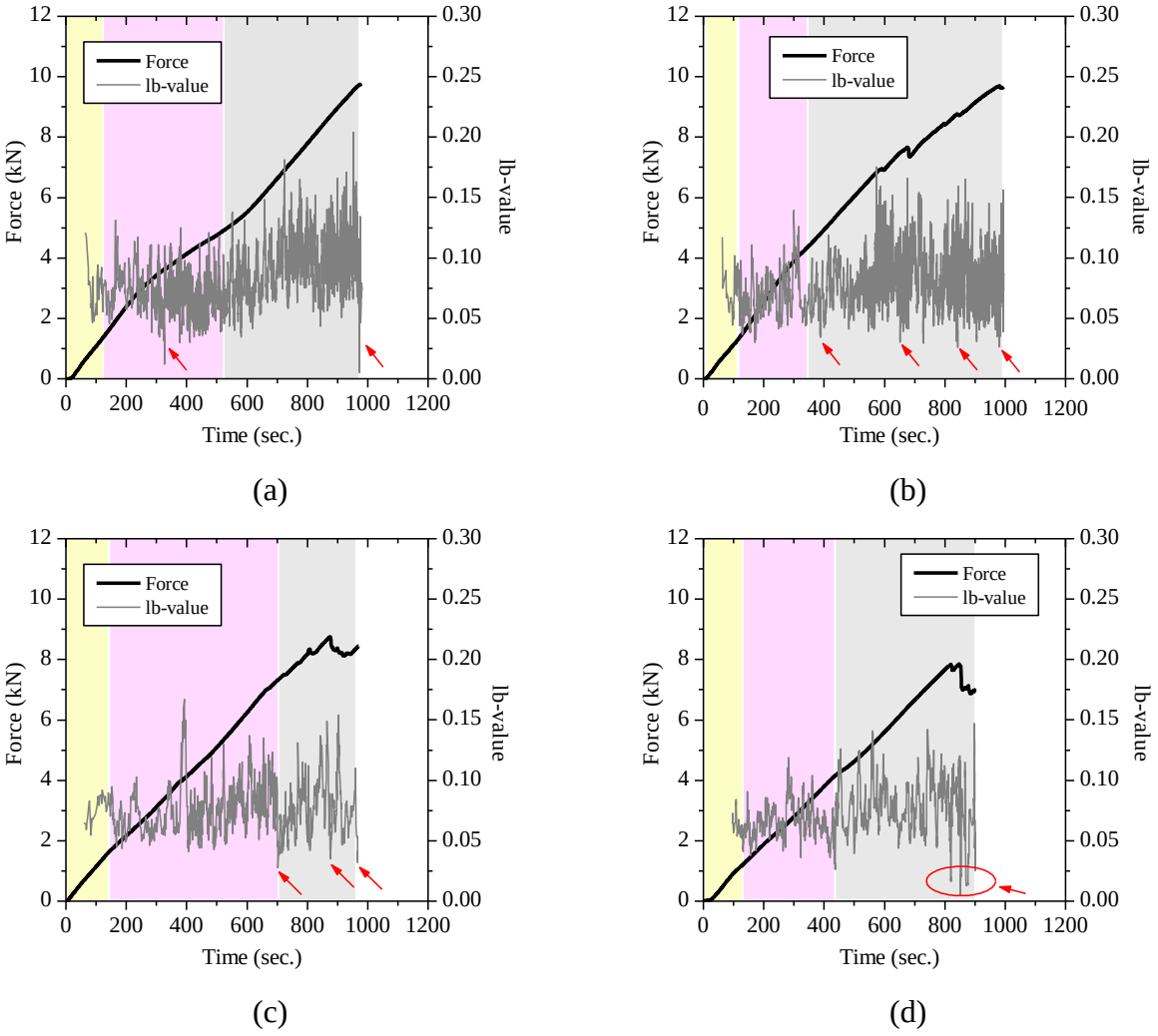

Figure 6-20: Ib-value analysis for different failure modes (a) cohesive; (b) cohesive/adhesive; (c) adhesive; (d) adhesive with brick bulb.

In the specimen with cohesive failure, Figure 6-20(a), the macro-cracks are accompanied by a sudden decrease in the Ib-value as expected. The lb-value trend shows that this failure mode is accompanied by few large cracks and sudden release of energy at the debonding moment. The lb-value in the cohesive/adhesive failure, Figure 6-20 (b), presents many drops during the test showing that the active failure is a combination of macro- and micro-fracture. The debonding has occurred with a progressive formation of large and small cracks. Although macro-fractures are distinguishable during the test, a decreasing trend in average lb-value is not observed, similar to the specimen with cohesive failure. In the specimen with adhesive failure, see Figure 6-20 (c), a decrease in the average lb-value can be observed when moving from the micro- to the macro-cracking range. The observed drops in the lb-value in macro-fracture range confirm the progressive nature and fracture release in this failure mode. The formation of the brick bulb at the free end is also observable at the end of the test in the other specimen, Figure 6-20 (d).

Although the micro- and macro-fracture can be distinguished from the lb-value analysis, the results are not very clear due to the large number of observed peaks and the fact that no general decreasing trend can be observed. For fracture mode characterization, the technique shows limited added value for short-term debonding tests as performed in this research. The technique can be of more interest during long-term debonding tests as the occurrence of macro-cracking might be more rare and alternated with long periods of no or only weak AE activity. On the contrary, the AE energy rate analysis, as presented in the previous section, was shown to be a valuable tool for characterizing the debonding phenomenon in FRP-strengthened masonry.

6.2.3.4 Modeling bond parameters with AE outputs

The experimental results showed that the released fracture energy during the debonding phenomenon can be correlated with the total emitted AE energy. Moreover, it was observed that the AE energy rate shows a trend similar to the FRP slip in FRP-strengthened brick specimens. In this regard, presenting a relation between these bond parameters and the AE outputs can be interesting for numerical modeling or structural health monitoring purposes. In this section, these relations are obtained from the experimental tests. Proposing a comprehensive relation between AE outputs and debonding parameters requires an extensive experimental program and thus the observations reported here can be seen as a first step towards this aim.

Figure 6-21 presents the FRP global slip in GFRP-strengthened specimens and the cumulative AE energy. A regression analysis is performed for obtaining a relation between the FRP slip and the AE energy. Since the fracture process, crack propagation and FRP slip change with the failure mode, different relations are proposed for adhesive and (mostly) cohesive debonding. For the adhesive failure, the results obtained from the only specimen with pure adhesive failure are considered in the analysis and the rest of the specimens are considered in the regression analysis for the (mostly) cohesive failure modes. A linear relation seems suitable for both failure modes (R^2=0.93 for adhesive failure and R^2=0.96 for cohesive failure). This relation can then be used as a new tool for obtaining the FRP slip in debonding tests or numerical modeling purposes.

The debonding fracture energy is an important parameter for numerical modeling of the bond behavior. This parameter is usually obtained from the experimental tests by using strain gauges [226]. It is also possible to obtain this parameter form the maximum debonding force as follows [1]:

$$G_f = \frac{P_{\max}^2}{b_f^2 (2E_f t_f)} \tag{6.6}$$

where, P_{max} is the debonding force, b_f is the FRP width, E_f is the FRP elastic modulus, and t_f is the FRP thickness. The fracture energy of the GFRP-strengthened specimens is obtained according to Eq (6.6) for different failure modes and is presented together with the corresponding total emitted AE energy in Table 6-2. Again, the value for the adhesive failure mode is obtained from the only specimen with pure adhesive failure, while the values presented for cohesive failure are the average of the specimens with (mostly) cohesive failure modes. It can be observed that the total emitted AE energy and the fracture energy in cohesive failure mode are much larger than in adhesive failure mode, as expected. However, obtaining an accurate relation between the fracture energy and AE emitted energy is not possible at this point due to the limited number of experimental results.

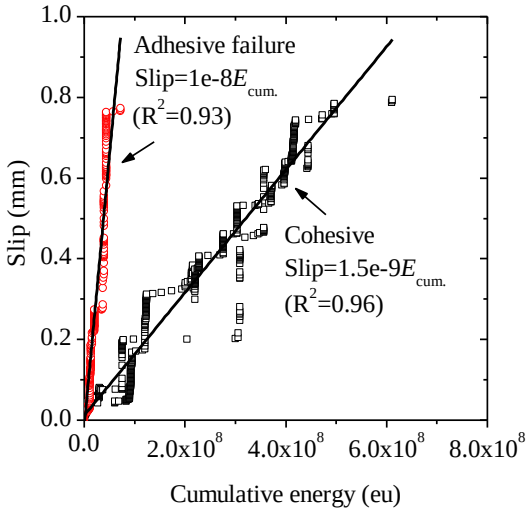

Figure 6-21: Correlations between slip and cumulative AE energy.

Table 6-2. Fracture energy and AE energy in different failure modes.

Failure mode	$G_{f\text{-ave.}}$ (N/mm)	$E_{cum.}$ (eu)
Cohesive	0.60	4.20E+08
Adhesive	0.40	7.20E+07

6.3 IR thermography technique

6.3.1 Principles

The IR thermography method has been extensively used in the last years for detection and evaluation of defects in FRP bonded components [230, 232, 233]. Applications are mostly focused on qualitative assessment and localization of the defects. However, once the defects are located, it is

interesting to characterize them quantitatively in order to evaluate the structure performance [234]. Infrared thermography methods can be divided into passive infrared thermography (PIT) and active infrared thermography (AIT) techniques. The difference between these two methods is that external surface heating is required in AIT, while the specimen itself is the source of temperature difference in PIT. In other words, in AIT, heat energy is applied to the specimen and the surface response to this energy is analyzed for localization and evaluation of the defects or material discontinuities. Alternatively, the surface temperature of the specimen at ambient conditions is monitored in PIT without application of any heat energy [234]. In both methods, any abnormal temperature profile on the surface is representative of a defect or flaw.

The main approaches used for surface external heating in AIT technique are pulse heating, step heating, and lock-in thermography [234]. In pulse heating method, a short burst of heat energy is applied to the specimen's surface and thermal images are captured during the surface cooling process. Step heating consists of application of lower intensity heat energy with a longer duration. In this technique, thermal imaging is conducted during the heating process. Finally, lock-in thermography is similar to the step heating process, however the applied heat energy is sinusoidal.

Pulse heating and lock-in thermography methods have been used more extensively for nondestructive evaluation purposes [286]. Each method has advantages and disadvantages. The main limitations of the pulse heating method are the area that can be uniformly heated and inspected, and the depth in which the defect can be detected. In the lock-in thermography method, larger areas can be inspected and defects at greater depths can be detected. However, each frequency of modulation is related to a special defect depth [286]. Therefore, for inspecting the specimens in their full depth, a range of exposure frequencies should be adopted, and this increases the number of required tests to a large extent. Since FRP delamination from the masonry substrate is interfacial, the pulse heating method has been used in this study. Fast and light heaters are available for practical applications, even if difficulties might arise in practical applications on very large structures (e.g. bridges) or rendered FRP applications. For non-rendered applications and for research purposes on the performance and durability of bond, no difficulties occur.

Generally, the adoption of the IR thermography technique for evaluation of bond quality is based on the fact that the heat flux is transmitted at different rates in materials with different thermal properties. In a FRP-strengthened element, any defect or delamination in the interfacial region changes the thermal properties in that area. Therefore, if a heat flux is applied to the surface of a FRP-bonded element, the heat is transferred with a different rate in the defected areas with respect to the perfectly bonded regions. This leads to the appearance of hot or cold spots in thermal images depending on the heat observation method [232]. Heat observation methods can be

categorized as reflection and transmission methods. In the reflection observation method, see Figure 6-22(a), the heat source and IR camera are placed at the same side of the specimen and the reflected heat from the specimen's surface is detected and captured as thermal images. In this method, defects appear as hot spots in the thermal images. Alternatively, the heat source and IR camera can be located in opposite sides of the specimen (transmission observation method) and the transmitted heat through the specimen's depth is measured on the surface under investigation, see Figure 6-22(b). In this method, the defects appear as cold spots in the thermal images. In the reflection observation method, higher resolution is obtained but the thickness of the material that can be investigated is small. The transmission observation method allows inspection of materials with larger thickness but the information through depth is lost [234]. The present study is focused on the use of reflection observation method in detecting interfacial delamination.

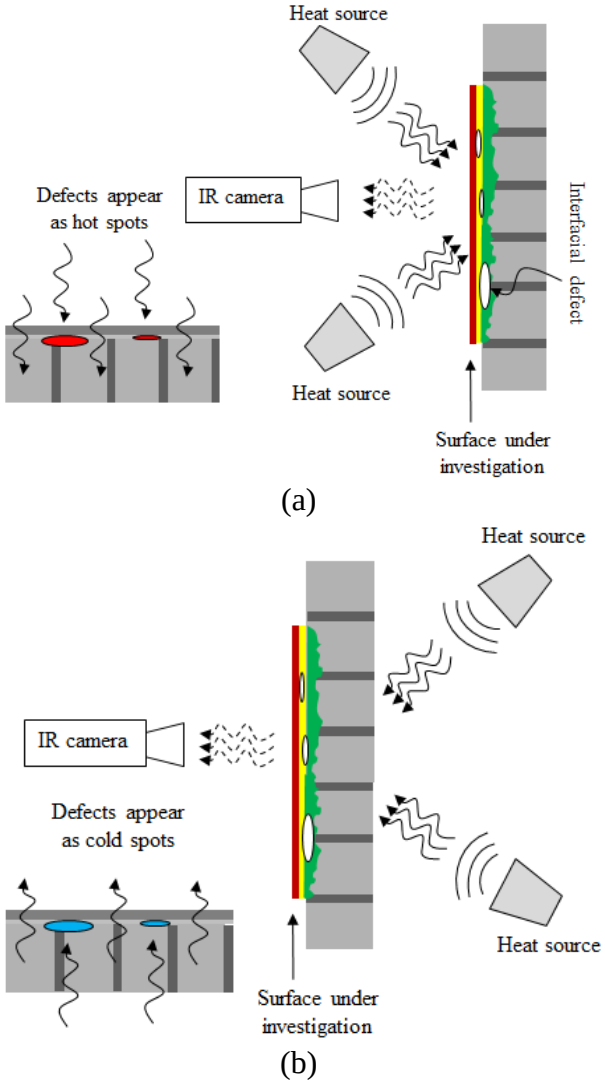

Figure 6-22: Different heat observation methods in IR thermography technique: (a) reflection observation method; (b) transmission observation method.

6.3.2 Quantitative IR thermography

In quantitative IR thermography, besides localization of defects or flaws, the physical characteristics of them, such as dimensions, depth and shape, can also be evaluated. Quantitative analysis can be performed following direct analytical methods or inverse methods [234, 287]. Since direct methods bring in much complexity to the analysis of the results, more attention has been devoted in the literature to inverse methods, see e.g. [230, 233].

As described before, in the pulse thermography technique some heat energy is applied to the specimen for a short period and sequential thermal images are taken from the surface during the cooling process. After application of the heat energy, the temperature decays with time and the resolution of the observed defects changes at different moments. For this reason, before application of any analytical algorithm for evaluating the physical properties of the defects, the selection of an appropriate thermogram with the best contrast and resolution is necessary to obtain the highest possible accuracy. It is usually considered that the most appropriate thermogram is the one with the maximum thermal contrast [230, 233]. Once the most appropriate thermogram is selected, the size of different defects can be estimated with an adequate algorithm. A simple inverse method called two-point inflection method has been selected here, as it was previously used for detection of flaws and defects in FRP-strengthened concrete elements with reasonable results in [233]. Details about these procedures are addressed next.

6.3.2.1 Maximum thermal contrast

Figure 6-23 shows a typical temperature history of a defect and a sound area obtained from IR thermography tests. The time corresponding to the maximum thermal contrast is defined as the time in which the temperature difference between the sound and defect area is maximum [234]. Therefore, the thermogram corresponding to the peak value of the difference curve should be selected for performing the quantitative analysis. The thermal contrast can also be defined as the differential temperature at the defect area normalized by the differential temperature at the sound area as follows [234]:

$$C(x,y,t) = \frac{\Delta T_{def}(x,y,t)}{\Delta T_{sound}(x,y,t)} = \frac{T_{def}(x,y,t) - T_{def}(x,y,t_0)}{T_{sound}(t) - T_{sound}(t_0)} \tag{6.7}$$

where, $C(x,y,t)$ is the thermal contrast at time t, $T_{def}(x,y,t)$ is the temperature at the defect area at time t, $T_{def}(x,y,t_0)$ is the initial temperature at the defect area, $T_{sound}(t)$ is the temperature at the sound area at time t, and $T_{sound}(t_0)$ is the initial temperature at the sound area. The maximum value of $C(x,y,t)$ is then defined as the maximum thermal contrast.

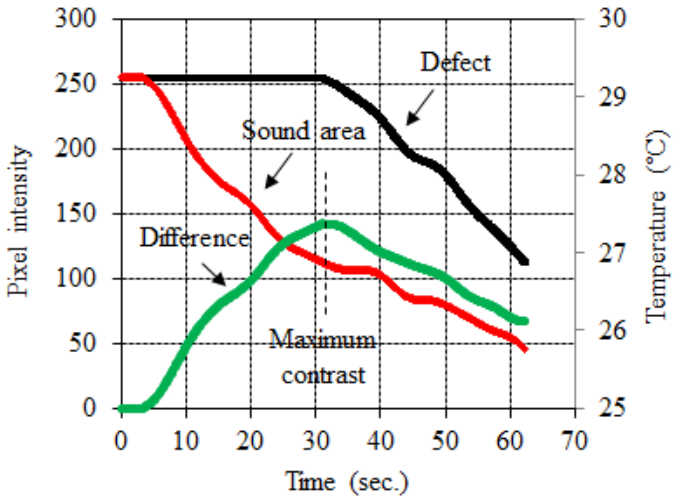

Figure 6-23: Thermal history curves of sound and delaminated areas.

6.3.2.2 Inflection point method

In this method it is assumed that the boundaries of the defects are the inflection points of a fourth order polynomial that is fitted through the temperature profile along the flaw [233]. Figure 6-24 shows the longitudinal and vertical temperature profiles of a defect in a sample thermogram. The temperature profile around the defect can be divided into two parts from its center point (left and right). Each part can be estimated with a fourth order polynomial and the inflection points are assumed to be the respective defect boundaries. The total length of the defect along the section under investigation can be obtained by measuring the distance between the two calculated boundaries, see Figure 6-25. To avoid dependency of the results on the defect's selected center point, each calculation is conducted three times considering a confidence level of 5% for the center point selection. In other words, the center point is moved 5% forward and backward and the calculations are repeated. The results are then presented as the average value of three boundary locations obtained for each zone. It is noted that the approximation should be conducted at different sections and angles along the localized defect for accurately evaluating its area and shape.

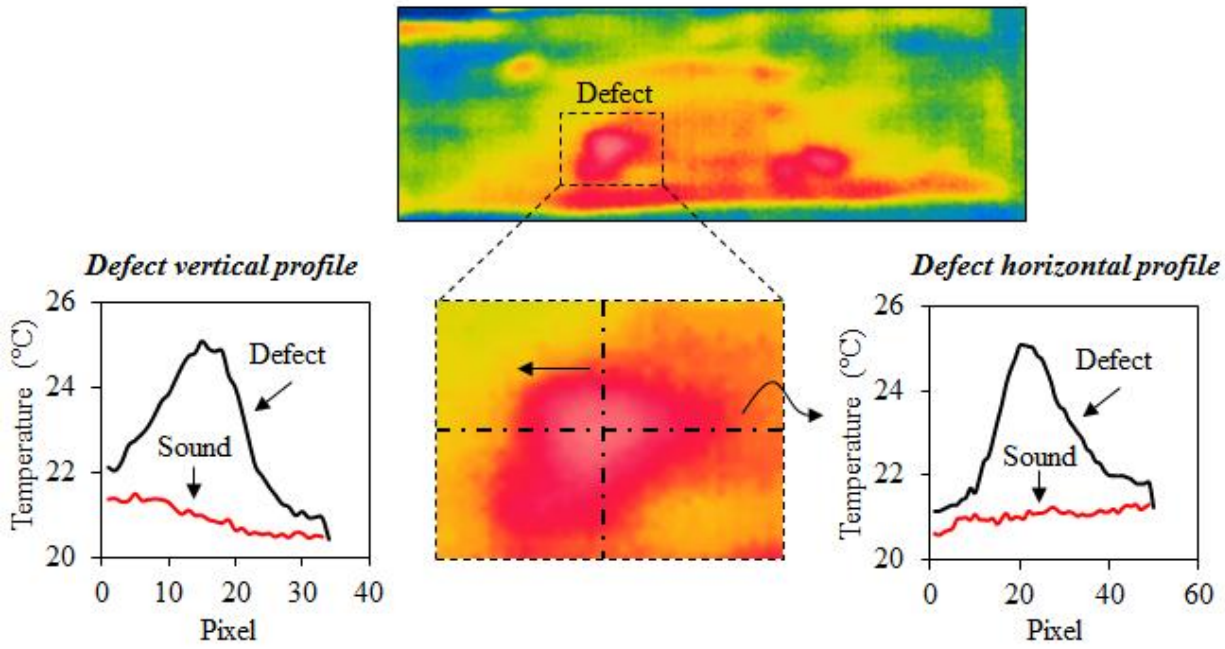

Figure 6-24: Thermogram of a defect.

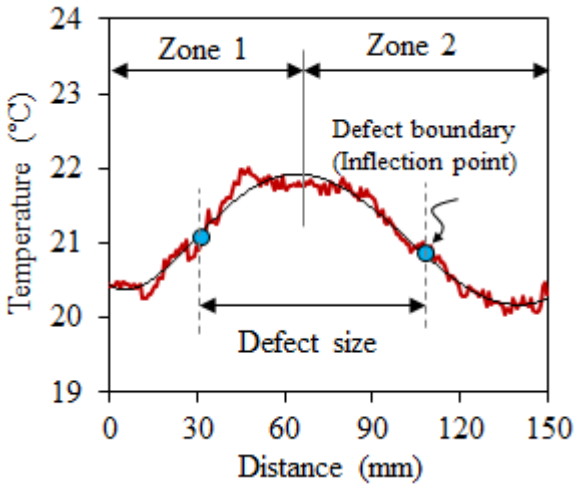

Figure 6-25: Defect boundaries. Zone 1 and Zone 2 represent different left and right sections of the defect around the center point.

6.3.3 Measurements

The tests are performed with a FLIR ThermaCAM T400 infrared camera with spectral range of 7.5-13 μm and thermal sensitivity of <0.07℃. Thermal videos are recorded at the rate of 9 frame/sec, at the cooling stage. The recorded videos are then converted into sequential 8-bit digitized photos of 320×240 pixels for each recorded frame. In 8-bit formatting system each pixel has a value between 0 to 255, which represents different colors and temperature variations in a linear scale. The data for each test are converted into 3D matrices with the size of 320×240×*t*, where the third dimension of

the matrix represents time. The temperature decay through time and analysis of the thermal images are performed through a Matlab code specially developed.

Two lamps with a maximum capacity of 2000 W are used as heating sources. The lamps were placed at 500 mm distance from the specimens, for 30 seconds. The position and duration of the heat exposure are optimized to obtain the best uniform heat distribution on the specimen's surfaces.

6.3.4 Method validation

Preliminary tests are performed for verification of the adopted IR thermography technique in the quantitative and qualitative assessment of interfacial defects. GFRP-strengthened masonry bricks with different artificial embedded defects in the interfacial layer are prepared to simulate environmental induced FRP delamination. After curing the specimens, the IR thermography method is used for defects localization and size estimation.

The embedded defects are circular plastic strips with diameters of 5, 10, 15, 20, and 25 mm, see Figure 6-26. The perimeter of the plastic strips is glued to the brick surface to avoid their movement during the application. Different defect sizes are selected to obtain the minimum detectable defect size. The plastic strips are glued to the brick surface only at their extreme boundaries. Therefore, not only the movement of the strips is avoided during the FRP application, but also an artificial delaminated area is produced under the strips where there is no bond between GFRP sheets and the brick surface.

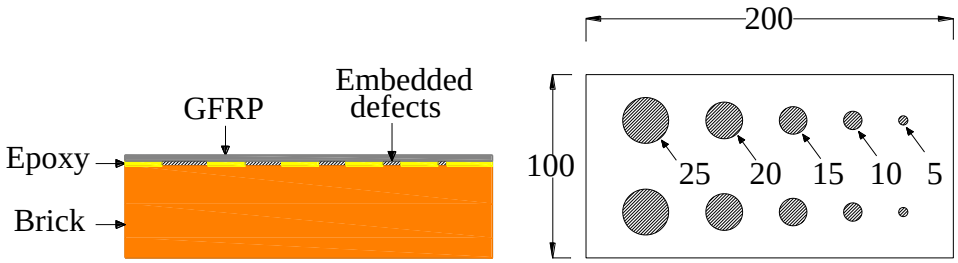

Figure 6-26: Details of the specimens with embedded interfacial defects.

The temperature history curves of defects with different sizes are shown in Figure 6-27. It can be observed that the temperature decay in 5 mm defect is similar to the sound area showing that this defect is not detected with the adopted IR thermography method. The minimum defect size that is detected in the thermal images is 10 mm. It is also shown that the temperature decay in 15, 20 and 25 mm defects are much different from the decay in 10 mm defect. For this reason, the maximum

thermal contrast for 10 mm defect is obtained separately from the other defect sizes, see Figure 6-28. It can be observed that the maximum thermal contrast for 10 and 25 mm defects occur at 15 and 31 s of thermal imaging, respectively. The corresponding thermograms are then selected for evaluating the defects sizes.

The defect dimensions are calculated following the two-point inflection method. The calculations are done at longitudinal and transverse sections of each defect to obtain the defect's diameter in both directions, see Table 6-3. Then, assuming the defect as an ellipse, the area of each defect is calculated. The predicted defects areas are given in Figure 6-29 for different defect sizes normalized to the actual defect area. It can be observed that the defect sizes larger than 10 mm diameter are predicted with a high degree of precision, with a maximum error lower than 10%. However, the error for the 10 mm defect size is relatively high (21%). These results validate the accuracy of the IR thermography technique used in this study for GFRP-strengthened masonry elements. Similar observations are reported in [233] for detecting the embedded flaws in CFRP-strengthened concrete elements.

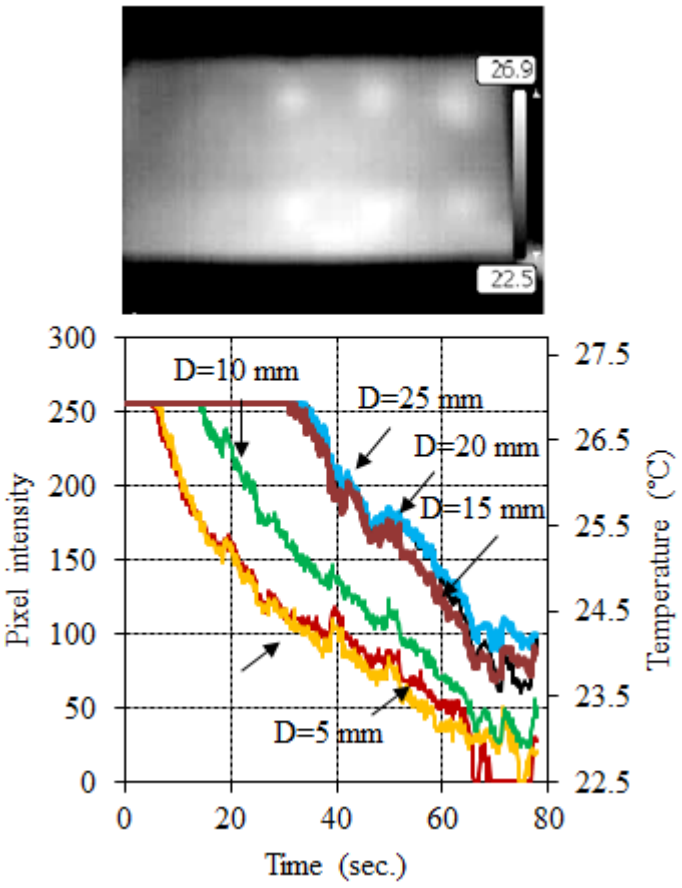

Figure 6-27: Thermal history curves at defect locations and a typical thermogram.

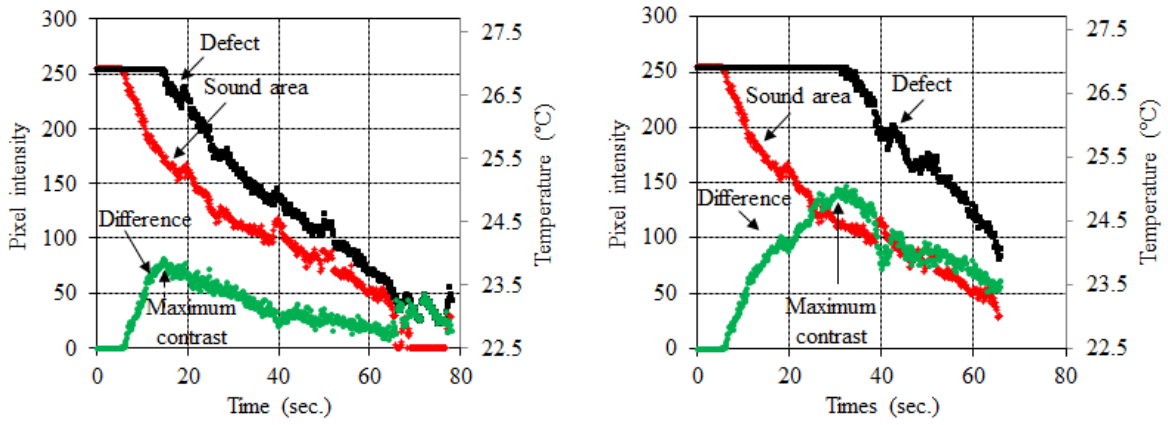

(a) (b)

Figure 6-28: Maximum thermal contrast evaluation for: (a) 10 mm defect; (b) 25 mm defect.

Table 6-3. Fracture energy and AE energy in different failure modes.

Actual defect diameter (mm)	IR thermography prediction		
	Horizontal diam., d_1 (mm)	Vertical diam., d_2 (mm)	Pred./Actual area
10	11.2 (err. 12.0%)	12.1 (err. 21.0%)	1.36
15	16.3 (err. 7.5%)	14.5 (err. -3.7%)	1.05
20	21.7 (err. 8.4%)	19.2 (err. -4.0%)	1.04
25	25.0 (err. 0.0%)	24.1 (err. -3.6%)	0.96

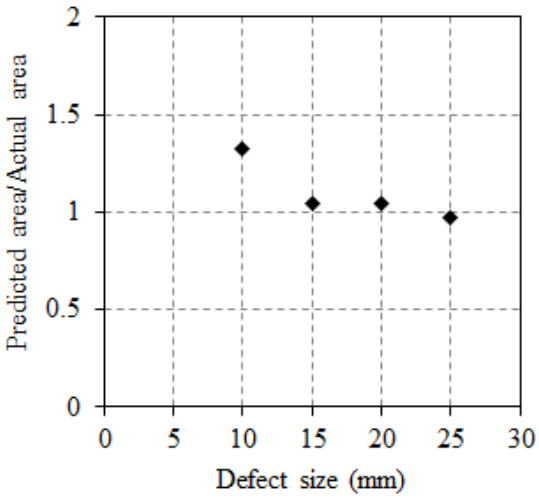

Figure 6-29: Comparison between real and calculated defect sizes.

6.3.5 Application to bond durability

For investigating the applicability of IR thermography technique in the detection of environmentally induced delamination, the GFRP-strengthened brick specimens exposed to HT1 (temperature cycles of +10°C to +50°C and 90% R.H.) and FT (temperature cycles of –10°C to +30°C and 90% R.H.) accelerated hygrothermal conditions, see Chapter 3, are inspected with this method after different periods of exposure. For each exposure period, after localization of interfacial delamination, its size and boundaries are evaluated quantitatively and the results are presented next.

As expected, FRP delamination is observed in some specimens after exposure to hygrothermal conditions. Figure 6-30 shows typical examples of specimens for each exposure period, where relatively large FRP delamination can be observed in the specimens exposed to HT1 conditions. On the contrary, the specimens exposed to FT conditions have very small delamination. As an example, the corresponding thermal images and detected FRP delaminated areas, from IR thermography tests, for the specimens exposed to HT1 conditions are presented in Figure 6-31. It can be observed that the FRP delamination is progressively increased with the exposure time. It should be noted that due to the physical properties of the materials used in this study, observation of delaminated areas is also possible with visual assessment, see Figure 6-30. However, in case of strengthening with other composite materials and matrices or application of renderings over the strengthening visual observation is not applicable.

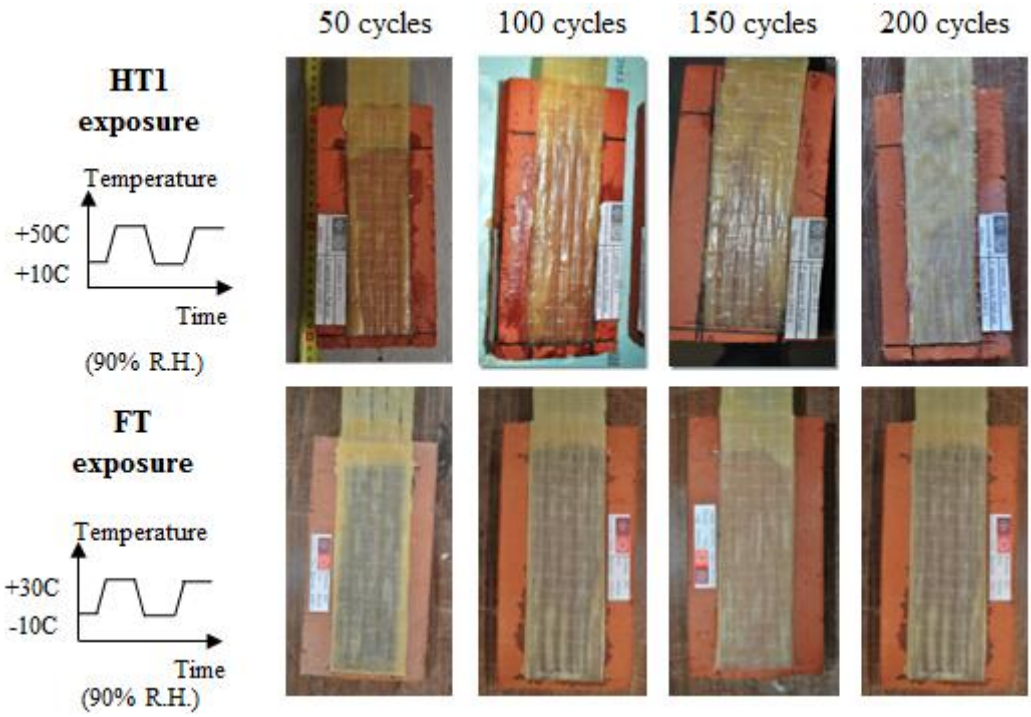

Figure 6-30: Examples of specimens for different exposure periods.

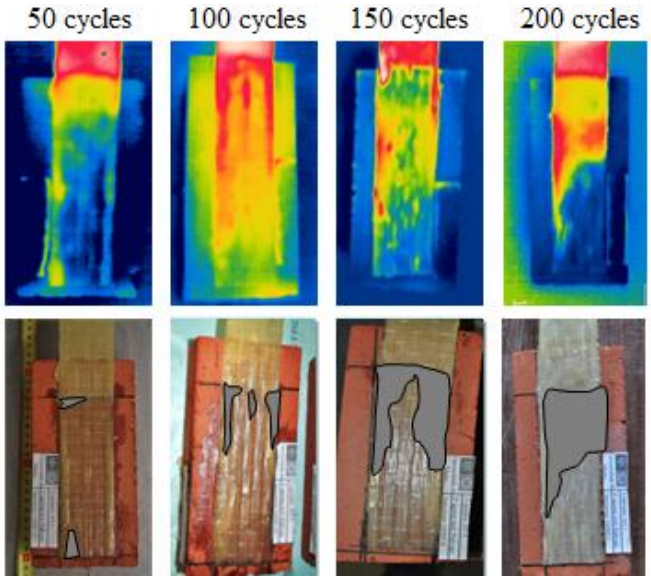

Figure 6-31: Qualitative assessment of delaminated areas after different periods of exposure to HT conditions, using IR tomography.

The observed delamination can be attributed to the thermal incompatibility between materials. However, moisture can also play an important role in weakening the bond strength [166, 186, 262]. The thermal expansion coefficient of clay bricks is in the order of 5×10^{-6}/℃ [125]. The thermal expansion coefficient of E-glass fibers is similar to the clay bricks, while for the epoxy resin is in the range of $3\sim5\times10^{-5}$/℃ [1]. This one-order magnitude difference of thermal expansion coefficient between epoxy resin and glass fibers/bricks produces large interfacial thermal strains at the fiber/epoxy and brick/epoxy interfaces. Cyclic temperature conditions induce thermal fatigue and may cause FRP delamination from the brick surface during the environmental exposure. It has also been reported that the thermal expansion coefficient of epoxy resins is much lower at low and negative temperatures [268]. This explains the small delaminated areas observed in the specimens exposed to the FT conditions.

Once the delamination is localized, the captured thermograms are analyzed according to the two-point inflection method to quantify the FRP delaminated areas. For this reason, the temperature profiles are obtained along the bonded length at longitudinal sections (trying to obtain the edge lines and the center line of the delamination area), see e.g. Figure 6-32 to Figure 6-34. Then, the temperature profiles near the detached areas are fitted with a 4^{th} order polynomial curve. The inflection point of the estimated curve is selected as the boundary of the FRP delaminated area.

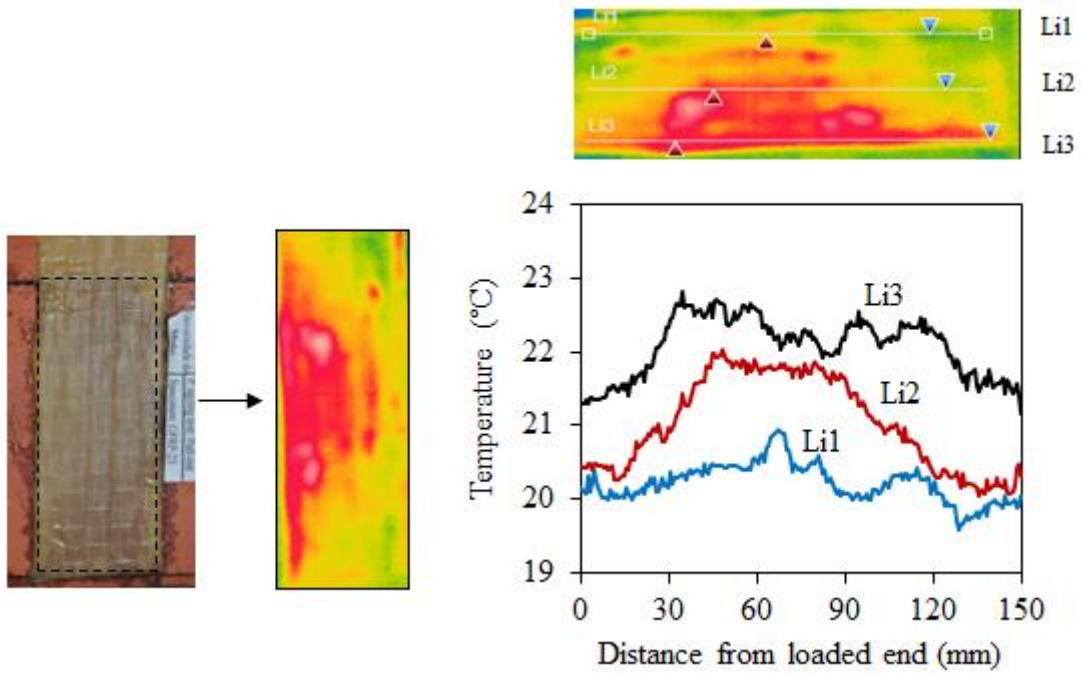

Figure 6-32: Temperature profiles in a specimen exposed to 100 cycles of HT1 exposure.

In the specimen exposed to 100 cycles, delamination is observed in the center of the bonded length, shown as a hot spot in the thermogram presented in Figure 6-32. Therefore, it is necessary to obtain the boundaries of the delaminated area on both sides of the defect in the longitudinal direction, as indicated in Figure 6-33. However, the delamination in the specimen exposed to 200 cycles starts from the loaded end of the specimen and progresses along the bonded length, see Figure 6-34. Therefore, just one boundary in the longitudinal direction should be located for obtaining the delamination size. The large FRP delaminated area in the specimen exposed to 200 cycles of HT1 exposure shows the severity of the thermal incompatibility in the specimens used in this study.

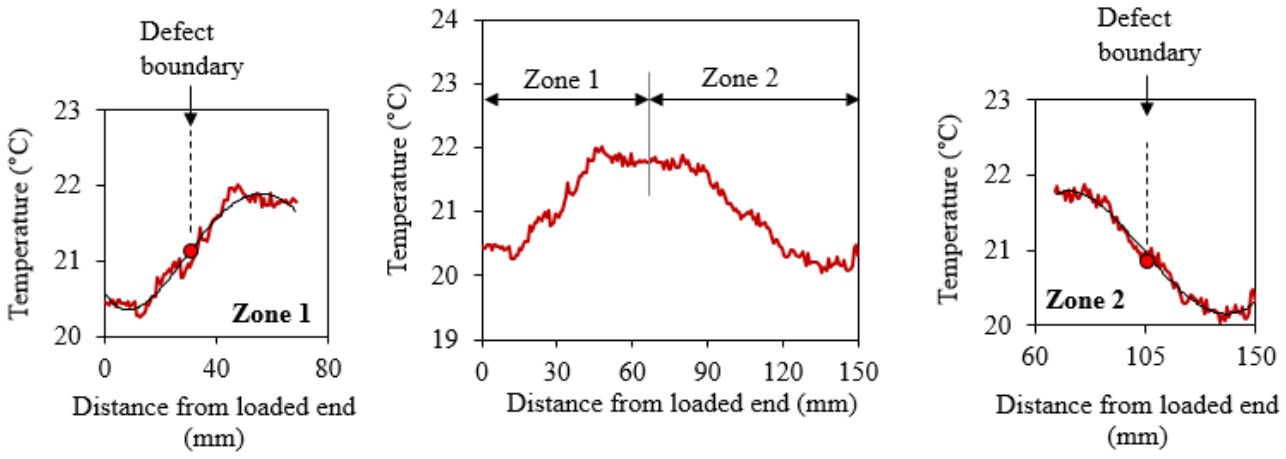

Figure 6-33: Delamination boundaries evaluation in a specimen exposed to 100 cycles of HT1

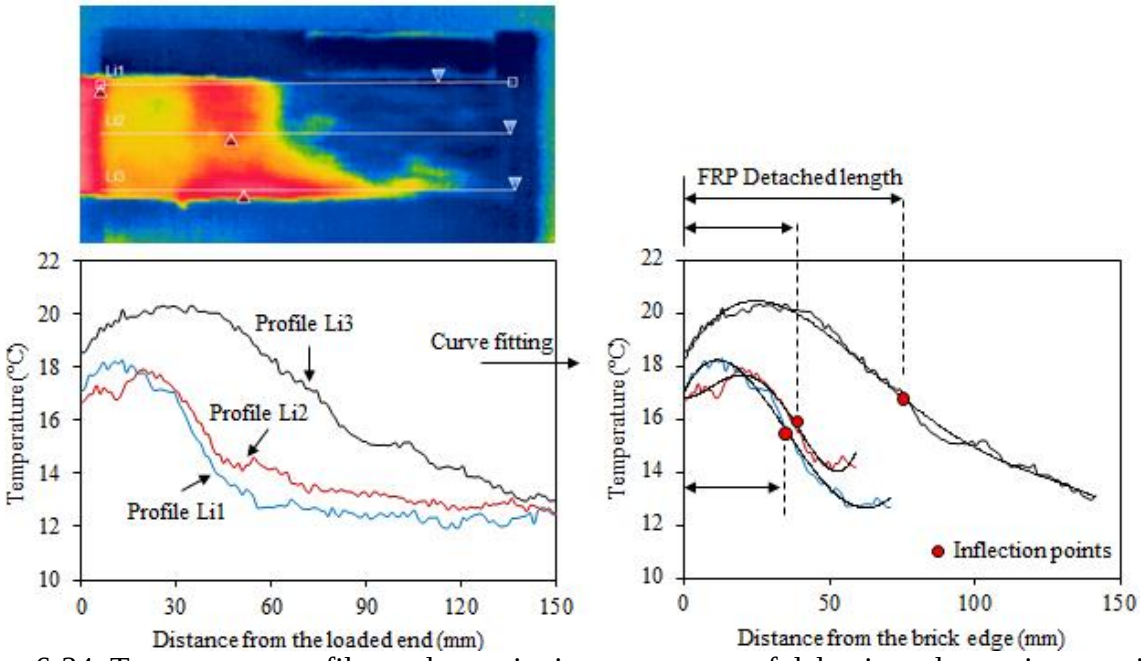

Figure 6-34: Temperature profiles and quantitative assessment of delaminated areas in a specimen exposed to 200 cycles of HT1 exposure.

The observed delaminations are evaluated quantitatively in all the specimens according to the described methodology. Figure 6-35 presents the results as the average of five specimens in terms of the remaining bonded area normalized to the initial bonded area. It can be observed that the delamination in the specimens exposed to HT exposure is relatively large (23% reduction of bonded area after 200 cycles). Meanwhile, the reduction in the bonded area in the specimens exposed to FT conditions is very limited (2% after 200 cycles). Moreover, a sudden increase in delamination rate can be observed after 100 cycles of exposure to HT conditions, followed by some stabilization.

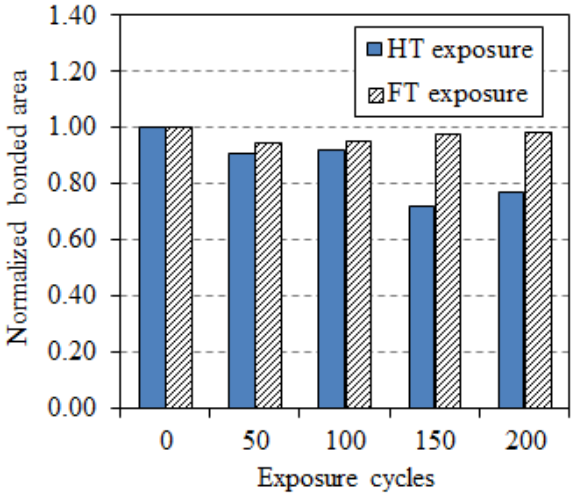

Figure 6-35: Reduction of the bonded area with exposure cycles.

6.4 Conclusions

Three full-field measurement and nondestructive testing technique were used in this chapter for characterization of debonding and fracture progress as well as bond quality assessment.

The digital image correlation technique was used for obtaining the full-field distribution of strains and displacements in tensile tests and single-lap shear debonding tests. The tensile tests were performed on aluminum and GFRP coupon specimens. Aluminum was used as a homogenous material in which a uniform distribution of strains is expected during tensile tests. A non-uniform distribution of strains was observed in GFRP coupons during tensile tests. These non-uniformities can affect the bond behavior in FRP-strengthened masonry elements and should be considered in the interpretation of experimental results.

The evolution of strains during the shear debonding tests was measured with the DIC technique. An advantage of DIC, when compared to conventional measurement techniques, is that a clear insight of distribution of strains can be obtained. This is much useful for investigating the three-dimensional aspects of the bond behavior and for characterizing bond-slip laws, which require a specific testing program. The results obtained showed also different longitudinal strain distributions along the bonded length at the FRP middle and edge sections. Moreover, large transversal strains were observed near the loaded end close to failure of the specimens, further confirming the three-dimensional nature of the bond behavior. Finally, it was shown how to calculate the effective bond length in GFRP-strengthened brick specimens from the DIC measurements and the obtained bond-slip behavior was presented.

The AE technique was applied to detect and characterize fracture and crack propagation during the debonding of composite materials from masonry bricks. The debonding phenomenon was investigated by performing single-lap shear bond tests on the specimens. In order to obtain different values of bond strength and failure modes, accelerated ageing tests were also carried out. The failure mode of the specimens changed after exposure from cohesive to adhesive failure.

The results showed that AE output can be efficiently used for investigation and interpretation of the fracture process during debonding. AE data, and more specifically the detected AE energy, was applied to characterize the different failure modes. Thereby, the cumulative energy/hit (E/h) ratio and Ib-value analysis were applied. While the AE energy could effectively be applied for failure mode characterization, the Ib-value analysis was inconclusive due to the progressive nature of the fracture process during debonding. A correlation was observed between the fracture energy and total emitted AE energy. Moreover, a close correlation was found between the FRP global slip and the cumulative AE energy, which can be applied for slip prediction and modeling purposes. The effect of failure mode on the AE outputs was significant.

The results indicate that the AE technique is suitable for obtaining a clearer insight into the debonding phenomenon and fracture propagation in laboratory tests and has potential for on-site health monitoring through debonding detection. Although performing comprehensive experimental tests is required for validation of the method and derivation of correlations with debonding fracture properties.

The active IR thermography technique was used for assessing the bond quality and degradation due to environmental conditions. For this purpose, a quantitative IR thermography method was adopted for evaluating the delamination in FRP-strengthened masonry elements. The applicability of this method for detecting FRP delamination in GFRP-strengthened masonry elements was initially validated using specimens with interfacial embedded defects of different sizes. The IR thermography results showed that the adopted method detects defects with a minimum size of 10 mm with a reasonable accuracy in quantifying the size.

The effect of environmental conditions on the bond quality was subsequently investigated by exposing GFRP-strengthened masonry bricks to two different accelerated hygrothermal conditions in a climatic chamber. The aim was to investigate the coupling effect of temperature and moisture on the bond quality. The IR thermography tests and visual inspection were performed periodically after each 50 cycles of exposure. Progressive FRP delamination was observed in the specimens after exposure to environmental conditions. The observed delamination, being more severe in specimens exposed to HT1 conditions, can be attributed to the thermal incompatibility between materials and induced thermal fatigue on the specimens. The size of delaminated areas was evaluated quantitatively with the adopted IR thermography method and the results were presented.

Moreover, the obtained results showed the applicability of IR thermography technique in quality assessment of bond in durability studies for research purposes. However, application of this technique for field assessment of strengthened structures remains open with issues such as far field assessments or assessment of strengthened elements with rendering.

Chapter 7

Numerical modeling of the bond behavior

Numerical modeling of the bond behavior is carried out using the finite element method (FEM). Within the finite element studies, due to the difficulties of adopting a micro-model where units, mortar, epoxy, and FRP are modeled separately, usually the bond behavior is modeled by using interface elements in a two- or three-dimensional space, see e.g. [53]. The adoption of a three-dimensional micro model-based approach able to follow crack propagation and failure is crucial for understanding the fundamental mechanics of FRP-masonry interfacial behavior. The numerical studies about interfacial behavior are mostly devoted to micro-modeling of externally bonded FRP-strengthened concrete elements, and only few investigations on masonry components strengthened with composite materials have been carried out. Usually, a two-dimensional modeling approach is used, e.g. [27, 39], and only a few three-dimensional analyses can be found, e.g. [70, 71]. However, most of the investigations have been carried out on FRP-concrete systems and scarce information can be found about FRP-masonry.

In this study, the bond behavior is modeled following both simplified and three-dimensional meso-scale modeling approaches. Each modeling approach is described in this chapter comprehensively and the results are presented and validated with available experimental results. The experimental results are selected from an extensive experimental campaign performed in the framework of RILEM TC 223-MSC [34].

For the meso-scale modeling approach, a three-dimensional finite element model in which FRP sheet, epoxy resin and brick are modeled separately is used. Three-dimensional aspects of bond behavior such as debonding and crack propagation, failure surface, and stress distributions, which are usually neglected in two-dimensional models, are investigated. The effect of mortar joints on the bond behavior is also studied. In this regard, mortar joints with different material properties representing poor quality and high quality mortars are considered, and their effects on the response

of the strengthened element are critically discussed. A comprehensive parametric study is also performed on FRP axial stiffness and width, and the effectiveness of mortar joints in each case is investigated.

For the simplified modeling approach, a two-dimensional plain stress finite element model is used. The bond behavior is modeled using interface elements with a tri-linear interfacial constitutive model which is proposed based on the presented experimental tests. The obtained numerical results are then presented and discussed critically. The validity of the approach is assessed through comparison with experimental data. It is shown that the FE simulations are in satisfactory agreement with the experimental results, in terms of force-displacement curves, strain distribution along the bonded length and failure mode. The proposed bond-slip model is also compared with the bond-slip model proposed by the Italian design code CNR DT200 [1] as an example of available relevant standards.

7.1 Reference experimental tests

7.1.1 Outline

A wide experimental campaign aimed at investigating the bond behavior of FRP-bricks through single-lap shear bond tests has been carried out at the University of Minho, using different composite materials namely carbon, glass, basalt, and steel. A short review of the experimental program and results are presented in this section, while the detailed description can be found in [34].

Single-lap shear bond tests were performed on the specimens for mechanical characterization of the bond behavior. The FRP/SRP strips of 50 mm width were applied on masonry bricks following the wet lay-up procedure. The bonded length of the strips was equal to 160 mm with a 40 mm unbonded part at the loaded end, as illustrated in Figure 7-1. Six specimens were tested for each type of composite material.

The tests were performed using a closed-loop servo-controlled testing machine under displacement controlled conditions. The displacements were imposed following a constant speed of 5μm/min at the end of the FRP strip. The resulting load was measured by means of a load cell, while the strain distribution was obtained from four strain gauges attached to the composite material surface, see Figure 7-1. In particular, three strain gauges were glued on the bonded area and one was glued on the unbonded area.

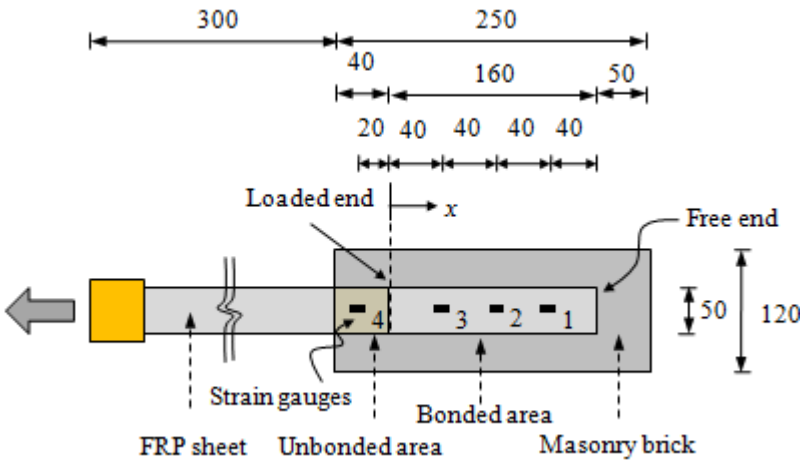

Figure 7-1: Geometry of the reference FRP-masonry brick specimens.

The masonry units used as the substrate were clay bricks with dimensions of 250×120×55 mm^3, a mean compressive strength of 19.8 MPa (CoV=2.5%), a tensile strength of 2.0 MPa (CoV=4%), and elastic modulus of 5580 MPa (CoV=5.2%). The compressive strength values of the bricks were kindly provided by the University of Padova in the framework of RILEM TC 223-MSC [34]. The fracture energy of the brick has been selected equal to 12.5 N/mm for compression, 0.19 N/mm in for tension, and Poisson's ratio equal to 0.2 based on the available data in the literature, e.g. [257, 288]. The experimentally obtained mechanical characteristics of the composite materials are shown in Table 7-1 in terms of elastic modulus, E_f, tensile strength, f_t, ultimate deformation, $\varepsilon_{\max}$, and composite thickness, t_f.

Table 7-1: Characteristics of the composite materials.

Material	E_f (MPa)	f_t (MPa)	ε_{max} (%)	t_f (mm)
CFRP	202100	2525	1.16	0.17
GFRP	77160	1350	1.86	0.12
BFRP	86090	1499	1.74	0.14
SRP	192900	2876	1.66	0.23

7.1.2 Experimental results

The local bond stress-slip (τ–s) curves have been obtained from the experimental strain profiles measured along the FRP reinforcement at different load levels based on the approach given in [59], see Figure 7-2. In fact the bond stress distribution within the bonded length can be evaluated by

imposing the equilibrium condition of an FRP strip with a length *dx* bonded to masonry, assuming an elastic behavior of the reinforcement, as:

$$\tau(x) = t_f E_f \frac{d\varepsilon_f}{dx} \tag{7.1}$$

where $d\varepsilon_f / dx$ is the gradient of FRP strain along the sheet length captured by the strain gauges, E_f is the FRP elastic modulus, and t_f is the FRP thickness. Moreover, the slip at distance *x* from the free end of the specimen can be calculated assuming a zero slip in the free end as:

$$s(x) = \int \varepsilon_f \, dx \tag{7.2}$$

As the strain values along the element are captured in a discrete form, the bond stress and slip values can be approximated numerically as:

$$\tau(x_i) = \frac{1}{2} E_f t_f \left[\frac{\varepsilon_f(x_i) - \varepsilon_f(x_{i-1})}{x_i - x_{i-1}} + \frac{\varepsilon_f(x_{i+1}) - \varepsilon_f(x_i)}{x_{i+1} - x_i}\right] \tag{7.3}$$

$$s(x_i) = \frac{1}{2} \sum_{k=1}^{i} [\varepsilon_f(x_k) + \varepsilon_f(x_{k-1})](x_k - x_{k-1}) \tag{7.4}$$

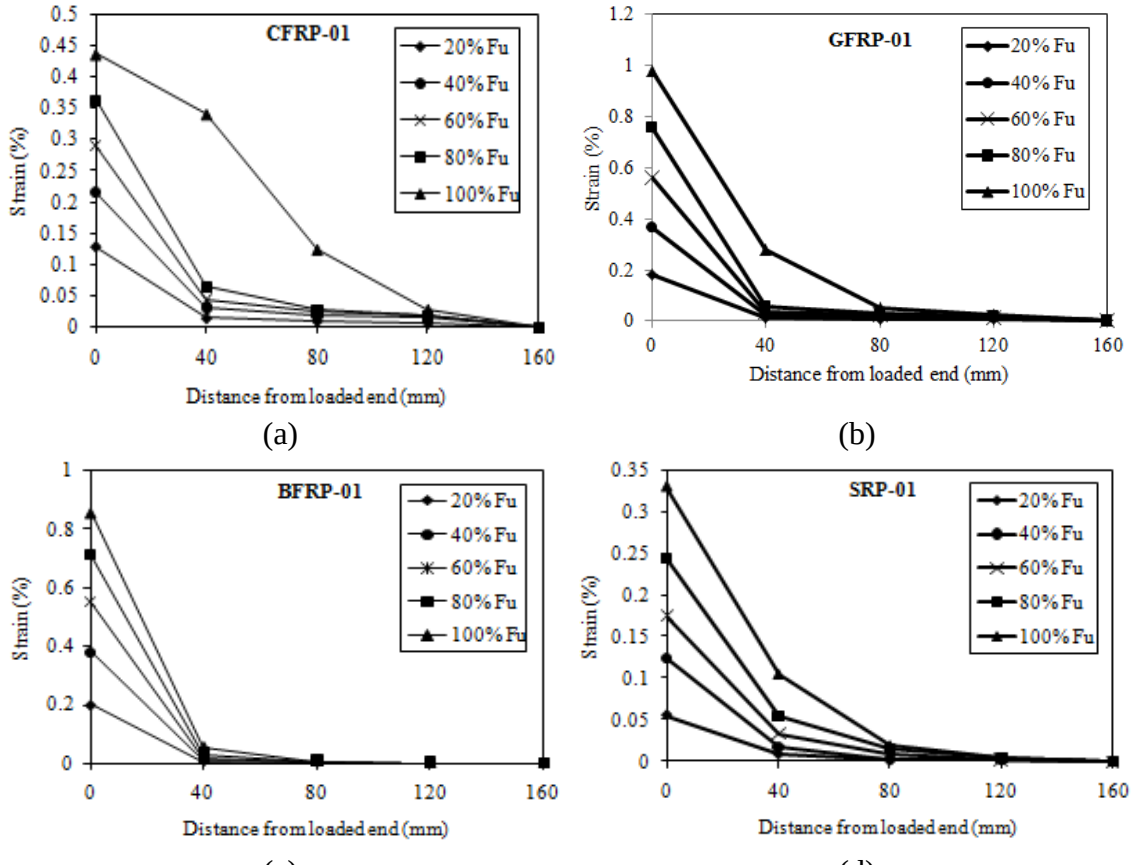

Figure 7-2: Experimental strain distributions along the bonded length for all strengthened specimens (only the first specimen is shown): (a) CFRP; (b) GFRP; (c) BFRP; (d) SRP.

The local bond-slip behavior (τ-s curve) along the bonded length in the tested specimens, which is used in this study as the basis for the adopted bond-slip model, can be obtained analytically using Eqs. (7.3) and (7.4). Furthermore, the total relative displacement of the composite strip can be obtained using Eq. (7.4) assuming that the strain at the loaded end is given by the strain gauge 4 placed in the unbonded zone. This evaluation is based on the assumption that strain is constant along the unbonded zone. The analytical τ–s curves may show some irregularity as they are obtained based on discrete and limited strain readings. While numerical integration has a smoothing effect, numerical differentiation tends to magnify these irregularities [59].

The strain profiles shown in Figure 7-2 are for different load levels of 20%, 40%, 60%, 80%, and 100% of the ultimate load. As it can be seen, for low load levels the strain profiles follow an exponential curve, indicating that the load transfer occurs along a short length close to the loaded end. With an increase in the load level, longer load transfer lengths are mobilized, which is in agreement with the behavior observed by other authors, e.g. [52, 56, 59].

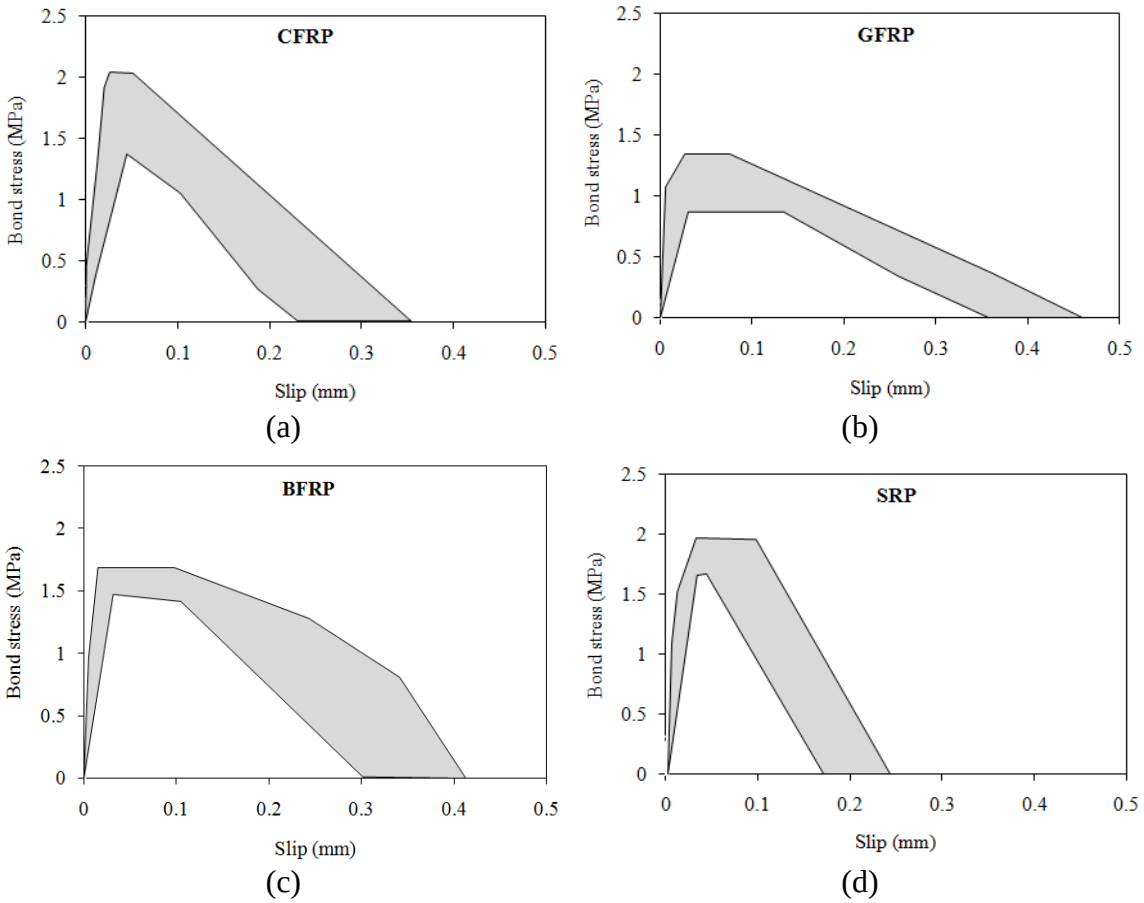

Figure 7-3: Local bond stress-slip curves for all strengthened specimens (the envelopes of six tests are shown): (a) CFRP; (b) GFRP; (c) BFRP; (d) SRP.

The local bond-slip curves of the specimens have been obtained by means of Eqs. (7.3) and (7.4) using the strain distributions obtained from the experimental tests. As an example the envelope of the local bond-slip behavior near the loaded end (strain gauge 3 in Figure 7-1) is shown in Figure 7-3 for each composite material. From visual observation it can be noted that a similar overall behavior is found for different composite materials with small differences in bond strength and slip. The bond-slip curves in all the specimens follow a tri-linear trend with a plastic branch in the middle. Based on this observation, a tri-linear bond-slip law has been adopted for numerical analyses, which is described in the next sections.

The global force–relative displacement behavior of the specimens has been obtained using the force-slip values at the loaded end of the specimens in each step. The resulting curves are shown in Figure 7-4 for all the specimens. A relatively ductile behavior is observed in the force–relative displacement curves for all FRP types.

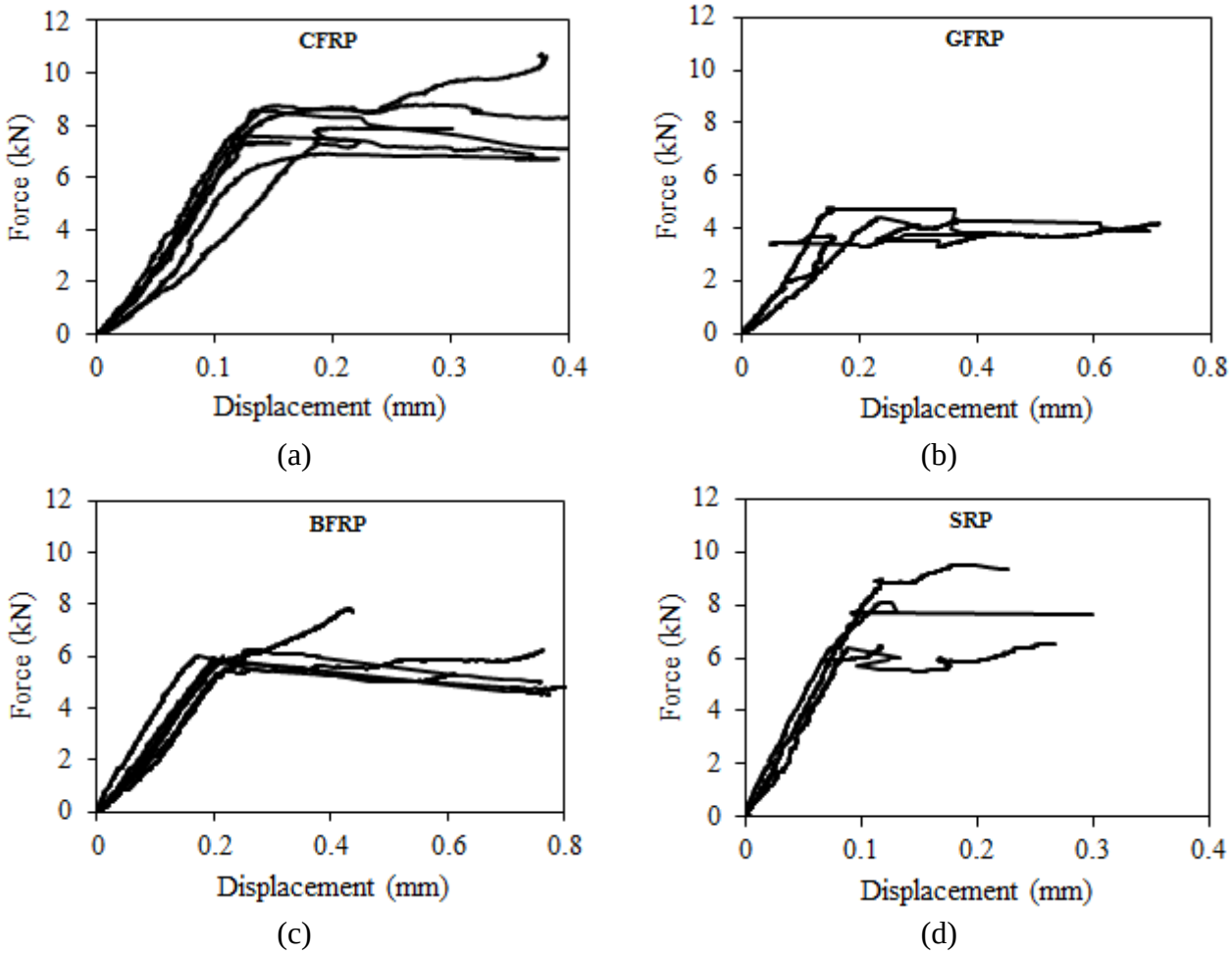

Figure 7-4: Experimental force–relative displacement curves for all strengthened specimens: (a) CFRP; (b) GFRP; (c) BFRP; (d) SRP.

In order to obtain better insight into the experimental results, a comparison is made between different FRP composites by illustrating the envelopes their of force–relative displacement curves in Figure 7-5. It can be seen that the specimens strengthened with CFRP and SRP have similar global behavior, while some similarity also exists between BFRP and GFRP strengthened specimens. In general, BFRP and GFRP specimens have lower strength and higher ductility than CFRP and SRP. This result seems to be a direct consequence of the mechanical and geometrical properties of the composite materials, see Table 7-1, and will be further discussed with the assistance of numerical modeling. In all specimens, delamination of the FRP strip with a thin and uniform layer of brick (approximately 1 mm) was observed.

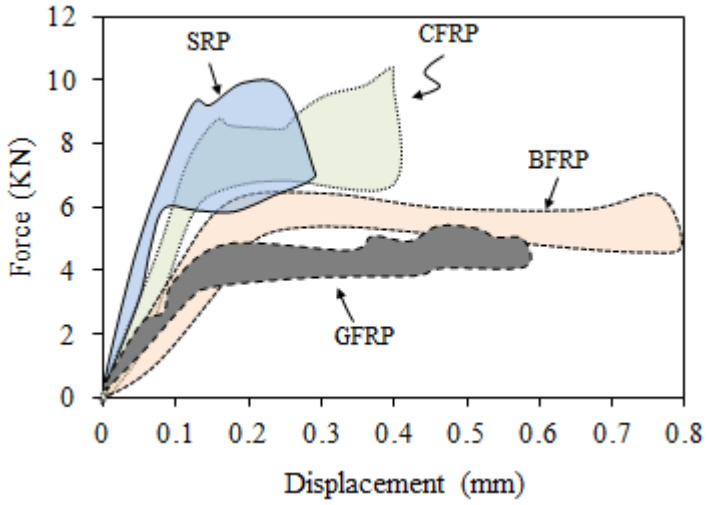

Figure 7-5: Envelope of experimental force–relative displacement curves.

7.2 Meso-scale modeling

7.2.1 Finite element model

7.2.1.1 Outline

A three-dimensional nonlinear Finite Element (FE) model is adopted for modeling the typical single-lap shear bond tests on FRP-strengthened masonry bricks, see Figure 7-6. Due to the symmetry of the model configuration, only half of the structure is modeled. The boundary conditions are applied as given in the reference experimental tests. A monotonic incremental displacement is applied at the end of the FRP sheet in order to simulate the pulling force.

The analysis is carried out in the FE code DIANA [289]. The adopted mesh includes twenty-node solid elements (denoted by CHX60) to model the brick and epoxy layer, and eight-node shell elements (denoted by CQ40F) for the FRP. Perfect bond is assumed between the FRP strip and the epoxy layer, and between the epoxy layer and brick.

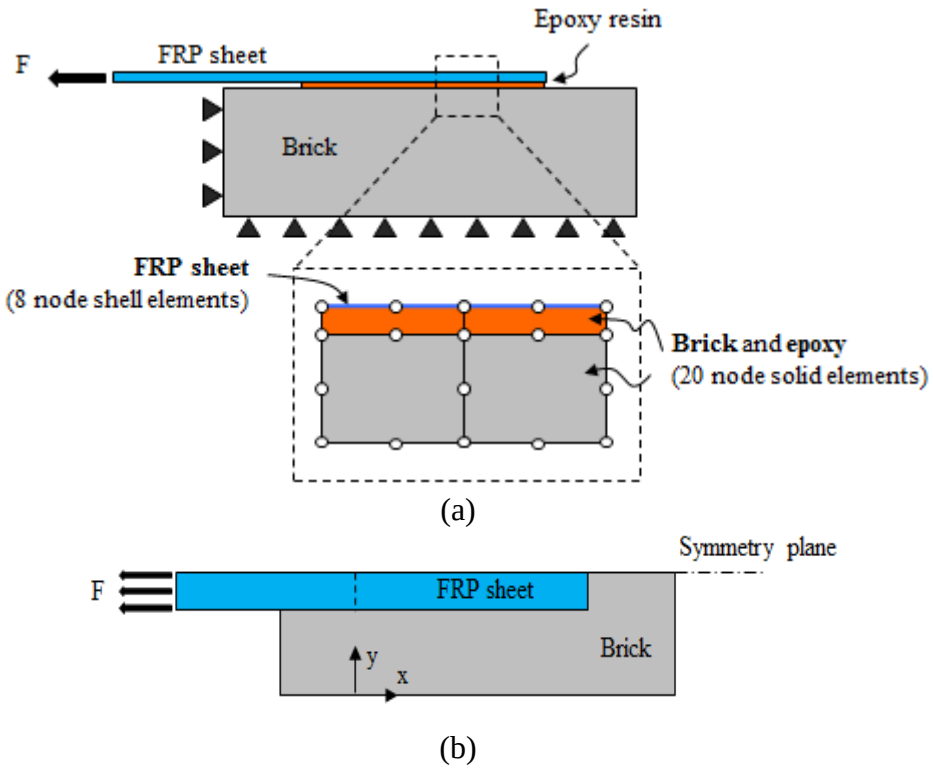

Figure 7-6: Adopted finite element model: (a) elevation; (b) top view (x-y plane).

7.2.1.2 Material models

A smeared crack model is used for modeling the debonding progress and crack propagation in masonry, while linear elastic behavior is assumed for the FRP and the adhesive layer. Since failure occurs in the upper layer of the brick, this assumption seems reasonable.

Crack models in advanced finite element software packages are usually based on the smeared crack or discrete crack modeling approaches. Since smeared crack modeling approaches do not require remeshing of the FE model after occurrence of cracks or *a priori* definition of possible location of cracks, they have been widely used in FE modeling. The FE code DIANA includes the following smeared crack modeling approaches: total strain fixed crack model (FCM), multi-directional fixed crack model (MFCM), and total strain rotating crack model (RCM).

In the fixed smeared cracking approach, the orientation of crack is fixed after appearance of the first crack. Consequently, shear stresses develop in the crack plane with the change in direction of principal stresses during the analysis. A reduction in severity of the mesh bias problem, a better representation of strut and tie mechanisms in the substrate, and the definition of the parameters from well-established standard tests are the advantages of this approach, while the shear stress locking problem can be noted as the main disadvantage [290, 291]. The shear stiffness after cracking is given by the shear retention factor, which can be a constant (low) value between 0 and 1, or a

vanishing value with crack opening. Here, constant values equal to 0.01 and 0.1 are adopted. Different solutions, such as mesh refinement or using negative values for the shear retention factor, have been proposed for solving the problem of shear locking, but following the crack development in delamination problems remains impossible using this method [291].

Multi-directional fixed crack or rotating crack models seem more suitable for debonding problems, in which high shear stresses develop. In the MFCM, if the angle between the principal tensile stress and crack orientation becomes larger than a specified value, θ, new orthogonal cracks form in the direction of the principal stresses and the old cracks become deactivated. In the special case where θ is equal to zero, the crack direction is always perpendicular to the principal stress direction, providing a rotating crack model (RCM) approach.

The ability of fixed and rotating smeared crack modeling approaches in simulating the bond behavior in FRP-strengthened masonry elements is investigated in section 7.3.2.2. Here, the behavior of the brick is modeled using a parabolic hardening/softening model in compression and an exponential softening model in tension. The reduction of compressive strength due to lateral cracking is also considered using the model proposed by Vecchio and Collins [290].

7.2.2 Model validation

The experimental results obtained for CFRP-strengthened brick specimens, explained in section 7.2, are used in this study for validation of the FE model. The experimental results are validated in terms of force-slip diagrams and strain distribution along the FRP.

7.2.2.1 Mesh dependency of the model

Three different mesh sizes are used, Mesh 1 (coarsest mesh) to Mesh 3 (finer mesh), in order to assess convergence of the results. The minimum element size, the total number of elements and the total number of nodes for each mesh are shown in Table 7-2.

Figure 7-7 presents the obtained force-slip curves with different mesh sizes, considering the usual regularization of the fracture energy according to the element size [292]. Mesh 2 and Mesh 3 produced similar results, while the results predicted with the coarsest mesh (Mesh 1) are slightly different and indicate that the mesh is not sufficiently refined. As for the local behavior, the strain distributions along the bonded length are shown in Figure 7-8 for two load levels of P/P_u =0.2 and P/P_u=1.0. In case of the P/P_u =0.2, the strain (and stress, as linear elastic behavior is assumed for the FRP) distributions predicted with different mesh sizes are almost identical, while in P/P_u=1.0, the results predicted by Mesh 1 are different from other mesh types.

Table 7-2: Adopted mesh types.

Mesh type	Minimum element size (mm)	Total no. of elements	Total no. of nodes
Mesh 1	1	2700	12271
Mesh 2	0.5	13900	59925
Mesh 3	0.25	106800	443849

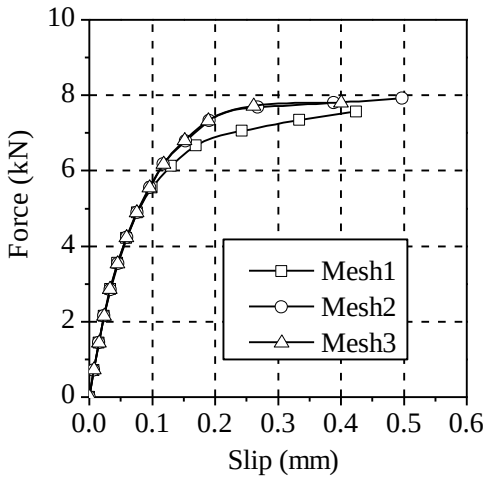

Figure 7-7: Force-slip curves obtained for different mesh sizes.

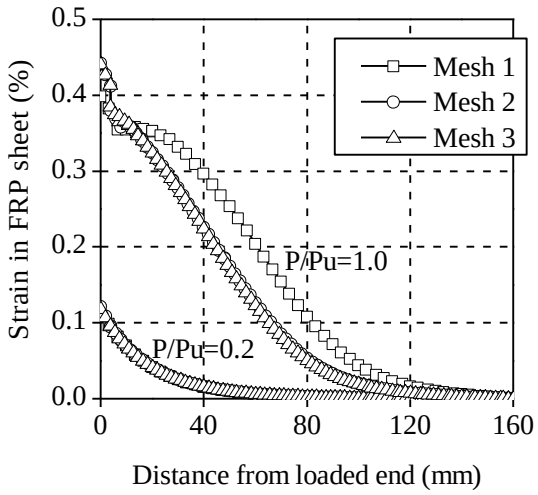

Figure 7-8: Effect of mesh size on strain distributions in the FRP sheet. Note that the results for all meshes coincide for P/Pu=0.2 and the results for P/Pu=1.0 coincide for Mesh 2 and Mesh 3.

The normal and shear stress distributions in the adhesive-brick interface and the adhesive mid-section are also investigated for different mesh sizes at the ultimate load level, see Figure 7-9. The stresses are obtained at the nodes by the usual averaging procedures. In the adhesive mid-section, the normal stresses in Mesh 1 are again slightly different from the stresses from other mesh

types near the loaded end. By moving towards the free end the results converge for all types of meshes. The shear stresses are almost identical for all mesh sizes with a slight difference of Mesh 1 and some fluctuations in Mesh 2 near the loaded end. The stress distribution coincides in all meshes after a short distance from the loaded end, similarly to the strain distributions. In the adhesive-brick interface a similar difference exists near the loaded end between the results obtained from Mesh 1 and the results obtained from Mesh 2 and Mesh 3. Moreover, the stresses increase with mesh refinement at the loaded end due to the existence of stress singularities, as expected and discussed e.g. in [27, 293, 294].

The comparison made indicates that Mesh 2 and Mesh 3 are fine enough for obtaining reasonable results. Therefore, the results presented hereafter are obtained using the model with Mesh 2.

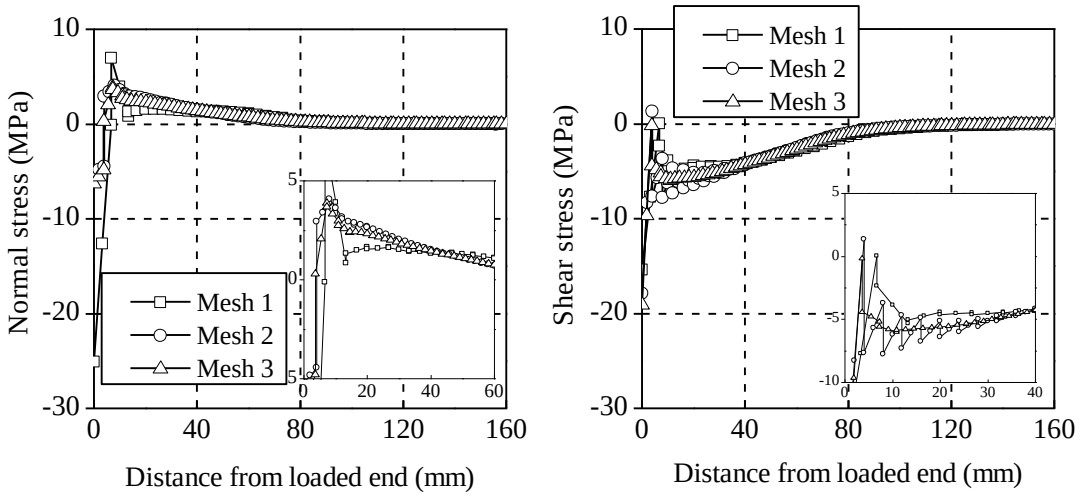

(a)

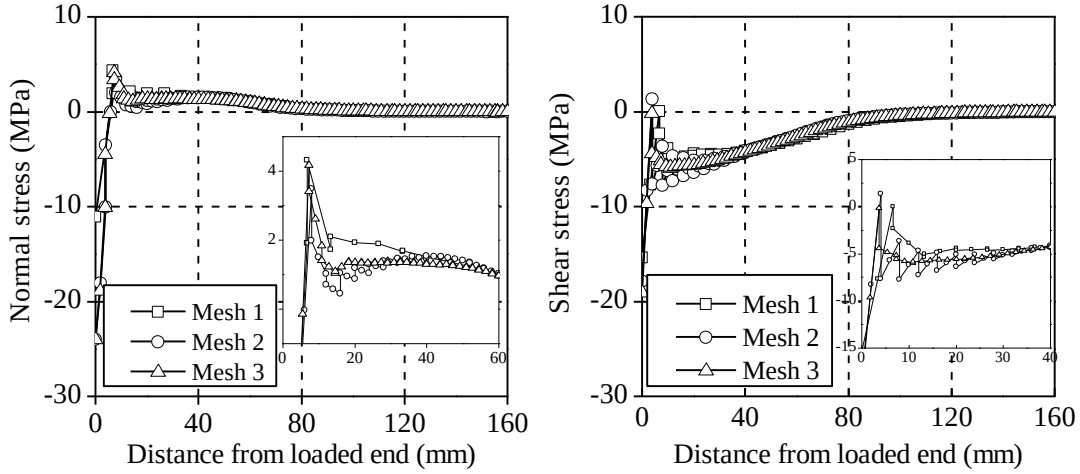

(b)

Figure 7-9: Effect of mesh size on stress distributions at the ultimate load level, P/P_u=1.0: (a) adhesive mid-section; (b) adhesive-brick interface.

7.2.2.2 Material crack models

The force-slip curves obtained using different crack models are shown in Figure 7-10 in comparison with the envelope of the experimental curves. Since the effect of using different softening models has been found to be negligible [27], an exponential softening model is adopted in this study for all cracking models. In the fixed smeared crack model (FCM), constant shear retention factors of β=0.1 and β=0.01 are used. It can be observed that the results predicted by the rotating crack model (RCM) is in reasonable agreement with the experimental results, while the other crack models do not produce satisfactory results. The shear stress locking problem in the fixed smeared crack models resulted in an increase in the shear stresses even after full crack development.

A comparison of experimental and numerical results in terms of strain distribution along the FRP sheets is also made for two different load levels of P/P_u=0.2 and P/P_u=1.0, see Figure 7-11. For P/P_u=0.2, the strain distributions are predicted accurately in all cracking models, as the results are mostly elastic. On the other hand, for P/P_u=1.0 only the results obtained from RCM and FCM (β=0.1) are in relatively good agreement with experimental results.

In general, the results show that RCM can provide better results than FCM. Therefore, this crack modeling approach is selected in this study for numerical simulation of the debonding phenomenon.

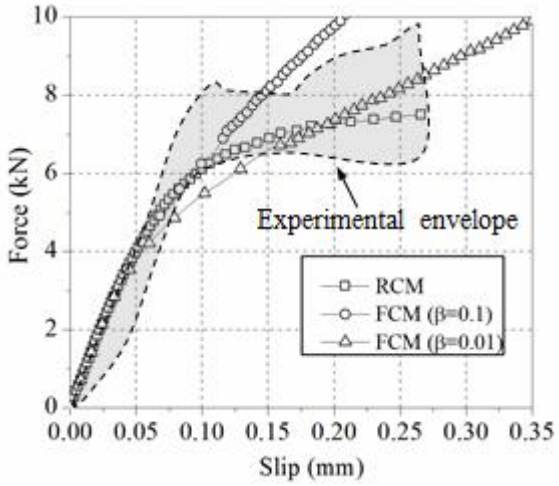

Figure 7-10: Force-slip curves obtained for different crack models.

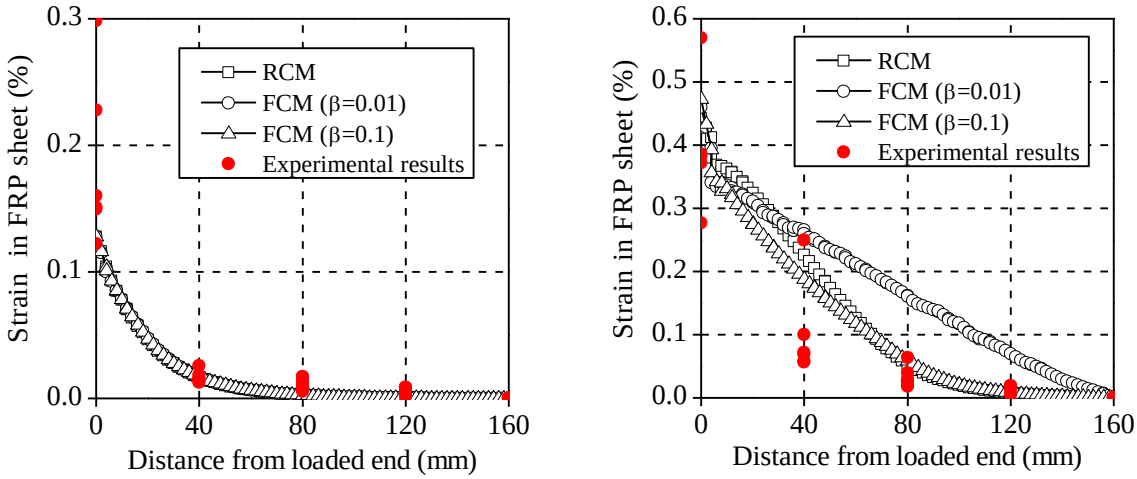

Figure 7-11: Strain distributions along the FRP sheet for different crack models: (a) P/P_u=0.2; (b) P/P_u=1.0.

7.2.3 Three-dimensional effects

The normal and shear stresses (at P/P_u=1.0) along the edge and middle (center line) of the FRP sheet are shown in Figure 7-12 and Figure 7-13 at mid-height-adhesive and brick-adhesive sections, respectively. It can be seen that the stress distribution is different along the FRP width, especially in the case of shear stresses (Figure 7-12 (b) and Figure 7-13 (b)), due to the boundary effect. In this case, at the mid-height-adhesive section the maximum normal compressive stress is 6.3 MPa along the edge of the FRP sheet, and 5.8 MPa along the middle. On the other hand, the maximum tensile stress along the FRP edge is 3.6 MPa and 4.5 MPa along the FRP middle. In case of the maximum shear stress, the difference is rather large in absolute value up to 80 mm from the loaded end. Along the FRP edge the maximum (absolute) shear stress is 10.8 MPa, while along the middle a value about 3.6 times lower was obtained (3.0 MPa). At the brick-adhesive section, the maximum normal compressive stress is 16.2 MPa along the edge of the FRP sheet, while it is 14.5 MPa along the FRP middle. The maximum tensile stress along the FRP edge is 2.8 MPa, while it is 3.4 MPa along the FRP middle. The maximum (absolute) shear stress approaches 13.5 MPa and 8.13 MPa along the FRP edge and middle, respectively. It can be observed that a considerable difference exists between the shear stresses along the FRP edge and middle. This difference, also reported for FRP-strengthened concrete elements in [71], shows the three-dimensional nature of the debonding problem which is neglected in conventional 2D modeling approaches. Moreover, the significant difference of compressive and tensile stresses between mid-height-adhesive and brick-adhesive sections shows the existence of relevant bending stresses near the loaded end, which are larger at the edge of the FRP sheet.

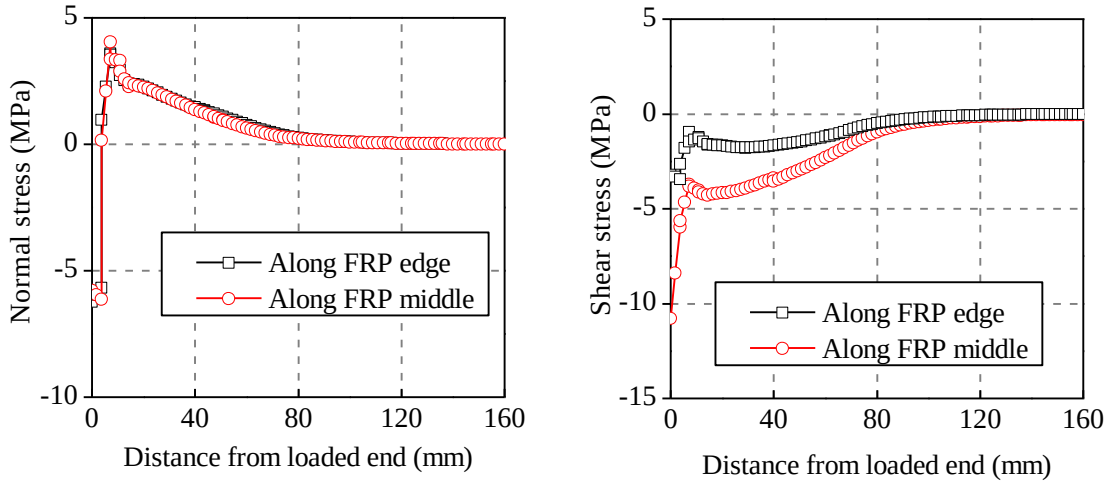

(a) (b)

Figure 7-12: Stress distributions along the bonded length at mid-height-adhesive section at P/P_u=1.0: (a) normal stress; (b) shear stress.

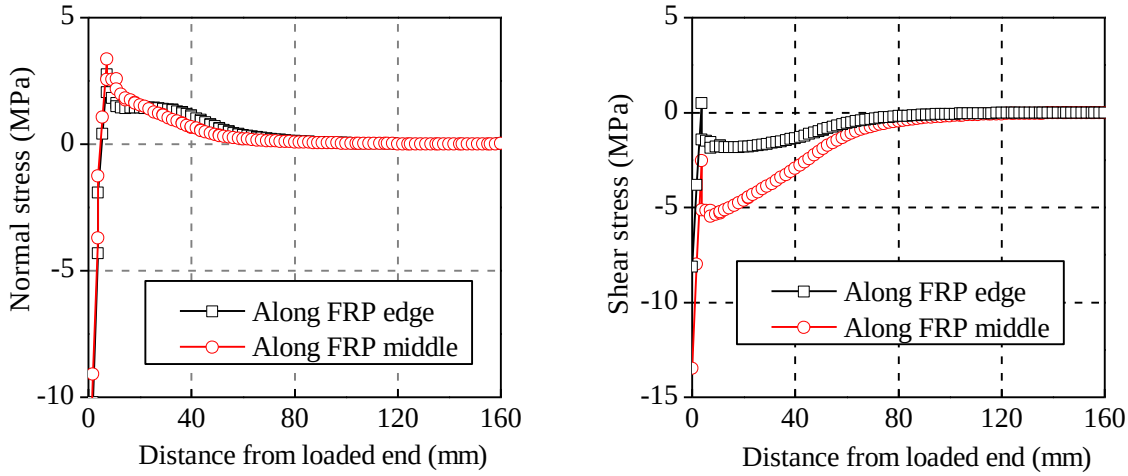

(a) (b)

Figure 7-13: Stress distributions along the bonded length at brick-adhesive section at the ultimate load level, P/P_u=1.0: (a) normal stress; (b) shear stress.

The numerical distribution of cracks inside the specimens is plotted in Figure 7-14 for the case of P/P_u=0.8. It can be seen that failure occurred involving a thin layer of the brick, whereas the remaining brick exhibits no damage. This result is in very good agreement with the experimental results. Another phenomenon observed in the experimental tests was that the debonded area was larger than the FRP bonded area, indicating the propagation of cracks along the FRP width and length. The adopted model was able to capture this aspect also. As shown in Figure 7-14 (b), the cracks propagate out of the bonded area in the brick surface.

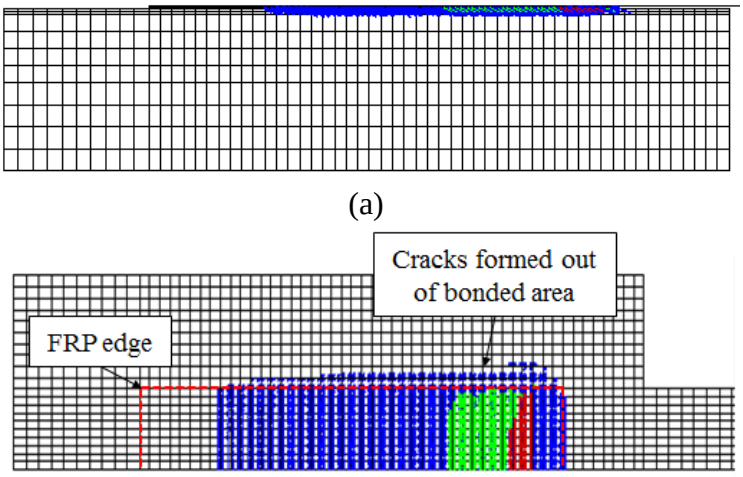

(a)

(b)

Figure 7-14: Numerical crack pattern of the FRP and brick specimen modeled in 3D at P/P_u=0.8: (a) side view; (b) top view.

7.2.4 Role of mortar joints

The effect of mortar joints on the debonding behavior of FRP-strengthened masonry elements is investigated in this section. It has been widely accepted in the literature that FE models, when validated with experimental results, can be used effectively to simulate similar problems and avoid performing extensive experimental tests. The debonding problem in masonry prisms is a very complex phenomenon, and the validated FE model is used to gain insight of the phenomenon, as a laboratory simulation. For this purpose, two mortar joints with 15 mm thickness are added to the brick model described in the previous section, see Figure 7-15. The total strain rotating crack model is used again for modeling the cracking behavior of bricks and mortar joints. The material properties used for the FRP sheet and bricks are kept unchanged. Two different material properties are used for the mortar joints, representing high (M1) and low quality (M2) mortars, respectively, with mechanical characteristics summarized in Table 7-3. Different FRP axial stiffness ($E_f t_f$) and width (the ratio of FRP width to brick width, r=b_f/b) are considered in the numerical analysis to understand the effect of the different parameters. The reference FRP axial stiffness, $E_f t_f$, and width ratio, r, are equal to 34.3 kN/mm and 0.42, respectively.

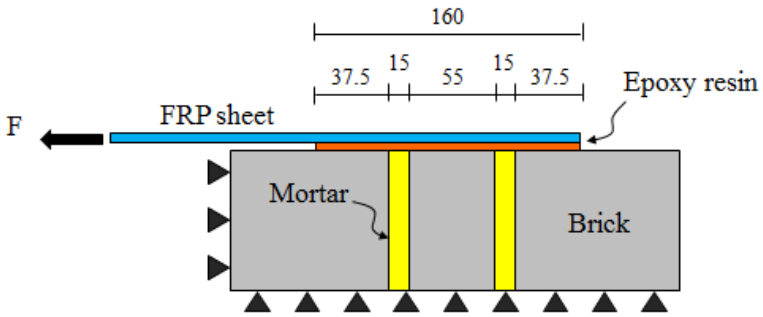

Figure 7-15: Adopted finite element model for FRP-strengthened masonry prism.

Table 7-3: Mechanical properties of the mortar types.

Mortar type	E (GPa)	v	f_c (MPa)	G_{fc} (N/mm)	f_t (MPa)	G_{ft} (N/mm)
M1	8	0.1	10	2.7	1.0	0.035
M2	2	0.1	3	1.8	0.25	0.018

7.2.4.1 Global behavior

The numerical force-slip curves obtained for mortars M1 and M2 are shown in Figure 7-16 together with the model without mortar joints (reference model) for different FRP axial stiffness. It can be observed that the bond strength tends to decrease when the mortar becomes weaker, as expected. Moreover, the decrease in the bond strength increases for higher FRP axial stiffness. For $E_f t_f$=34.3 kN/mm, the maximum debonding force in the model without mortar is 7.5 kN, while it is 7.0 kN (–6%) for mortar M1 (with high quality) and 5.2 kN (–30%) for mortar M2 (with poor quality). For $E_f t_f$=20.2 kN/mm, the maximum debonding force in the model without mortar is 5.9 kN, while it is 5.5 kN (–6.14%) for mortar M1 and 5.2 kN (–10.9%) for mortar M2. For $E_f t_f$=8.4 kN/mm, the maximum debonding force in the model without mortar is 4.2 kN, while it is 3.9 kN (–5.7%) for mortar M1 and 3.8 kN (–9%) for mortar M2. The variation of bond strength with FRP axial stiffness is shown in Figure 7-17. The effect of high quality mortar in the bond strength seems negligible for the cases studied here. On the other hand, the bond strength decreased significantly in the models with poor quality mortar for higher values of FRP axial stiffness.

The effect of mortar joint quality on the bond strength is also investigated for different r (FRP width to brick width) ratios. Three different r ratios equal to 0.42, 0.7, and 0.9 are considered. The modeling strategy is to keep the brick width constant (120 mm) and increase the FRP width according to the corresponding r ratio. The bond strength variation for different r ratios and mortar quality is shown in Figure 7-18. The bond strength increases with the FRP width. Again, the mortar quality affects the bond strength, especially for higher FRP axial stiffness.

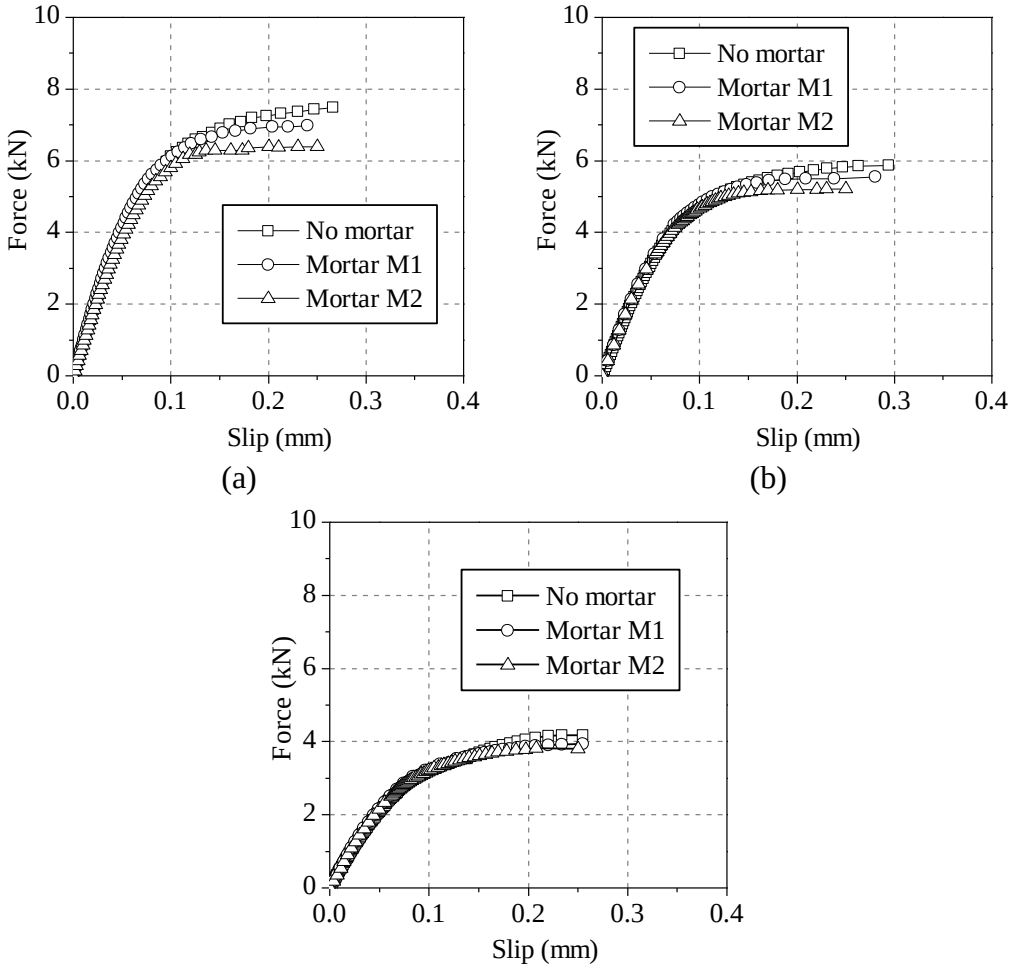

Figure 7-16: Force-slip curves for different mortar types and FRP axial stiffness for r=0.42: (a) $E_f t_f$=34.3 kN/mm; (b) $E_f t_f$=20.2 kN/mm; (c) $E_f t_f$ =8.4 kN/mm.

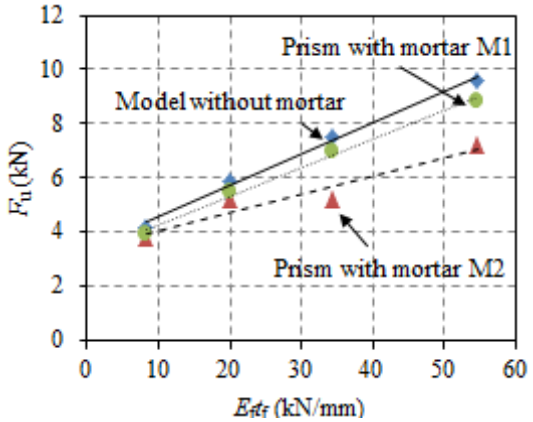

Figure 7-17: Variation of bond strength with FRP axial stiffness for r=0.42.

It is expected that the decrease in bond strength in the models with poor quality mortar can be regained by increasing the bond length. This is investigated by increasing the bond length in the M2 models from 160 mm to 190 mm. The 30 mm increase in bond length is equal to the total thickness of mortar joints. The results are shown in Figure 7-19 in terms of force-slip curves. It can

be seen that the original bond strength of the model without mortar has been regained, which is a much relevant result for practical applications.

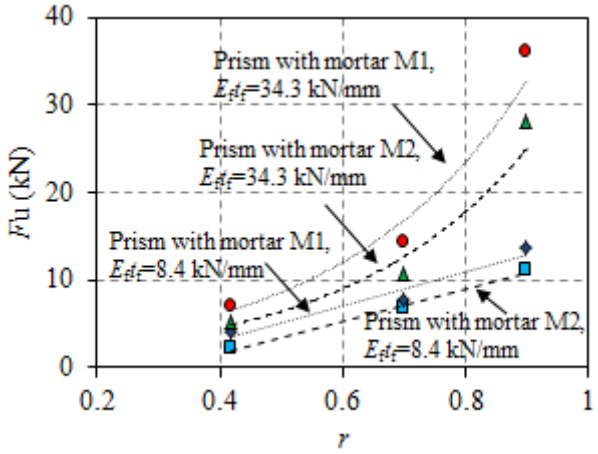

Figure 7-18: Effect of FRP width ratio, r, on the bond strength: (a) $E_f t_f$ =34.3 kN/mm; (b) $E_f t_f$ =8.4 kN/mm.

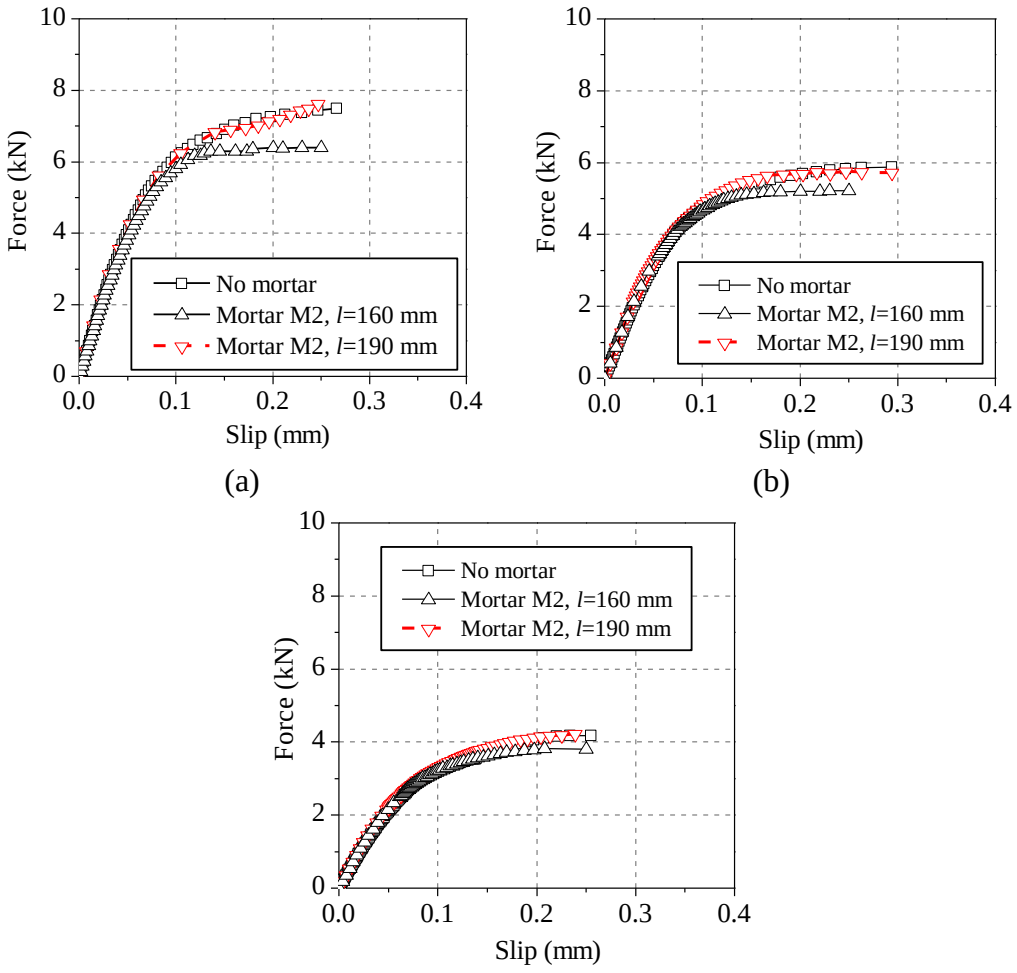

Figure 7-19: Effect of increase in the bond length in model M2 for r=0.42: (a) $E_f t_f$ =34.3 kN/mm; (b) $E_f t_f$ =20.2 kN/mm; (c) $E_f t_f$ =8.4 kN/mm.

7.2.4.2 Local stress and strain distributions

Investigating the local stress and strain distributions is crucial for the understanding of the interfacial behavior obtained in numerical models with a bond-slip law. Moreover, the three-dimensional nature of debonding can be investigated from the analysis of local stress and strain distributions.

The normal and shear stress distributions along the bonded length in the brick-adhesive interface are shown in Figure 7-20 for $E_f t_f$=34.3 kN/mm and P/P_u=1.0. The normal stress distribution in model M1 is similar to the reference model, with slightly higher stress values near the loaded end. The normal stresses of M2 exhibit fluctuations near the loaded end and the mortar joints. The shear stress distributions of the reference model and of model M1 have similar behavior, with only small differences near the loaded end. On the other hand, the shear stress distribution in model M2 shows sudden drops in correspondence of the mortar joints, due to the formation of large cracks. Moreover, a different distribution of stresses is observed between the FRP edge and middle in both M1 and M2 prisms, see Figure 7-21. This difference, being an evidence of three-dimensional nature of debonding problem, significantly increases with the FRP axial stiffness. However, for higher values of *r* ratio the difference between stress distributions along the FRP edge and middle decreases.

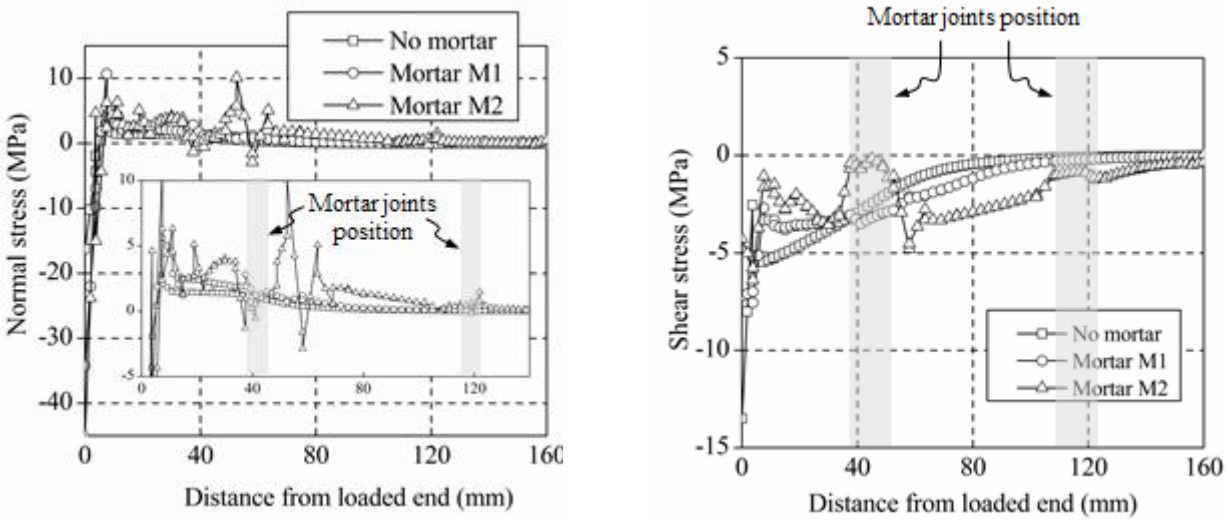

(a) (b)

Figure 7-20: Stress distributions along the bonded length at brick-adhesive section at the ultimate load level, P/P_u=1.0: (a) normal stress; (b) shear stress.

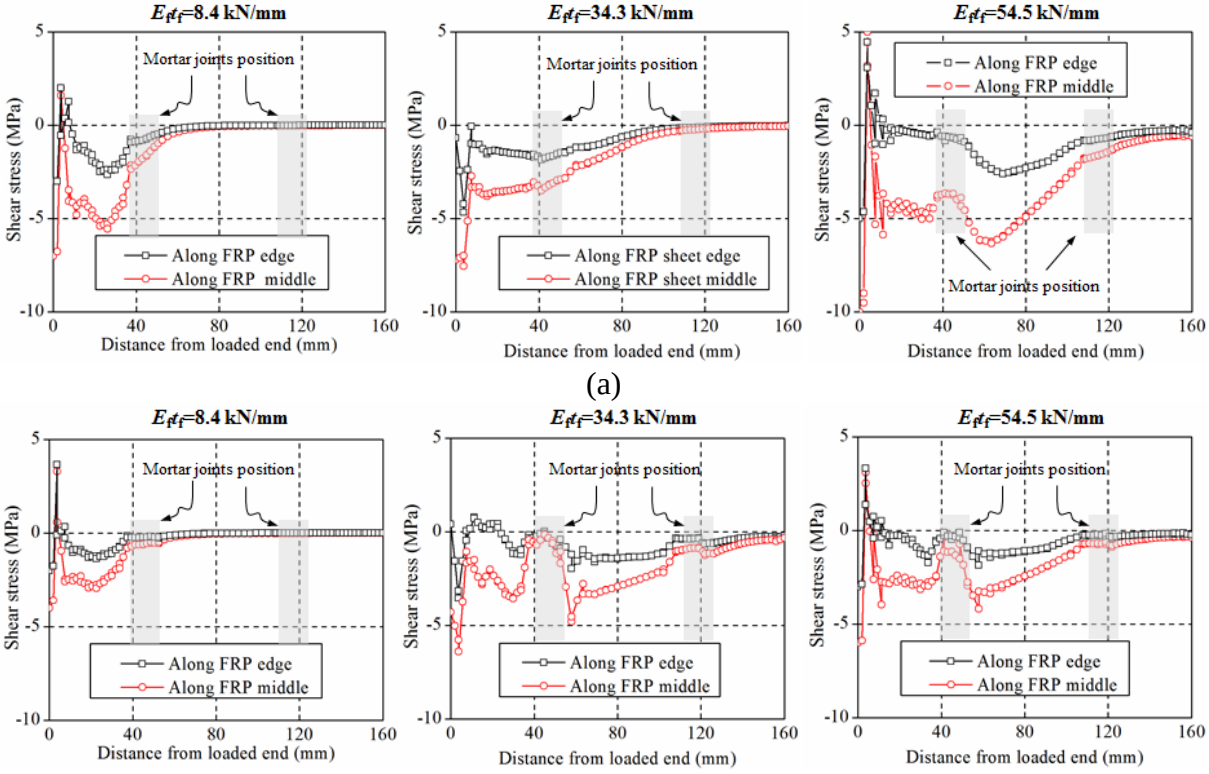

Figure 7-21: Shear stress distributions along the bonded length at the interface for P/P_u=1.0: (a) prism with mortar M1; (b) prism with mortar M2.

7.2.4.3 Local FE bond-slip behavior

The local bond-slip curves along the bonded length can be obtained from FE results. As an example, the bond-slip behavior at four different sections is presented in Figure 7-22 for the reference model, $E_f t_f$ =34.3 kN/mm and r=0.42. The sections are selected in such a way to understand the differences of local bond-slip behavior in the brick-adhesive and mortar-adhesive interfaces in different positions.

The numerical bond-slip curves obtained at sections 1 (first brick) and 2 (first mortar joint) are characterized by an almost bilinear trend with ascending and descending branches. The descending branch starts when the substrate material reaches its softening behavior due to the occurrence of large cracks. Such behavior is common in M1 and M2 models. The bond-slip curves evaluated at points 3 and 4 are characterized by an ascending branch with low slip values showing that these sections are still in their linear range of behavior. In the M2 model, brick and mortar in sections 1 and 2 have reached the maximum slip and the FRP has completely debonded in these sections. The bond strength in the brick-adhesive section, section 1, is 1.7 MPa. However, the bond strength in the mortar-adhesive section, section 2, is 1.5 MPa in model with mortar M1 and 0.5 MPa in model with mortar M2.

It can be seen that the response of the brick-adhesive and mortar-adhesive in terms of bond-slip curves can be different, especially when poor mortar quality is considered. This aspect requires further consideration when interface elements or bond-slip models are used. Possible solutions are to use an average bond-slip model or different bond-slip models for FRP-brick and FRP-mortar interfaces.

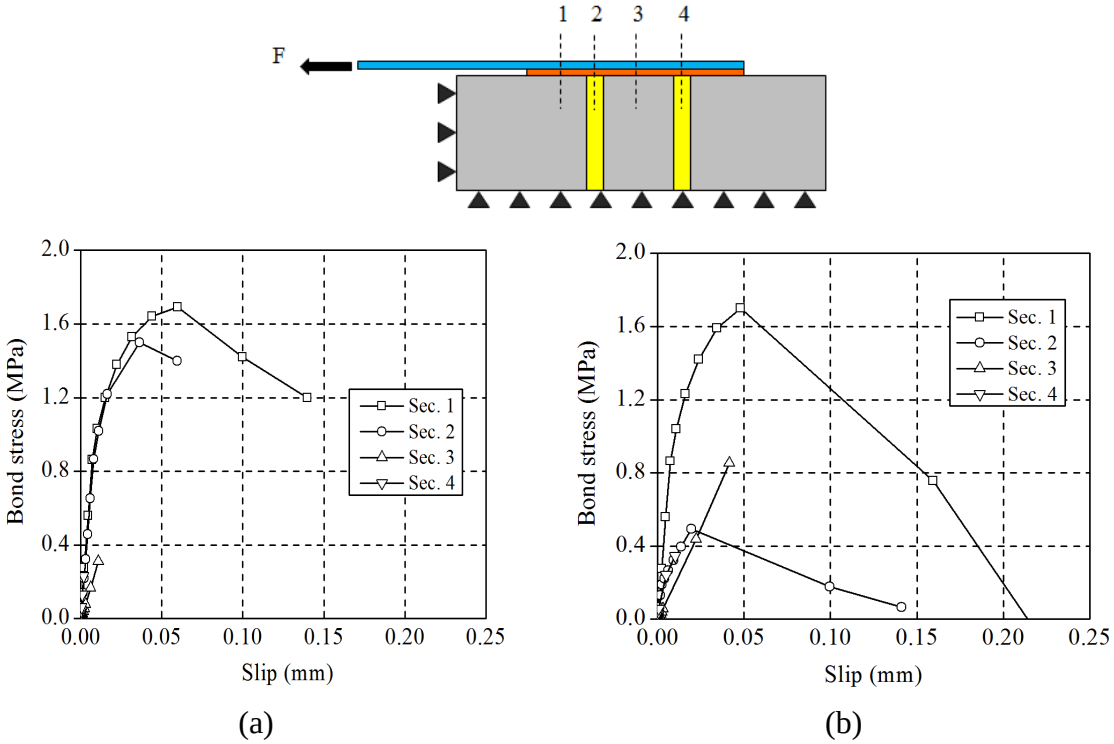

Figure 7-22: FE local bond-slip curves: (a) model with mortar M1; (b) model with mortar M2.

7.2.4.4 Crack distribution

As discussed before, the failure mechanism in the experimental tests using FRP-brick specimens involved only the external layer of the bricks. The crack patterns obtained at the peak load for the models with mortar joints are now illustrated in Figure 7-23 for two *r* ratios of 0.42 and 0.9. In case of *r* equal to 0.42 and mortar type M1, the cracks propagate slightly inside the masonry prism, while in model M2 they propagated in depth within the specimens. The crack propagation occurs especially near the mortar joints, as it is expected from the strain and stress distributions described. However, in the model with *r* equal to 0.9 the cracks propagated deeply inside the brick and mortar in both models, being deeper in model M2.

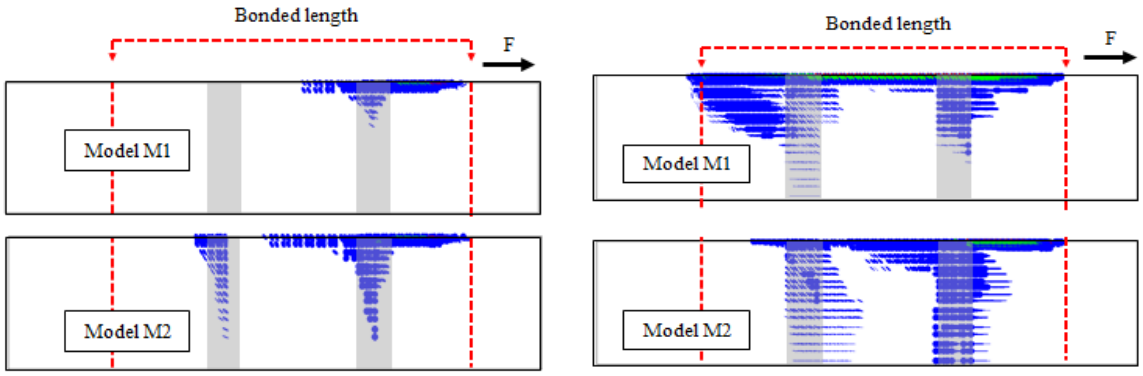

(a) (b)

Figure 7-23: Crack distributions for $E_f t_f$ =34.3 kN/mm and different r ratios: (a) r=0.42; (b) r=0.9.

7.3 Simplified modeling

7.3.1 Finite Element model

7.3.1.1 Outline

The numerical analysis is performed with a plane stress model in the FE code DIANA, see Figure 7-24. The adopted mesh includes eight-node plane stress elements (denoted as CQ16M) for representing the masonry unit, two-node truss elements (denoted as L2TRU) for the FRP strip, and six-node zero-thickness interface elements (denoted as CL12I) for the FRP-brick interface. The constraints and loading conditions are applied to the model as shown in Figure 7-24. An incremental monotonic displacement load is applied to the free end of the FRP strip for simulating the test conditions. A modified Newton-Raphson iterative scheme together with the line search method is used for solving the nonlinear equations.

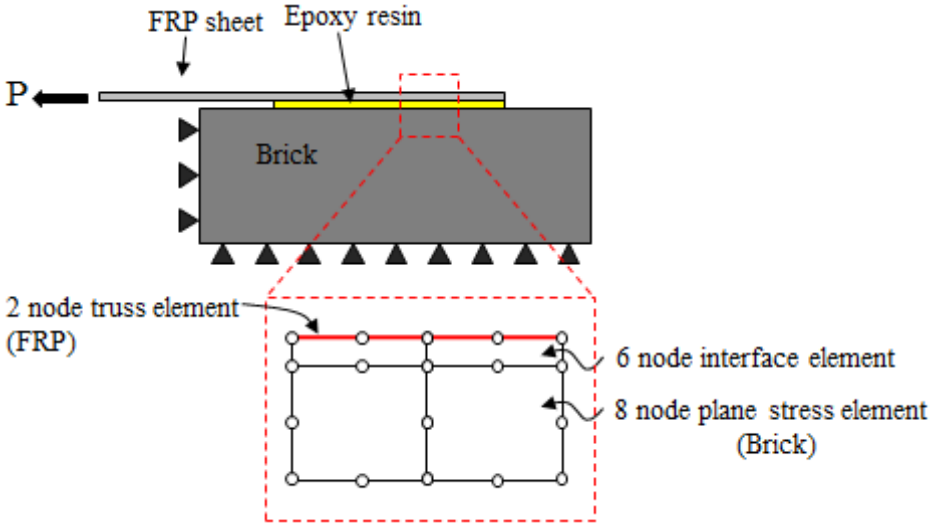

Figure 7-24: 2D finite element model.

7.3.1.2 Material models

Isotropic elastic material models are used for brick and FRP sheets. The validity of this assumption is discussed comprehensively in Section 7.4.2. The mechanical properties selected for brick and FRP sheets are those obtained from the tests.

Based on the observed local bond response of specimens, a bond-slip model is proposed for simulating the bond behavior, see Figure 7-25. The adopted bond-slip model is defined by four parameters being bond strength, $\tau_{\max}$, the slip value corresponding to the elastic limit, $s_\circ$, the slip at the end of the plastic branch, s_1, and the ultimate slip, s_u. These parameters are obtained for each composite material by performing a parametric study to obtain the best global (force–relative displacement behavior) and local (strain distribution along the bonded length) responses in comparison to the experimental results. The values adopted for these parameters are shown in the same figure.

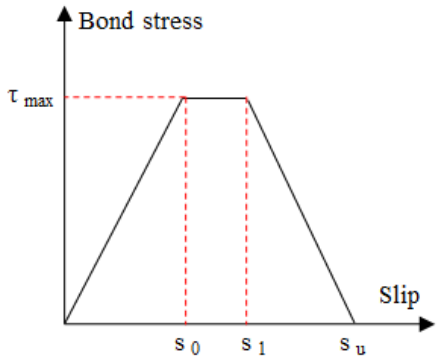

Specimen	τ_{max} (MPa)	s_0 (mm)	s_1 (mm)	s_u (mm)	G_f (N/mm)
CFRP	1.80	0.04	0.09	0.35	0.36
GFRP	1.20	0.03	0.10	0.45	0.31
BFRP	1.70	0.02	0.12	0.33	0.36
SRP	1.80	0.02	0.10	0.20	0.25

Figure 7-25: Proposed bond-slip model.

7.3.2 Model validation

7.3.2.1 Comparison with experimental results

The numerical results are compared with the experimental results in Figure 7-26 to Figure 7-28 in order to assess the reliability of the proposed model.

Figure 7-26 shows the comparison between the global force–relative displacement curves obtained from numerical analysis and the envelope of the experimental results. The numerical results fit the experimental results with reasonable accuracy. It can be seen that the bond strength, bond stiffness, and ductility have been simulated reasonably.

Accurate prediction of strain distribution along the bonded length is crucial in predicting the evolution of debonding and computing the effective transfer length, which are key issues in design procedures. It is observed in this study that the adopted bond-slip model plays an important role in predicting the strain distribution along the bonded length of the FRP sheets and its proper selection

is crucial in delamination problems. Figure 7-27 and Figure 7-28 show that the numerical strain distribution along the bonded length is in good agreement with the corresponding experimental values captured by the strain gauges. The comparison is made for P/P_u=0.4 and 0.8, corresponding to moderate and high levels of nonlinear behavior, respectively. To the knowledge of the authors, in the previous studies this comparison was usually made at low load levels such as P/P_u=0.2 in [53].

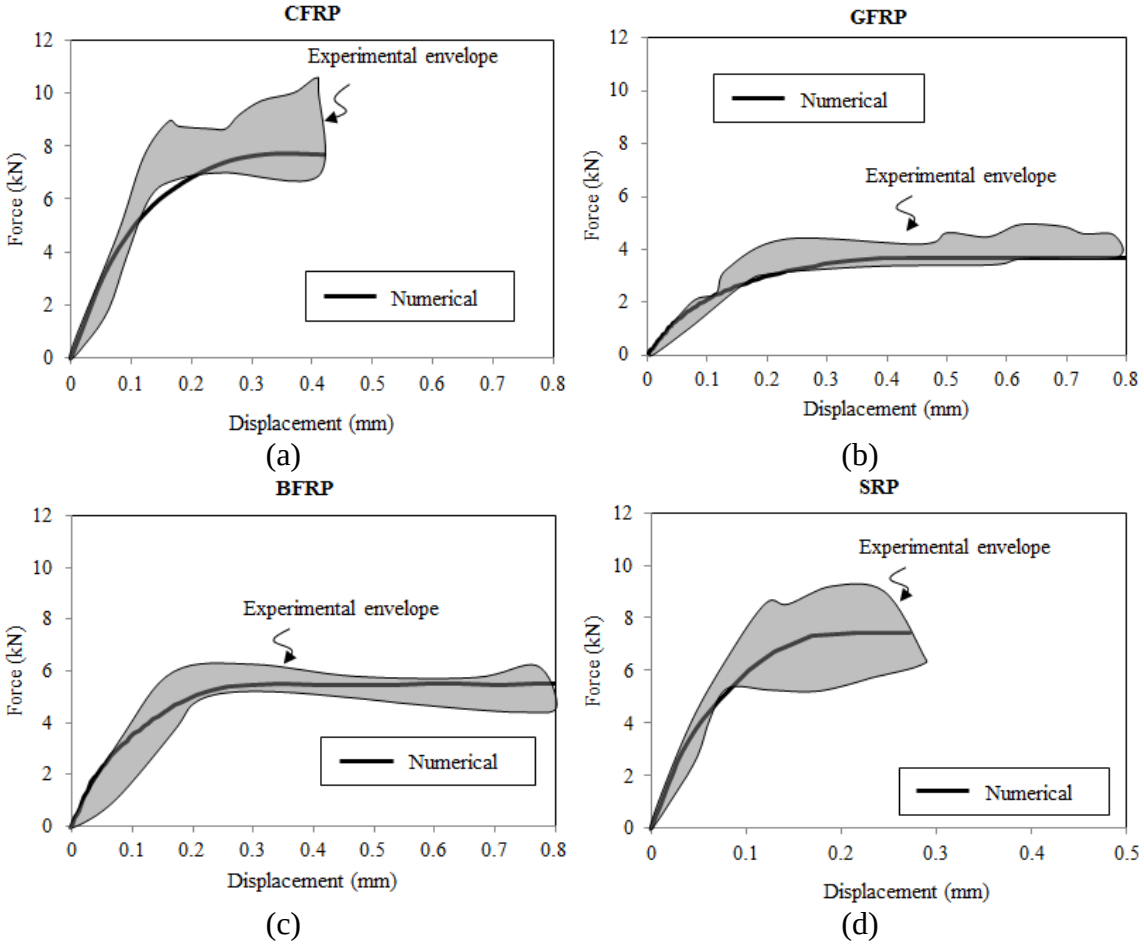

Figure 7-26: Force–relative displacement curves for all strengthened specimens: (a) CFRP; (b) GFRP; (c) BFRP; (d) SRP.

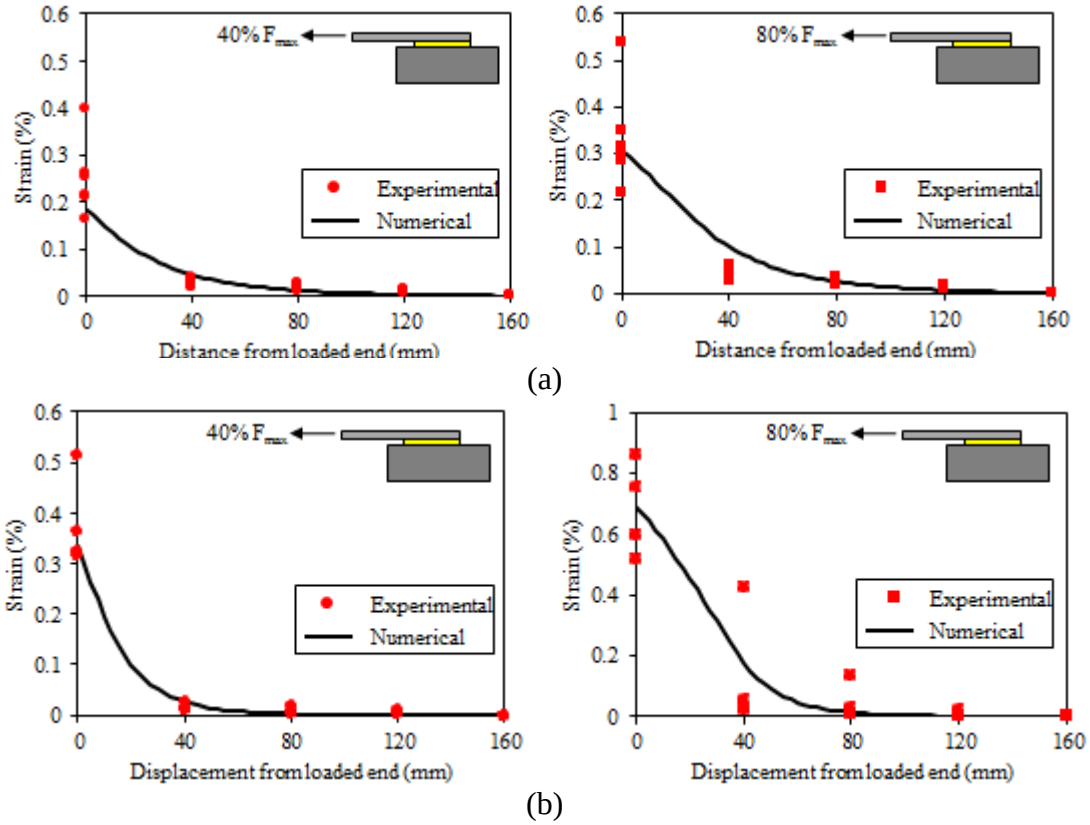

Figure 7-27: Strain distributions: (a) CFRP-; (b) GFRP-strengthened specimens.

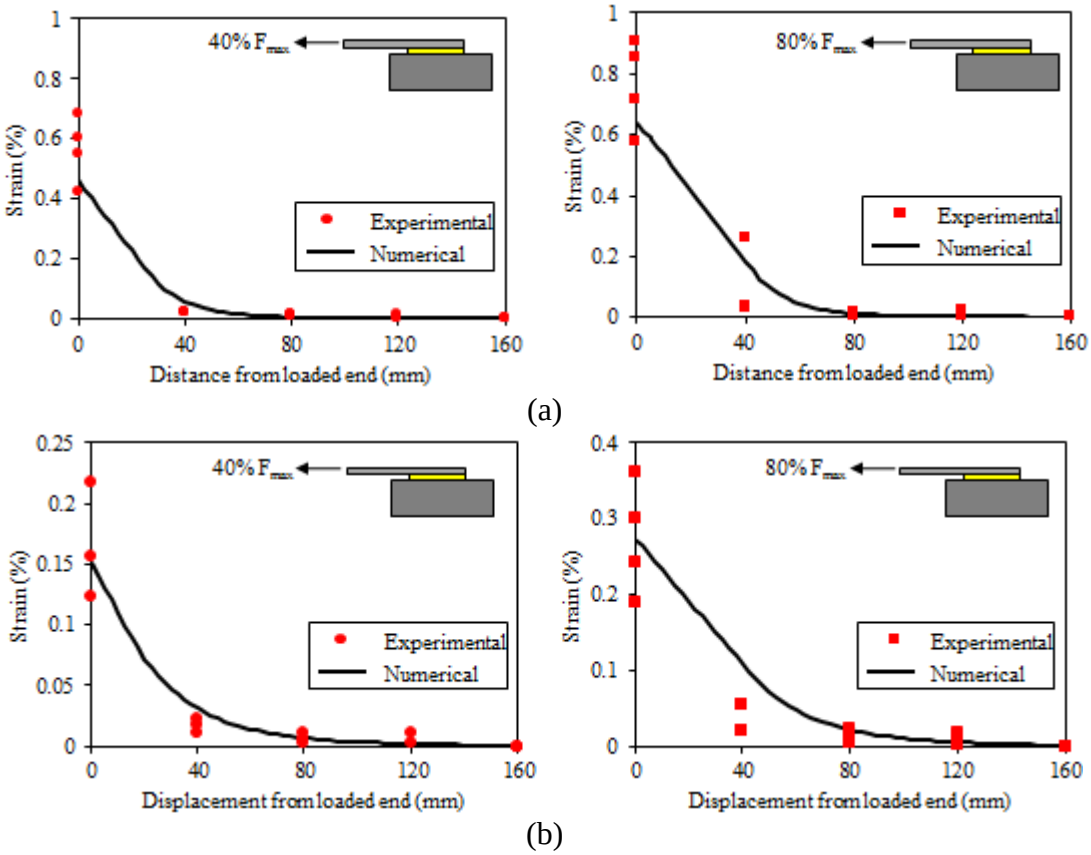

Figure 7-28: Strain distributions: (a) BFRP-; (b) SRP-strengthened specimens.

A comparison of the experimental local bond-slip behavior with the adopted bond-slip model is shown in Figure 7-29. It can be observed that the proposed bond-slip model fits the experimental bond behavior quite well.

BFRP- and GFRP-strengthened specimens have shear fracture energies comparable to CFRP-strengthened specimens, which can be attributed to the same failure mechanism, see Figure 7-25. BFRP- and GFRP-strengthened specimens exhibit higher ductility than SRP- and CFRP-strengthened specimens, see Figure 7-26. This similarity also exists in the case of effective transfer length. The effective transfer length in BFRP- and GFRP- strengthened specimens is around 80 mm and it is 120 mm in SRP- and CFRP-strengthened specimens, see Figure 7-27 and Figure 7-28.

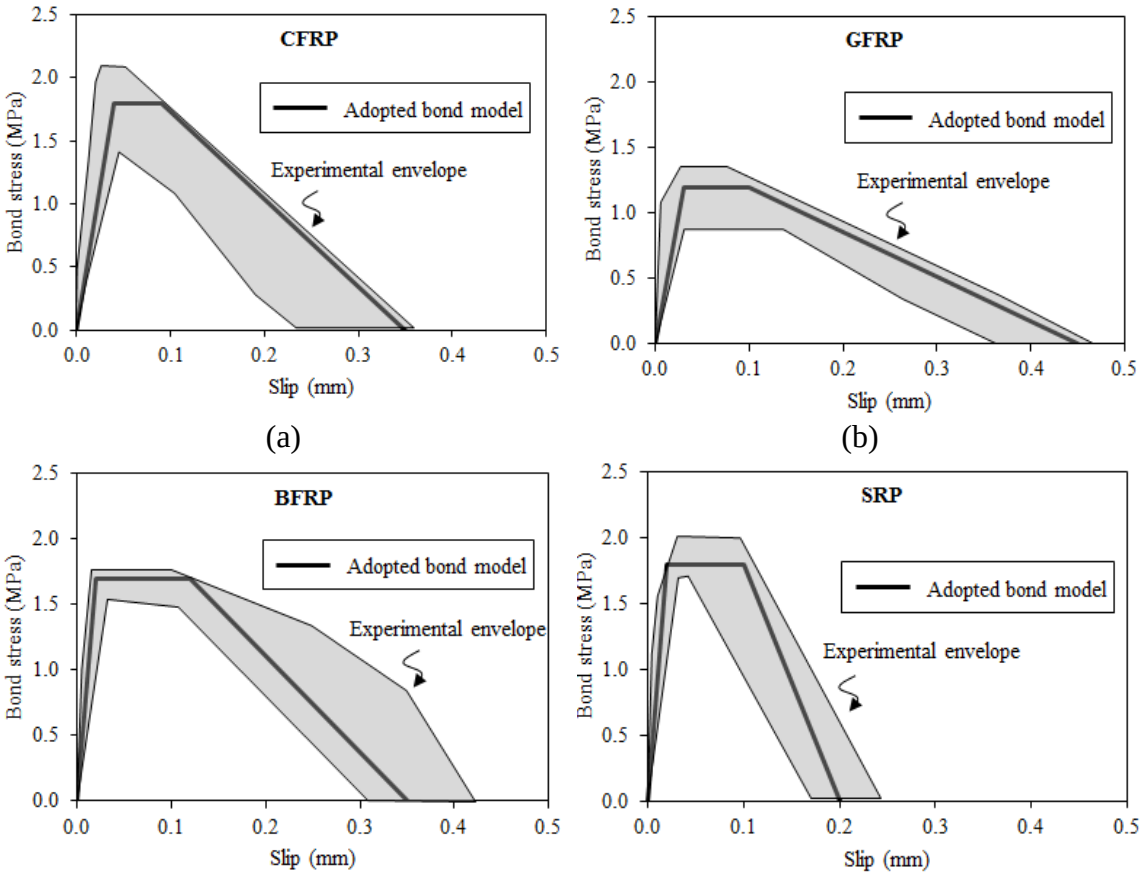

Figure 7-29: Comparison of the adopted bond-slip model and experimental bond behavior: (a) CFRP-; (b) GFRP-; (c) BFRP-; (d) SRP-strengthened specimens.

7.3.2.2 Verification of the model assumptions

The main assumption made in this modeling approach is that the brick and FRP composite materials are elastic and all the nonlinearities are concentrated in the interface region. This assumption is verified in this section by investigating the stress fields in the FRP and masonry brick.

The normal stresses along the FRP sheets at the ultimate stage of the nonlinear analysis are presented in Figure 7-30. The maximum stress values are considerably lower than the tensile strength of FRP composites given in Table 7-1, which confirms the elastic behavior of FRP strips in the analysis. This figure also shows that the maximum stress developed in the FRP sheets is almost the same for all FRP types, which can be attributed to the same failure mode observed in all specimens. The maximum principal stress distributions in the bricks are also controlled at the ultimate stage of the nonlinear analysis, see Figure 7-31. As expected, with the exception of some localized peak values, the tensile stresses in the bricks are lower than their corresponding strengths. The results show that FRP composites and bricks are in their elastic regime.

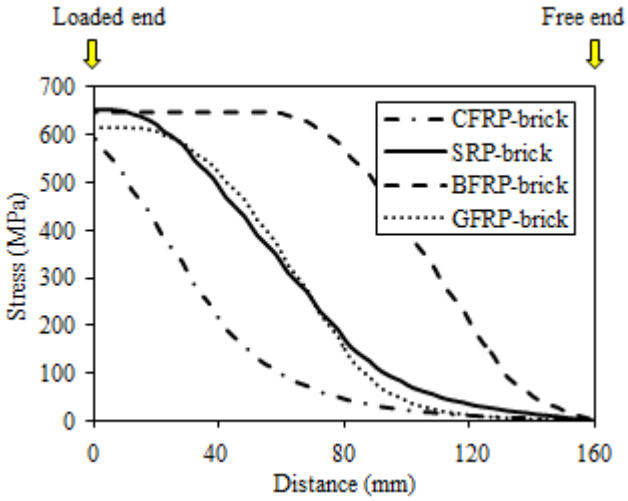

Figure 7-30: Normal stresses along the FRP composites.

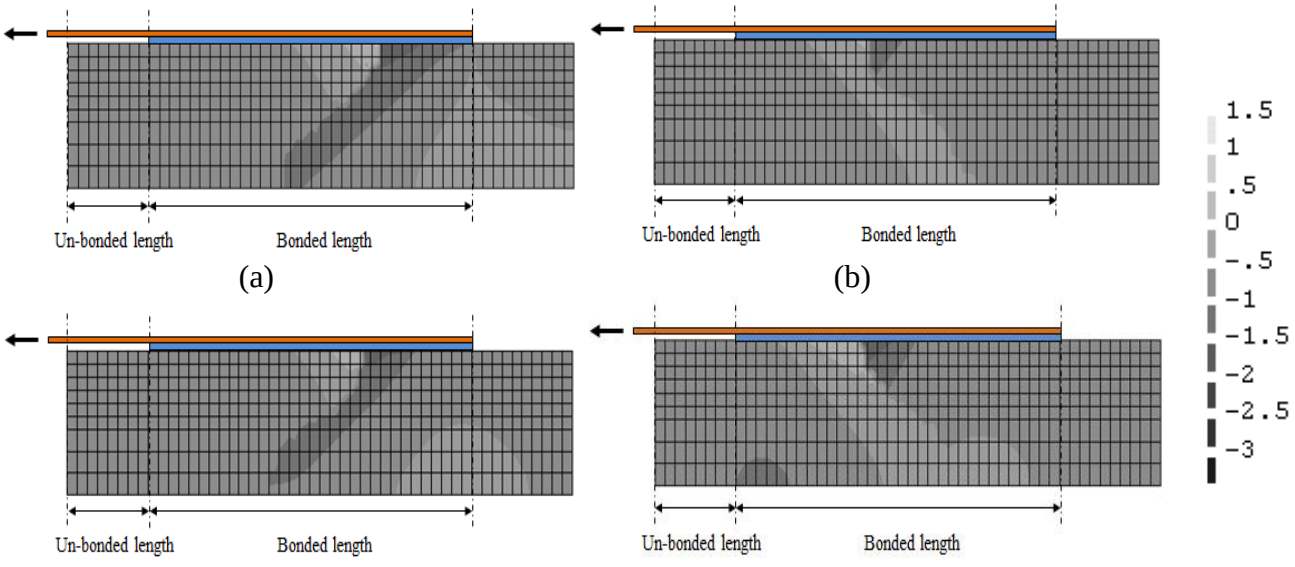

Figure 7-31: Stress contours in the bricks for the maximum principal stresses for all strengthened specimens: (a) CFRP; (b) GFRP; (c) BFRP; (d) SRP.

7.3.3 Discussion on guideline provisions

The proposed tri-linear bond-slip model is compared with the bond-slip model proposed in the Italian CNRDT200 provisions [1]. CNR DT200 proposes a bi-linear bond-slip model as illustrated in Figure 7-32. This model, which is provided for FRP-strengthened concrete elements but also used for masonry elements, can be obtained by identifying three parameters, namely the characteristic fracture energy, G_f, the elastic stiffness, k_1, and the ultimate slip, s_u.

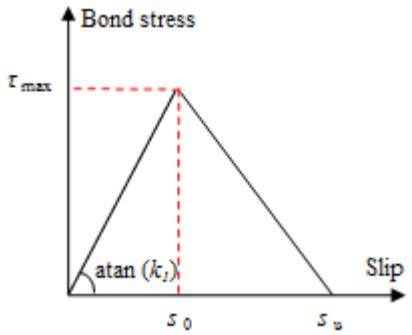

Figure 7-32: Bilinear bond-slip law proposed by CNR DT200.

A simplified relation is proposed in CNR DT200 for calculating the characteristic fracture energy of the FRP-masonry elements, defined as the area under the bond-slip curve:

$$G_f = c_1 \sqrt{f_{Mk} f_{Mtm}} \tag{7.5}$$

where c_1 is an empirical coefficient that should be obtained experimentally or can be assumed to be equal to 0.015, f_{Mk} is the characteristic compressive strength of masonry, and f_{Mtm} is the average masonry tensile strength. The characteristic compressive strength can be evaluated according to the Eurocode 6 [295], see Eq. (7.6), and the masonry average tensile strength can be assumed to be equal to 10% of the characteristic compressive strength according to CNR DT200. Another approach for obtaining the characteristic values is dividing the mean values by 0.7, which is followed in this study for obtaining the characteristic compressive strength of masonry bricks.

$$f_{Mk} = K f_{cb}^{0.7} f_{cm}^{0.3} \tag{7.6}$$

where K is assumed to be equal to 0.55, and f_{cb} and f_{cm} are the compressive strengths of brick and mortar, respectively. The slope of the elastic part of the bond-slip law can be calculated as:

$$k_1 = \frac{c}{\frac{t_a}{G_a} + \frac{t_M}{G_M}} \tag{7.7}$$

where for c a range of 0.5 to 0.7 is suggested (0.5 was selected for this study), t_a and t_M are the adhesive and masonry nominal thickness, and G_a and G_M are the adhesive and masonry shear modulus, respectively. For the value of ultimate slip, s_u in Figure 7-32, CNR DT200 suggests a range of between 0.2 and 0.3 mm. These parameters are calculated following the CNRDT200 approach and are presented in Table 7-4. Moreover, the corresponding bond-slip curves are compared with those proposed in this study in Figure 7-33.

Table 7-4: Parameters of the bond-slip model proposed by CNR DT200.

Specimen	c_1	c	K_1	τ_{max} (MPa)	G_f (N/mm)
CFRP	0.055	0.50	103.89	2.38	0.36
GFRP	0.048			2.20	0.31
BFRP	0.052			2.38	0.34
SRP	0.038			1.65	0.25

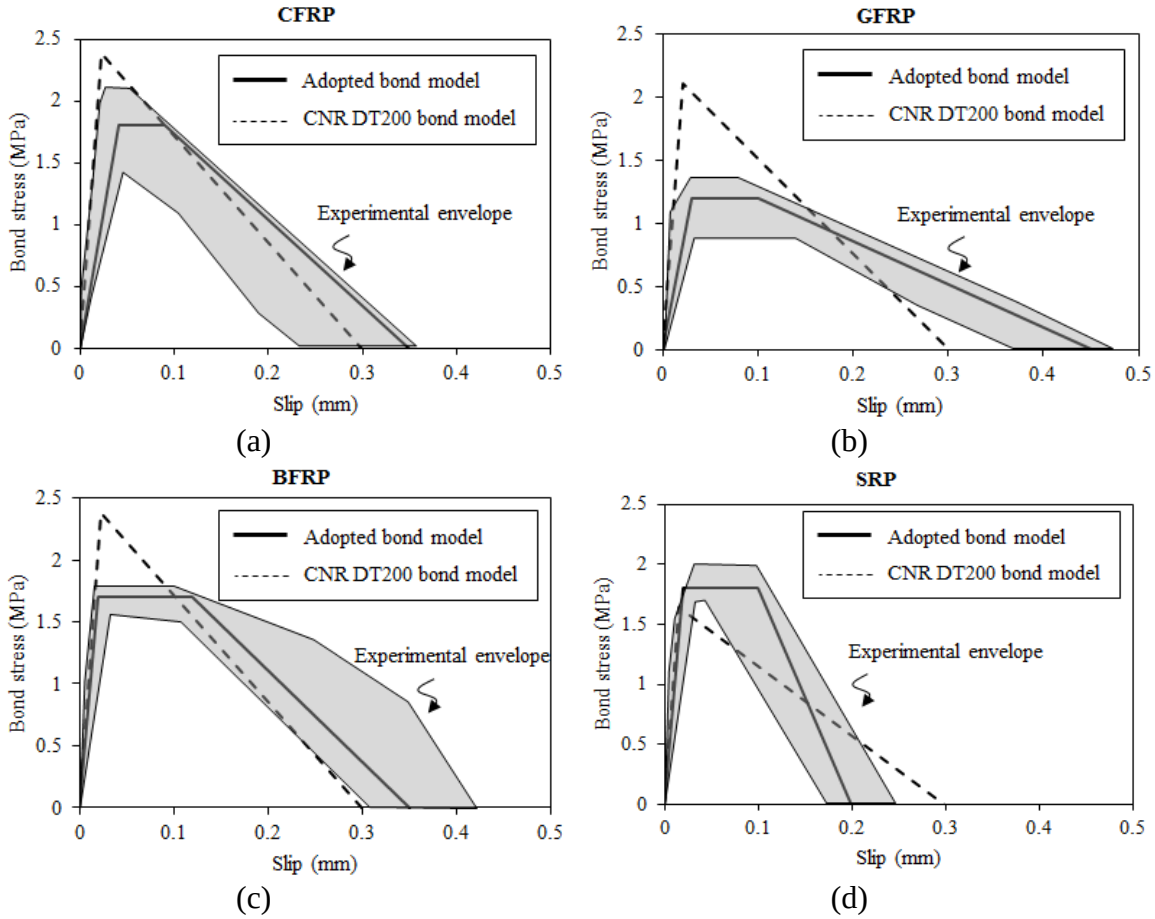

Figure 7-33: Bond-slip models proposed by CNR DT200 for all strengthened specimens: (a) CFRP; (b) GFRP; (c) BFRP; (d) SRP.

Assuming the value of 0.015 for the parameter c_1 resulted in a low fracture energy, 0.098 N/mm, compared to the experimental fracture energy. For this reason, this parameter is obtained experimentally by rewriting Eq. (7.5) as follows, see Table 7-5:

$$c_1 = \frac{G_f}{\sqrt{f_{Mk}\, f_{Mtm}}} \tag{7.8}$$

A comparison of the CNR DT200 bond-slip model with the proposed bond-slip model and experimental bond behavior, Figure 7-33, shows that the bond-slip model proposed by CNR DT200 differs slightly from the observed experimental bond behavior in GFRP-, BFRP-, and SRP-strengthened specimens. This difference is more clearly observed in the peak strength values, which are always higher than experimental and numerical results. The maximum slip differs slightly from the experimental envelope, see Table 7-6, but it does not greatly affect the global behavior since the same fracture energy has been obtained. The stiffness of the bond-slip model falls inside the experimental envelope when the parameter c is set equal to 0.5 as the best choice.

An issue worth noting is that the bond-slip model proposed in CNR DT200 is similar for different FRP types. For instance, the predicted bond-slip models for CFRP-, GFRP-, and BFRP-strengthened bricks are almost the same, while different behavior has been observed in the presented experimental and numerical results in terms of local bond behavior and global force–relative displacement curves. The results show that the bond-slip behavior is a function of mechanical properties of both the composite material and substrate, taking into consideration the governing failure mode, which should be considered in design procedures. However, it is still necessary to perform comprehensive experimental and numerical studies to propose such a general bond-slip model for FRP-strengthened masonry elements.

Table 7-5: Experimental values of parameter c_1.

Material	f_{mk} (MPa)	f_{mtm} (MPa)	G_f (N/mm)	c_1
CFRP	28.57	1.5	0.36	0.055
GFRP	28.57	1.5	0.31	0.048
BFRP	28.57	1.5	0.34	0.052
SRP	28.57	1.5	0.25	0.038

Table 7-6: Comparison of the values for ultimate slip.

Specimen	s_u (mm)		
	Experimental envelope	Proposed model	CNR DT200 [26]
CFRP	0.22–0.36	0.35	0.2-0.3
GFRP	0.37–0.48	0.45	
BFRP	0.31–0.43	0.33	
SRP	0.17–0.24	0.20	

7.4 Conclusions

Finite element analysis was used in this chapter to model the bond behavior between FRP and masonry. The modeling was conducted at two different scales.

First, a fully three-dimensional nonlinear model was adopted, in which FRP, epoxy and the brick substrate were modeled separately. Different smeared cracking models and mesh sizes were used to obtain numerical convergence and results that compare well to available experimental data. It was found that the rotating smeared crack model is suitable for predicting debonding. The accuracy of the model was verified by comparing the overall (force-slip curves) and local (strain distributions along the bonded length) response of the model with experimental results. The crack distribution and the failure mode were found in good agreement with the experimental results. It was shown that failure surfaces and crack propagation have a three-dimensional nature. In particular, the interfacial stress distributions were different along the FRP edge.

The effect of mortar joints on the bond behavior was studied by modeling two mortar joints along the bonded length. Different material properties were used for the mortar joints representing poor and high quality mortars. The effects of mortar joints were investigated on the global and local response of the strengthened elements. It was observed that a poor quality mortar may lead to a significant reduction of the bond strength. This effect reduces with decreasing FRP axial stiffness. It was also shown that a solution to regain the original bond strength is to increase the effective bond length in the presence of poor quality mortar. Moreover, the difference of stress distributions between the FRP edge and FRP middle sections was larger in the model with poor quality mortar. The effective bond length was observed to increase significantly in the model with poor quality mortar. The local bond-slip curves obtained from the FE results showed that the bond behavior is different in brick-adhesive and mortar-adhesive interface, with much larger slip in the model with

poor mortar quality. A solution to this problem for macro-modeling approaches is to use an average bond-slip model or different bond-slip models in brick-adhesive and mortar-adhesive interfaces.

Second, a simple two-dimensional plan stress model, in which the bond behavior is presented with interface elements, was adopted. Based on the available experimental results a simple tri-linear bond-slip model was proposed in this study to be used for the interface elements. The proposed bond-slip model was validated by comparing the experimental and numerical results. A good agreement was found between the analysis and experimental results in terms of global and local behavior. This agreements also found in highly nonlinear ranges of behavior (80% of the peak load), confirming the accuracy of the adopted method and appropriate selection of the bond-slip model.

A comparison was also performed between the proposed bond-slip model and the one proposed by the Italian design code CNR DT200, and some relevant aspects for design procedures were presented. It was shown that the code proposes the same bond-slip model for strengthened masonry with different FRP types. However, results presented in this study showed that the bond behavior varies from one FRP type to another, depending on the mechanical properties and governing failure mode.

Chapter 8

Bond degradation effects at structural level

The effect of accelerated environmental conditions on the bond behavior and mechanical properties of materials was investigated in Chapter 5. The observed degradation levels due to environmental conditions varied, being the highest degradation related to exposure HT1 (high humidity environment). However, it was not clear how these degradations at the material and interface level affect the global performance of the structure and this is the main subject of the present chapter.

The effect of local material degradation on the performance of FRP-strengthened masonry panels is now numerically investigated through FE modeling. The aim is to discuss how the global performance and failure mode of structural components change due to the local environmental induced degradation at material level.

A two-dimensional macro-modeling approach is used for modeling the masonry. Externally bonded FRP is attached to the surface of masonry panels with interface elements to account for the interfacial bond behavior. The structural model is initially validated by comparing the numerical results with experimental tests on the FRP-strengthened masonry panels. A good agreement is found between numerical and experimental results in terms of load-displacement curves and failure modes of the panels.

Once the model is validated against experimental results, the effect of environmental degradation on the performance of the strengthened panels is investigated. The procedure adopted is presented in Figure 8-1. The degradation data are taken from the experimental results presented and discussed in Chapter 5, which are subsequently used for obtaining the material properties at aged conditions. These material properties are then used as input for the numerical model to investigate the performance of the structure at aged conditions. The results obtained from numerical analysis are presented and critically discussed.

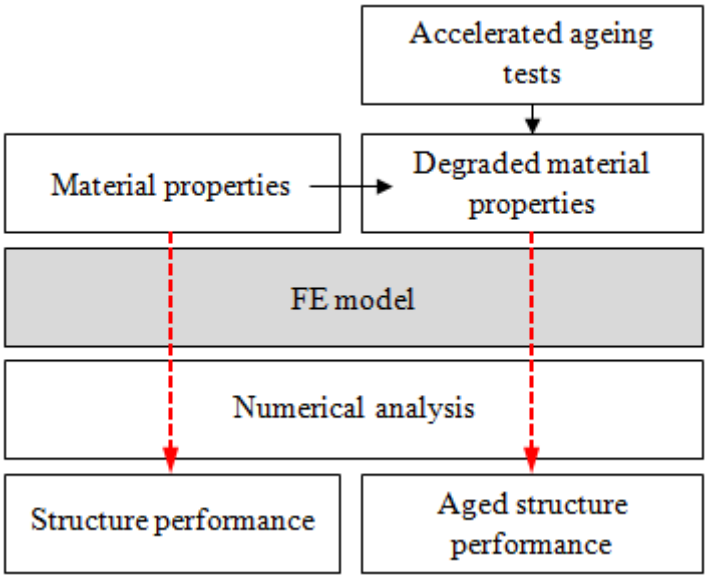

Figure 8-1: Procedure followed for modeling the performance of the structure at aged conditions.

8.1 Reference experimental tests

Reference tests are chosen, among available experimental tests on FRP-strengthened components, to serve as a basis for numerical validation. In this regard, the tests performed by Milani et al. [296] are used next.

Milani et al. [296] performed tests on small-scale masonry panels strengthened with CFRP strips to investigate the effectiveness of externally bonded reinforcement on the in-plane response of masonry walls. The specimens consisted of 9 panels of 290×270 mm^2 (L×H) named Pan A, Pan B and Pan C, and 3 panels of 416×414 mm^2 (L×H) named PanWin A and Pan Win B with a central opening with dimensions of 184×156 mm^2. The panels were built of small clay bricks with dimensions of 56×15 mm^2 and cement-lime mortar joints. The thickness of the walls was equal to 30 mm. Panels Pan A, Pan B and Pan C were placed on two steel plates with length of 40 mm disposed at the lower edge corners and positioned on steel rollers to allow rotation of the supports, see Figure 2-2. Series PanWin A and PanWin B were placed on two steel plates positioned directly on a stiff beam, precluding the rotation of the supports in this case.

Panels Pan A (bare masonry wall) and Pan C (strengthened panel with diagonal strips) are selected here for verification of the numerical model and also for investigating the effect of bond degradation on the performance of structural components. Geometrical details of the panels are shown in Figure 8-2. In Pan C, the reinforcement consists of CFRP strips with 12.5 mm width and 0.2 mm thickness applied on both sides of the wall. The elastic modulus of FRP strips was 160 GPa.

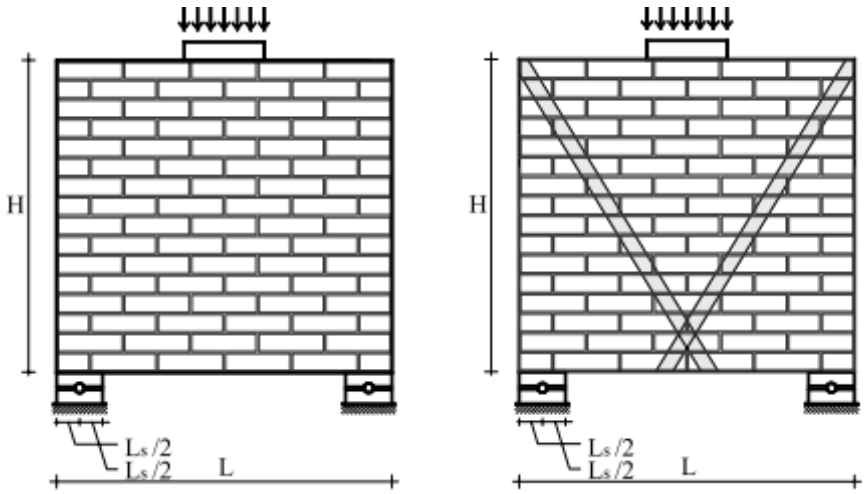

(a) (b)

Figure 8-2: Geometrical details of panels tested by Milani et al. [296]: (a) Pan A; (b) Pan C.

The panels were loaded vertically with the aim of a steel plate with dimensions of 70×30 mm^2. The loads were applied by means of a 100 kN load cell and the displacements were measured with two LVDTs placed on top of the walls, next to the load cell (on the steel plate used for load application). The mechanical parameters of masonry panels obtained based on experimental results and theoretical considerations and also were used for numerical modeling in [296, 297] are presented in Table 8-1. Here, *x* is the bed joint direction and *y* is the head joint direction.

Table 8-1: Masonry mechanical parameters.

Masonry mechanical parameters		
Elastic modulus along x-direction	E_{xx} (MPa)	1400
Elastic modulus along y-direction	E_{yy} (MPa)	1050
Poisson's ratio	v_{xy}	0.18
Shear modulus	G_{xy} (MPa)	370
Tensile strength along x-direction	f_{tx} (MPa)	0.8
Tensile strength along y-direction	f_{ty} (MPa)	0.2
Compressive strength along x-direction	f_{cx} (MPa)	8.0
Compressive strength along y-direction	f_{cy} (MPa)	6.7
Fracture energy in tension along x-direction	G_{ftx} (N/mm)	0.02
Fracture energy in tension along y-direction	G_{fty} (N/mm)	0.02
Fracture energy in compression along x-direction	G_{fcx} (N/mm)	5.0
Fracture energy in compression along y-direction	G_{fcy} (N/mm)	10.0

The experimental load-displacement curves of the panels are presented in Figure 8-3. The FRP strips increases about three times the panel strength. Regarding the observed failure mode, Pan A (bare masonry panel) failed due to cracking of masonry showing vertical tensile cracks followed by a relatively ductile behavior. In case of Pan C (strengthened panel), vertical and diagonal cracks were observed in the masonry panel combined with delamination of FRP strips at the lower extremes.

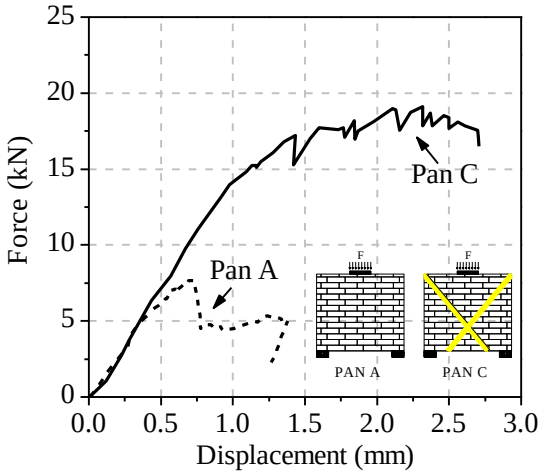

Figure 8-3: Experimental behavior of Pan A and Pan C

8.2 Finite element model

8.2.1 Outline

A two-dimensional nonlinear Finite Element (FE) model is adopted for modeling the behavior of the panels. For the masonry, a macro-modeling strategy is followed using a softening anisotropic elasto-plastic continuum model [298]. The FRP strips, which are assumed to have linear elastic behavior, are attached to the masonry surface using interface elements.

The boundary conditions are applied as given in the reference experimental tests. The panels are placed on two steel plates which are constrained against vertical displacements at their center and which allow rotation of the wall base. A monotonic incremental load is applied on top of the wall according to the experimental test setup, see Figure 8-2.

The analysis is carried out in the FE code DIANA [289]. The adopted mesh includes eight-node (denoted by CQ16M) and 6-node plane stress elements (denoted by CT12M) to model the masonry panel. The FRP strips are modeled, in a simplified way, with truss elements (denoted by

LT2RU), and 6-node zero-thickness interface elements (denoted as CL12I) are used for the FRP-masonry interface. A schematic view of the adopted FE mesh is shown in Figure 8-4.

The nonlinear analysis is performed by incremental application of the load until specimen failure. The arc-length method, combined with the linear stiffness iteration method and an energy norm criterion is adopted to solve the resulting system of non-linear equations.

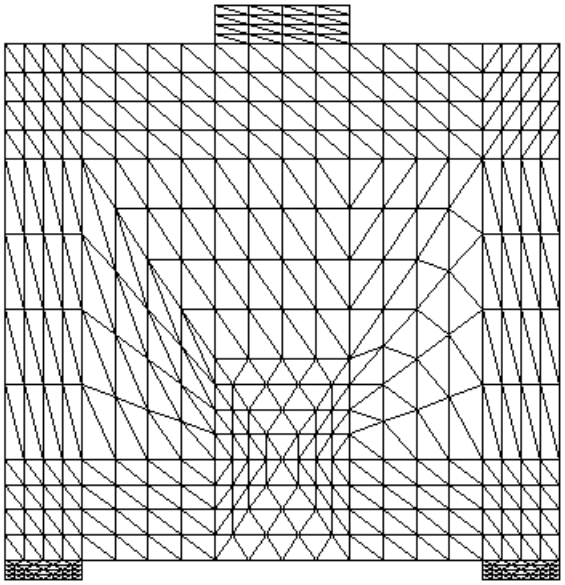

Figure 8-4: Adopted FE mesh for PAN A and PAN C.

8.2.2 Material models

The softening anisotropic elasto-plastic continuum model used for modeling the masonry behavior is based on the studies of Lourenço et al. [298]. This model consists of an extension of conventional formulations for quasibrittle materials to describe the orthotropic behavior. A Hill-type yield criterion in compression and a Rankine-type yield criterion in tension are used as yield functions. The nonlinear behavior in compression is characterized by parabolic hardening followed by parabolic/exponential softening, while exponential softening is used for tension. A detailed explanation of the material model and its theoretical background can be found in [298]. The material parameters used for masonry are presented in Table 2-1. Additionally, three factors called α, β and γ are required for this material model which are taken equal to 1.73, –1.05 and 1.2 as suggested in [297]. Here, α accounts for the contribution of shear stress in tensile failure, β couples the normal compressive stresses and γ considers the contribution of shear stress in compressive failure. The equivalent plastic strain corresponding to the peak compressive stress is taken as 0.0008.

Isotropic elastic material models are used for FRP strips. For the interface elements, since there is no information available regarding the bond behavior between FRP composites and masonry panels in the selected experimental tests, the bond parameters are taken from Chapter 6, see Figure 7-25, and are calibrated next, see Table 8-2.

Table 8-2: Bond-slip law parameters.

Exposure	τ_{max} (MPa)	S_0 (mm)	S_1 (mm)	S_u (mm)
No ageing	2	0.03	0.12	0.45

8.2.3 Comparison of experimental and numerical results

The accuracy of the adopted macro-modeling approach is assessed in this section by comparing the obtained numerical results with the experimental results.

The load-displacement curves obtained from numerical modeling are compared with the experimental results in Figure 8-5. The displacements are obtained at the same point of loading similar to experimental tests. It can be observed that the numerical model shows a good agreement with experimental results for both un-strengthened (Pan A) and strengthened (Pan C) panels. The developed plastic strains in the panels at the peak load level are presented in Figure 8-6. Similar to experimental results, Pan A has flexural cracks at the bottom while vertical cracks are occurred in Pan C at higher load levels. The results show the accuracy of the adopted model in numerical modeling and therefore it will be used in the next section to investigate the effect of local bond degradation on the global performance of the strengthened panels.

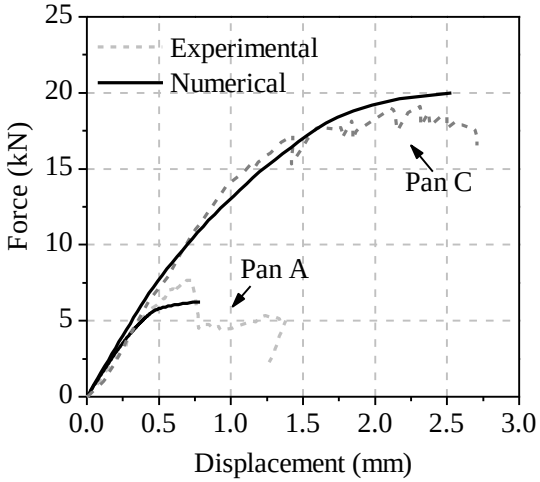

Figure 8-5: Comparison between numerical and experimental results.

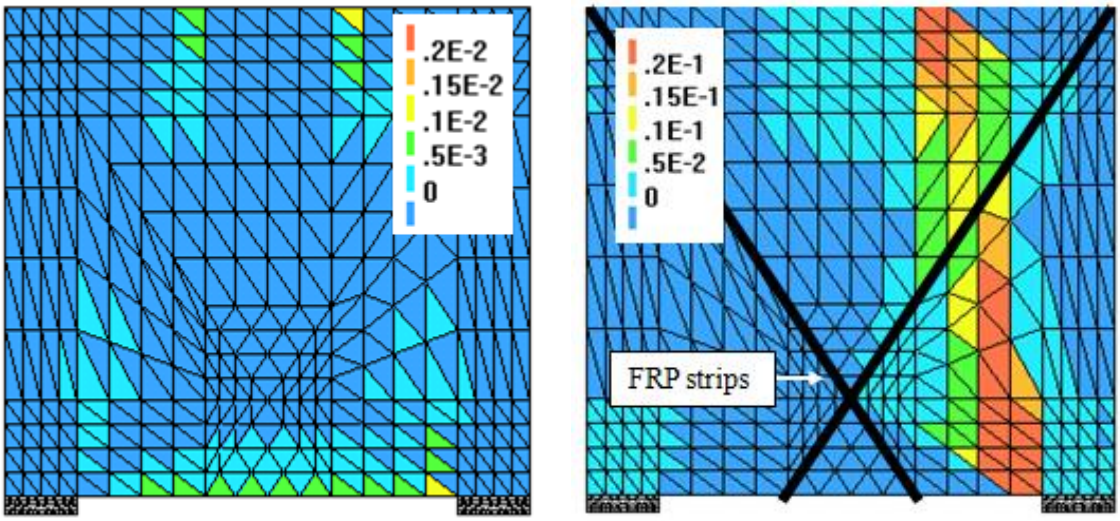

(a) (b)

Figure 8-6: Plastic strains in: (a) Pan A; (b) Pan C.

8.3 Effect of bond degradation on the structure performance

The effect of bond degradation on the global performance of FRP-strengthened panels is investigated in this section. Two hypothetical FRP-strengthened panels with different strengthening configurations and ratio, and different types of load application are used to investigate the dependency of the results on ageing.

The panels are first analyzed without considering any degradation to obtain the initial response of the structure. The analysis is then repeated with the degraded material properties including the bond and FRP mechanical properties. The degradation data are taken from accelerated ageing results (presented in Chapter 5) at 225 cycles of HT1 (temperature cycles of +10°C to +50°C with 90% constant relative humidity), HT2 (temperature cycles of +10°C to +50°C with 60% constant relative humidity) and FT exposures (temperature cycles of –10°C to +50°C with 90% constant relative humidity). 225 cycles is selected at the end of exposure HT1 to avoid extrapolation of the degradation data. Since no degradation was observed in the mechanical properties of bricks, this material is assumed intact after degradation. The changes in the global performance of the panels and a detailed discussion of the obtained results are presented next.

8.3.1 Strengthened panels

The first hypothetical panel considered, Pan C1, is similar to Pan C, see Figure 8-2 with the exception of the FRP material used for strengthening. Here, a GFRP composite is used for

strengthening of the panels with elastic modulus of 80 GPa and equivalent thickness of 0.48 mm. GFRP is selected due to the fact that the degradation data produced in experimental studies of this thesis are for the bond degradation between this composite material and bricks.

The second hypothetical panel, called Pan D, has the same dimensions as Pan C (290×270 mm^2) with different strengthening configuration and loading conditions, see Figure 8-7. The strengthening in this panel includes two vertical GFRP strips attached to the masonry surface neat the panel edges. The panel is loaded horizontally through a steel plate placed on top of the wall. At its bottom, the panel is completely constrained against horizontal and vertical displacements. The material properties used for masonry behavior in both panels are the same as presented in Table 8-1.

In both panels, FRP strips with widths of 6 mm, 12.5 mm and 25 mm are used to investigate the effect of FRP axial stiffness on the performance of the panels. The numerical load-displacement curves of the panels before and after strengthening (with different FRP widths) are presented in Figure 8-8. The behavior of Pan C1 remains unchanged from the tested specimen. Before strengthening, Pan D has a cantilever behavior with a low peak strength and flexural rocking failure mode. The tensile plastic strains at the bottom of the wall indicate the occurrence of this failure mode, see Figure 8-9 (a). After strengthening, the peak strength of the wall increases, cracking and the associated loss of stiffness is delayed, and the failure mode changes to diagonal tensile cracking. As an example, the distribution of tensile plastic strains at the peak load in the model with 12.5 mm FRP width is shown in Figure 8-9 (b). The observed diagonal compression chord shows the change of failure mode in this model, when compared to the model before strengthening.

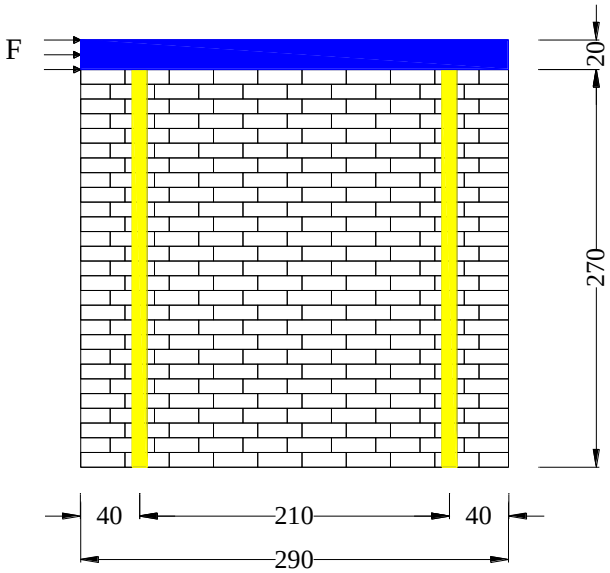

Figure 8-7: Geometrical details of Pan D.

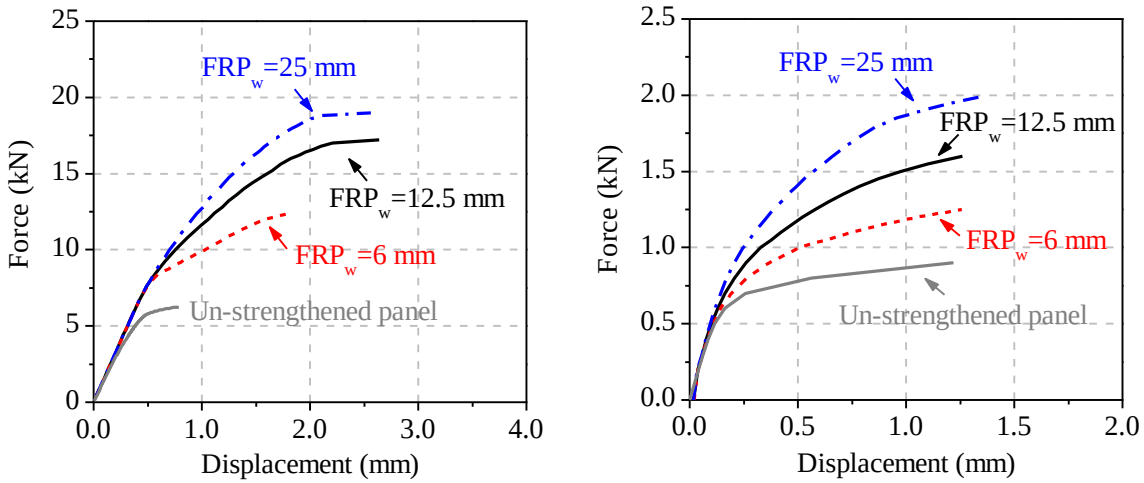

Figure 8-8: Load-displacement curves of panels before and after strengthening: (a) Pan C; (b) Pan D.

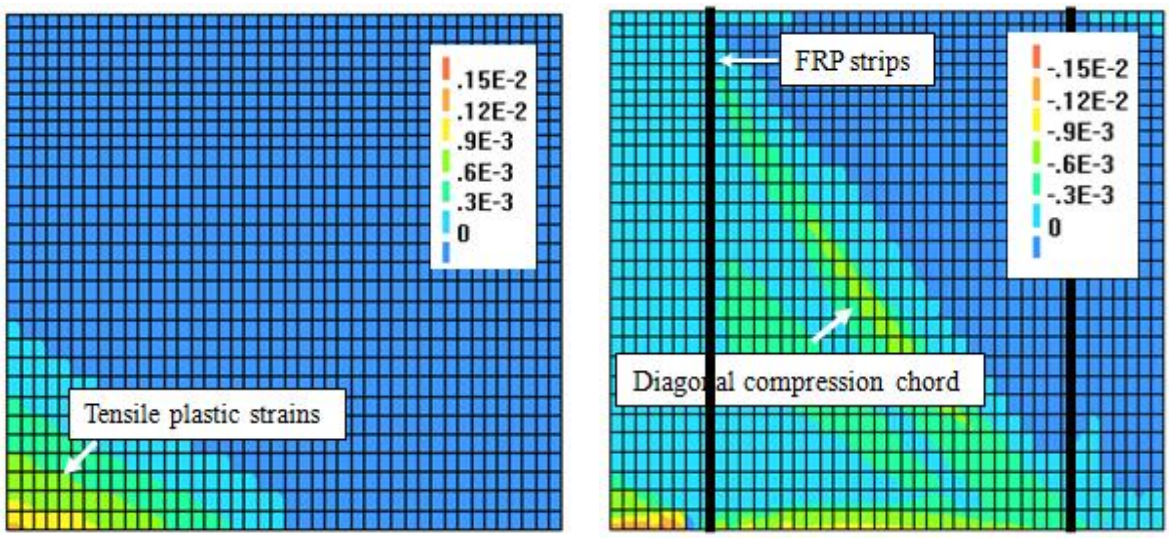

Figure 8-9: Tensile plastic strains in Pan D: (a) bare panel; (b) strengthened panel.

8.3.2 Materials degradation

The degraded material properties including bond and FRP mechanical characteristics are used in the numerical model for modeling the structure at aged conditions. The reduction factors and the degraded material properties after 225 cycles of HT1, HT2 and FT exposures, taken from Chapter 5, are presented in Table 8-3. Here, it is noted that only the value of the fracture energy of the bond is shown, even if the bond peak load is also reduced according to the tests. As the bond peak load is related to bond fracture energy and FRP axial stiffness, its degradation is automatically considered in the model.

For the FRP, the degraded elastic modulus is used as the input of the numerical model, while the tensile failure of the strips is controlled at the end of the analysis by comparing the numerical stresses in the FRP strips with the degraded tensile strength values given in Table 8-3 for each exposure condition.

Table 8-3: Material degradation after 225 cycles of all exposures.

Exposure	Bond properties		FRP properties			
	G_f		E_{tf}		f_{tf}	
	Red.	Value (N/mm)	Red.	Value (GPa)	Red.	Value (MPa)
No ageing	0%	0.54	0%	80	0%	1250
HT1	-60%	0.22	-23%	62	-22%	975
HT2	-25%	0.41	-9%	73	-13%	1088
FT	0%	0.54	-14%	69	-7%	1163

For the bond behavior, the tri-linear bond-slip law proposed in Chapter 6 and calibrated in sec. 8.4.3 is used. A simple degradation model is assumed for the bond-slip law to consider the bond environmental degradation, see Figure 8-10. Based on this model, the bond strength and inelastic stiffness decrease according to the degradation in the bond fracture energy, while the other slip parameters remain constant. The changes in the bond-slip law according to the fracture energy degradation data are presented in Table 8-4.

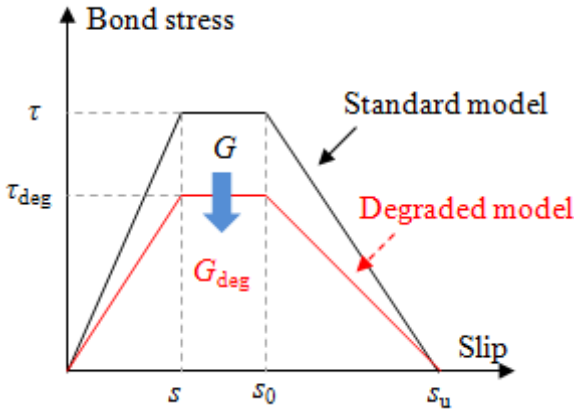

Figure 8-10: Degradation model for the bond-slip law.

Table 8-4: Bond-slip parameters at 225 cycles of all exposures.

Exposure	τ_{max} (MPa)	S_0 (mm)	S_1 (mm)	S_u (mm)
No ageing	2	0.03	0.15	0.45
HT1	0.8	0.03	0.15	0.45
HT2	1.5	0.03	0.15	0.45
FT	2	0.03	0.15	0.45

8.3.3 Analysis results

The force-displacement curves of panels type Pan C1 before and after ageing in exposures HT1 and HT2 are shown in Figure 8-11. Exposure FT did not induce any changes in the specimens and therefore the force-displacement curves are not presented here. This was expected as the only influence of exposure FT was 14% reduction of FRP elastic modulus. In general, the peak load and stiffness of the specimens show a negligible change after exposure to HT2 conditions, while exposure HT1 induced more reduction of the peak load and post cracking behavior. It seems that the axial stiffness and strength of FRP affect the reduction level as more reduction is observed in the peak load of the specimens with 6 mm width FRP, see Figure 8-11 (a). This seems acceptable and indicates that the amount of FRP was excessive in terms of wall capacity, i.e. for larger widths failure is mostly controlled by the masonry.

The changes in the peak load of the panels as well as the failure mode are tabulated in Table 8-5 for all the exposure conditions. 26%, 6% and 4% reduction of the peak load is observed in the specimens aged in HT1 conditions with FRP widths of 6 mm, 12.5 mm and 25 mm, respectively. The local bond degradation has therefore a major effect when smaller FRP widths are used, which is expected in real applications as FRP as the amount of FRP should be optimized (note that panel failure load increases only about 10% when the FRP width is doubled from 12.5 mm to 25 mm). The failure of the panels is generally tensile cracking of masonry, although a change of failure mode to FRP delaminations after ageing is observed in some panels, see Table 8-5.

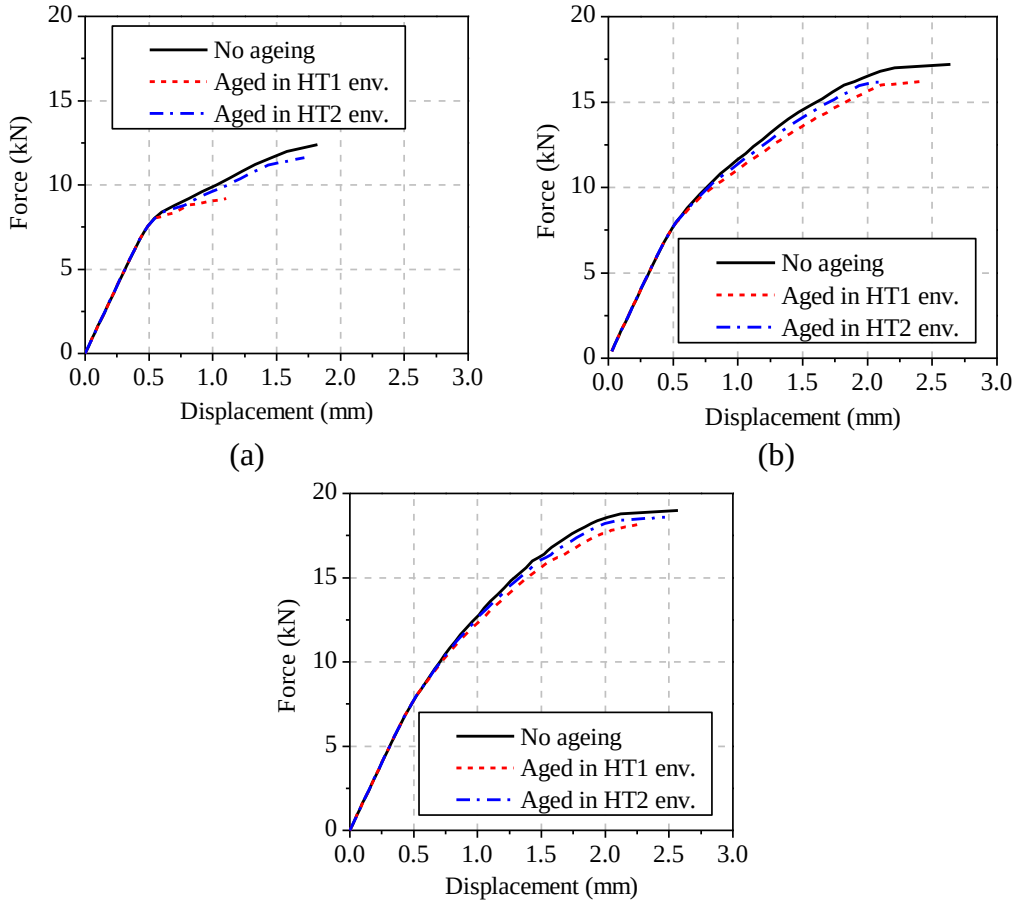

Figure 8-11: Force-displacement behavior of Pan C before and after ageing: (a) FRP_w=6 mm; (b) FRP_w=12.5 mm; (c) FRP_w=25 mm.

Table 8-5: Peak strength and failure mode of PAN C before and after ageing.

FRP_w (mm)	Exposure	P_{max} (kN)	Reduction (%)	Failure mode	FRP delaminations
6	No ageing	12.4	-	FRP tensile rupture	N
	HT1	9.2	25.8	Masonry tensile cracking	Y
	HT2	11.6	6.5	FRP tensile rupture	N
	FT	12.4	0.0	FRP tensile rupture	N
12.5	No ageing	17.2	-	Masonry tensile cracking	Y
	HT1	16.2	5.8	FRP tensile rupture	Y
	HT2	17.1	0.6	Masonry tensile cracking	Y
	FT	17.1	0.6	Masonry tensile cracking	Y
25	No ageing	19.0	-	Masonry tensile cracking	Y
	HT1	18.2	4.2	Masonry tensile cracking	N
	HT2	18.6	2.1	Masonry tensile cracking	Y
	FT	19.00	0.0	Masonry tensile cracking	Y

Regarding panels type Pan D, again the effect of exposure FT was negligible on the peak loads and load-displacement curves of the panel. The force-displacement curves of the panels

before and after ageing in exposures HT1 and HT2 are shown in Figure 8-12. In general, the peak load and stiffness of the specimens show a negligible change after exposure to HT2 conditions, while exposure HT1 induced more reduction of the peak load and post cracking behavior. The FRP width has an opposite effect on the reduction level comparing to Pan C1 panels, which is partly unexpected (note that here the panel failure load is more sensitive to the amount of FRP used, an increase about 25% is found when the FRP width is doubled from 12.5 mm to 25 mm). In this case, larger reductions are observed in the peak load of the specimens with 12.5 mm and 25 mm FRP widths, see Figure 8-11 (a), which is due to the different loading and active failure mechanisms.

The changes in the peak load of the panels as well as in the failure mode are tabulated in Table 8-6 for all the exposure conditions. 16%, 19% and 22% reduction of peak load is observed in the specimens aged in HT1 conditions with FRP widths of 6 mm, 12.5 mm and 25 mm, respectively, which shows that the response is not so different. No change of failure mode is observed in the specimens with 6 mm FRP width after ageing. However in the specimens with 12.5 mm and 25 mm FRP widths, the failure mode has changed after ageing in HT1 exposure. Small FRP delaminations are observed in all the panels as tabulated in Table 8-5.

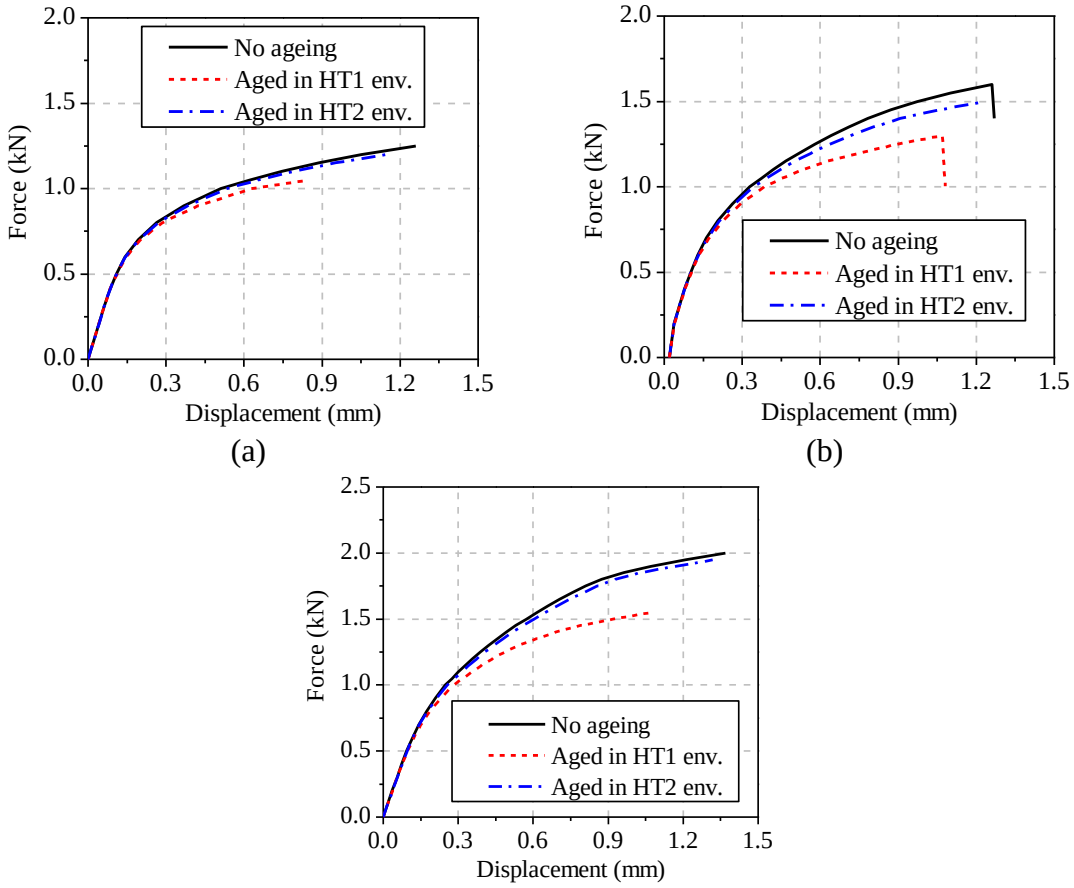

Figure 8-12: Force-displacement behavior of Pan D before and after ageing: (a) FRP_w=6 mm; (a) FRP_w=12.5 mm; (a) FRP_w=25 mm.

Table 8-6: Peak strength and failure mode of PAN D before and after ageing.

FRP_w (mm)	Exposure	P_{max} (kN)	Reduction (%)	Failure mode	FRP delaminations
6	No ageing	1.30	-	Rocking	Y
	HT1	1.05	16.0	Rocking	Y
	HT2	1.20	4.0	Rocking	Y
	FT	1.25	0.0	Rocking	Y
12.5	No ageing	1.60	-	Diagonal tension cracking	Y
	HT1	1.30	18.8	Diagonal tension/ rocking	Y
	HT2	1.55	3.1	Diagonal tension cracking	Y
	FT	1.60	0.0	Diagonal tension cracking	Y
25	No ageing	2.00	-	Diagonal tension cracking	Y
	HT1	1.55	22.5	Diagonal tension/ rocking	Y
	HT2	1.95	2.5	Diagonal tension cracking	Y
	FT	2.00	0.0	Diagonal tension cracking	Y

In general, the results show that the local bond degradation might affect significantly the global structural performance, depending on the geometry of the strengthening, the details of the structural components and the loading conditions. The peak load, the post cracking stiffness and the failure mode may change due to environmental conditions. It is also observed that the reduction levels may depend on the axial stiffness of the reinforcement.

8.4 Conclusions

The effect of local bond degradation on the global performance of strengthened masonry panels was numerically investigated in this chapter.

Two hypothetical GFRP-strengthened masonry panels with different strengthening details and load applications (vertical and horizontal) were selected for this purpose. A two-dimensional FE model, with plane stress elements adopted for masonry and truss elements for FRP connected with interface elements to the masonry surface, was used for modeling FRP-strengthened masonry panels.

The model was initially validated by comparing the numerical results with experimental results. Once the model was validated, the panels were analyzed with degraded material properties and bond characteristics. The degradation data was extracted from accelerated ageing tests, performed in this thesis and presented in Chapter 5, at 225 cycles of all environmental conditions.

The changes in the global performance of the strengthened panels after ageing were investigated in terms of force-displacement curves and failure mode.

Different degradation levels in the global performance of the panels with different strengthening details were observed. The most severe degradation level occurred due to exposure HT1 (temperature cycles of +10°C to +50°C with 90% constant relative humidity) representing environments with high relative humidity conditions. In some cases a change of failure mode due to degradation was also found. It was observed that the axial stiffness of FRP may also affect the degradation level in the peak loads.

The results are a first step towards investigating the effect of local materials degradation on the global performance of strengthened masonry structures. Modeling other strengthened panels and structures with different geometrical and strengthening details within three-dimensional FE models is necessary for better understanding the key factors and proposing a durability-based design framework. But this requires sound provisional models and more extensive results on bond durability.

Chapter 9

Conclusions and future work

Externally bonded reinforcement of masonry structures with composite materials has received extensive attention in the last years. However, issues related to durability and long-term performance of strengthened components and the bond between the composite material and the masonry substrate, as a key mechanism, are still unknown. The main objective of this thesis was thus to investigate the durability of bond in FRP-strengthened masonry systems. The work consisted of experimental, analytical and numerical investigations. Advanced non-destructive and full field measurement techniques for bond quality and degradation assessment were also adopted in this study.

9.1 Research outline

Accelerated ageing tests at the material and interfacial bond level were performed and the degradation mechanisms due to different environmental conditions were investigated. The tests included water immersion tests and hygrothermal exposure conditions. For the hygrothermal conditions three different exposures were considered namely HT1 (temperature cycles of +10°C to +50°C with 60% constant relative humidity), HT2 (temperature cycles of +10°C to +50°C with 90% constant relative humidity) and FT (temperature cycles of –10°C to +30°C with 90% constant relative humidity). Analytical degradation models were also used for simulating the observed degradation mechanisms. Time-dependent (cycle-dependent) material properties and a bond constitutive model were obtained from the experimental tests which were used as the input for the numerical modeling. Moreover, the results provided a large degradation database for brick, glass fibers, epoxy resin and the bond between GFRP and brick units which can be used as a baseline for further studies.

Digital image correlation (DIC), acoustic emission (AE) and IR thermography techniques were used for bond quality and degradation assessment. Digital image correlation was used during

the debonding tests for full field measurement of surface strains which allowed better understanding of the debonding phenomenon, three-dimensional nature of the bond behavior and characterization of the bond mechanisms. Acoustic emission technique was also used during the debonding tests. The technique allowed characterization of debonding initiation and fracture mode, estimation of the failure mode, and assessment of FRP slip. Infrared thermography technique was used for detection and measurement of the size of FRP delaminations and defects that occurred due to environmental exposures.

For the numerical modeling, the short-term bond behavior was initially modeled and fully investigated. Different modeling approaches, meso-scale and macro-modeling, were adopted. The models were validated with available experimental data, and from the obtained results, a suitable constitutive model for bond behavior in FRP-masonry systems was proposed. Moreover, the effect of issues such as FRP width, mortar joints and three-dimensional aspects of the bond behavior were investigated. A combination of the proposed bond-slip model and degradation models provided a time-dependent (cycle-dependent) bond model for different environmental conditions. This model was finally used for investigating the effect of local bond degradation on the global performance of structural components.

9.2 Conclusions

9.2.1 Experimental work

Water immersion leads to a reduction of mechanical properties of epoxy resin, composite material and bricks. It is worth noting that the rate and extent of this degradation is dependent on the chemical characteristics of materials and may be different in other cases. For the bond behavior, degradation in pull-off and shear bond strength was observed with immersion time. The pull-off strength of the specimens decreased significantly (about 60%) after 24 weeks of immersion. However, the results obtained from the pull-off tests were not completely consistent with the shear bond tests, where a different degradation trend was observed. The failure mode remained cohesive during the tests but the fracture surface moved from the brick to the brick/primer interface. Shear bond tests showed that the ductility of the bond behavior increases with immersion time in the tested specimens. The bond strength and stiffness were observed to decrease, while the peak slip increased. It was observed that the degradation in the bond strength and stiffness diminishes with time and possibly a residual value is obtained after a certain immersion time. However, performing water immersion tests for longer periods is necessary for having a clear idea about the degradation trend upon time. A similar degradation was also observed in interfacial fracture energy. The failure

mode was cohesive in all the specimens, with the fracture surface inside the brick. However, the fracture surface moved towards the brick/primer interface with time. Available predictive models were used for modeling the observed degradation in the material properties and bond behavior. It was observed that the moisture dependent and exponential degradation models predict the degradation in mechanical properties of epoxy resin and GFRP with a reasonable accuracy, and therefore it was proposed to use them for simulations. A degradation model was also proposed for simulating the bond degradation evolution with environmental changes.

Accelerated hygrothermal ageing tests were performed following three different hygrothermal conditions consisting of thermal cycles from +10℃ to +50℃ (90% R.H.) called HT1 exposure, +10℃ to +50℃ (60% R.H.) called HT2 exposure, and –10℃ to +30℃ (90% R.H.) called FT exposure. The HT1 exposure was used for simulating the thermal variations in wet environments, while HT2 simulated relatively dry conditions. Finally, exposure FT was used to simulate freeze-thaw actions in cold regions. The hygrothermal exposures did not affect the mechanical properties of bricks. However, epoxy resin and GFRP coupons showed some degradation. Generally, higher degradation levels were observed when exposing the specimens to HT1 conditions. FRP delamination was observed at the FRP/brick interface after exposure to environmental conditions. The delamination, being due to the thermal incompatibility between brick and adhesive, was progressively increased with the number of cycles. Moreover, significantly larger FRP delaminations with higher growth rates were observed in the specimens exposed to HT1 conditions. This was attributed to the effect of moisture on the debonding growth behavior and adhesive fracture properties. A progressive degradation of bond strength and fracture energy was observed in the specimens in all exposure types. However, the degradation in the specimens exposed to HT2 and FT conditions was very small in contrary to the large reductions observed in the specimens exposed to HT1 conditions. Analytical predictive models were finally used for modeling the degradation in the material properties and bond behavior.

The Digital Image Correlation (DIC) technique was used for obtaining the full-field distribution of strains and displacements in tensile tests and single-lap shear debonding tests. The evolution of strains during the shear debonding tests was measured and the results showed different longitudinal strain distributions along the bonded length at the FRP middle and edge sections. Moreover, large transversal strains were observed near the loaded end close to failure of the specimens, further confirming the three-dimensional nature of the bond behavior.

The Acoustic Emission (AE) technique was used during the debonding tests to detect and characterize fracture and crack propagation during the debonding of composite materials from masonry bricks. The results showed that AE outputs can be efficiently used for investigation and

interpretation of the fracture process during debonding. AE data, and more specifically the detected AE energy, was applied to characterize the different failure modes. A correlation was observed between the fracture energy and total emitted AE energy. Moreover, a close correlation was found between the FRP global slip and the cumulative AE energy, which can be applied for slip prediction and modeling purposes. The effect of failure mode on the AE outputs was significant.

The active IR thermography technique was used for assessing the bond quality and degradation due to environmental conditions. For this purpose, a quantitative IR thermography method was adopted for evaluating the delamination in FRP-strengthened masonry elements. The applicability of this method for detecting FRP delamination in GFRP-strengthened masonry elements was initially validated using specimens with interfacial embedded defects of different sizes. The IR thermography results showed that the adopted method detects defects with a minimum size of 10 mm with a reasonable accuracy in quantifying the size. The effect of environmental conditions on the bond quality was subsequently investigated by exposing GFRP-strengthened masonry bricks to HT1 and FT hygrothermal conditions. Progressive FRP delaminations were detected with the IR technique after exposure to environmental conditions. The size of delaminated areas was also evaluated quantitatively with the adopted method.

9.2.2 Numerical modeling

Finite element analysis was used for modeling the bond behavior between FRP and masonry and also for simulating the global performance of FRP-strengthened components. Modeling the bond behavior was conducted at two different scales. Firstly, a fully three-dimensional nonlinear model was adopted, in which FRP, epoxy and the brick substrate were modeled separately. Different smeared cracking models and mesh sizes were used and it was found that the rotating smeared crack model is the most suitable for predicting the debonding phenomenon with regard to the reference experimental tests. It was shown that failure surfaces and crack propagation have a three-dimensional nature. In particular, the interfacial stress distributions were different along the FRP width and transverse strains were found at the loaded end. The effect of mortar joints on the global and local response of the strengthened elements was also investigated. It was observed that a poor quality mortar may lead to a significant reduction of the bond strength. This effect reduces with decreasing FRP axial stiffness. It was also shown that a solution to regain the original bond strength is to increase the effective bond length in the presence of poor quality mortar. Secondly, a simple two-dimensional plan stress model, in which the bond behavior is presented with interface elements, was adopted. Based on the available experimental results a simple tri-linear bond-slip model was proposed in this study to be used for the interface elements. The proposed bond-slip

model was validated by comparing the experimental and numerical results. A comparison was also performed between the proposed bond-slip model and the one proposed by the Italian design code CNR DT200 [1], and relevant aspects for design procedures were discussed.

Afterwards, the effect of degradation of bond and materials mechanical properties on the global performance of strengthened masonry panels was numerically investigated. Two GFRP-strengthened masonry panels with different strengthening details and load application schemes were selected for this purpose. A two-dimensional FE model, with plane stress elements adopted for masonry and truss elements for FRP connected with interface elements to the masonry surface, was used for modeling FRP-strengthened masonry panels. The model was initially validated by comparing the numerical results with experimental results. Once the model was validated, the panels were analyzed with degraded material properties and bond characteristics ,extracted from the accelerated ageing tests. The changes in the global performance of the strengthened panels after ageing were investigated in terms of force-displacement curves and failure mode. Diverse degradation levels in the global performance of the panels with different strengthening details were observed. The largest degradation level occurred due to exposure HT1 representing environments with high relative humidity conditions. In some cases a change of failure mode due to degradation was also observed. It was observed that the axial stiffness of FRP also affects the degradation level in the peak loads.

9.3 Future work

Since the available information on durability of FRP-strengthened masonry is scarce, there are several critical gaps that have to be further studied. Some of the important tasks to be followed are presented next.

Regarding the experimental tests, full characterization of hygro-thermo-mechanical properties of bricks, mortars and commercial epoxy resins and fibers are necessary. This can assist in understanding the degradation mechanisms involved in durability tests, compatible and consistent strengthening designs, and also for numerical modeling approaches involving multi-physics and multi-scale levels.

Durability tests concerning other exposures are also of special importance. Considering degradation agents such as salt or alkaline environment are also required. Regarding the hygrothermal exposures, the tests performed in this study can serve as a reference for new exposure conditions. The main parameters to be studied can be the level of relative humidity, cycle rates, longer exposure periods in case of HT1 and FT exposures, and temperature level. Water immersion

tests can be performed also using different temperatures. Combination of environmental conditions with sustained loads can also produce a significant outcome. Performing real exposure tests in different environmental regions and conditions (outdoor and indoor) are also of great importance for establishing reliable links between accelerated and real exposure conditions.

Regarding the bond characterization, in addition to shear debonding tests, performing pull-off tests can be very helpful in characterization of bond degradation under mixed-mode debonding. Regarding advanced measurement techniques, investigating the debonding phenomenon under mixed-mode debonding and creep tests with the aim of DIC are suggested. Investigating issues such as the effect of FRP width, bonded length and surface preparation on the debonding can also be carried out with this technique. Performing comprehensive experimental tests on the use of AE technique during the debonding tests are required for obtaining reliable correlation between debonding parameters such as fracture energy and failure mode, and acoustic emission outputs. The development of refined detection techniques (such as fiber optics) for detecting the acoustic data can be a large step forward on using this technique for onsite structural health monitoring purposes. Finally, it is relevant to develop suitable NDT techniques for subjects such as bond strength assessment, for far field structures and for cases in which the surface of the composite material is not in direct access.

Regarding the numerical modeling, three-dimensional FE analysis of FRP-strengthened structural elements is still a challenge. The development of a framework for hygro-thermo-mechanical analysis of multilayer structures considering the effect of interfaces is also required. Advanced constitutive and damage models for modeling the bond degradation considering chemo-thermo-physical reactions is needed for such a framework. Hygrothermal modeling of FRP bonded components and investigating the effect of issues such as boundary conditions, real exposure conditions, hygrothermal material properties and size effect on the hygrothermal interfacial stresses and mechanical response of strengthened component is also interesting. Moreover, investigating the effect of local bond degradation, as well as local FRP delaminations and defects, on strengthened structures with different geometrical details and loading conditions is of critical importance for development of durability-based design relations.

References

[1] CNR-DT200. Guide for the design and construction of externally bonded FRP systems for strengthening existing structures. National Research Council (CNR), Italy. 2009.

[2] ACI 4407R-10. Guide for the design and construction of externally bonded FRP systems for strengthening unreinforced masonry structures. American Concrete Institute. 2010.

[3] Karbhari VM, Chin JW, Reynaud D. Critical gaps in durability data for FRP composites in civil infrastructure. Proc of 45th Int Symposium. Long Beach, Claif. 2000:549-63.

[4] Briccoli Bati S, Rotunno T. Environmental durability of the bond between the CFRP composite materials and masonry structures. Struct Anal Historic Constr. 2001:1039-46.

[5] Aiello MA, Sciolti MS. Influence of environmental agents on bond between FRP reinforcement and calcarenite ashlars. Struct Anal Historic Constr. 2005:875-81.

[6] Desiderio P, Feo L. Durability Evaluation of EBR CFRP Strengthened Masonry Structures. Proc. of BBFS. 2005.

[7] Karbhari VM, Chin W, Hunston D, Benmokrane B, Juska T, Morgan R et al. Durability gap analysis for fiber-reinforced polymer composites in civil infrastructures. J Compos Constr. 2003;7:238-47.

[8] ASTM E632. Standard practice for developing accelerated tests to aid prediction of service life of building component and materials. ASTM. 1998.

[9] ASTM C67-12. Standard test methods for sampling and testing brick and structural clay tile. 2012.

[10] RILEM TC 127-MS.A.3. Tests for masonry materials and structures. Unidirectional freeze-thaw test for masonry units and wallets. RILEM. 1998.

[11] RILEM TC 127-MS.A.2. Tests for masonry materials and structures. Unidirectional salt crystallization test for masonry units. RILEM.

[12] ASTM D2565-99. Standard practice for Xenon-Arc exposure of plastics intended for outdoor applications. 2008.

[13] Martin R. Ageing of composites. Woodhead Publishing. 2008.

[14] Daniotti B, Cecconi FR. Accelerated laboratory tests procedures and correlation between laboratory tests and service life data. Test methods for service life prediction. CIB W080.

[15] Baldan A. Adhesion phenomena in bonded joints. Int J Adhes Adhes. 2012;38:95-116.

[16] Fourche G. An overview of the basic aspects of polymer adhesion. Poly Eng Sci. 1995;35:957-67.

[17] Lee LH. Adhesive bonding. Plenum Press; 1991.

[18] Kinloch AJ. Interfacial fracture mechanical aspects of adhesive bonded joints-a review. J Adhes. 1979;10:193-219.

[19] Lee YJ, Boothby TE, Bakis CE, Nanni A. Slip modulus of FRP sheets bonded to concrete. J Compos Constr ASCE. 1999;3:161-67.

[20] Bizindavyi L, Neal KW. Transfer length and bond strength for composites bonded to concrete. J Compos Constr ASCE. 1999;3:153-60.

[21] Maeda T, Asano Y, Sato Y, Ueda T, Kakuta Y. A study on bond mechanism of carbon fiber sheet. Proc of Third International Symposium of Non-Metallic (FRP) Reinforcement for Concrete Structures. 1997. 279-86.

[22] Chajes MJ, Finch WW, Januszka TF, Thomson TA. Bond and force transfer of composite material plates bonded to concrete. ACI Struct J. 1996;93:208-17.

[23] Horiguchi T, Saeki N. Effect of test methods and quality of concrete on bond strength of CFRP sheet. Non-Metal (FRP) Reinf Conc Struct. 1997;1:265-70.

[24] Willis CR, Yang Q, Seracino R, Griffith MC. Bond behavior of FRP-to-clay brick masonry joints. Eng Struct. 2009;31:2580-7.

[25] Sato Y, Katsumata H, Kobatake Y. Shear strengthening of existing reinforced concrete beams by CFRP sheet. Proc of 3rd International Symposium of FRP Reinforcement for Concrete Structures. Spporo, Japan; 1997. 507-14.

[26] Nakaba H, Kanakubo T, Furuta T, Yoshizawa H. Bond behavior between fiber-reinforced polymer laminates and concrete. ACI Struct J. 2001;98:359-67.

[27] Lu XZ, Ye LP, Teng JG, Jiang JJ. Meso-scale finite element model for FRP sheets/plates bonded to concrete. Eng Struct. 2005;27:564-75.

[28] Savoia M, Ferracuti B, Mazzotti C. Non-linear bond-slip law for FRP-concrete interface. Proc. of FRPRCS-6. Singapore. 2003. 1-10.

[29] Ferracuti B, Savoia M, Mazzotti C. Interface law for FRP-concrete delamination. Compos Struct. 2007;80:523-31.

[30] Mazzotti C, Savoia M, Ferracuti B. A new single-shear set-up for stable debonding of FRP-concrete joints. Constr Build Mater. 2009;23:1529-37.

[31] Dai JG, Sato Y, Ueda T. Developement of the nonlinear bond stress-slip model of fiber reinforced plastics sheets-concrete interfaces with a simple method. J Compos Constr. 2005;9:52-62.

[32] Sato Y, Asano Y, Ueda T. Fundamental study on bond mechanism of carbon fiber sheet. Conc Lib Inter, JSCE. 2000:97-115.

[33] Sato Y, Kimuram K, Kobatake Y. Bond behavior between CFRP sheet and concrete. J Struct Constr Eng, AIJ. 1997;500:75-82.

[34] Valluzzi MR, Oliveira DV, Caratelli A, et al. Round robin test for composite-to-brick shear bond characterization. J Mater Struct. 2012;45:1761-91.

[35] Carrara P, Ferretti D, Fereddi F. Debonding behavior of ancient masonry elements strengthened with CFRP sheets. Compos Part B. 2012;45:800-10.

[36] Chen JF, Teng JG. Anchorage strength models for FRP-to-concrete bonded joints. J Struct Eng ASCE. 2001;127:784-91.

[37] Chen JF, Yang ZJ, Holt GD. FRP or steel plate-to-concrete bonded joints: effect of test methods on experimental bond strength. Steel Compos Struct Int J. 2001;1:231-44.

[38] Yao J, Teng JG, Chen JF. Experimental study on FRP-to-concrete bonded joints. Compos Part B. 2005;36:99-113.

[39] Fedele R, Milani G. A numerical insight into the response of masonry reinforced by FRP strips. The case of perfect adhesion. Compos Struct. 2010;92:2345-57.

[40] Momayez A, Ehsani M, Ramezanianpour A, Rajaie H. Comparison of methods for evaluating bond strength between concrete substrate and repair materials. Cem Concr Res. 2005;35:748-57.

[41] Aiello MA, Leone M. Interface analysis between FRP RBR system and concrete. Compos Part B. 2008;39:618-26.

[42] Brosens K. Anchorage of externally bonded steel plates and CFRP laminates for the strengthening of concrete elements. University of Leuven, Belgium. 2001.

[43] Miller B, Nanni A. Bond between CFRP sheets and concrete. Proc of fifth ASCE materials congress. 1999. 240-7.

[44] Cao SY, Chen JF, Pan JW. ESPI measurement of bond-slip relations of FRP-concrete interface. J Compos Constr ASCE. 2007;11:149-60.

[45] Xavier J, Sousa AMR, Morais JJL, Filipe VMJ, Vaz M. Measuring displacement fields by cross-correlation and a differential technique: experimental validation. Opt Eng. 2012;51:043602.

[46] Dahl K, Malo K. Planar strain measurements on wood specimens. Exp Mech. 2009;49:575-86.

[47] Sousa AMR, Xavier J, Vaz M, Morais J, Filipe VMJ. Cross-correlation and differential technique combination to determine displacement fields. Strain. 2011;47:87-98.

[48] Carloni C, Subramaniam K. Investigation of the interface fracture during debonding between FRP and masonry. Adv Struct Eng. 2009;12:731-43.

[49] Carloni C, Subramaniam K. Direct determination of cohesive stress transfer during debonding of FRP from concrete. Compos Struct. 2010;93:184-92.

[50] Briccoli Bati S, Rovero L, Tonietti U. Adhesion tests between brick and CFRP strip. Proc. of FRPRCS-9. Sydney, Australia. 2009.

[51] Garbin E, Panizza M, Valluzzi MR. Experimental assessment of bond behavior of fiber-reinforced polymers on brick masonry. Struct Eng Inter. 2010;20:392-9.

[52] Capozucca R. Experimental FRP/SRP- historic masonry delamination. Compos struct. 2010;92:891-903.

[53] Grande E, Imbimbo M, Sacco E. Bond behavior of CFRP laminates glued on clay bricks: Experimental and numerical study. Compos Part B. 2011;42:330-40.

[54] Faella C, Camorani G, Martinelli E, Paciello S, Perri F. Bond behavior of FRP strip glued on masonry: Experimental investigation and empirical formulation. Constr Build Mater. 2012;31:353-63.

[55] Ceroni F, Pecce M, Manfredi G, Marcari A. Experimental bond behavior in masonry elements externally reinforced with FRP laminates. Proc. of International Conference Composites in Constructions. Cosenza, Italy. 2003. 313-8.

[56] Aiello MA, Sciolti SM. Bond analysis of masonry structures strengthened with CFRP sheets. Constr Build Mater. 2005;20:90-100.

[57] Faella C, Martinelli E, Paciello S, Perri F. Composite materials for masonry structures: the adhesion issue. Proc. of MuRico3. Venezia, Italy. 2009. 22-4.

[58] Cancelli AN, Aiello MA, Casadei P. Experimental investigation on bond properties of SRP/SRG-masonry systems. Proc. of FRPRCS8. Greece. 2007.

[59] Oliveira D, Basilio I, Lourenço P. Experimental bond behavior of FRP sheets glued on brick masonry. J Compos Constr, ASCE. 2011;15:32-41.

[60] Capozucca R. Effects of mortar layers in the delamination of GFRP bonded to historic masonry. Compos Part B. 2012;44:639-49.

[61] Briccoli Bati S, Rotunno T, Rovero L, Tonietti U. Experimental study on CFRP brick bonded joints. Proc. of the fourteenth international conference on mechanics of composite materials. Riga, Latvia. 2006.

[62] Casareto M, Oliveri A, Romelli A, Lagomarsino S. Bond behavior of FRP laminates adhered to masonry. Proc of the International Conference Advancing with Composites. Milan, Italy. 2003.

[63] Panizza M, Garbin E, Valluzzi MR, Modena C. Bond behaviour of CFRP and GFRP laminates on brick masonry. Proc of IV Int Seminar of Structural Analysis of Historical Constructions. 2008. 763-70.

[64] Valluzzi MR, Tinazzi C, Modena C. Shear behavior of masonry panels strengthened by FRP laminates. Constr Build Mater. 2002;16:409-16.

[65] Grande E, Imbimbo M, Sacco E. Bond behavior of historical clay bricks strengthened with steel reinforced polymers (SRP). Mater. 2011;4:585-600.

[66] Wu Z. Element-level study on stress transfer based on local bond properties. Technical report of JCI technical committee on retrofit technology. 2003.

[67] Lu XZ, Jiang JJ. A concrete constitutive relationship with various damage models. China Civil Eng J. 2003;36:70-4.

[68] Lu XZ, Yan JJ, Wei H, Ye LP, Jiang JJ. Discussion on the key difficulties of finite element analysis for the interface between FRP sheet and concrete. Proc of 2nd National Civil Engineering Forum of Graduate Students of China. China. 2004. 134-7.

[69] Coronado C, Lopez M. Damage approach for the prediction of debonding failure on concrete elements strengthened with FRP. ASCE J Compos Constr. 2007;11:391-400.

[70] Fedele R, Milani G. Three-dimensional effects induced by FRP-from-masonry delamination. Compos Struct. 2011;93:1819-31.

[71] Chen JF, Pan JW. Three dimensional stress distribution in FRP-to-concrete bond test specimens. Constr Build Mater. 2006;20:46-58.

[72] Wu Z, Yin J. Fracturing behaviors of FRP-strengthened concrete structures. Eng Fract Mech. 2003;70:1339-55.

[73] Wu Z, Yuan H, Niu HD. Stress transfer and fracture propagation in different kinds of adhesive joints. J Eng Mech. 2002;128:562-73.

[74] Monti G, Renzelli M, Luciani P. FRP adhesion in uncracked concrete zones. Proc of 6th international symposium on FRP reinforcement for concrete structures. Singapore. 2003. 183-92.

[75] Grande E, Imbimbo M, Sacco E. Simple model for bond behavior of masonry elements strengthened with FRP. J Compos Constr ASCE. 2011;15:354-63.

[76] Smith S, Teng JG. Interfacial stresses in plated beams. Eng Struct. 2001;23:857-71.

[77] Robinovitch O, Frostig Y. Delamination failure of RC beams strengthened with FRP strip- A closed-form high-order and fracture mechanics approach. J Eng Mech. 2001;127:852-61.

[78] Suo ZG, Hutchinson JW. Steady-state cracking in brittle substrates beneath adherent films. Int J Solids Struct. 1989;25:1337-53.

[79] Suo ZG, Hutchinson JW. Interface crack between two shear deformable elastic layers. Int J Fract. 1990;43:1-18.

[80] Au C, Buyukozturk O. Debonding of FRP plated concrete: A tri-layer fracture treatment. Eng Frac Mech. 2006;73:348-65.

[81] Chen JF, Yuan H, Teng JG. Debonding failure along a softening FRP-to-concrete interface between two adjacent cracks in concrete members. Eng Struct. 2007;29:259-70.

[82] Yang QD, Thouless MD. Mixed-mode fracture analysis of plastically-deformation adhesive joints. Int J Fract. 2001;110:175-87.

[83] Wang JL. Cohesive zone model of FRP-concrete interface debonding under mixed-mode loading. Int J Solids Struct. 2007;44:6551-68.

[84] Holzenkämpfer P. Ingenieurmodelle des verbundes geklebter bewehrung fur Betonbauteile: TU Braunschweig; 1994.

[85] Neubauer U, Rostasy F. Design of concrete structures strengthened with externally bonded CFRP plates. Proc of 7th International conference on structural faults and repairs. 1997. 109-18.

[86] Taljesten B. Strengthening of concrete prisms using the plate bonding technique. Int J Fract. 1996;82:253-66.

[87] Maurenbrecher AHP, Trischuk K, Rousseau MZ. Review of factors affecting the durability of repointing mortars for older masonry. Proc of 9th Canadian Maonsry Symposium. Fredericton, N.B. 2001. 1-12.

[88] Karbhari VM. Durability of composites for civil structural applications. Washington, DC: CRC Press. 2007.

[89] Gates T. The physical and chemical ageing of polymeric composites. In: Martin R, editor. Ageing of composites. Cambridge: Woodhead. 2008.

[90] Frigione M, Aiello MA, Naddeo C. Water effects on the bond strength of concrete/concrete adhesive joints. Constr Build Mater. 2006;20:957-70.

[91] Karbhari VM. Durability of FRP composites for civil infrastructure-myth, mystery or reality. Proc of the First International Conference of Advanced Polymer Composites for Structural Applications in Construction. UK. 2002. 33-43.

[92] Ivanova KI, Pethrick RA, Affrossman S. Investigation of hydrothermal ageing of a filled rubber toughened epoxy resin using dynamic mechanical thermal analysis and dielectric spectroscopy. Poly. 2000;41:6787-96.

[93] Li C, Dickie R, Morman K. Dynamic mechanical response of adhesively bonded beams-eefect of environmental exposure and interfacial zone properties. Polym Eng Sci. 1990;30:249-55.

[94] Lapique F, Redford K. Curing effects on viscosity and mechanical properties of a commercial epoxy resin adhesive. Int J Adhes Adhes. 2002;22:337-46.

[95] Buck S, Lischer D, Nemat-Nasser S. The durability of EGlass/Vinyl ester composite materials subjected to environmental conditioning and sustained loads. J Compos Mater. 1998;32:874-92.

[96] Zhou J, Lucas J. Hygrothermal effects of epoxy resins. Part II: variations of glass transition temperature. Polym. 1999;40:5513-22.

[97] Schutte CL. Environmental durability of glass-fiber composites. Mater Sci Eng. 1994;13:265-322.

[98] Abanilla M, Li Y, Karbhari VM. Durability characterization of wet layup graphite/epoxy composites used in external strengthening. Compos Part B. 2006;37:200-12.

[99] Phifer SP, Verghese KNE, Lesko JJ. Remaining strength of hygrothermally aged pultruded vinyl ester E-glass laminates. Proc of the 3rd International Conference on the Advanced Composite Materials in Bridges and Structures (ACMBS MCAPC). 2000. 29-36.

[100] Bradley WL, Grant TS. The effect of moisture absorption on the interfacial strength of polymeric matrix composites. J Mater Sci. 1995;30:5537-42.

[101] Collings TA, Harvey RJ, Dalzeil AW. The use of elevated temperature in the structural testing of FRP components for simulating the effects of hot and wet environmental exposure. Compos. 1993;24:625-34.

[102] McClurg JA, Vaughan JG. Characterization of degradation for pultruded glass reinforced composite materials when immersed in high temperature water. Proc of the 43th International SAMPE Symposium. 1998. 2134-43.

[103] Guo S, Kagawa Y. Temperature dependence of in situ constituent properties of polymer-infiltration-pyrolysis-processed NicalonTM Sic fiber-reinforced SiC matrix composite. J Mater Res. 2000;15:961-0.

[104] Sciolti MS, Frigione M, Aiello MA. Wet lay-up manufactured FRPs for concrete and masonry repair: influence of water on the properties of composites and on their epoxy components. J Compos Constr. 2010;14:823-33.

[105] Cultrone G, De la Torre MJ, Sebastian EM, Cazalla O, Rodriguez-Navarro C. Behavior of brick samples in aggressive environments. Water, Air, Soil Pollut. 2000;119:191-207.

[106] Elert K, Cultrone G, Navarro CR, Pardo ES. Durability of bricks used in the conservation of historic buildings- influence of composition and microstructure. J Cult Herit. 2003;4:91-9.

[107] Silva M, Biscaia HC. Effects of exposure to saline humidity on bond between GFRP and concrete. Compos Struct. 2010;93:216-24.

[108] Hayes M, Garcia K, Verghese KNE, Lesko J. The effects of moisture on the fatigue behavior of a glass/vynil ester composite, Fiber composites in infrastructure. ICCI'98. Tucson. 1998.

[109] Toutanji HA, Gomez W. Durability characteristics of concrete beams externally bonded with FRP composite sheets. Cem Conc Compos. 1997;19:351-8.

[110] Malvar L, Joshi N, Bearn J, Novinson T. Environmental effects on the short term bond of carbon fiber reinforced polymer (CFRP) composites. ASCE J Compos Construct. 2003;7:58-63.

[111] Grace NF, Singh SB. Durability evaluation of carbon fiber-reinforced polymer strengthened concrete beams: experimental study and design. ACI Struct J. 2005;102:40-51.

[112] Silva MAG, Biscaia H. Degradation of bond between FRP and RC beams. Compos Struct. 2008;85:164-74.

[113] Karbhari VM, Ghosh K. Comparative durability evaluation of ambient temperature cured externally bonded CFRP and GFRP composite system for repair of bridges. Compos Part A. 2009;40:1353-63.

[114] Karbhari VM, Engineer M. Effect of environmental exposure on the external strengthening of concrete with composites-Short term bond durability. J Reinf Plast Compos. 1996;15:1194-216.

[115] Gledhill R, Kinloch AJ, Shaw S. A model for predicting joint durability. J Adhes. 1980;11:3-15.

[116] Kinloch AJ. Predicting the lifetime of adhesive joints in hostile environments Environmental durability of adhesive bonds: Technical report. NPL. 1994.

[117] Kinloch AJ, Little MSG, Watts JF. The role of the interphase in the environmental failure of adhesive joints. Acta Materialia. 2000;48:4543-53.

[118] Ouyang Z, Wan B. Nonlinear deterioration model for bond interfacial fracture energy of FRP-concrete joints in moist environments. J Compos Constr. 2009;13:53-63.

[119] Bowditch M. The durability of adhesive joints in the presence of water. Int J Adhes Adhes. 1996;16:73-9.

[120] Kumar A, Gupta R. Fundamentals of polymer engineering. New York: Marcel Dekker, Inc. 2003.

[121] Kumar A, Gupta R. Fundamentals of polymers. New York: McGraw-Hill. 1998.

[122] Green MF. FRP repair of concrete structures: performance in cold regions. Int J Mater Prod Technol. 2007;28:160-77.

[123] Green MF, Bibsy LA, Fam AZ, Kodur VKR. FRP confined concrete columns: Behavior under extreme conditions. Cem Conc Compos. 2006;28:928-37.

[124] Mufti A, Erki M, Jaeger L. Advanced composite materials with application to bridges. Montreal, Quebec, Canada: Canadian Soci Civil Eng. 1991. 21-70.

[125] Kralj B, Pande GN, Middleton J. On the mechanics of frost damage to brick masonry. Compos Struct. 1991;41:53-66.

[126] Dutta PK, Taylor S. A fractographic analysis of graphite-epoxy composites subjected to low temperature thermal cycling. Proc of the International Symposium for Testing and Failure Analysis. Los Angeles, USA. 989. 429-35.

[127] Rivera J, Karbhari VM. Cold temperature and simultaneous aqueous environment related degradation of carbon/vinylester composites. Compos Part B. 2002;33:17-24.

[128] Hollaway LC. A review of the present and future utilization of FRP composites in the civil infrastructure with reference to their important in-service properties. Constr Build Mater. 2010;24:2419-45.

[129] Carol L, Schutte CL. Environmental durability of glass-fiber composites. Mater Sci Eng A. 1994;13:265-323.

[130] Carlson NM, Blackwood LG, Torres LL, Rodriquez JG, Yoder TS. Accelerated ageing of polymer composite bridge materials. SPIE 6th Symp on Smart Structures and Materials. CA, USA1999.

[131] Demuts E, Shyprykevich P. Accelerated environmental testing of composites. Compos. 1984;15:25-31.

[132] Freitag S, Beer M, Graf W, Kaliske M. Lifetime prediction using accelerated test data and neural networks. Comput Struct. 2009;87:1187-94.

[133] Purnell P, Cain J, van Itterbeek P, Lesko J. Service life modeling of fiber composites: A unified approach. Compos Sci Technol. 2008;68:3330-6.

[134] Jedidi J, Jacquemin F, Vautrin A. Design of accelerated hygrothermal cycles on polymer matrix composites in the case of a supersonic aircraft. Compos Struct. 2005;68:429-37.

[135] Jedidi J, Jacquemin F, Vautrin A. Accelerated hygrothermal cyclical tests for carbon/epoxy laminates. Compos Part A. 2006;37:636-45.

[136] Purnell P. Interpretation of climatic temperature variations for accelerated ageing methods. J Mater Sci. 2004;39:113-8.

[137] Maxwell AS, Broughton WR, Dean G, Sims GD. Review of accelerated ageing methods and lifetime prediction techniques for polymeric materials. DEPC MPR 016. Technical report, NPL. 2005.

[138] Binda L, Molina C. Building materials durability: Semi-Markov approach. J Mater Civil Eng. 1990;2(4), 223–39.

[139] Blakely RR. Evaluation of paint durability- Natural and accelerated. Prog Org Coat. 1985.

[140] Fischer RM, Ketola W, Murray WP. Inherent variability in accelerated exposure methods. Prog Org Coat. 1991.

[141] Riedl A. What makes a Xenon weathering instrument high-end? Atlas Sunspots. 2003;33.

[142] Sullivan CJ, Cooper CF. Polyester weatherability: coupling frontier molecular orbital calculations of oxidative stability with accelerated testing. J Coat Technol. 1995;67.

[143] Meeker WQ, Escobar LA. Accelerated degradation tests: modeling and analysis. Technometrics, ASCE. 1998;40:89-99.

[144] Barnes BA. Bond and low cycle fatigue behavior of thermoset composite reinforcing for the concrete industry. Ames, Iowa: Iowa State University; 1990.

[145] Lesko JJ. Freeze-thaw durability of polymer matrix composites in infrastructure. Proc of Duracosys 99. Brussels, Belgium. 1999.

[146] Soudki KA, Green MF. Freeze-thaw response of CFRP wrapped concrete. ACI Conc Int. 1997;19:64-7.

[147] Gomez JP, Castro B. Freeze-thaw durability of composite materials. Richmond, Va.: Vrginia Transportation Research Council; 1996.

[148] Karbhari VM, Rivera J, Dutta PK. Effect of short-term freeze-thaw cycling on composite confined concrete. J Compos Constr. 2000;4:191-7.

[149] Belarbi A, Bae S. An experimental study on the effect of environmental exposures and corrosion on RC columns with FRP composite jackets. Compos Part B. 2007;38:674-84.

[150] Myers JJ, Murthy SS. Effects of combined environmental cycles on the bond of FRP sheets to concrete. Proc of Composites in construction. Porto, Portugal. 2001.

[151] Chajes MJ, Thomson TAJ, Farschman CA. Durability of concrete beams externally reinforced with composite fabrics. Constr Build Mater. 1995;9:141-8.

[152] Toutanji HA, Ortiz G. Durability of concrete beams strengthened with FRP plates. International conference on rehabilitation and development of civil engineering infrastructure systems. Beirut, Lebanon. 1997.

[153] Huitao R, Shan L, Chengkui H, Yunfei C. Durability of RC beams reinforced with CFRP sheet under wet-dry environmental and loading conditions. FRPRCS-9. Australia. 2009.

[154] Karbhari VM, Zhao L. Issues related to composite plating and environmental exposure effects on composite-concrete interface in external strengthening. Compos Struct. 1998;40:293-304.

[155] Leung H, Balendran R, Lim C. Flexural capacity of strengthened concrete beam exposed to different environmental conditions. Conference of FRP Composites in Civil Engineering. Hong Kong, China. 2001. 1597-606.

[156] Toutanji HA. Durability characteristics of concrete columns confined with advanced composite materials. Compos Struct. 1999;44:155-61.

[157] Toutanji HA, Balaguru P. Durability characteristics of concrete columns wrapped with FRP two sheets. J Mater Civil Eng. 1998;10:52-7.

[158] Dai JG, Yokota H. Experimental study on durability of the bond between FRP and concrete subjected to cyclic dry/wet action. FRPRCS-9. Australia. 2009.

[159] Karbhari VM, Engineer M, Eckel DA. On the durability of composite rehabilitation schemes for concrete: Use of a peel test. J Mater Sci. 1997;32:147-56.

[160] Wan B, Petrou MF, Harries KA. Effect of the presence of water on the durability of bond between CFRP and concrete. J Reinf Plast Compos. 2006;25:875-90.

[161] Tuakta C, Buyukozturk O. Deterioration of FRP/concrete bond system under variable moisture conditions quantified by fracture mechanics. Compos Part B. 2011;42:145-54.

[162] Tuakta, Buyukozturk O. Conceptual model for prediction of FRP/Concrete bond strength under moisture cycles. J Compos Constr. 2011;15(5):743-56.

[163] Benzarti K, Chataigner S, Quiertant M, Marty C, Aubagnac C. Accelerated ageing behavior of the adhesive bond between concrete specimens and CFRP overlays. Constr Build Mater. 2010;25:523-38.

[164] Cromwell JR, Harries KA, Shahrooz BM. Environmental durability of externally bonded FRP materials intended for repair of concrete structures. Constr Build Mater. 2011;25:2525-39.

[165] Silva MAG, Biscaia HC, Marreiros R. Bond-slip on CFRP/GFRP-to-concrete joints subjected to moisture, salt fog and temperature cycles. Compos Part B. 2013;55:374-85.

[166] Sciolti MS, Aiello MA, Frigione M. Influence of water on bond behavior between CFRP sheet and natural calcareous stones. Compos Part B. 2012;43:3239-50.

[167] Kaiser H. Strengthening of reinforced concrete with epoxy-bonded carbon-fiber plastics. Zurich, Switzerland: ETH. 1989.

[168] Arnsten B, Pedersen V. Freeze-thaw durability of concrete beams strengthened with CFRP. Eighth international conference on structural faults+repairs-99. London. 1999.

[169] Aiello MA, Frigione M, Domenico A. Effects of environmental conditions on performance of polymeric adhesives for restoration of concrete structures. J Mater Civil Eng. 2002;14(2):185-89.

[170] Fava G, Mazzotti C, Poggi C, Savoia M. Durability of FRP-concrete bonding exposed to aggressive environment,. Proc of FRPRCS-8. Patras, Greece. 2007. 16-28.

[171] Colombi P, Fava G, Poggi C. Bond strength of CFRP-concrete elements under freeze-thaw cycles. Compos Struct. 2010;92:973-83.

[172] ASTM C666-03. Standard tests method for resistance of concrete to rapid freezing and thawing. 2008.

[173] Subramaniam KV, Ali-Ahmad M, Ghosn M. Freeze-thaw degradation of FRP-concrete interface: Impact on cohesive fracture response. Eng Fract Mech. 2008;75:3924-40.

[174] Green MF, Dent AJS, Bibsy LA. Effect of freeze-thaw cycling on the behavior of reinforced concrete beams strengthened in flexure with fiber reinforced polymer sheets. Can J Civ Eng. 2003;30:1081-8.

[175] Homam SM, Sheikh SA. Durability of Fiber Reinforced Polymers Used in Concrete Structures. Third Annual Conference on Advanced Composite Materials in Bridges and Structures. Ottawa, Canada. 2000. 751-58.

[176] Yun Y, Wu Y. Durability of CFRP-concrete joints under freeze-thaw cycling. Cold Reg Sci Technol. 2011;65:401-12.

[177] Gamage K, Al-Mahaidi R, Wong B. Investigation of CFRP-concrete bond under long-term exposure to cyclic temperature. FRPRCS-9. Sydney, Australia. 2009.

[178] Loh WK, Crocombe AD, Abdel Wahab MM. Modeling interfacial degradation using interfacial rupture elements. J Adhes. 2003;79:1135-60.

[179] Maekawa K. Multi-scale modeling of structural concrete. Taylor & Francis. 2009.

[180] Maekawa K, Chaube R, Kishi T. Modeling of concrete performance. Hydration, microstructural formation and mass transport. E & FN SPON. 1999.

[181] Maekawa K, Ishida T. Modeling of structural performances under coupled environmental and weather conditions. Mater Struct. 2002;35:591-602.

[182] Philip JR, De Vries DA. Moisture movement in porous materials under temperature gradients. Trans Am Geophys. 1957;38:222-32.

[183] Luikuv A. Heat and mass transfer in capillary porous bodies. Pergamon, Oxford. 1966.

[184] Tariku F, Kumaran K, Fazio P. Transient model for coupled heat, air and moisture transfer through multilayered porous media. Int J Heat and Mass Trans. 2010;53:3035-44.

[185] Ouyang Z, Wan B. An analytical model of FRP-concrete bond deterioration in moist environment. Adv Struct Eng. 2009;12:761-9.

[186] Ouyang Z, Wan B. Experimental and numerical study of water effect on bond fracture energy between FRP and concrete in moist environments. J Reinf Plast Compos. 2008;27:205-23.

[187] Khoshbakht M, Lin MW, Berman JB. Analysis of moisture-induced stresses in an FRP composites reinforced masonry structure. Finite Elem Anal Des. 2006;42:414-29.

[188] Khoshbakht M, Lin C, Fieckert C. A finite element model for hygrothermal analysis of masonry walls with FRP reinforcement. Finite Elem Anal Des. 2009;45:511-18.

[189] Lin MW, Berman JB, Khoshbakht M. Modeling of moisture migration in an FRP reinforced masonry structure. Build Env. 2006;41:646-56.

[190] Bazant ZP, Najjar LJ. Nonlinear water diffusion in nonsaturated concrete. Mater Constr. 1972;5:3-20.

[191] Crocombe AD. Durability modeling concepts and tools for the cohesive environmental degradation of bonded structures. Int J Adhes Adhes. 1997;17:229-38.

[192] Barenblatt G. The mathematical theory of equilibrium cracks in brittle fracture. In: Advances in Applied Mechanics. 1962. 55-129.

[193] Dugdale D. Yielding of steel sheets containing slits. J Mech Phys Solids. 1960;8:100-8.

[194] Hillerborg A, Modeer M, Peterson F. Analysis of crack formation and crack growth in concrete by means of fracture mechanics and finite elements. Cem Concr Res. 1976;6:773-82.

[195] Peter A, Anthony M. The influence of adhesive constitutive parameters in cohesive zone finite element models of adhesively bonded joints. Int J Solids Struct. 2009;46:2201-15.

[196] Liljedahl C, Crocombe AD, Wahab M, Ashcroft I. Damage modeling of adhesively bonded joints. Int J Fract. 2006;141:147-61.

[197] Katnam KB, Sargent JP, Crocombe AD, Khoramishad H, Ashcroft I. Characterization of moisture-dependent cohesive zone properties for adhesively bonded joints. Eng Fract Mech. 2010;77:3105-19.

[198] Roe KL, Siegmund T. An irreversible cohesive zone model for interface fatigue crack growth simulation. Eng Frac Mech. 2003;70:209-32.

[199] Nguyen T, Meftah F, Chammas R, Mebraki A. The behavior of masonry walls subjected to fire: Modeling and parametrical studies in the case of hollow burnt-clay bricks. Fire Safe J. 2009;44:629-41.

[200] Freddi F, Fremond M. Damage in domains and interfaces: a coupled predictive theory. J Mech Mater Struct. 2006;1:1205-33.

[201] Benzarti K, Freddi F, Fremond M. A damage model to predict the durability of bonded assemblies- part I: debonding behavior of FRP strengthened concrete structures. Constr Build Mater. 2009;25(2):547-55.

[202] Argoul P, Benzarti K, Freddi F, Fremond M, Nguyen T. A damage model to predict the durability of bonded assemblies- Part II: Parameter identification and preliminary results for accelerated ageing tests. Constr Build Mater. 2011;25(2):556-67.

[203] Gamage K, Al-Mahaidi R, Wong B. Fe modeling of CFRP-concrete interface subjected to cyclic temperature, humidity and mechanical stress. Compos Struct. 2010;92:826-34.

[204] Hu P, Han X, da Silva LFM, Li WD. Strength prediction of adhesively bonded joints under cyclic thermal loading using a cohesive zone model. Int J Adhes Adhes. 2013;41:6-15.

[205] Nelson W. Accelerated testing: Statistical models, test plans and data analysis. NY: Wiley. 1990.

[206] Purnell P, Bentur A, Raupach MO, J., Hempel R, Schiekel M. Textile reinforced concrete: state-of-the-art report of RILEM committee 201-TRC. 2006. 187-210.

[207] Brown RP, Kockott D, Trubiroha P, Ketola W, Shorthouse J. A review of accelerated durability tests. Versailles Project on Advanced Materials and Standards. 1995.

[208] Brown RP, Greenwood JH. Practical Guide to the Assessment of the Useful Life of Plastics.: Rapra Technology Limited; 2002.

[209] Phani KK, Bose NR. Hygrothermal ageing of CSM-laminate during water immersion- an acoustic-ultrasonic study. J Mater Sci. 1986;21:3633-7.

[210] Chamis CC, Murthy PLN. Simplified procedures for designing bonded composite joints. J Reinf Plast Compos. 1991;10:29-41.

[211] Chamis CC, Sinclair JH. Durability/life of fiber composites in hygrothermo-mechanical environments. ASTM STP 7871982. 498-512.

[212] Broughton WR. Analytical models for assessing environmental degradation of unidirectional and cross-ply laminates. NPL Report MATC(A). 2001.

[213] Kelley FN, Bueche F. Viscosity and glass temperature relations for polymer-diluent systems. J Polym Sci. 1961;50:549-56.

[214] Liljedahl C. Modeling the interfacial degradation in adhesively bonded joints: University of Surrey; 2006.

[215] Springer G. Environmental effects on Composite Materials. In: Environmental effects on Composite Materials. Lancaster: Technomic Pub. 1988. 1-34.

[216] Purnell P. A static fatigue model for the durability of glass fiber reinforced cement. J Mater Sci. 2001;36:5385-90.

[217] Orlowsky J, Raupach M, Cuypers H, Wastiels J. Durability modeling of glass fiber reinforcement in cementations environment. Mater Struct. 2005;38:155-62.

[218] Nissan AH. H-bond dissociation in hydrogen bond dominated solids. Macromolecules. 1976;9:840-50.

[219] Papanicolaou GC, Kosmidou TV, Vatalis AS, Delides CG. Water absorption mechanism and some anomalous effects on the mechanical and viscoelastic behavior of an epoxy system. J App Polym Sci. 2006;99:1328-39.

[220] Nakamura T, Maruno T, Sasaki S. Theoretical analysis of the decay of shear strength of adhesion in metal/epoxy/metal joints in an aqueous environment. J Adhes Adhes. 1987;7:209-12.

[221] Nakamura T, Maruno T, Sasaki S. Theory for the decay of the wet shear strength of adhesion and its application to metal/ epoxy/ metal joints. J Adhes Adhes. 1987;7:97-102.

[222] McManus HL, Foch BJ, Cunningham RA. Mechanism-based modeling of long-term degradation. J Compos Technol Res. 2000;22:146-52.

[223] Chamis CC. Probabilistic simulation of multi-scale composite behavior. Proc of 53rd SDM. Hawaii. 2012.

[224] Sutton MA, Orteu JJ, Schreirer H. Image correlation for shape, motion and deformation measurements: Basic concepts, theory and applications: Springer. 2009.

[225] Ghiassi B, Xavier J, Oliveira DV, Lourenço PB. Application of digital image correlation in investigating the bond between FRP and masonry. Compos Struct. 2013;106:340-49.

[226] Ghiassi B, Marcari G, Oliveira DV, Lourenço PB. Numerical analysis of bond behavior between masonry bricks and composite materials. Eng Struct. 2012;43:210-20.

[227] Hung YY. Shearography: a novel and practical approach for nondestructive inspection. Nondestruct Eval. 1989;8:55-67.

[228] Hung YY. Shearography: An optical measurement technique and applications. Mater Sci Eng R. 2005;49:61-87.

[229] Taillade F, Quiertant M, Benzarti K, Aubagnac C. Shearography and pulsed stimulated infrared thermography applied to a nondestructive evaluation of FRP strengthening systems bonded on concrete structures. Constr Build Mater. 2011;25:568-74.

[230] Lai WL, Kou SC, Poon CS, Tsang WF, Ng SP, Hung YY. Characterization of flaws embedded in externally bonded CFRP on concrete beams by infrared thermography and shearography. J Nondestruct Eval. 2009;28:27-35.

[231] Hung YY, Liang CY. Image-shearing camera for direct measurement of surface strains. Appl Opt. 1979;18:1046-51.

[232] Tashan J, Al-mahaidi R. Investigation of the parameters that influence the accuracy of bond defect detection in CFRP bonded specimens using IR thermography. Compos Struct. 2012;94:519–31.

[233] Lai WL, Kou SC, Poon CS, Tsang WF, Lai CC. Characterization of the deterioration of externally bonded CFRP-concrete composites using quantitative infrared thermography. Cem Concr Compos. 2010;32:740-46.

[234] Maldague X. Theory and practice of infrared technology for nondestructive testing. Wiley-Interscience, John Wiley&Sons Inc. 2001.

[235] Malhotra VM, Carino NJ. CRC handbook on nondestructive testing of concrete. CRC Press. 1991.

[236] Kaiser H, Karbhari VM, Sikorsky C. Non-destructive testing techniques for FRP rehabilitated concrete-II: an assessment. Int J Mater Prod Technol. 2004;21:385-401.

[237] Heller K, Jacobs LJ, Qu J. Characterization of adhesive bond properties using Lamb waves. NDT & E Inter. 2000;33:555-63.

[238] Bastianini F, Di Tommaso A, Pascale G. Ultrasonic non-destructive assessment of bonding defects in composite structural strengthenings. Compos Struct. 2001;53:463-67.

[239] Mahmoud AM, Ammar HH, Mukdadi OM, Ray I, Imani FS, Chen A, et al. Non-destructive ultrasonic evaluation of CFRP–concrete specimens subjected to accelerated ageing conditions. NDT & E Inter. 2010;43:635-41.

[240] Grosse CU, Ohtsu M. Acoustic emission testing - basics for research - applications in civil engineering. Springer. 2008.

[241] Grgic D, Amitrano D. Creep of a porous rock and associated acoustic emission under different hydrous conditions. J Geophys Res-Solid Earth. 2009;114.

[242] Verstrynge E, Schueremans L, Van Gemert D, Wevers M. Monitoring and predicting masonry's creep failure with the acoustic emission technique. NDT & E Inter. 2009;42:518-23.

[243] Carpinteri A, Lacidogna G, Paggi M. Acoustic emission monitoring and numerical modeling of FRP delamination in RC beams with non-rectangular cross-section. Mater Struct. 2007;40:553-66.

[244] Degala S, Rizzo P, Ramanathan K, Harries K. Acoustic emission monitoring of CFRP reinforced concrete slabs. Constr Build Mater. 2009;23.

[245] Masera D, Bocca P, Grazzini A. Frequency analysis of acoustic emission signal to monitor damage evolution in masonry structures. J Phys Conf Ser. 2011;305.

[246] Fernandes F, Lourenco PB. Evaluation of the compressive strength of ancient clay bricks using microdrilling. J Mater Civil Eng, ASEC. 2007;19:791-800.

[247] EN 772-1. Methods of test for masonry units -Part 1: Determination of compressive strength. 2002.

[248] UNI EN 8942-3. Clay bricks and blocks. Test methods. 1986.

[249] Frigione M, Lettieri M, Mecchi AM. Environmental effects on epoxy adhesives employed for restoration of historical buildings. J Mater Civil Eng. 2006;18:715-22.

[250] ISO 527-1. Plastics-determination of tensile properties- Part 1: general principles. 2012.

[251] ASTM E1356. Standard test method for assignment of the glass transition temperature by differential scanning calorimetry. 2008.

[252] Ratna D. Handbook of thermoset resins.: iSmithers. 2009.

[253] ASTM D638-10. Standard test method for tensile properties of plastics. 2010.

[254] ASTM D3039/3039M. Standard test method for tensile properties of polymer matrix composite materials. 2008.

[255] ACI 440.03-R. Guide test methods for fiber-reinforced polymers (FRPs) for reinforcing or strengthening concrete structures. 2004.

[256] ASTM D7565-10. Standard test method for determining tensile properties of fiber reinforced polymer matrix composites used for strengthening of civil structures. 2010.

[257] Lourenço PB, Fernandes F, Castro F. Handmade clay bricks: Chemical, physical and mechanical properties. Int J Archit Herit. 2010;41:38-58.

[258] ASTM D570-98(2010)e1. Standard test method for water absorption of plastics. 2010.

[259] Frigione M, Lettieri M. Procedures conditioning the absorption/desorption behavior of cold-cured epoxy resins. J Polym Sci B Polym Phys. 2008;46:1320-36.

[260] ASTM D4541. Standard tests method for pull-off adhesion strength of coatings using portable adhesion testers. 2009.

[261] Haldar A, Mahadevan S. Probability, reliability and statistical methods in engineering design: John Wiley. 2000.

[262] Lau D, Buyukozturk O. Fracture characterization of concrete/epoxy interface affected by moisture. Mech Mater. 2010;42:1031-42.

[263] Moy P, Karasz F. Epoxy-water interactions. Polym Eng Sci. 1980;20:315-9.

[264] Tavakkolizadeh M, Saadatmanesh H. Environmental effects on tensile properties of FRP laminates made using wet-lay-up method. Proc of the Second International Conference on Advanced Polymer Composites for Structural Applications in Construction. University of Surrey, Guilford, U.K. 2004. 619-32.

[265] Bonaldo E, Barros JO, Lourenco P. Bond characterization between concrete substrate and repairing SFRC using pull-off testing. Int J Adhes Adhes. 2005;25:463-74.

[266] Dutta PK, Hui D. Low-temperature and freeze-thaw durability of thick composites. Compos Part B. 1996;27:371-79.

[267] Karbhari VM. Response of fiber reinforced polymer confined concrete exposed to freeze and freeze-thaw regimes. J Compos Constr. 2002;6:35-40.

[268] Dohnalek P. Environmental durability of FRP bond to concrete subjected to freeze-thaw action. MIT. 2006.

[269] Davalos JF, Kodkani SS, Ray I, Lin C. Fracture evaluation of GFRP-concrete interfaces for freeze-thaw and wet-dry cycling. J Compos Mater. 2008;42:1439-66.

[270] Green MF, Bibsy LA, Beaudoin Y, Labossière P. Effect of freeze-thaw cycles on the bond durability between fiber reinforced polymer plate reinforcement and concrete. Can J Civil Eng. 2000;27:949-59.

[271] Pan B, Qian K, Xie H, Asundi A. Two-dimensional digital image correlation for in-plane displacement and strain measurement: a review Meas Sci Technol. 2009;20:2001.

[272] ARAMIS user manual- Software- v6.0.2-6. 2009.

[273] Xavier J, de Jesus A, Morais J, Pinto J. Stereovision measurements on evaluating the modulus of elasticity of wood by compression tests parallel to the grain. Constr Build Mater. 2012;26:207-15.

[274] Brynk T, Molak RM, Janiszewska M, Pakiela Z. Digital Image Correlation measurements as a tool of composites deformation description. Comput Mater Sci. 2012;64:157-61.

[275] Ghiassi B, Oliveira DV, Lourenço PB, Marcari G. Numerical study of the role of mortar joints in the bond behavior of FRP-strengthened masonry. Compos Part B. 2012;46:21-30.

[276] Wevers M. Listening to the sound of materials: Acoustic emission for the analysis of material behavior. Ndt & E Inter. 1997;30:99-106.

[277] Tomor AK, Verstrynge E. A fatigue - creep deterioration model for masonry and study of the deterioration processes using acoustic emission monitoring (in preparation). 2013.

[278] Eberhardt E, Stead D, Stimpson B, Read RS. Changes in acoustic event properties with progressive fracture damage. Int J Rock Mech & Min Sci. 1997;34:3-4.

[279] Shiotani T, Yuyama S, Li ZW, Ohtsu M. Quantitative evaluation of fracture processes in concrete by the use of improved b-value. Nondestruct Test Civil Eng. 2000:293-302.

[280] Kurz JH, Finck F, Grosse CU, Reinhardt HW. Stress drop and stress redistribution in concrete quantified over time by the b-value analysis. Struct Health Monit. 2006;5:69-81.

[281] Grosse CU, Finck F. Quantitative evaluation of fracture processes in concrete using signal-based acoustic emission techniques. Cem Conc Compos. 2006;28:330-6.

[282] Aggelis DG, Soulioti DV, Sapouridis N, Barkoula NM, Paipetis AS, Matikas IE. Acoustic emission characterization of the fracture process in fiber reinforced concrete. Constr Build Mater. 2011;25:4126-31.

[283] Soulioti D, Barkoula NM, Paipetis A, Matikas TE, Shiotani T, Aggelis DG. Acoustic emission behavior of steel fiber reinforced concrete under bending. Constr Build Mater. 2009;23:3532-36.

[284] Aggelis DG, Shiotani T, Papacharalampopoulos A, Polyzos D. The influence of propagation path on elastic waves as measured by acoustic emission parameters. . Struct Health Monit-an Intern J. 2012;11:359-66.

[285] EN 13477-2 Non-destructive testing. Acoustic emission. Equipment characterization. Verification of operating characteristic. London: British Standard Institution. 2010.

[286] Brown J, Hamilton H. Quantitative infrared thermography inspection for FRP applied to concrete using single pixel analysis. Constr Build Mater. 2010.

[287] Krapez J, Cielo P. Thermographic nondestructive evaluation: data inversion procedures part I: 1D analysis. Res Nondestruct Eval. 1991;3:81-100.

[288] Lourenço PB. Recent advances in masonry structures: Micromodeling and homogenization. In: Multiscale Modeling in Solid Mechanics: Computational Approaches: Imperial College 2009. p. 251-94.

[289] DIANA. Displacement analysis finite element software. V. 9.4, TNO Building Division, Delft, The Netherlands, 2009.

[290] Vecchio FJ, Collins MP. Compression response of cracked reinforced concrete. J Struct Eng. 1993;119:3590-610.

[291] Rots J. Crack models for concrete: discrete or smeared? fixed, multidirectional or rotating. Heron. 1989;34.

[292] Bazant ZP, Oh BH. Crack band theory for fracture of concrete. Mater Struct. 1983;16:155.

[293] Teng J, Zhang J, Smith S. Interfacial stresses in reinforced concrete beams bonded with a soffit plate: a finite element study. Constr Build Mater. 2002;16:1-14.

[294] Hein V, Erdogan F. Stress singularities in a two-material wedge. Int J Fract Mech. 1971;7:317-30.

[295] Eurocode 6. Design of masonry structures, Part 1-1: General rules for building –Rules forreinforced and unreinforced masonry. 2005.

[296] Milani G, Rotunno T, Sacco E, Tralli A. Failure load of FRP strengthened masonry walls: Experimental results and numerical models. SDHM. 2006;2:29-50.

[297] Grande E, Milani G, Sacco E. Modeling and analysis of FRP-strengthened masonry panels. Eng Struct. 2008;30:1842-60.

[298] Lourenço PB, Rots G, Blaauwendraad J. Continuum model for masonry: parameter estimation and validation. J Struct Eng. 1998;124:642-52.